CIC biomaGUNE
CENTER FOR COOPERATIVE RESEARCH IN BIOMATERIALS

eman ta zabal zazu
Universidad del País Vasco
Euskal Herriko Unibertsitatea

Modifications of Graphene Prepared by Chemical Vapor Deposition for Diagnostic Applications

Juan Pedro Merino Rusillo

Carbon Bionanotechnology Lab

2020

Agradecimientos/Acknowledges:

Every great adventure needs heroes without whom these would not be possible. Fortunately, I have been surrounded by the best possible traveling companions. Four years, too much time and so many people with whom I have shared experiences in a professional or personal way. Thank you so much.

I would like to thank my supervisor Prof. Maurizio Prato. Thank you so much for giving me the opportunity and the means for performing this work.

Thank you to the Graphene Flagship Project for supporting this work.

Dr. Alejandro Criado, pocas personas tienen la suerte de tener un director de tesis como tú. Gracias por darme esta oportunidad, ser el mejor guía posible, por tu entusiasmo (menos mal que lo ponías tú) y por estar siempre ahí. Gracias por ser ese héroe de película que todos querríamos ser.

Manu, un porcentaje muy alto de esta tesis es gracias a ti. Gracias por ser un gran apoyo y por todo lo que me enseñaste. Por tu paciencia, por dejarme ir a tus hombros. Gracias por ser "mama". Pocas personas como tú existen en este mundo. No cambies nunca.

Hui-Lei, you know that I could not have done it without you, man. Xièxiè.

Fortunately and unfortunately, a lot of people have come and go during this period. Thank you to the members of the Prato's group for your help as researchers and as people. Jenni, Nuria, Antonio, Blanca, Paolo, Engin, Natalia, Nina, Donato, Riccardo, Alessandro, Ricard, Lucía, Matteo, Cecilia, Shadi, Taherek, Dario, Paula, Lydia and Guille.

Niels' group, an office does not have to be boring. Thank you to Alvaro, Juan, Nerea, Bego, María, Eli, Olatz, Anna, Julie, Rachel, Bárbara, Niels, Cris, Raik, María, Damian and Annna.

I want to show all my gratitude to the technicians and the administration department people from CICbiomaGUNE. Thank you so much to Javi Calvo, Daniel Padró, Judith Langer, Marco Möller, Charo, Dorleta, Isaac, Sonia, Josune, David, Jorge… Your help and support have been fundamental, you are my new superheroes! Especially Luis Yate, I have met few people with your patience and kindness. I have learned a lot from you. Thank you. In the same way, I would like to thank to Janire and Belén for your time. And thanks to Loli for spending so much time looking for holes.

Thank you so much to that CICbiomaGUNE-people, that maybe just for a few weeks or for years, with whom have shared experiences. Ángel, Ada, Marta, Lucio, Natalie, Gregorio, Sven, Susana, Carmen, Stefan, David, Cristina… I might be forgetting someone, sorry. Possibly, it was "the best summer of our life".

Thank you so much to the Graphene Flagship project-crew and to our collaborators during these years. Thank you Rosa Villa for allowing me to spend time in your group and to Eli,

Antón, Jose and Edu for your help and your patience to explain your “electronic stuffs” for dummies.

Regarding experiences... Thank you so much to the Prof. Yuyong Mai for giving me the opportunity to spend three months in his lab and the opportunity to learn about the Chinese culture (and about its work, for sure…). Ann, thank you for helping me with all the paperwork, Fugui and Luan, for your time, Peng Fei for the gameplay-nights and Silver for the adventures.

A aquellas personas que se montaban en el 17 o 28 camino del Oncológico que a veces me tenían que recordar porqué seguir yendo a trabajar.

Thanks to Alexandra Elbakyan for doing this thesis easier.

Patrizia, Marco y Karolina. Habéis sido como una familia para mí en San Sebastián. Gracias por todo.

Dorleta, gracias por mostrarme Euskalherria desde dentro.

A la otra mitad de mi vida: Gracias a la pachanga de los sábados, al futbol de los jueves, al trail de los domingos, al surf de los martes, a la escalada de los viernes, a basket Sagües, a PolyGUNE F.C., a los miles de km que aguantaron mis piernas, a toda la gente con la que compartí esos momentos y al País Vasco por tener tanto monte y tantas olas. Mila esker!

A mi familia química de Santiago por haberme ayudado a llegar hasta aquí. Enrique Guitián, Dolores Pérez, Diego Peña, José Miguel, Manu, Sara, Sabela, Berta, Jesús, Diego García, Félix, Vero, Amorín, Roi, Samu... A Iago y Cris por tantas cosas pasadas. Por la “movida intramolecular del chisme”.

Echando mucho más la vista atrás, mil gracias Justo Cobo, Pablo Linares, Joaquín Altarejos, Manuel Nogueras y Adolfo Sánchez por enseñarme química orgánica con tanto cariño. A Puche, Gea, Pepelu ¿Quién lo iba decir? A Alba, por marcar un punto de inflexión. Gracias Paloma y Cris por seguir aguantándome.

A los Chumbis y a los Espartanos por ser mi guardián entre el centeno durante tanto tiempo. A los Pistachos del Infierno… helado de pistacho.

A mis antiguos compañeros del Juleca, por enseñarme cosas buenas y cosas malas.

A Sherlock Holmes, Indiana Jones, Batman, Flash, al Doctor, a la comunidad del anillo, Spiderman, Valenti Sanjuan y a los Junior de Oro por haber sido buenos compañeros de viaje.

A Gabriela, por ser la persona más comprensiva que me he encontrado en este camino. Gracias por aguantarme, nunca dejaré de agradecértelo.

A mis padres por ser las personas más fuertes que conozco, apoyarme y seguir luchando.

A mi hermano por hacer el esfuerzo de entenderme.

Resumen de Tesis

El grafeno es un alótropo de carbono que ha demostrado tener excelentes propiedades electrónicas, mecánicas y térmicas. Gracias a ello, tiene un gran potencial en campos como biomedicina o electrónica. Entre sus distintos derivados, el grafeno crecido por deposición química de vapor (CVD) y transferido sobre superficie, ha demostrado ser un material idóneo para este tipo de aplicaciones debido a su elevada conductividad, carácter ambipolar de efecto campo, y una relación calidad/coste de producción conveniente.

Sin embargo, la investigación del grafeno aún está en sus inicios y es necesaria una alta reproducibilidad de sus resultados para la futura comercialización y estandarización de los dispositivos de grafeno. Para ello, en esta tesis se ha desarrollado un protocolo de limpieza posterior al proceso de litografía con el fin de eliminar los residuos poliméricos de dicho proceso y obtener el mejor rendimiento electrónico. Además, la implementación de capacidades sensóricas sobre dispositivos electrónicos como los transistores de grafeno permite el desarrollo de herramientas para diagnóstico y tratamiento de diversas condiciones neurológicas como epilepsia o Parkinson. Con este propósito, el grafeno ha sido modificado covalentemente vía una adición radicalaria siguiendo diferentes estrategias compatibles con el diseño del dispositivo, con el fin de anclar los bio-receptores de interés. Como prueba de concepto, el sistema descrito se usó con un aptámero selectivo para trombina, demostrando resultados prometedores.

Así mismo, se demostró por primera vez el uso del grafeno CVD en espectrometría de masas MALDI-TOF gracias a su capacidad de ionización/desorción. En concreto, se ha desarrollado un sistema compuesto por diferentes azucares modificados sobre grafeno como herramienta diagnóstica para la detección de proteínas. En este dispositivo se usó el grafeno como superficie asistente para la ionización/desorción láser en espectrometría de masas que, combinado al carácter conductor del grafeno, ha permitido reemplazar ITO como material de soporte y trabajar en condiciones de ausencia de matriz.

Abstract

Graphene is a carbon allotrope with a unique set of electrical, mechanical and thermal properties. For that reason, graphene has a great potential in biomedical or electronic applications. Graphene grown by Chemical Vapor Deposition (CVD) and transferred on substrate has shown to be a suitable material for these kind of applications due to its high conductivity, ambipolar behavior in field effect transistors and a good quality/price production ratio.

Since it is necessary standardization and thus commercialization, the development of reproducible measures is required. For that reason, in this thesis a cleaning protocol for CVD graphene transistors after the photolithography process was developed in order to reduce the polymeric residues of this process. The sensing properties implementation in electronic devices like graphene transistors allows the development of diagnostic tools and the treatment of different neural diseases such as epilepsy or Parkinson. With this purpose, graphene has been covalently modified by radical addition following different compatible strategies with the device design in order to anchor bioreceptors. As proof of concept, the described system was used with a selective thrombin aptamer, obtaining promising results.

In addition, the use of CVD graphene was developed in MALDI-TOF mass spectroscopy for the first time. In particular, a microarray composed by different modified sugars on graphene was developed as a diagnostic tool for protein detection. Graphene was used as surface-assisted laser desorption/ionization in mass spectrometry. This, combined with the conductive character of graphene allowed the replacement of ITO as material support and in matrix absent conditions.

Index:

List of abbreviations:

AAL: *Auleria aurantia* lectin

AAL-555: *Auleria aurantia* lectin labeled with Alexa Fluor™ 555

AFM: Atomic morce microscopy

ATP: Adenosine triphosphate

BSA: Bovine serum albumin

C-dots: Carbon dots

CCD: Charge-couple device

CNMs: Carbon Nanomaterials

CNTs: Carbon nanotubes

CNP: Charge neutrality point

COVID-19: Coronavirus disease 2019

CVD: Chemical vapor deposition

DBT: 4-docosyloxy-benzenediazonium tetrafluoroborate

DC: Direct current

DFT: Discrete Fourier Transfom

DHB: 2,5-dihydoxybenzoic acid

DIAD: Dialkyl azodicarboxylate

DNA: Deoxyribonucleic acid

DOS: Density of states

DMF: N,N-dimetilformamida

ECL: Electrochemiluminiscence

EDCL: Electrochemical double layer capacitor

EDL: Electrical double layer

EG: Epitaxial growth

FAM: Fluorescein amidite

FET: Field effect transistor

FRET: Fluorescence resonance energy transfer

g-SGFET: Graphene solution gate field effect transistor

GBMs: Graphene-based materials

GFET: Graphene field effect transistor

g_m: Transconductance

GO: Graphene oxide

GOx: Glucose oxidase

GONRs: Graphene oxide nanoribbons

GlcNac: N-acetyl-D-glucosamine

GQDs: Graphene-quantum dots

HA: Hemagglutinin

hBN: Hexagonal boron nitride

HOMO: Highest occupied molecule orbital

I-V curve: Current voltage curve

***Ids*:** Drain-source current

ITO: Indium tin oxide

Lac: Lactose

LacNac: N-acetyl-D-lactosamine

LDI: Laser desorption/ionization

Le^x: Lewis^x trisaccharide

LUMO: Lowest unoccupied molecular orbital

LOD: Limit of detection

MALDI: Matrix-assisted laser desorption/ionization

mGFET: Graphene chip

MGFET: Graphene macrotransistor

MS: Mass spectrometry

MWCNTs: Multiwalled carbon nanotubes.

NBD: 4-nitrobenzenediazoniume

NHS: N-hydroxysuccinimide

NMP: N-methyl-2-pyrrolidone

NPs: Nanoparticles

ODCB: *Ortho*-dichlorobenzene

OFETs: Organic field-effect transistors

OLEDs: Organic light emitting diodes

OLC: Onion like carbon

OTS: Octadecyltrichlorosilane

PCB: Printed circuit board

PDMS: Polymethylsiloxane

PMMA: polymethyl metracrylate

PTCDA: Perylene-3,4,9,10-tetracaarboxylic dianhydride

PVA: Poly(vinyl alcohol)

rGO: Reduce graphene oxide

RMS: Root mean square

RNA: Ribonucleic acid

SARS-CoV-2: Severe acute respiratory syndrome coronavirus 2

SALDI: Surface-assisted laser desorption/ionization

SELDI: Surface enhance laser desorption/ionization

SEM: Scanning electron microscopy

SERS: Surface-enhanced Raman spectroscopy

SWCNTs: Singlewalled carbon nanotubes

STM: Scanning tunneling microscopy

t-BLG: twisted bilayer graphene

TBA-NH2: Anti-thrombin aptamer funcionalized with NH_2 group

TBD: 3,5-bis-tert-butylbenzenediazonium

TCNE: Tetracyanoethylene

TEM: Transmission electron microscopy

TFA: Trifluoroacetic acid

TOF: Times of flight

U_D: Dirac Point

UHV: Ultra-high vacuum

***Vds*:** Drain-source voltage

***Vgs*:** Gate-source voltage

XPS: X-ray photoelectron spectroscopy

1. INTRODUCTION

"While it is fun to think about the wonderful role of serendipity in the story, one should also spend a bit of time comprehending the inevitability of the discovery as well. The only character of true genius in the story is carbon. Fullerenes are made wherever carbon condenses. It just took us a little while to find out."

DISCOVERING THE FULLERENES

Nobel Lecture, December 7, 1996

Richard E. Smalley

1. Introduction

In this introduction, we will try to show and explain, as briefly as possible, one of youngest (in its fifteens now) carbon nanomaterial, Graphene. From its structure, chemistry and properties to the current and potential applications that this material could offer us.

Carbon comes from the Latin *carbo* meaning "charcoal". It was proposed as an element by Antoine-Laurent de Lavoisier in the second half of the 18th century. In 1772, while burning diamond and carbon samples, Lavoisier, discovered that both substances do not produce water vapor and they generated the same amount of carbon dioxide gas per gram, elucidating with this experiment the two firsts allotropic form of the carbon.[1]

Depending on the different ways that the carbon atoms can bond, added to the ability to hybridize as *sp*, sp^2 or sp^3, give rise to different allotropic forms.[2] Taking this different hybridization into account, one of those allotropic forms that we can find are Carbon Nanomaterials (CNMs).[3]

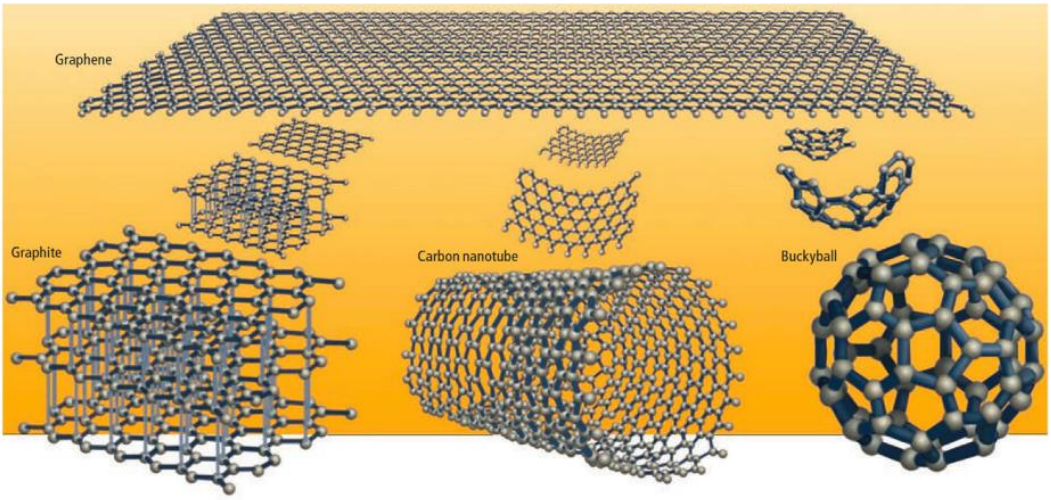

Figure 1. Different allotropes of carbon. Adapted from Geim et *al*. 2008.[4]

Within the possible classification ways, we can categorize them according to the structure dimensionality (Figure 1). So, starting with the 0D CNMs, in 1985, striking a laser on a sheet of graphite, Kroto, Curl and Smalley found the spherical structure that was called Buckminsterfullerene or C_{60}, composed by sp^2-sp^3 carbon atoms.[5] In addition, in a serendipitously way, onion like carbon (OLC) and Carbon dots (C-dots) were discovered, the first one through the irradiation of carbon nanotubes (CNTs) with electron beams[6] and the second one during a purification of CNTs, prepared by arc-discharge technique, using gel electrophoresis.[7]

The discovering of 1D CNMs was more controversial. The first time that CNTs were observed in a transmission electron microscopy (TEM) was in 1952 by a Russian group[8], and the next in 1976 by Agnes Oberlin.[9] But it was not until 1991 when the discovering of the single walled carbon nanotubes (SWCNTs, composed by sp^2 carbon atoms) was attributed to Iijima.[10]

However, it was in 2004, when Geim and Novoselov isolated and characterized Graphene for the first time, composed by a hexagonal lattice of sp^2 carbon atoms. Thanks to this finding they were awarded with the Novel Price in 2010.[11] Starting with their "Friday evening experiment" the real revolution in the 2D material field, and consequently in the CNMs one.

In this thesis Graphene, its chemical modification and its applications in biosensing will be the main spotlight.

1.1. Graphene-Based Materials

Despite the term "graphene" refers to a single atom thick sheet of hexagonally arranged *sp*^{2}-bonded carbon atoms,[12] it was used without precision to describe many different graphene-based materials (GBMs) due to the emerging numbers of researches and publications in the last decade. GBMs include also few-layers graphene, graphene oxide (GO) reduce graphene oxide (rGO), graphene nanosheets, graphite plates, graphene ribbons and graphene quantum dots (GQDs). For that reason, in 2014, was developed by Wick and coworkers a nomenclature model to classified the different graphene derivatives based on three morphological parameters: lateral dimensions, carbon/oxygen ratio and number of layers.[13]

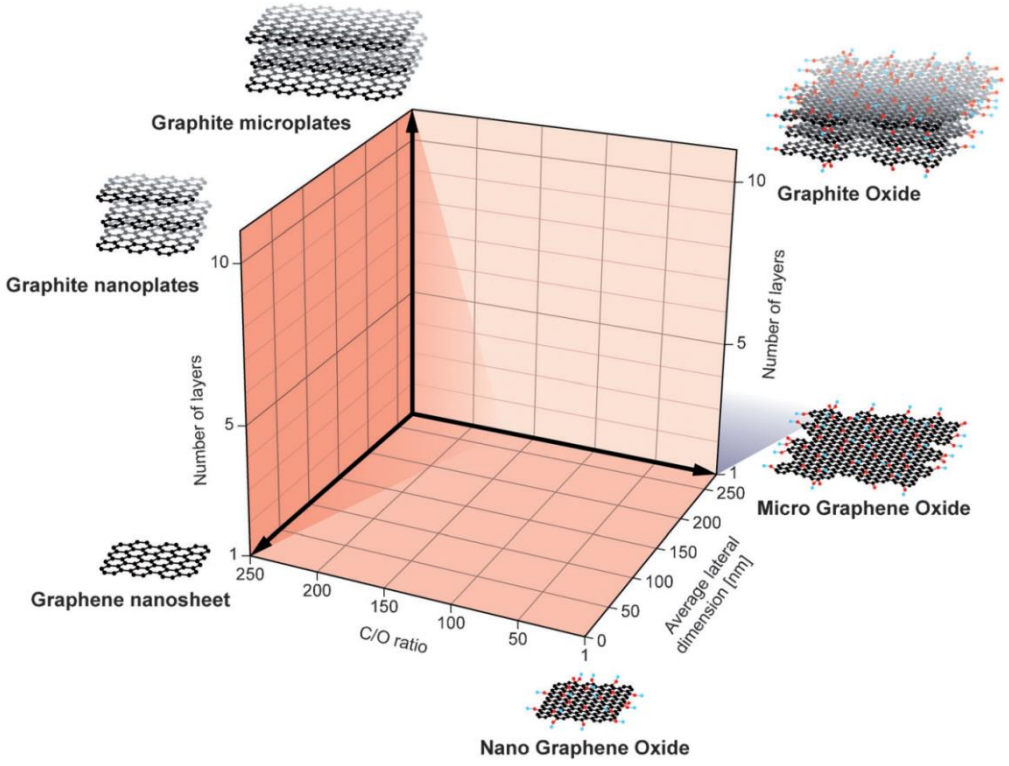

Figure 2. Classification of the different graphene derivatives in function of their principal properties. Adapted from Wick *et al.* 2014.[13]

The definition of these parameters is crucial because the GBM properties extremely depend on them. For example, elasticity, adsorptive capacity or surface area are given by the number of layers as well as conductivity is related with the C/O ratio.[14]

The biological relevance of this material is in correlation with its surface hydrophobicity/hydrophilicity. Therefore, the surface inhomogeneity produced for the

oxidation to obtain GO derivatives can enhance the biocompatibility and the dispersibility of graphene. Generally, GO presents a C/O ratio from 4:1 to 2:1 but, as will be explained in the production method section, it can be reduce and the C/O ratio is decreased to values from 12:1 to 246:1.[15] In correlation with these biological properties, graphene sheets must have a suitable size (lateral dimension) for the chosen environment. For example, graphene nanoribbons which have less than 100 nm of lateral size or GQDs with even smaller lateral dimension (< 10 nm). In order to modulate these three parameters (number of layers, C/O ratio and lateral dimension), the production of graphene is a relevant topic in this thesis.

1.2. Graphene production.

The manufacture of graphene with controlled size, morphology, edge structure and number of layers is a challenging process. In addition, there is a need to find a method which achieves a large-scale production with reproducibility and homogeneity. Graphene can be obtained by two approaches: top-down, starting with graphitic material and splitting graphene layers from it;[16] and bottom-up approaches from small carbon precursors, such as chemical vapor deposition (CVD) or chemical synthesis of nanographenes.[17] Graphene was initially produced by **mechanical exfoliation** of graphite in the mentioned sticky tape experiment by separation of the graphite layers into individual graphene sheets.[11] This top-down method provides the highest quality graphene sheets. However, it is not suitable for mass production. Due to the limitation in the layer control and in the dimension, since the maximum sample size is around 1 mm.[18]

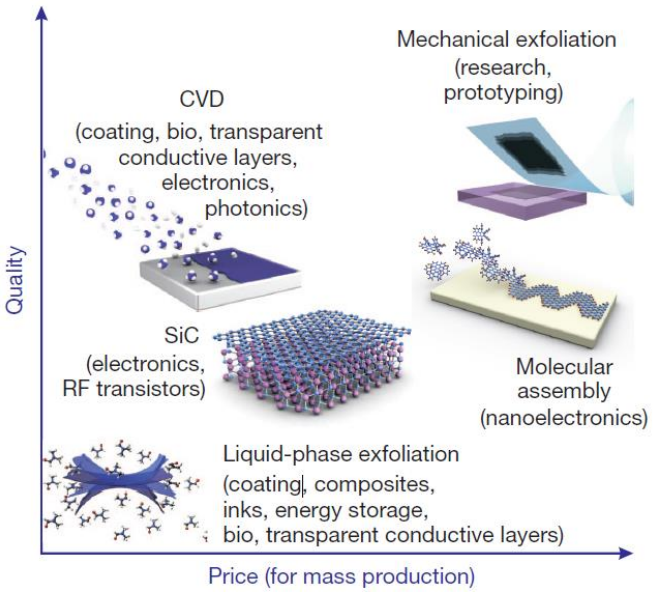

Figure 3. Summary of the different methods for graphene production. Adapted from Novoselov *et al.* 2012.[19]

To overcome the van der Waals forces which bonded the graphene sheets in graphene is necessary to apply energy by mechanical or chemical methods. One of the most used methods to overcome this interaction between layers is the **liquid phase exfoliation**.[20] This method is based on the exposure of the graphite to a solvent, in which graphite and graphene are dispersible, usually NMP, DMF or ODCB,[21] followed by a sonication step to split the

monolayer/few-layers graphene. To separate the resulting graphene from the dispersion, it is necessary to centrifuge the suspension and, by precipitation of the graphitic n-layer graphene, isolate the suspended few-layers material. In order to obtain an exfoliated material with a low number of layers, it is necessary to repeat the centrifugation step several times. Liquid phase exfoliation represents an easy and low cost approach. However, it has important disadvantages. It is required a large volume of solvents (which are usually highly toxic), the obtained yield respect to the starting graphite is low[22] and the use of additives which are employed to enhance the exfoliation efficiency and suspension stability are difficult to remove.[23]

Oxidation of graphite leads to a delamination process by the incorporation of oxygenated functional group such as epoxy, hydroxyl and carbonyl to overcome the attractive van der Waals forces. The amount and ratio of the different introduced groups depend on the oxidative methods. In 1859, Brodie explored the reaction of graphite with $KClO_3$ in HNO_3 and found that the resulting material was dispersible in pure or basic water.[24] Years later, Staudenmaier improved the method adding chlorate and sulfuric acid.[25] Hummers and Offeman developed an alternative oxidation method with a mixture of $KMnO_4$ and H_2SO_4.[26] Despite this method has been improved in the last years to tune the amount or distribution of the oxygen-containing groups and to avoid the production of toxic gases,[27] it has been the most used one for the generation of GO because of the relatively high ratio C/O (≈ 2.30) compared to others approaches.[28] In 2010 it was described a method to obtain graphene oxide nanoribbons (GONRs) from multiwalled carbon nanotubes (MWCNTs).[29] The produced GONRs have a higher degree of oxidation but lower amount of holes on the basal plane. And more recently in 2019, a microwave-assisted method was reported.[30] This method significantly reduced the reaction time to 20 minutes (from 5 days). The generated GO has higher C/O ratio, but also higher D/G band ratio (i.e. more defects).

By the **reduction of graphene oxide** is possible to remove partially the oxygenated groups, partially restoring the π-network in order to get similar properties that graphene. The obtained material is usually called as reduce graphene oxide (rGO).[31] The reduction could be carrying out mainly by three strategies: [32] Thermal reduction, which involves temperature of 250 °C,[33] chemical reduction using hydrazine[34] or, as a new environmentally friendly, ascorbic acid[35] or electrochemical reduction.[36] These are very scalable methods, however, rGO has relatively poor yields in terms of surface area due to the imperfections and vacancies creation. In the same way that for the synthesis of GO, recently a microwave-assisted method has been developed.[37] Thanks to the residual oxygen groups that still remain, rGO has better dispersibility in polar solvent like water which makes it suitable for biological applications.

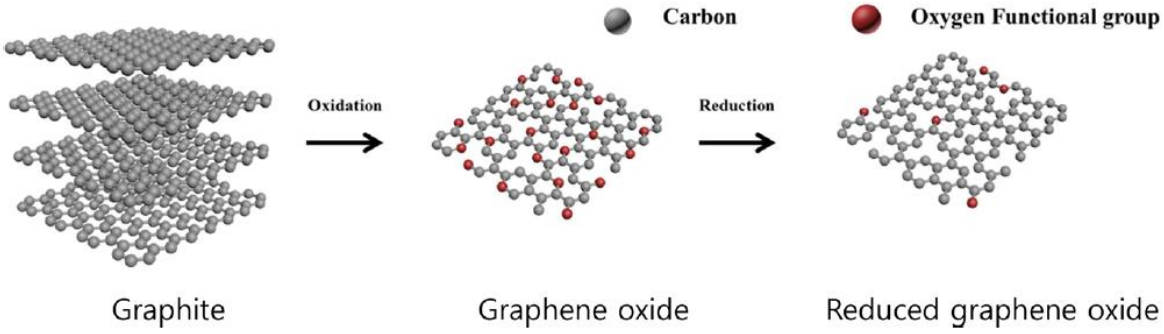

Figure 4. Structure of the species involves in the graphite oxidation and reduction of the graphene oxide to obtain graphene oxide. Adapted from Lee *et al.* 2015.[38]

Another promising method is the **thermal decomposition of SiC**. In this method, a SiC bulk sample is annealed at ≈ 1400 °C in vacuum conditions. At that temperature, the silicon atoms sublimate and the surface carbon atoms rearrange in order to form the graphitic layers. [39] One of the advantages of the thermal decomposition SiC method is that the graphene can be directly obtained onto the semiconductive desired surface, so it is not necessary a transfer step, avowing some possible contamination. However, this method is still really expensive and has size limitation.

One of the most promising applications of graphene is in the field of electronics. However, these applications require high quality large-area graphene. In the last years, large domain size **Chemical Vapor Deposition (CVD)** graphene grown on metal surface makes it possible to explore within this potential application that graphene had been so far. CVD is a technique where a gas precursor is decomposed over a substrate surface and films of the material are deposited on it.[40] This process is thermally and catalytically driven by the substrate.

In the case of graphene, methane is the chemical vapor precursor. In particular, when a mixture of CH_4 and H_2 gases get in contact with the catalytic surface (such as Ni, Pd, Ru, Ir or Cu) in a heated chamber, they decompose over the surface to form the desired material film.[41] In terms of uniform deposition of high quality, single layered graphene over large areas have been achieved on polycrystalline copper foils.[42]

The growth of graphene by CVD starts as nucleation of graphene island (Figure 5a).[43] These initial graphene forms have different lattice orientations depending on the crystallographic orientations of the Cu grains on which they are growing. The created film is predominantly single-layer graphene (< 95%). In this process, wrinkles in the graphene are produced due to the different thermal expansion coefficient (Figure 5b).

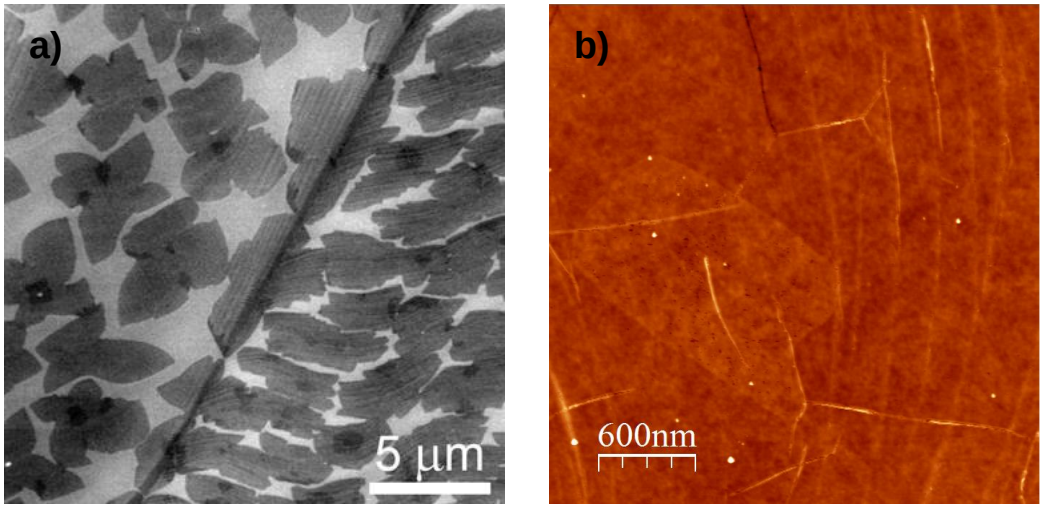

Figure 5. SEM image of the graphene nucleation on a Cu substrate for 1 min growth time adapted from Li *et al.* 2009[43] and b)AFM image of CVDG single and bilayer wrinkles (Grown on Cu and transfer onto SiO_2.

In 2009, Li and coworkers studied the differences in the surface catalyst mechanism for graphene on Cu and Ni.[44] They used the separation of the $^{12}CH_4$ and $^{13}CH_4$ Raman modes to observe the distribution of graphene domains for the different surfaces. For that, they used sequential dosage of these two chemical vapored isotopes and studied the growth mechanism in function of the diffusion of these isotopes into the metal. For metal like Ni where the solubility of $^{x}CH_4$ is high, the gas diffuses into the metal surface and then, segregation and precipitation happened. The resulting graphene will consist in randomly mixed isotopes (Figure 6a). In an opposite way, if the diffusion is low, graphene grows by surface adsorption in function of the dosage sequence employed (Figure 6b).

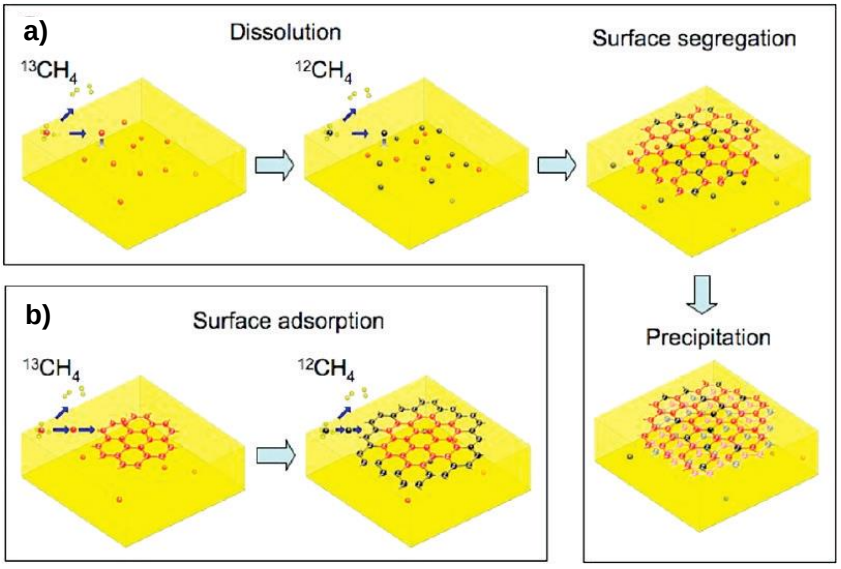

Figure 6. Schematic representation of the graphene growth mechanism. a) by CH_4 diffusion in the metal surface and b) Graphene growth by surface adsorption. Adapted from Li *et al.* 2009.[44]

Tuning of the properties of graphene is a point of great interest. It is reported the band gap opening in order to get a semiconductor behavior with the introduction of a second graphene layer (Figure 12).[63] Despite the generation of bilayer graphene or few-layer graphene is usually produced accidentally by the stacking of them,[22] a controllable development of this stacking

was required. The called AB-stacked bilayer graphene (i.e. the half of the atoms in the second layer is on top of the empty center of the hexagons of the second one) is generated by the combination of an existing monolayer and a second step growth in the furnace.[45] A less common interaction is the AA-stacked bilayer graphene where layer are aligned. It is generated by a sequential graphene hexagonal boron-nitride (hBN) flake pick-up steps using a hemispherical handle substrate.[46] In fact, with this last approach the local bilayer configuration could be modulated to get AA or AB.

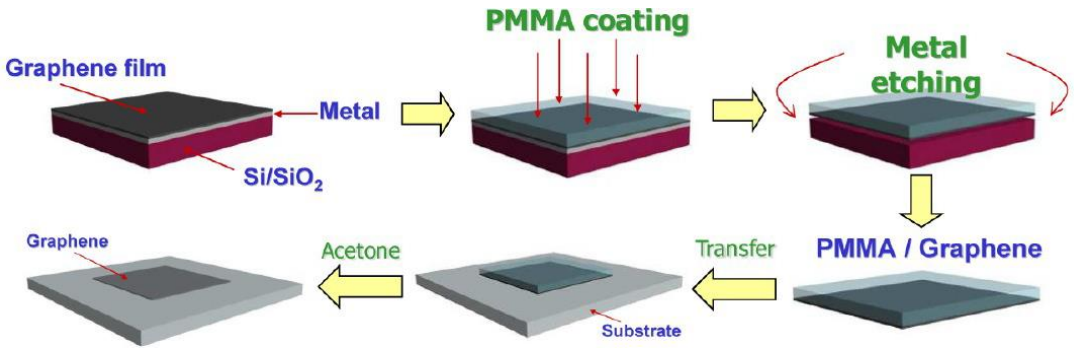

Figure 7. Schematic representation of the transfer process. Adapted from Zhang *et al.* 2013.[47]

In order to deposit the graphene in the desired surface for the corresponding application, transfer method is required. Thereby, graphene is coated with a polymethyl metracrylate (PMMA) layer to facilitate the transfer to the alternative surface with the minimum damage.[48] Then, the metal layer is etched and deposited onto the target substrate. Finally, the PMMA layer is removed with acetone (Figure 7).

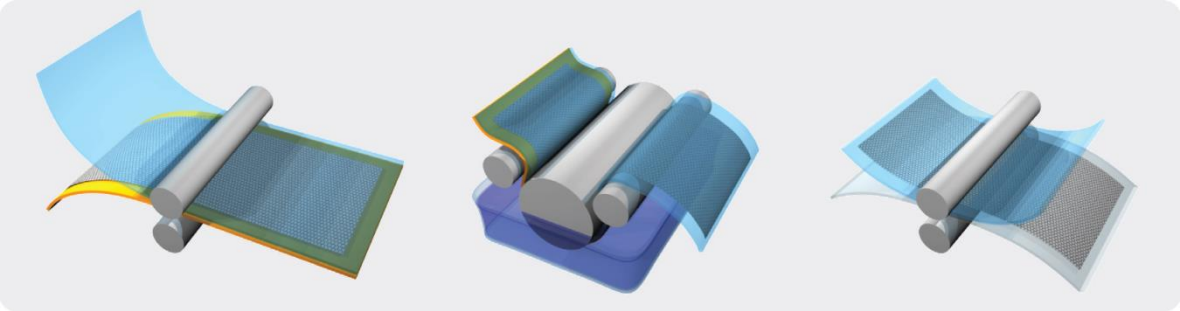

Figure 8. General scheme of the roll-based production of CVDG. Adapted from Bae *et al.* 2010.[49]

For the scale-up production of CVD graphene, Ijima and coworkers reported a roll-to-roll production and of predominantly monolayer 30-inch graphene films grown by chemical vapor deposition onto flexible substrates (Figure 8).[49] This method is perfectly suitable for the production of graphene at industrial level. Electronic applications required high quality large surfaces for its implementation in devices as will be shown in the following sections. CVD graphene has become in the most promising graphene in terms of quality/price ratio with a higher uniformity and homogeneity. For that reason, this graphene derivative will be the main material use in this thesis because of its potential in the field of electronics, and due to that fact, we will focus on this graphene derivative in the following sections.

This transfer method used to be source of contamination which might introduce chemical doping species, reduces carrier mobility, and degrades the signal to noise ratio. Since alternative

microfabrication technology is not currently identified, solutions based on post-lithography cleaning processes have been evaluated. For example Yurgens and coworkers reported a mechanical cleaning of CVD graphene by using of atomic force microscopy (AFM) tips.[50] As shown in Figure 9, an AFM tip in contact mode is able to remove the residual PMMA and AZ5214E polymer of the measured squared. It is described as an effective method, but it cannot be applied to large areas. Ozone plasma environments have been reported as effective dry cleaning process, but the time exposure should be in function to the quantity of polymer residues, since a long exposure could damage the graphene lattice, induce defects or generate local oxidation.[51] The most common methods are based on solvents that can solve PMMA like acetone, chloroform, toluene or N,N-Dimethylacetamide.[52] Nevertheless, removing the PMMA residue cannot be completely dissolved with any known organic solvents. In addition, they are not compatible with others added elements that are necessary in the different electronic devices of graphene.[53]

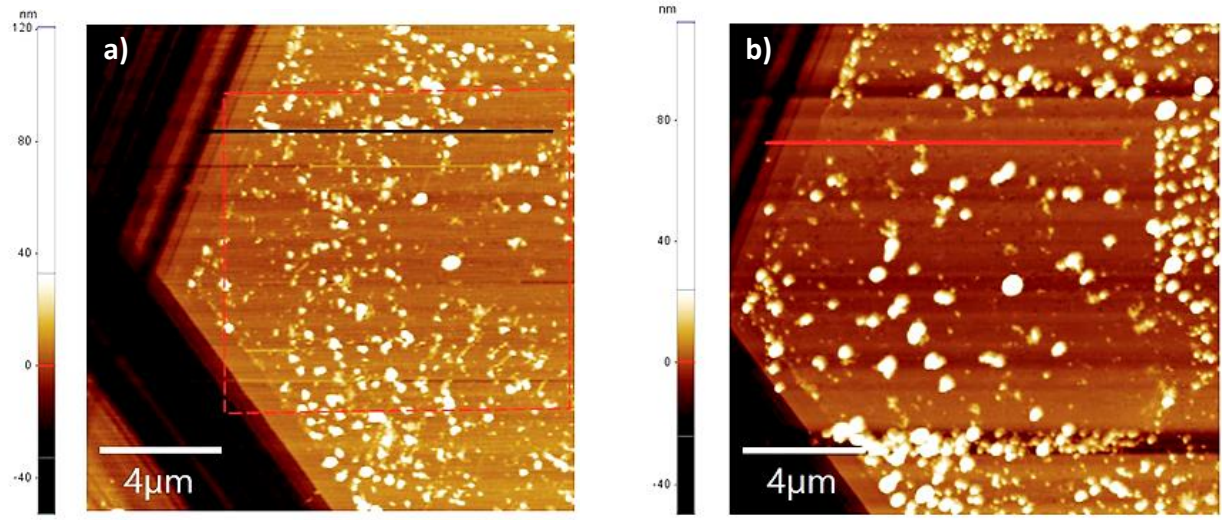

Figure 9. Tapping mode AFM image with PMMA residue a) before and b) after cleaning with AFM tip. Adapted from Choi *et al.* 2017.[54]

1.3. Graphene properties

GBMs present a unique set of electronic, magnetic, thermal, optical and biological properties. Consequently, they have been used for several applications. As mentioned above, in graphene structure, each hybridized sp^2 carbon atom is bonded with other three carbon atoms arranged in a honeycomb lattice to obtain a single atom thick sheet. Presumably with that thickness (0.335 nm) should not exist a material with useful mechanical properties; however, a stress-strain curve of 130GPa was found for graphene by AFM.[55] By using the same characterization technique, Prof. Hone and coworkers reported that graphene has a really high flexibility, with a young modulus of 1TPa. This is particularly important for electrophysiological applications since there is a poor match between devices and biological texture surface. In this aspect, it should also be noted that its weight is 0.77 mg m^{-2}, which makes graphene a light material and the strongest one ever measured.

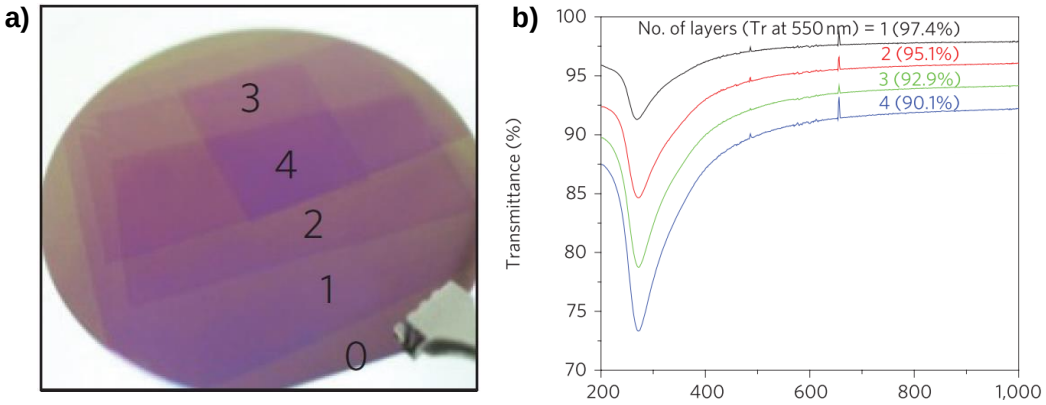

Figure 10. a) Transferred graphene layers on SiO_2 wafer and b) UV-Vis spectra of transferred graphene showing >95% transmittance. Adapted from Bae *et al.* 2010.[49]

In addition to the graphene properties due to the single atom thickness, this material presents a high optical transparency, 97.7%.[49] Due to that fact, the number of layers can be determined by the transmittance of light.[56] Furthermore, with the correct physical or chemical treatments, the connectivity of electrons can be reduced to generate photoluminescence.[57] This property makes graphene, together with his electronic properties, as a new material for optoelectronics, photodetectors or transparent electrodes.

Regarding the thermal properties of graphene, it has the highest thermal conductivity known: 5000 W m^{-1} K^{-1}.[58] Thanks to its capacity to dissipate heat, graphene can be used as thermal interface material and heat spreader. Particularly, the use of graphene in micro- and nano-electronic devices where heat could be a limiting factor is a topic of great interest.

The electronic properties of graphene come from its orbital hybridization and structure. While one *s*-orbital and two *p*-orbital (*pz* and *px*) are hybridized to create the sp^2 hybrid orbital, which contributes to the planar assembling, the additional *pz*-orbital is perpendicular. This orbital leads to delocalized π bonds with its neighboring atoms.[59] Thus, π electrons are free to move in the plane with a good conductivity. In the graphene band structure (Figure 11), its conduction and valance bands meet at the Dirac points with a linear shape instead of the parabolic one for insulators and conductive materials. As a result, graphene is defined as a zero-band gap semiconductor.[60] Thus, charge carries on graphene behave as Dirac fermions (relativistic particles), allowing a high charge mobility ($2 \cdot 10^5$ cm^2 V^{-1} s^{-1}), low resistivity (10^{-8} $\Omega \cdot m$), and avoiding the scattering mechanism.

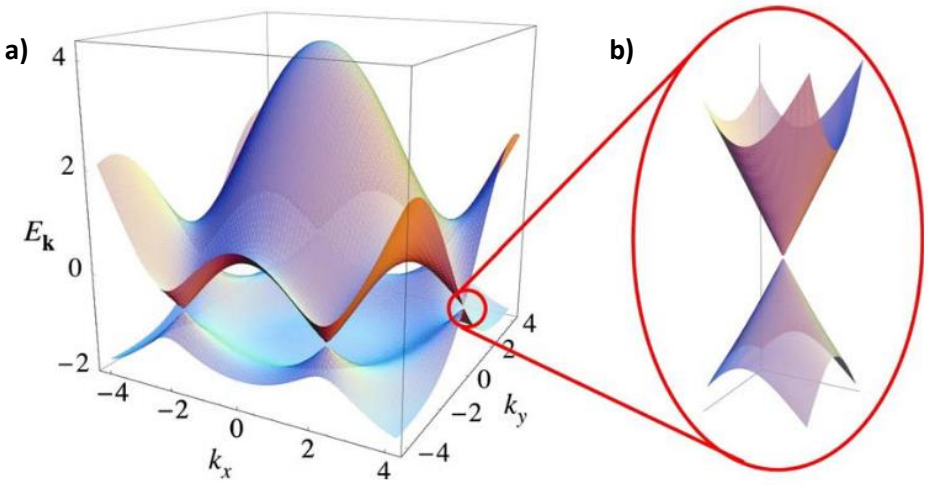

Figure 11. a) Graphene band structure and b) Dirac point energy band. Adapted from Neto *et al.* 2009.[61]

Due to the lack of an intrinsic band gap, graphene has ambipolar behavior. This property opens new opportunities in the field of biochemical sensors related to the graphene field-effect transistors (GFETs) devices.[62] As it will be explained more in details during this thesis, different parameters could affect these electronic properties. In 2007, it has been reported that the stacking of a second graphene layer could induce insulating state.[63] In Figure 12 is shown the change in the band structure for a bilayer graphene when a magnetic field is applied.

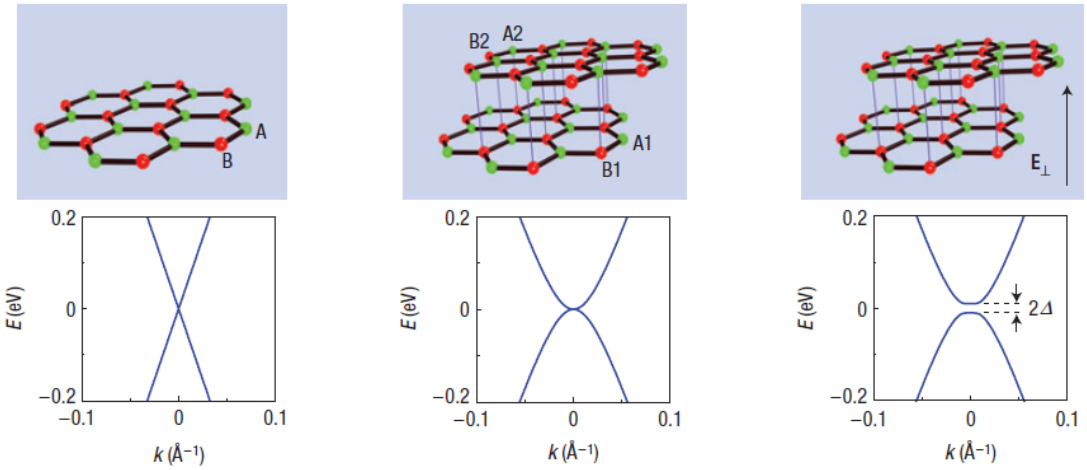

Figure 12. Schematic energy diagrams of a) monolayer graphene and bilayer graphene b) before and c) after to applied a perpendicular electric field ($E_\perp$) Adapted from Oostinga *et al.* 2007.[63]

Recently, Jarrillo-Herrero and coworkers reported that twisting 1.1° two layers of graphene (the "magic angle") at 1.7 K, the material exhibits flat bands near zero Fermi level, getting an insulator state.[64]. Besides, when the same twisted bilayer graphene is submitted to a magnetic field, it become to a superconductor.[65] But an increment in the number of layer leads to more complicated band structures with different overlapping.[66]

1.4. Functionalization of graphene

Graphene can be modified for tailoring their properties and for the introduction of different functionalities (*e.g.* carboxyl, hydroxyl, amine, azide groups) in which, subsequently, other

molecules can be anchored. In most cases, functionalization is the best way to achieve the best performance of graphene. The activation of graphene with reactive molecules has many advantages: oriented immobilization of the analytes, enhanced dispersibility, biocompatibility, sensing properties or the passivation of the surface, which can avoid the unspecific adsorption of contaminants that would interfere in the analysis.

Graphene functionalization can be performed in two different ways: covalent or non-covalent modification. On the one hand, covalent functionalization modifies the sp^2 net introducing sp^3 carbon-type defects. Consequently, this chemical modification can deteriorate the electronic graphene properties but enhances others to adapt graphene to a specific application and to achieve the best performance.[67] On the other hand, non-covalent functionalization does not damage the graphene π-conjugation. With this synthetic method, functional groups can be attached to the graphene surface through π-interactions with different species; however, this modification yields lower stable bounds than the covalent one due to the interaction nature.[68]

1.4.1. Covalent functionalization

Despite the covalent functionalization, decreases the number of sp^2 carbons and could affect the electronic behavior of the graphene, which consequently alters its electronic properties.[69] Band gap opening of graphene by doping, would be useful for functional nanoelectronic devices. It is reported that the electrical properties can be tuned by chemical functionalization in three different ways: the mentioned conversion of the sp2 net to sp^3, molecular dipole interactions associated with the quantum capacitance and hybridization of molecular orbitals with graphene's electronic bands.[70] For that reason, covalent modification has been widely study in order to modulate the gap and thus to adapt graphene as semiconductor for electronic applications.[71] Exfoliated graphene usually are few-layer structures that are difficult to handle and present a high number of defects, which does not make it suitable for these purpose. However, supported graphene derivatives such as CVD graphene or epitaxial growth (EG) graphene are more suitable for electronic application due to their homogeneous and single-layer structure and high quality.[72] In the following paragraphs, we will try to classify the different types of graphene covalent functionalization on substrate and clarify their principal advantages and disadvantages.

The introduction of **single atoms**, including hydrogen, halogens or oxygen is a good choice to design semimetal, semiconductor or insulator material, due to the high functionalization degree. Traditionally, oxidation has been the most used method to modified graphene. However, the acid treatments described above[26-30] could be too aggressive for the graphene properties. For that reason, alternative approaches have been studied for CVD[73] and EG graphene. Monolayer and bilayer CVD graphene were treated to 550 °C under air. Structurally, a reduction of the wrinkles was observed, possibly, due to the generation of nanoholes which led to a reduction in the compressive stress within the graphene layer.[74] As was expected, a higher resistant to the oxidation was found in the bilayer graphene due to the increased stability and for a lower interaction with the substrate.[108b] The introduced epoxy and hidroxyl groups could be subjected to nucleophilic Mitsunobu substitution in the presence of dialkyl

azodicarboxylate (DIAD). This proposal was explored by Kalbác and coworkers in oxidized CVD graphene.[75] Due to DIAD is decomposed photochemically, the use of mask could allow the generation of spatially functionalization. For EG, two approaches have been studied for its oxidation: electrochemical treatment with HNO_3 by applying the corresponding potential[76] and by exposing to oxygen under ultra-high vacuum to obtain a chemically homogeneous and reversible modification.[77]

Hydrogenation can be performed in liquid and plasma based environments and is easily reverted using high temperature treatments.[78] Recently, the synthesis of a hydrogenated single layer graphene deposited on Cu substrate has been reported by laser-heating in a hydrogen environment, in which the amount of hydrogens bonded increase as a function of the pressure at which the sample was laser-heated.[79]

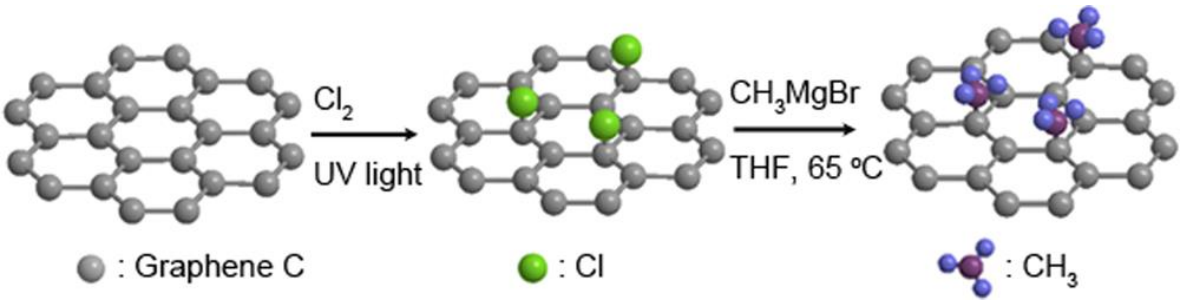

Figure 13. Schematic representation of the graphene modification using a Grignard reagent through a photochlorination on epitaxial graphene. Adapted from Yoshimoto et al. 2014.[82]

Halogenations can be achieved from the decomposition of fluorinating agents such as XeF_2. However, this reaction has fast kinetic which makes it poor controllable.[80] As consequence, the electronic properties are heavily affected. In contrast, the introduction of Cl atoms, with slower kinetics, allows a better functionalization control and lower structure damage.[81] This functionalization could be useful for a second modification step, the introduction of other groups via nucleophilic attack like Grignard reaction (Figure 13).[82]

Given that graphene has polyaromatic character **cycloaddition reactions** can be employed to modify it. For example, the widely used pericyclic reaction in organic chemistry, Diels Alder cycloadditions where a diene and a dienophile react to form cyclic adduct. The reactivity in Diels Alder is inversely proportional to the energy gap. Due to the graphene HOMO and LUMO cross at the Dirac Point, it can act as both, dienophile or diene (Figure 14).[83,84] On the one hand, the use of graphene as diene was performed with the activated dienophiles tetracyano-ethylene (TCNE) and the reaction was monitored by Raman spectroscopy (Figure 14). The corresponding modified graphene derivative at room temperature showed a significant increase of the I_D/I_G ratio and the reaction was reversed when the temperature was raised, confirming the reversibility of the process (retro Diels-Alder). On the other hand, the role of graphene on substrates as dienophile was investigated using 2,3-dimetoxy-1,3-butadiene. The corresponding graphene adduct was obtained at 50ºC and the complete retro- Diels–Alder reaction was also in this case accomplished at 150 ºC.

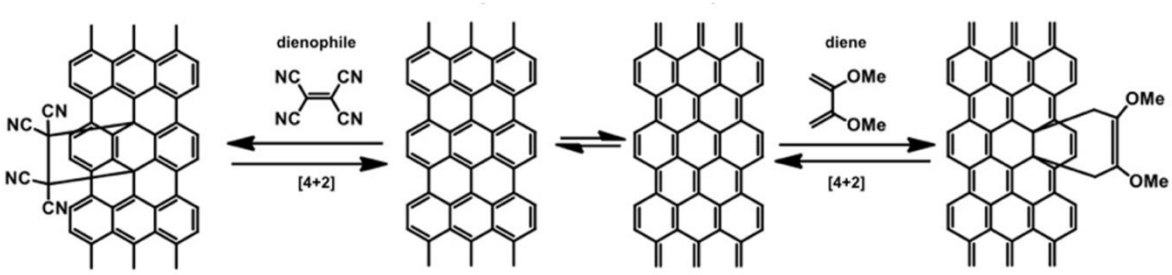

Figure 14. Diels-Alder reaction of graphene as diene (left) and dienophile (right). Adapted from Sarkar *et al.* 2011.[84]

These covalent functionalization strategies are remarkably interesting for the reversible engineering of the graphene band gap and conductivity for electronic applications. For example, in 2016 was reported a Diels Alder reaction with non-planar dihydronaphtalene on Cu graphene supported as dienophile.[85] This graphene modification resulted in *p*-type doping and an improvement of the conductivity due to the increase of the electron-withdrawing groups, i.e. the increase of the hole density. In addition, the use of PMMA mask allowed the selective region functionalization that could be used in the manufacture of electronic devices. Against the assumption that the cycloaddition reactions of graphene only occur in defective regions (i.e. edges and/or holes),[86] the functionalization of defect-free graphene with a substituted maleimide has been recently reported. The chemical modification was confirmed by Raman spectroscopy and XPS. Both of them showed sp^3 carbon atoms increment. Besides, in order to clarified the cycloaddition adduct obtained, scanning tunneling microscopy (STM) and by Discrete Fourier Transform (DFT) were used (Figure 15).[87] The geometry visualized by STM suggested that the (1,2) and (1,4) configuration were possible. DFT calculations showed that only the cycloaddition adduct (1,2) resulted in a stable bond for graphene on SiC(0001).

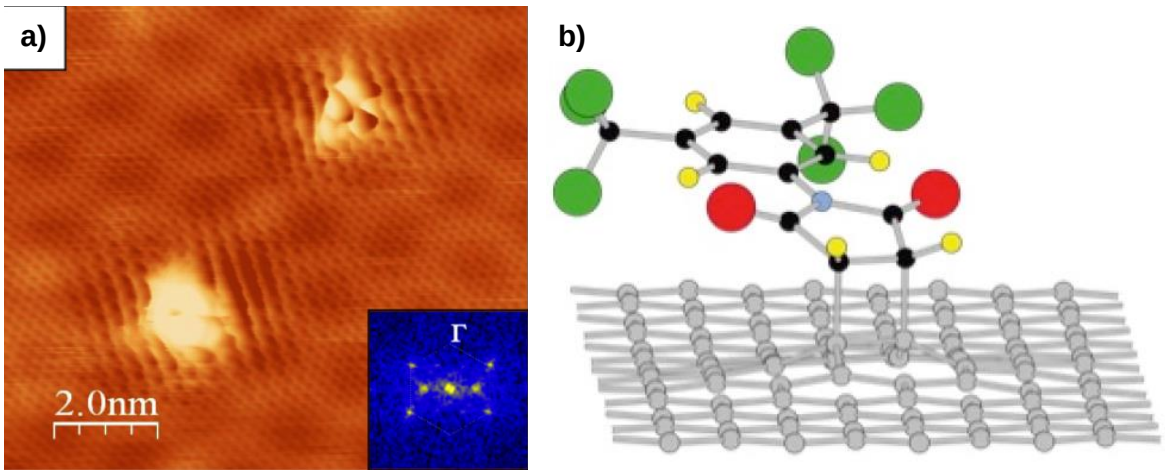

Figure 15. a) STM image of the functionalized graphene and b) DFT optimized structure of the (1,2) cycloadduct. Adapted from Daukiya *et al.* 2017.[87]

Several [2+1] cycloadditions have been developed on graphene using azides to form azirine-rings. 3-D CVD graphene on copper was modified with a substituted perfluorophenyl azide to incorporate an acid functionality.[88] The carboxylic group worked as anchor point for TiO_2 nanoparticles with high photocatalytic activity in CO_2 reduction due to the good dispersibility of the covalent molecules attached. The incorporation of functionalities allowed an increment of

hydrophilicity and good interaction with biological environment. For that reason, the cycloaddition of nitrenes using azido aniline was also used for the development of an electronic glucose sensor through the glucose oxidase linkage.[89]

In this thesis, **radical addition** has been the main tool to modify the graphene surface. This reaction has the advantage that is tolerant to different experimental conditions, such as compatibility with different solvents, low temperatures, dry or wet conditions. In addition, the radical precursor can be generated *in situ* or *ex situ*. The radical is generated through hemolytic bond cleavage of the diazoanhydre **12** which after decomposition release N_2 to produce an aryl radical **13** (16C). The reaction of aniline **4** with alkylnitrite also leads to the generation of the radical *via* formation of the diazotate **11** *in situ* (16B). The produced radical reacts with the graphene double bond **15**, followed by delocalization and reaction with a second aryl radical **13** (16D).[90] Modifications of the aryl diazonium salts allow the introduction of different groups on the graphene surface, like carboxylic group which could be easily modified through esterification or amidation in order to attach covalently biomolecules.[91]

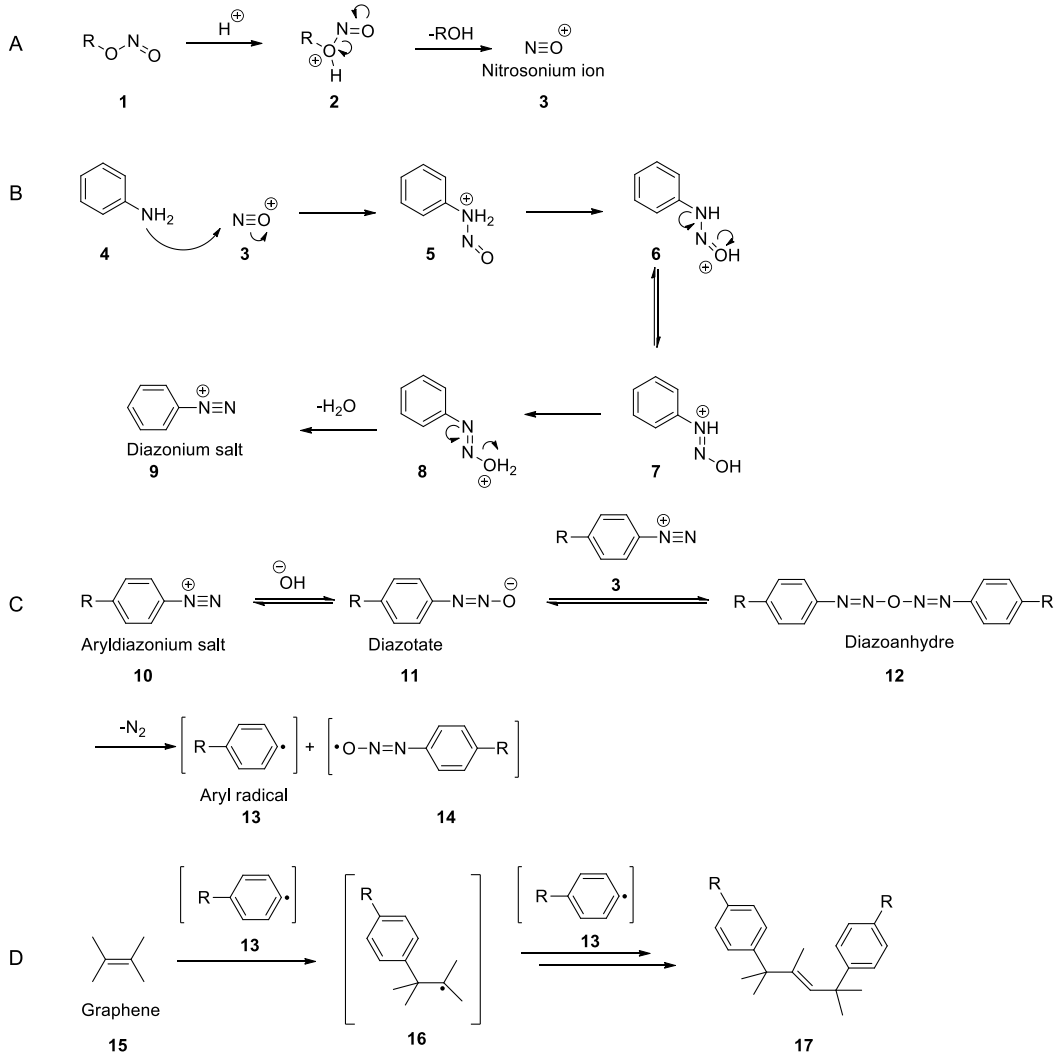

Figure 16. Mechanism of (A) formation of nitrosonium ion from alkyl nitrite, (B) generation of diazonium salt from aniline, (C) generation of Aryl radical from diazonium compound and (D) radical addition of radical specie to a carbon surface. Adapted from Dyke *et al*. 2004.[92]

The proposed mechanism for this reaction suggests the initiation *via* an electron transfer from the graphene to diazonium salt. According to the Gerischer-Marcus theory, electron transfer is proportional to the allowed redox potential gap between different reactants.[93] The reactivity of the graphene is determined by the overlap of the graphene electronic density of states (DOS) and the unoccupied states in the diazonium molecule in solution (Figure 17). For this reason, the reactivity is governed by the type of doping. Hence, the chemical reactivity can be modulated adjusting the graphene Fermi Level. It has been reported that n-doped CVD graphene on SiO_2 showed a higher reactivity for organic molecules and metal ions.[94]

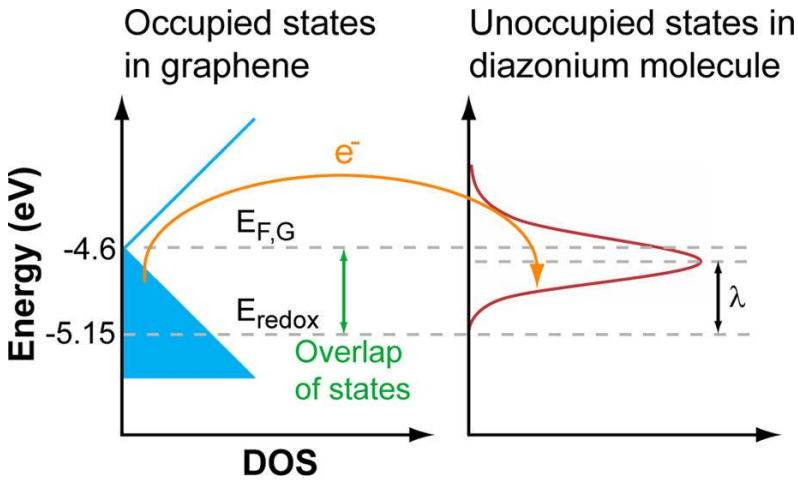

Figure 17. Scheme of the graphene and diazonium salt DOS. Adapted from Paulus et al. 2012.[93]

Due to the high reactivity of the generated radicals, the formation of oligomers and a not-well-defined chemical structures can occur (Figure 18).[95] STM and AFM revealed an irregular graphene surface after radical reactions by diazonium salt decomposition, sometimes this kind of oligomerization evolves to a completely covering of the graphene surface by irregular organic chains. It is well-known that this reaction results in polyaryl growth due to the radical attachment to the pre-grafted species, limiting with the generated cluster density, the number of species directly binding to the surface.[96] In addition, the diazonium decomposition byproducts could be absorbed on the functionalized graphene surface and their vibration modes hinder a proper characterization [97]

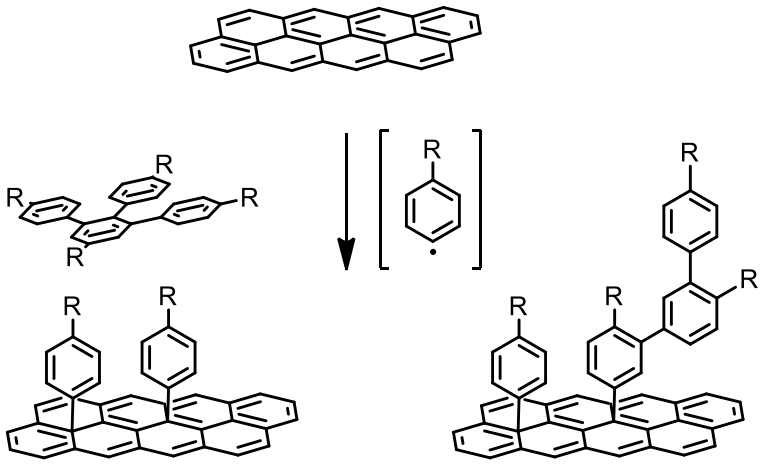

Figure 18. Scheme of the possible decomposition products in a radical addition. Adapted from Hossain *et al.* 2010[95] and Kalbáč et al. 2019.[97]

The employment of graphene supported on a substrate limited in number their characterization methods to monitor chemical transformations. In addition, diverse support substrates complicate the sensitivity and the reaction conditions. Therefore, there is an urgent need for extended characterization methods for on-surface chemical transformations. In 2018, Kalbáč and coworkers described innovative characterization techniques for a vapor-phase functionalization with diazonium salt (and the previously mentioned fluorination) of CVD graphene on Cu. The covalent modification on Cu allowed to avoid the polymer residues generated when is typically transferred onto another substrate. On the one hand, the modified CVD graphene was characterized by SERS because of the caused benefit by Cu as SERS-active substrate.[98] The vibrational modes of the attached molecules were perfectly identified. On the other hand, graphene surface enhance laser desorption/ionization (SELDI) mass analysis were performed due to the graphene capability as efficient matrix for matrix-assisted laser desorption/ionization (MALDI).[99] For that reason, LDI were directly performed over the substrate to identify the attached molecules again. This work provided alternative solutions for some of the characterization problems.

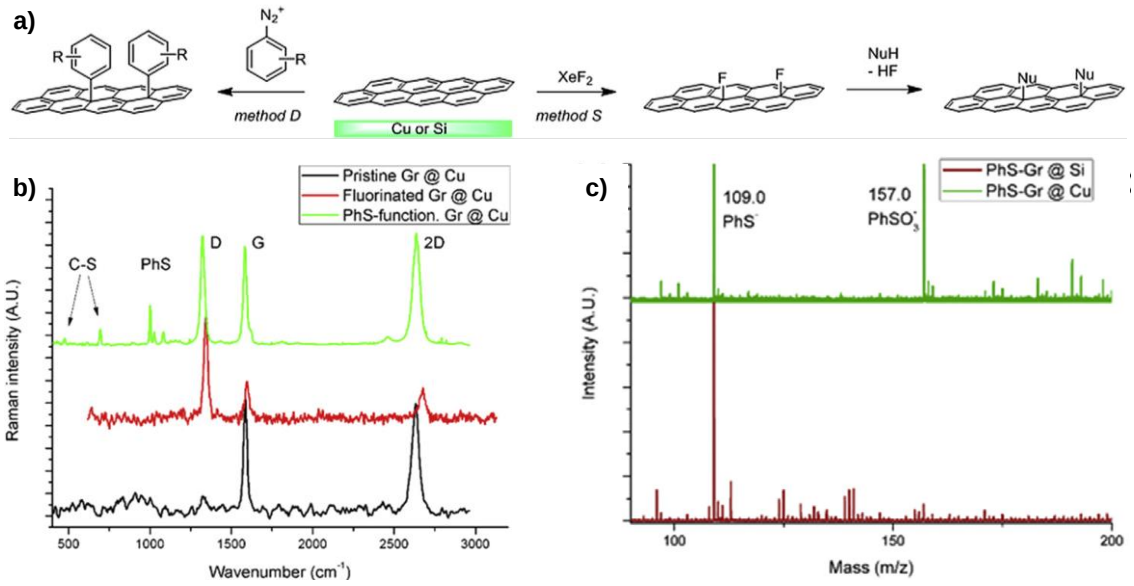

Figure 19. a) General scheme of graphene functionalization by substituted diazonium salt and by gas phase activation followed by nuclephlic substitution, b) SERS characterization and c) SELDI analysis of the functionalized graphene with thiophenol. Adapted from Kalbac *et al.* 2018.[98]

The chemical properties of graphene on a substrate strongly depend on different parameters such as the supporting substrate, external strain, number of layers or other reaction parameter. And this dependence is clearly reflected in the widely used diazonium chemistry.

The **supporting substrate** has a remarkable influence on graphene reactivity, especially to CVD graphene reactivity. CVD graphene was transferred onto different substrates and it was subsequently functionalized with 4-nitrophenyl diazonium tetrafluoroborate (Figure 20).[100] The selected substrates with different hydrophobicity were: a single-crystal wafer of α-Al_2O_3 ;and three substrates of SiO_2 on a silicon wafer, namely bare SiO_2, and SiO_2 coated with a self-assembled monolayer of octadecyltrichlorosilane (OTS) or a mechanically exfoliated flake of single- crystal hexagonal boron nitride (hBN). The Raman spectroscopic characterization revealed that a higher functionalization for graphene on the bare SiO_2 and Al_2O_3 substrates respect to graphene on hBN- and OTS-treated substrates, indicating lower reactivity for hydrophobic substrates. The chemical reactivity of graphene on different substrates can be explained considering the reaction kinetics from electron-transfer theory as a function of the Fermi level of graphene respect to the reacted site density. Thus the charged groups/impurities mostly presented on hydrophilic surfaces can induce local electron-hole fluctuation (puddles) with higher reactivity due to the locally n-doped puddles. In fact, the graphene which is suspended (without influence from the substrate) present the highest carrier mobility.[101] The graphene reactivity in systems with the absence of these interactions, such as suspended graphene and graphene membranes, has not been studied in detail. However, the development of new modification procedures for these graphene-based systems will be mandatory to manufacture new electronic devices which required suspended graphene or graphene membranes.

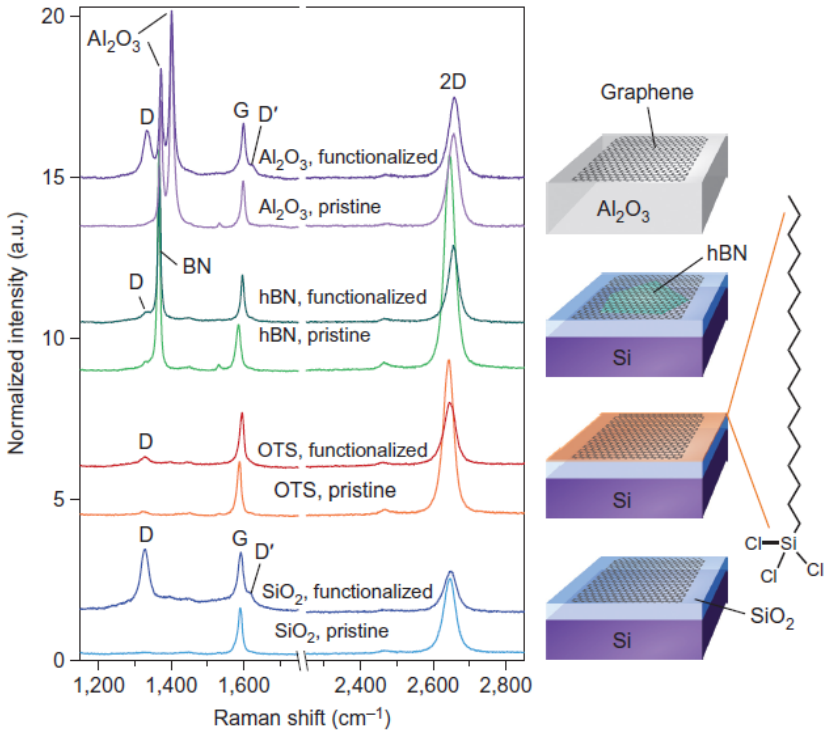

Figure 20. Raman spectra before and after reaction of graphene on different substrate with 4-nitrobenzenediazonium tetrafluoroborate. Adapted from Strano *et al.* 2012.[100]

More recently, a covalent pattering based on a radical reaction has been reported taking in advance of the nanostructure induce on graphene grown on Ru (0001).[102] Acetonitrile is homolytically broken by electron bombardment producing cyanomethyl radicals which react with graphene to functionalize it with atomic-level selectivity and spatial periodicity. For the same architecture, it was tested how the temperature tuning involves yield increment.[103]

The graphene reactivity is also affected by certain **mechanical strengths**. In 2013, Ago and coworkers reported that the chemical reactivity of the graphene can be enhanced by a factor of up to 10 when an **external strain** is applied to graphene via stretching of the flexible polydimethylsiloxane (PDMS) substrate where the carbon material is supported.[104] When a mechanical strain of 8.7% was applied the reactivity increased around a 50%. When that mechanical strain increased to 15%, the reactivity increased to 100%. The strain causes an extension of the π orbital with a localized electron available to form a perpendicular covalent bond.[105] After the application of the strain, the graphene recovered its unstrained conformation and recovered its initial low reactivity. With this approach, functionalization approaches that would otherwise not proceed, such as phenyl radicals with electron donating substituent, could be performed.

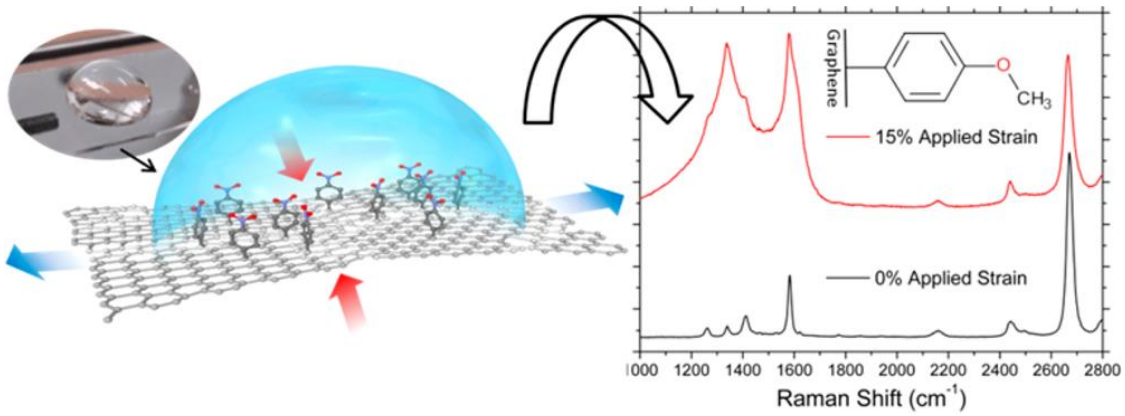

Figure 21. Strained graphene and the resulted Raman spectra. Adapted from Bisset *et al.* 2013.[104]

Localized deformations on graphene layers produced by nanoparticles can also tune the chemical reactivity of graphene. To this end, the decoration of the Si substrate with SiO_2 nanoparticles (NPs) induced local regions of mechanical strain, increasing the chemical reactivity and leading to a selective spatial functionalization (Figure 22).[106] The average size nanoparticles deposited over the SiO_2 substrate was 50 nm, however cluster were formed as the profiles height revealed. Due to the NPs height, some wrinkles with different curvatures degrees were observed in the graphene. In fact, the increase of the functionalization was not exclusive of the curvatures generated for the nanoparticles. In the wrinkle regions were observed a higher increased of the D band compared with the relaxed graphene. However, despite they attribute the higher functionalization degree to the local curvature, from our experience, the doping of the SiO_2 NPs may be higher than the effect induced by the mechanical strain.

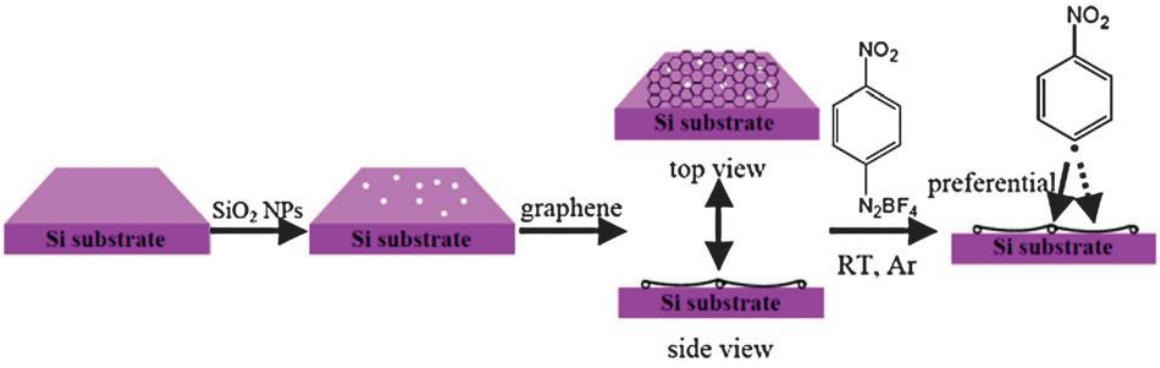

Figure 22. a) General scheme of the Si decorated substrate with SiO_2 NPs. Adapted from Ruoff *et al.* 2013.[106]

The mechanical deformation also influences the graphene reactivity in other radical reactions. In particular, a curvature is induced in the graphene layer by its deposition on a restrained polymeric substrate; thus, a wrinkled pattern is generated on the graphene.[107] The treatment of this wrinkled graphene under CF_4 plasma led to a spatially selective functionalization. Consequently, this treatment allowed to perform localized tuning of the electrical conductivity at the microscale in function of the local curvatures.

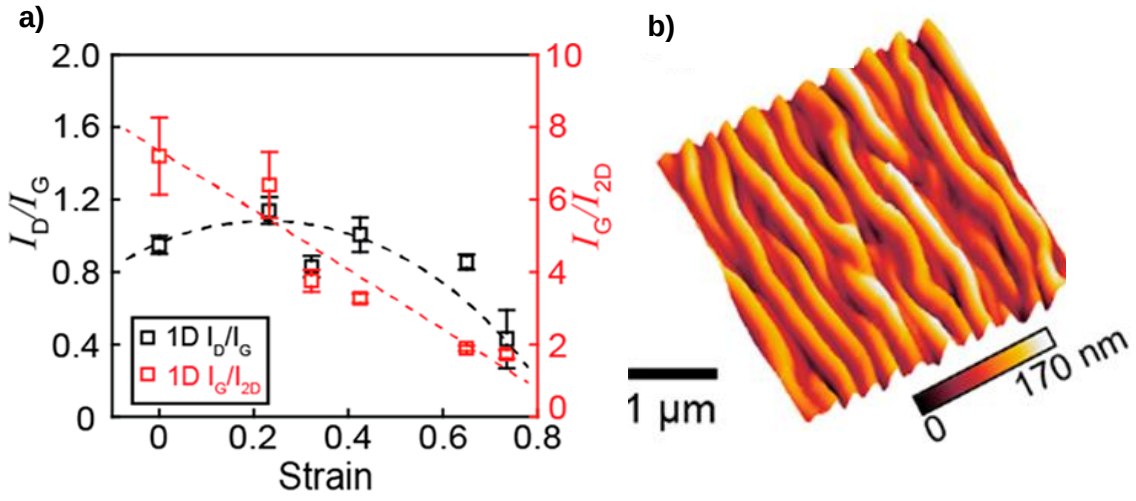

Figure 23. a) I_D/I_G and I_G/I_{2D} ratios at different substrate strains for 1D wrinkles and b) 1D graphene wrinkles. Adapted from Deng *et al.* 2019.[107]

In addition, a similar scenario can be described to explain the reactivity of bilayer or **few layers graphene** on substrate. It is reported that the reactivity of single layer graphene is ten times higher than the bilayer one due to the presence of the interlayer graphene hinders the interaction between the substrate and the upper layer of graphene.[108] In addition, a reactivity difference was found for this electron transfer chemistry depending on the stacking mode of graphene layers. The different reactivities mainly result from distinct variations in the DOS distribution in the gap region. Particularly, the reactivity of the twisted bilayer graphene (t-BLG) is five times higher than for the AB-stacking graphene due to the variation in the electron distribution.[109].

The graphene reactivity is also influenced by **reaction parameters**. An interesting work about the factors that can influence the reactivity in radical additions has been recently reported by Steven De Feyter and coworkers.[110] The simultaneously use of two different diazonium salts with different reactivities, such as 4-nitrobenzenediazonium (NBD) and 3,5-bis-tert-butylbenzenediazonium (TBD), led to a spatially inhomogeneous functionalization as quasi-uniform spaced islands on graphene, coined nanocorrals (Figure 24a). The diameter of nanocorrals can be tuned by controlling the electrochemical activation conditions and the ratio between both diazonium compounds. They hypothesized that the formation of nanobubbles of N_2 and NO_2 generated during the grafting on the graphene interface might be responsible for the nanocorrals formation (Figure 24b). The increasing HNO_2 concentration combined with the water insoluble byproducts (which improve the stability of the bubbles) led to nanobubbles observation, which resulted in a large nanocorrals formation. These nanopatterned graphene can be used as templates for the nanoconfined formation of self- assembled molecular networks and for on-surface reactors.

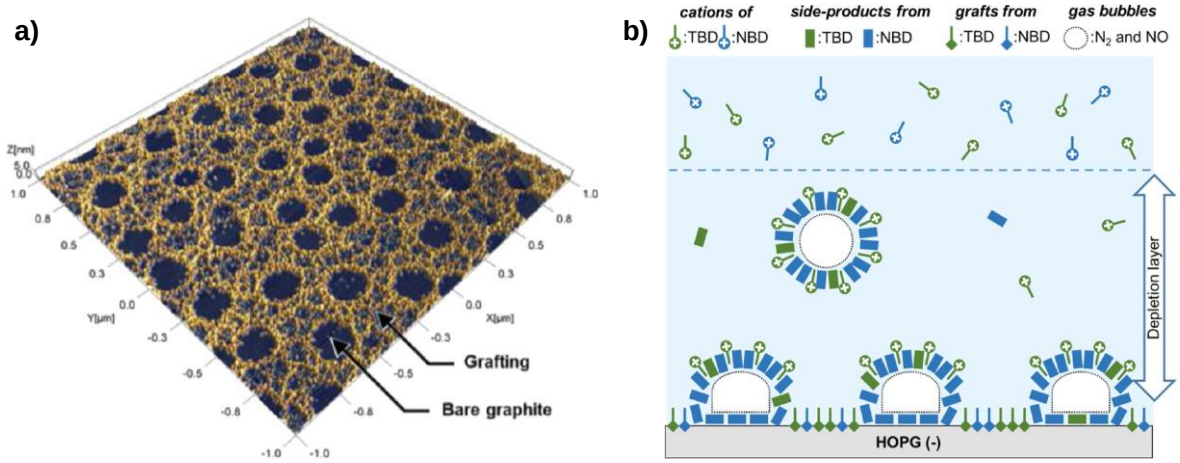

Figure 24. a) STM topography image of nanocorrals on HOPG and b) schematic representation of stabilized nanobubbles hypothesized as responsible for the nanocorrals formation. Adapted from De Feyter *et al.* 2019.[110]

One of the most efficient methods for the functionalization of graphene is the treatment of the corresponding graphene precursor with alkaline metals in suitable solvents followed by quenching of the intermediately formed reduced graphene (graphenide) with diazonium salts. The high functionalization efficiency is due to the negative charges on the surface which allow a high electron transport.[111] By employing this method, the bisfunctionalization of CVD graphene was achieved using two successive reduction and covalent bond forming steps.[112] In particular, the CVD graphene was bisfuntionalized with aryl diazonium salt and alkyl halide (Figure 25); however, the modification strongly depended on the addition sequence of the reagents. CVD graphene modifications are restricted to only one side of the basal plane producing strained structures. As consequence, the retrofunctionalization can occur with good leaving groups. In this manner, the addition of an alkyl chain and the subsequent reaction with an aryl radical led to bisfuntionalized graphene. But, when the addition sequence changed, a lower functional degree was obtained because aryl anion act as good leaving group in a strained geometry derived from the first modification step.

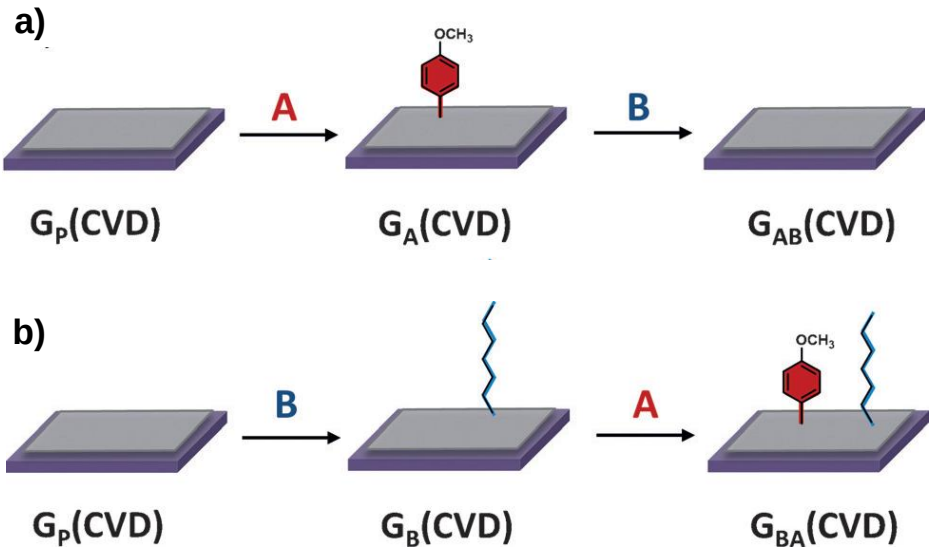

Figure 25. General scheme for bisfunctionalization of CVD graphenide. Adapted from Hirsch *et al.* 2016.[112]

Other radical reactions on graphene are arising in order to overcome the limitations of the most popular modification strategies of graphene such as the heterogeneous oligomers obtained by phenyl radical reactions, or the previous preparation of the corresponding phenyl radical precursor depending on the desired surface function.[113] Recently, Xu and coworkers reported a direct azidation of CVD graphene on Cu by *in situ* electrochemical oxidation of an aqueous sodium azide (NaN_3, Figure 26).[114] The click chemistry of the modified graphene can be employed for expanding surface functions. Particularly, they developed a copper(I)-catalyzed alkyne–azide cycloaddition and copper-free click chemistry, as well as subsequent bioconjugation. This functionalization method has a great potential for the application of graphene in biosensing and electronics.

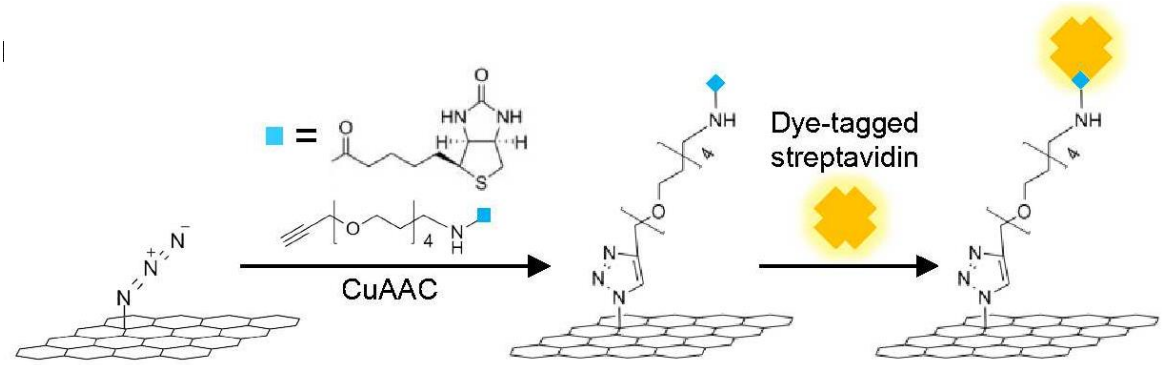

Figure 26. General scheme of the click chemistry of azidated graphene and subsequent bioconjugation. Adapted from Li *et al.* 2020.[114]

1.4.2. Non-covalent functionalization

As we mentioned above, the non-covalent modification involves polymer wrapping, π-π interaction, electro donor acceptor complexes, hydrogen bonding and van der Waals forces, which do not introduce defects in the graphene structure.[115] For individual non-covalent interactions, the energies are normally lower than in covalent bound; however, the advantage of these systems is that the low interaction energies allow non-desired reversibility. Mainly this kind of functionalization was employed to avoid the re-aggregation of the layers, to increase the dispersibility of graphene and for the introduction of different molecules that induce new properties.[116]

π-π stacking between graphene sheets results in aggregation between layers. In addition, graphene sheets have hydrophobic nature, therefore, they are practically insoluble in water. Thus, non-covalent functionalization approaches with organic compounds to avoid the stacking were developed. The employed of planar aromatic molecular like pyrene, perylene and their derivatives are used as driving forces for the exfoliation of graphite and stabilization of graphene derivatives in dispersion.[117] With the modification of these species Lee and coworkers developed an amphiphilic structure composed by four pyrenes to generate a stable aqueous dispersion. The flexible conformation of the structure maximizes the π-π interaction with the graphene surface (Figure 27).[118] A similar approach was reported by Mann and coworkers in 2011.[119] They developed a tripodal binding structure which can allow different functionalities.

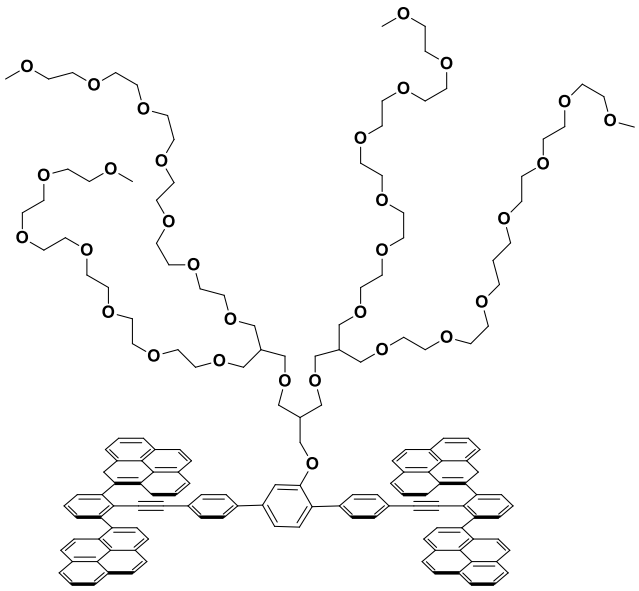

Figure 27. Tetra-pyrene derivative structure. Adapted from Lee *et al.* 2011.[118]

Graphene and GO are ideal substrates for the dispersion of NPs due to their large surface areas. In this manner, modified graphene with Fe_3O_4 can be used in different applications: water cleaning[120], biomedical application[121] such as contrast agent in magnetic resonance image,[122] drug delivery nanocarriers,[123] phototermal therapy[124] and cellular separation and isolation.[125] On the other hand nanocomposites of graphene-gold NPs prepared by simple physisorption method have been widely studied as SERS agents with potential application in sensing.[126]

Graphene non-covalent modification can also be performed on substrates. The molecule assembling is determinated by the interaction with the substrate, which can be weak for Ir(111), Pt(111) and SiC(0001) or strong for Ni(111) and Ru(0001).[127,128] For systems where the graphene-substrate interaction is weak, e.g. SiC(0001), the molecular self-assembly is driven for the intermolecular forces.[130] Figure 28 shows molecular assembly on surface (SiC(0001)), perylene-3,4,9,10-tetracarboxylic dianhydride (PTCDA) molecules formed a well ordered monolayer.[129] The PTCDA follow the graphene continuously over the defects and edges. The ordering of molecular deposited at surfaces is relevant for the performance of organic electronic and optoelectronic devices, such as organic field-effect transistors (OFETs) or organic light-emitting diodes (OLEDs).[129]

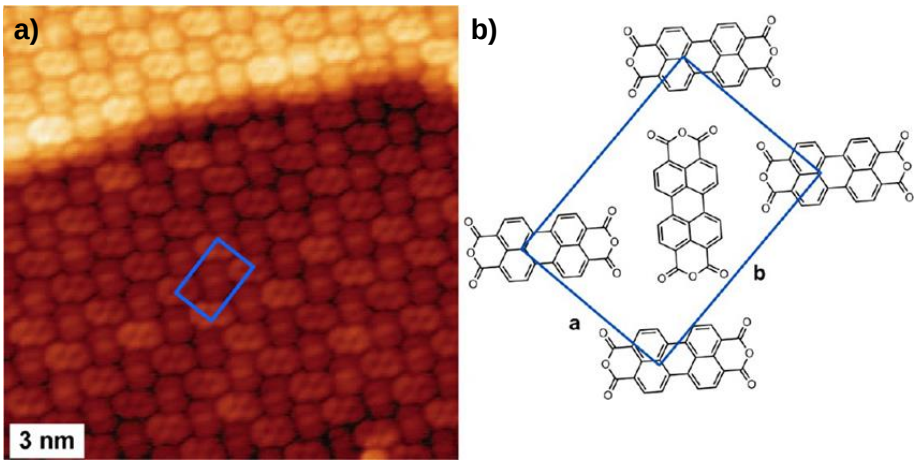

Figure 28. a) STM image of a monolayer of perylene tetracarboxylic dianhydre, PTCDA deposited on epitaxyal graphene and b) unit cell structure. Adapted from Wang *et al.* 2009.[130]

Due to the hydrophobic character of graphene, hydrophobic molecules are also adsorbed. For example, the use of alkoxy chains on phenyldiazonium salts permit patterned covalent modification of graphene. In particular, 4-docosyloxy-benzenediazonium tetrafluoroborate (DBT) promoted its physisorption onto the graphene surface (Figure 29).[131] Then, the adsorbed DBT molecules yielded a well-ordered layer when were immersed in an aqueous solution. Finally, an electrochemical potential triggered the covalent attachment of the diazonium specie. This is a good example of how non-covalent functionalization can guide the generation of a covalent pattern. In addition, this strategy was successfully performed using SiO_2, plastic and quartz as substrate. However, the grafting density for this approach is lower compared to the standard reaction because the dendritic growth of radicals is avoided.

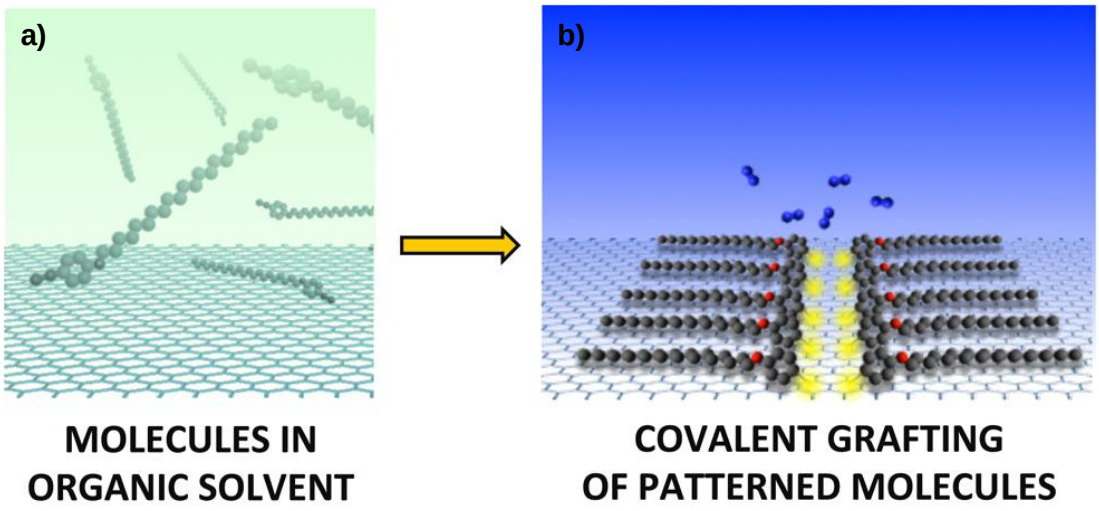

Figure 29. Scheme of diazonium salt molecules on graphene using a) organic solvents and b) aqueous solvents. Adapted from Xia *et al.* 2016.[130]

In a similar manner, interactions of graphene with biomolecules through hydrophobic or π-π interactions are possible.[132] For this reason, graphene can be used as platform for selective detection of biomolecules since can interact with DNA[133], protein, enzimes[134] and peptides[135] as will be shown in the following section.

1.5. (CVD) Graphene applications

The above mentioned unique set of properties makes graphene suitable for a wide spectrum of applications ranging from electronics to optics, sensors, and biodevices.[136] In this section we will summarize the state of the art of graphene applications with special attention in CVD graphene as graphene derivative and in sensing applications.

1.5.1. General applications of graphene

The field of **composites** focuses on combining graphene with other materials to mainly exploit its mechanical properties.[137] A representative example in biomedicine is its combination with $CaSiO_3$ by laser sintering in order to reinforce the ceramic matrix, improving the fracture toughness and compressive strength for scaffolds in the application of bone tissue engineering.[138] Similarly, graphene is combined with metals to modify its mechanical strength and fatigue life.[139]

As explained in the graphene properties section, thanks to the sp^2 hybridization and the delocalized π electrons, the carrier mobility of the graphene makes this material a promising candidate for **electronic applications** such as energy storage, energy generation and sensing.[61] In addition, its flexible nature enables the manufacture of flexible devices, which could be bendable, foldable, rollable and wearable, improving the contact and interface for biological measures as required.[140]

Over the course of the last years, the social demand for energy increases and the current trend in portable electronic require for a continuous miniaturization. Graphene can be used for **energy storage** in two different ways: on the one hand, graphene would be a catalyst in metal-air batteries;[141] on the other hand, taking advantage of graphene's ability to host ions, it could be used as an electrochemical double layer capacitor (EDLC),[142] storing electrostatic charges on the electrode double layer leading to a new supercapacitors generation.

In line with the increasing of the energy demand, graphene can be used in the scope of **energy generation** in solar photovoltaic technology thanks to its transparency, flexibility and charge transport properties. Lots of impressive results have been reported where graphene was used as electrode, (transparent anode[143] or cathode[144]) or active layer (Schottky junction[145], electron and/or hole transport layer,[146] etc). For example, Figure 30 shows graphene being used as both hole- and electron- extraction layer in bulk heterojunction solar cells.

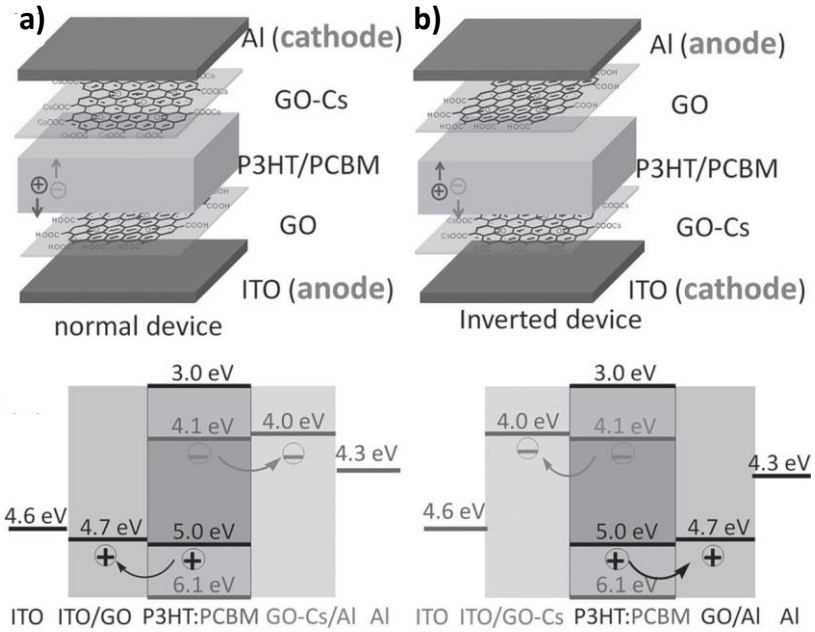

Figure 30. General schemes and level diagrams of the solar cell device using: a) GO as hole transport layer and GO-Cs as the electron transport layer, and b) using GO and GO-Cs in the opposite way. Adapted from Liu *et al.* 2012.[146]

Biomedical technologies are limited by the intrinsic properties of the materials currently employed.[147] For instance, metal and silicon are among the most used materials for the fabrication of conventional implant devices. However, their poor long-term stability in physiological environments, rigid mechanical properties and high inflammatory potential, may result in strong limitations. Graphene is a strong candidate for replacing current devices, in particular, because of its mechanical and electronic capabilities. For that reason, graphene is especially involved as advanced tool for drug delivery, tissue engineering and biosensing. However, the use of graphene for biomedical applications has more controversial, due to its impact on health. As with carbon nanotubes, chemical modification and production method used modulate the toxicity of graphene.[148]

The main advantage of graphene over other nanomaterials for its use as platform for stabilization and delivering of drugs is the large surface area, which allows a high loading efficiency. Particularly, GO hidrophilicity promotes an easy dispersion in the biological fluid, therefore it is an excellent option for this application.[149] In addition, this material could be modified in order to be a selective target for cancer cells through the immobilization of antigens for over expressed protein in these cells.[150] As a representative example, GO/Fe_3O_4 nanocomposite was used to develop with a weight drug/GO ratio of 200%.[151] Drug delivery can be easily manipulated by an external magnetic field thanks to the incorporation of the iron oxide component. The use of external field as stimulated strategy has been widely employed. An electrically response system was reported using a rGO/poly(vinyl alcohol) (PVA) composite.[152] The same material also exhibits a pH-induce gel-sol transition, which is a property that can be used for a selective release of drugs at physiological pH.[153]

For tissue engineering, three dimensional porous scaffolds are required for a good cell growth and tissue regeneration. The integration of nanomaterials to the existing polymer scaffolds

enhances the electrical conductivity for cell stimulation. The utilization of 3D graphene foams not only can support neuron stem cells growth, but also can enhance differentiation to specialized neurons.[154] In addition, graphene does not alter the physiological properties of the target tissue,[155] and it has shown the capacity to control and accelerate osteogenic differentiation.[156] Despite studies are still in the early steps, modified GO has been also tested as potential scaffold for bone tissue.[157] Scaffold place in cranial bone defects of rabbits showed a higher proliferation of bone mineral density.

1.5.2. Biosensors and other diagnostic tools

In general, devices for biosensing are one of the most promising applications for graphene and will be one of the milestones to reach in this thesis. One of the many remaining challenges in biosensing concerns the efficiency and selectivity of the recognition event. In order to achieve low limit of detections (LOD), graphene has been extensively investigated as transducer components.[158] Biosensor is a chemical sensor in which the recognition system uses a biochemical mechanism.[159] In general term, it is composed by a receptor and a transducer material, which is able to transform the physiological information to a measurable signal (Figure 31).

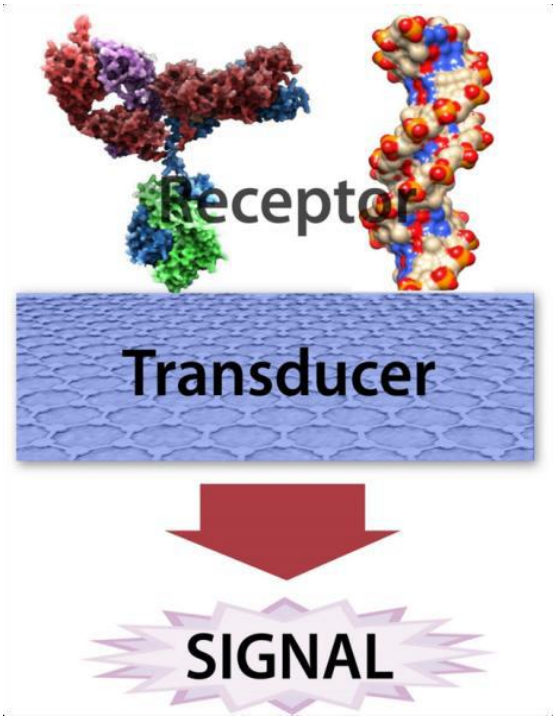

Figure 31. Schematic representation of a general biosensor.

Graphene is a material that is able to transform physical, chemical and biochemical information into an electrical or optical signal that can be measured. These properties, together with its large surface area, electron conductivity and capacity to immobilize different molecules, makes graphene as an ideal material to be used as transducer component. In particular, different sensing mechanisms including optical, electrochemical or electrical can be employed. With respect to the receptors, the most employed are enzymes for detection of ions or small molecules, DNA for different sequence-specific DNA or antibodies for bacterial, viruses and

other biomarkers (Figure 32).[160] However, the receptor could be omitted since the direct interaction of the analyte with the transducer produce specific measurable changes (label-free sensors).

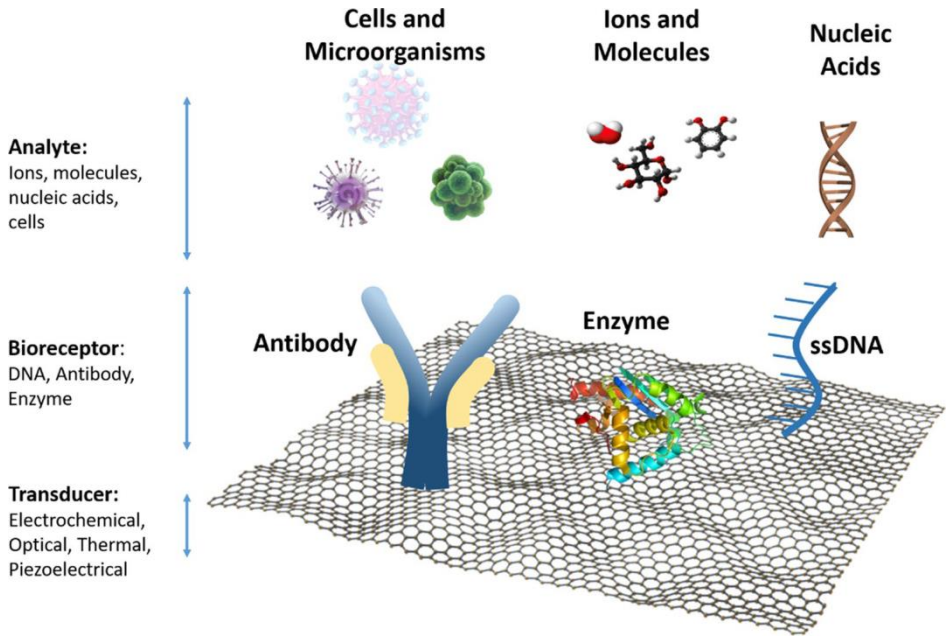

Figure 32. General scheme for selective bioreceptor in function of the analyte. Adapted from Peña-Bahamonte *et al*. 2018.[160]

GBMs are very useful in electrochemical sensors since they allow the increment of the signal-to-noise ratio due to its good electrons transfer characteristics, a large electrochemical potential window and electrochemical stability (i.e. being resistant to oxidizing agent).[161] Some examples have been described about enzymatic sensors of glucose with modified GBMs-electrode.[162] Most of them are based on the electrochemical detection of hydrogen peroxide produce by Glucose Oxidase (GOx) which is usually linked to the GBMs. Some approach using N-doped graphene or the introduction of nanoparticles showed better limit of detection in the presence of interference.[163] This is due to the transfer efficiency is enhanced because of a change in the Fermi potential. In addition, Qu and coworkers showed that the presence of carboxylic groups on the GO sheets enables the peroxidase catalytic activity, without the presence of GOx.[164]

Electrochemiluminescence (ECL) sensors have been successfully developed using graphene as luminophore, electrode material and platform.[165] ECL is currently a leading transduction technique in immunosensors due to its advantages compared to other luminescence techniques, such as low background, high sensitivity, electrochemical controllability, and wide dynamic range for sensing. They are based on the emission of light produced by an electron transfer triggered by an electrochemical reaction. The combination between graphene and ECL led to many applications, in particular, concerning as support of luminescent probes and as electrode component. In 2018, Yang and coworkers developed a sensor based on a 3D nanostructured graphene-aerogel as electrocatalytic support which amplified the ECL signal for a real-sample analysis of prostate specific antigen (Figure 33).[166] Particularly, the use of high porosity GO enhanced the amount of the secondary antibody and the luminescence probe enhancing the sensitivity of the method. Besides, the ECL electrodes can be coated with graphene derivatives

to improve the sensing performance. For example, Zhou and coworkers developed an ECL immunosensor which was able to detect different multiple tuberculosis infection markers with a low LOD (10 fg mL^{-1}).[167] The proposed sensing platform was composed of a coated ITO electrode with GO and gold nanoparticles. These nanomaterials were able to enhance the ECL signal intensity by promoting the electron-transfer reaction on the electrode.

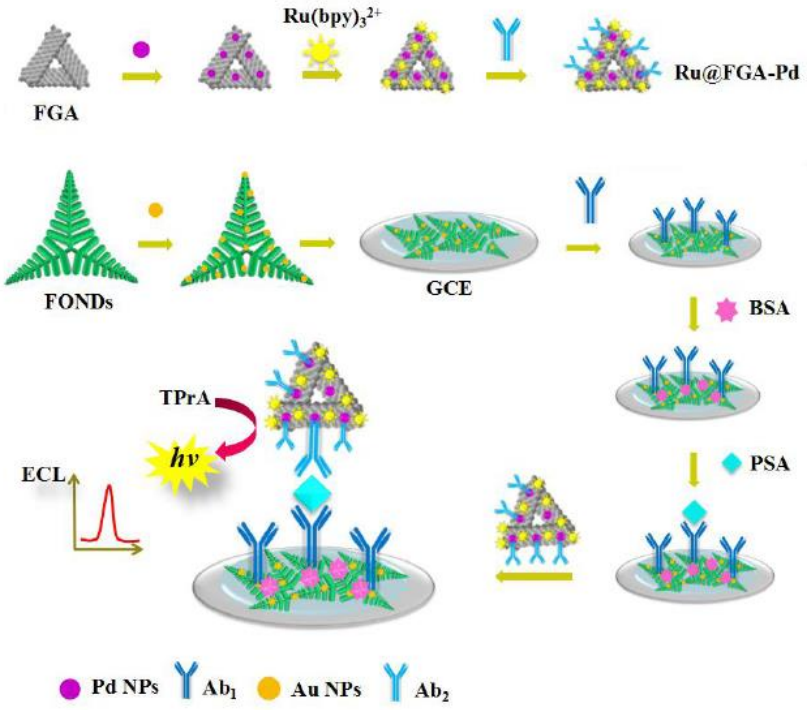

Figure 33. General scheme of the ECL immunosensor. Adapted from Yang *et al.* 2017. [166]

Besides, graphene can be used in optical sensors.[168] GO worked as fluorescence quencher through fluorescence resonance energy transfer (FRET) mechanism when the energy is transferred from a donor to an acceptor dye molecule. A similar work was reported by the noncovalent conjugation of a dye-label thrombin aptamer to the graphene surface (Figure 34).[169] The weak aptamer conformation is affected by its interaction with graphene surface losing the fluorescence capability. Then, the fluorescence recovery is induced for the thrombin attachment generating a measurable signal. When the protein is selectively recognized the quaternary formation of the aptamer is recovered. An antibody sensor was developed in order to address the problem of detection of low concentration of circulating cancer cells, which are responsible of the cancer metastases.[170] Noncovalent functionalized GO on flower gold patterns showed excellent sensitivity such as 3–5 cells per mL of blood for the tested circulating cancer cells.

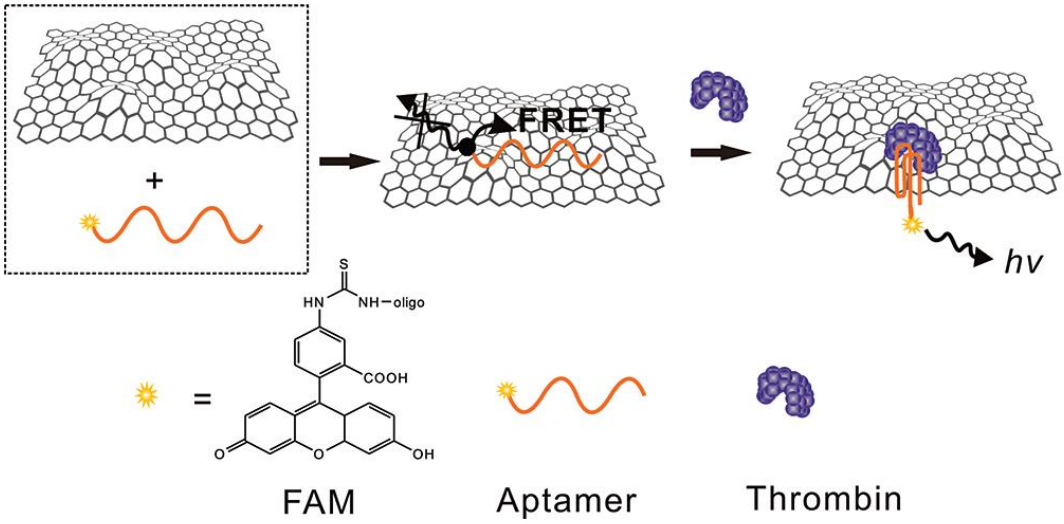

Figure 34. General scheme of the optical sensor based on the aptamer conformation change. Adapted from Chang et al. 2010.[169] Fluorescein amidite (FAM)

1.5.2.1. Biosensors based on graphene transistors

In relation with the potential graphene electronic applications, the use of graphene as biosensor significantly improve the performance of these devices. Currently, the use of-wearable devices is a hot topic in medical research because allow *in vivo*-real time long-term and non-invasive studies. In 2012, it was developed a tooth tattoo for cows in order to study the saliva bacteria.[171] They fabricated an extremely sensitive wearable sensor to real-time monitoring. This flexible device is based on graphene electrodes in which graphene is functionalized with selective peptides to recognize saliva bacteria that involved in the stomach cancer generation. The obtained sensor was implanted onto the tool enamel and the results could be wirelessly followed. The mesurable signal consisted in the resistant change in function of the bonded bacteria. More recently, a flexible graphene photodetector for wearable fitness monitoring has been developed.[172] This device monitored real-time photoplethysmography, which is a non-invasive technique to detect blood volume changes. With this measurement, the heart rate, respiration rate and artery oxygen saturation can be controlled, offering a potential platform for health-care monitoring.[173]

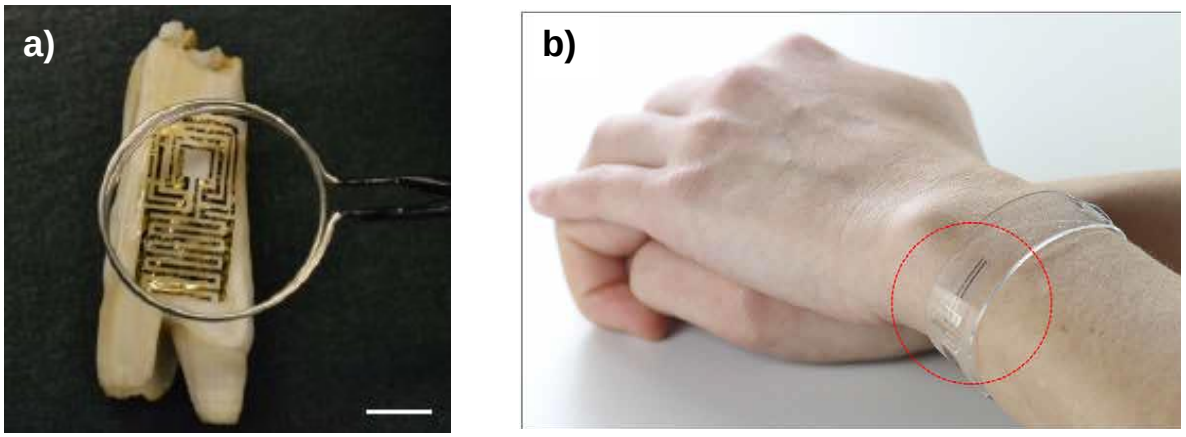

Figure 35. a) Optical image of the graphene tooth sensor. Adapted from Mannoor *et al.* 2012.[171] And b) optical image of the flexible, wearable and transparent integrated detector bracelet. Adapted from Polat *et al.* 2019.[172]

A Field Effect Transistor (FET) is a transistor which is composed by three electrodes (source, drain and gate), a dielectric and a semiconductor components. Source and drain electrodes are conductive metals such as gold or aluminium. The FET performance is based on the control of the conductivity of a semiconductor material channel by an electric field.[174] Source is defined as the electrode through the carriers flow into the channel, while drain is the electrode in which the carriers flow out of the channel and gate is the third electrode that modulate the channel conductivity. Currently, there are many different types of FETs, all of them are based on the distinguished by the insulating method between the channel and the gate.[175] Despite the number of possible FETs configurations, a bottom-gate top-contact FET will be explained in order to clarify how it works (Figure 36).

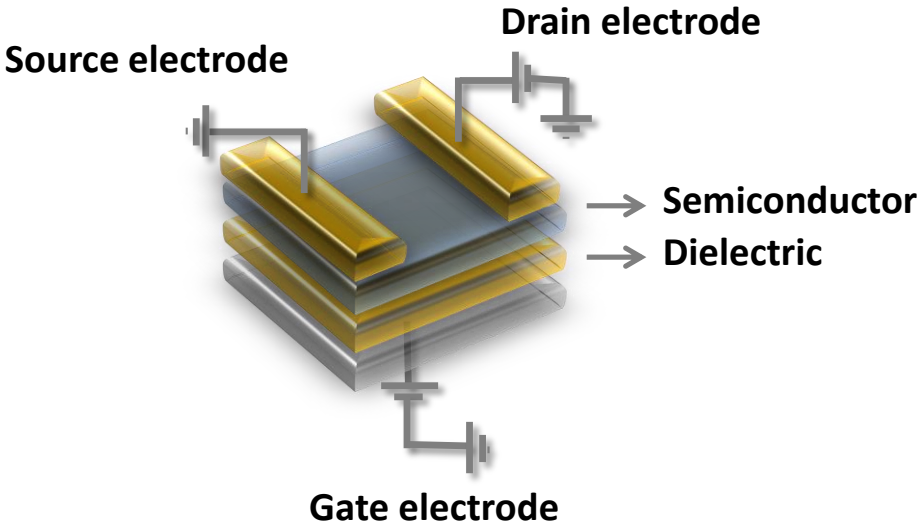

Figure 36. Schematic representations of a FET.

When a voltage difference is applied between source and gate, an electric field is generated in the semiconductor-dielectric interface allowing/controlling the conductivity between drain and source electrodes. Conventionally, a FET is a unipolar transistor as involves the transport of electrons or holes. Depending on the semiconductor type, n-type or p-type, the applied voltage is negative or positive, respectively.

However, graphene can improve the FET performance. The parameter that involves the conductive or the insulating character of a material is the position of the electronic bands (valence and conduction band, Figure 37). For insulator, the two bands are separated by an energy gap (*Eg*) where no electron states can exist. In semiconductor, the *Eg* between the two bands has an energy distance which could be overcome the excitability of the electrons of the valence bands. While for conductive material, there is an overlapping between their conductive and valence bands.

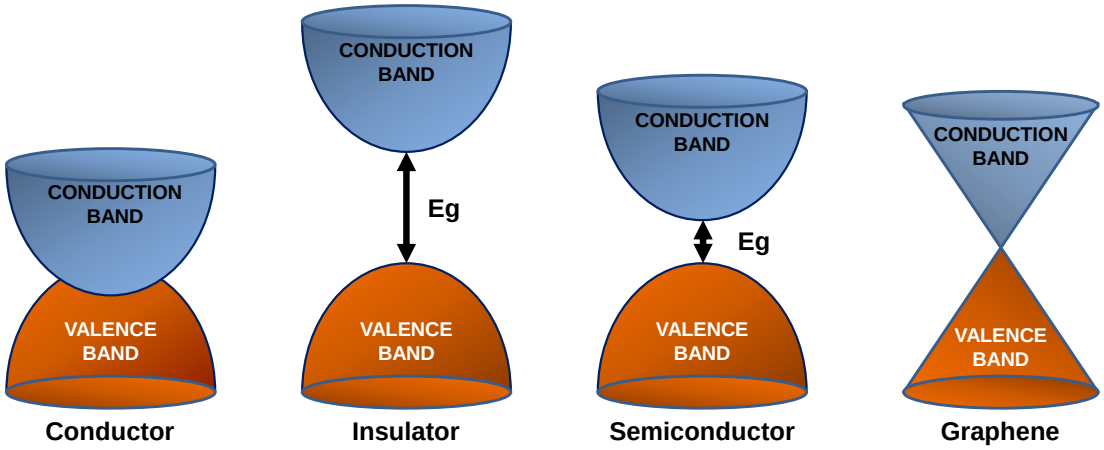

Figure 37. Band structure for the different materials.

Generally, the main material used as a semiconductor was the inorganic amorphous silicon. Before graphene electronic properties discovering, it was common the use of bilayer of organic heterostructure. In 1995, Dodabalapur and co-workers combined layers of hole-conducting α-hexathienylene and the electron-conducting C_{60} to achieve the first ambipolar organic field-effect transistor.[176] Despite graphene is a zero band-gap material, which makes it useless as a conventional transducer material for FETs, the influence of the atomic defects leads to an adjustment of the energy gap. In the following paragraphs, it will be explained how the electronic field takes advantages of the graphene properties for a better understanding of graphene FET biosensors.

As was previously commented, graphene has ambipolar behavior since is a zero band gap semiconductor and its conductive and valence bands meet at the Dirac point (Figure 37). So, it can be an n-type and p-type semiconductor depending of the applied voltage or the charge species near the surface.[177] Therefore, three situations can be found with graphene (Figure 38a): (i) the Fermi level of graphene has the same energy that the Dirac point, then graphene is neutral, and its conductivity is minimum. (ii) The Fermi level is above zero, there is transport of electrons, so graphene behaves like a n-type semiconductor. (iii) The Fermi level is below zero, there is transport of holes, so graphene behaves like a p-type semiconductor.[178] The Dirac point can also be shifted by doping as a result of impurities or introduction of sp^3 carbon in the graphene lattice by chemical functionalization.[179]

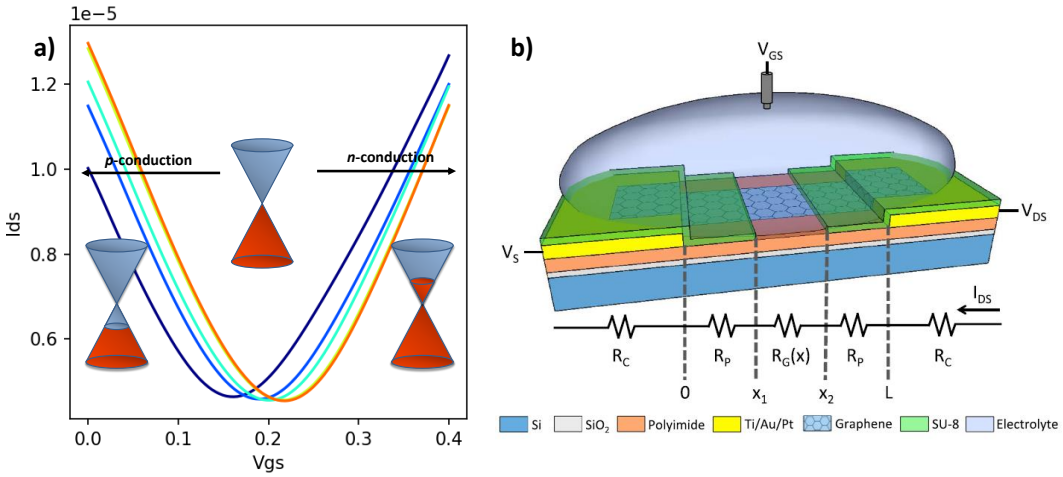

Figure 38. a) Changes in the position of the Fermi level energy with changing the gate voltage for graphene Dirac cones and b) General scheme of a Graphene solution-gated field-effect transistor (g-SGFET). Adapted from Mackin *et* al 2014.[180]

Since most of the biological processes happen in aqueous solution, the development of graphene sensors which are able to detect molecules in an electrolyte solution is mandatory. For this purpose, the most suitable graphene transistor is graphene-Solution Gate Field Effect Transistor (g-SGFET, Figure 38b), in which the reference electrode immersed in an electrolyte solution behaves like the gate electrode. When graphene (or any charged surface) is immersed in the electrolyte solution, the ions dissolved in water with the opposite charge are accumulated at the graphene interface, to compensate the charge generated in the surface due to the electrochemical potential applied between the source and the gate/reference-electrode.[181] The redistribution of these ions is predicted by different theories. For high concentration, i) Helmholtz model describes that the hydrated-counter-ions form a monolayer near the surface shaping an electrical double layer (EDL). However, the EDL is not constant. It can vary according to the ionic concentration and the applied potential. ii) The Gouy-Chapman model considers that the ions are mobile in the solution and suggests that there is ion diffusion driven by a gradient concentration. A last modification was done by Stern to introduce iii) the Gouy-Chapman-Stern model which proposed, adding to the previous model, ions physically adsorbed in the surface (Figure 39).[182] In summary, the length of the effective distance to compensate the solid charge where electrostatic effect persists is called Debye length (λ_D), which involves the compact layer (Helmholtz layer) and the diffusive layer until the electrostatic effect persists according to the mentioned models. [183]

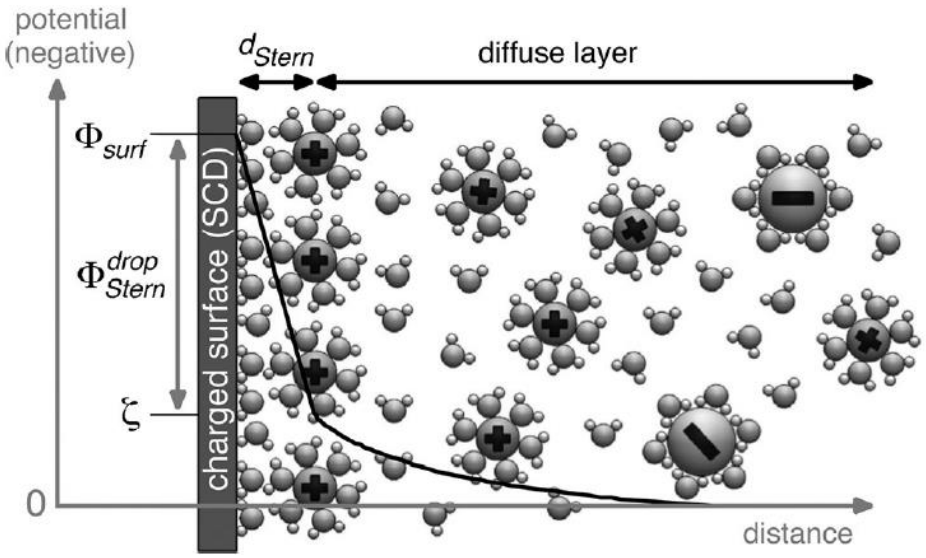

Figure 39. Gouy-Chapman-Stern model of the electrical double layer showing the distribution of hydrates ions for a negative charged surface and the potential profile as a function of distance. Adapted from Brown *et* al 2016.[184]

The working principle of FET sensor is based on the conductivity change in the sensing channel, that is at the graphene interface. To enable specific detection, a selective receptor is needed on the graphene surface. In the sensing step, when a target analyte binds to the receptor, it causes an electric change on the graphene that can be externally measured. In particular, the recognition event by the receptor will generate an ionic dispersion in function of the analyte, which will be shielded by the ionic solution. Thus, depending on the concentration of the detected analyte the conductivity can be altered. It is crucial to take into account the length of the conjugated receptor-analyte and the distance from the surface in which molecules can be detected. The λ_D is inversely proportional to the concentration of the buffer used. In Figure 40 is shown the variation of the λ_D according with different electrolytic buffer concentrations. [185]

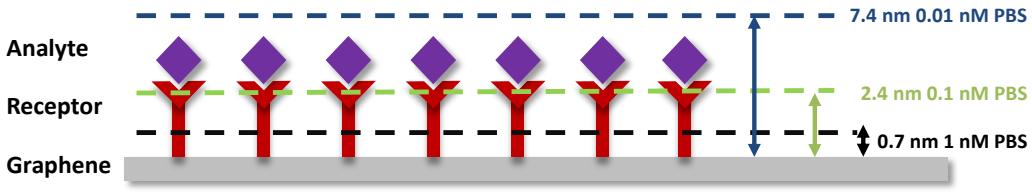

Figure 40. Scheme showing the height of Debye length (λ_D) on a sensor surface for different electrolytic buffer concentrations.

By using graphene-based FETs the detection of a large variety of analytes was reported.[186] The employment of single-strained polynucleotides as receptor in graphene-based FETs is promising for the detection of DNA and RNA due to the often-high sensitivity and selectivity avoiding any fluorescence or electrochemical labeling. For example, for a CVD graphene-based FET using DNA strands as receptor reached a detection limit of 10 pM.[187] An extraordinary higher sensitivity in a DNA FET has been recently reported using a deformed monolayer CVD graphene channel in millimeter scale structures.[188] In particular, the device showed a LOD in buffer and human serum sample down to 600 zM and 20 aM, respectively, which are ~18 and ~600 nucleic acid molecules detected. Theoretical studies suggested that this state-of-the-art

performance is achieved because the nanoscale graphene deformation can generate 'electrical hot spots' in the sensing channel which reduce the charge screening at the concave regions. Besides, the deformed graphene could exhibit a band-gap, allowing an exponential change in the source-drain current from small numbers of charges (Figure 41).

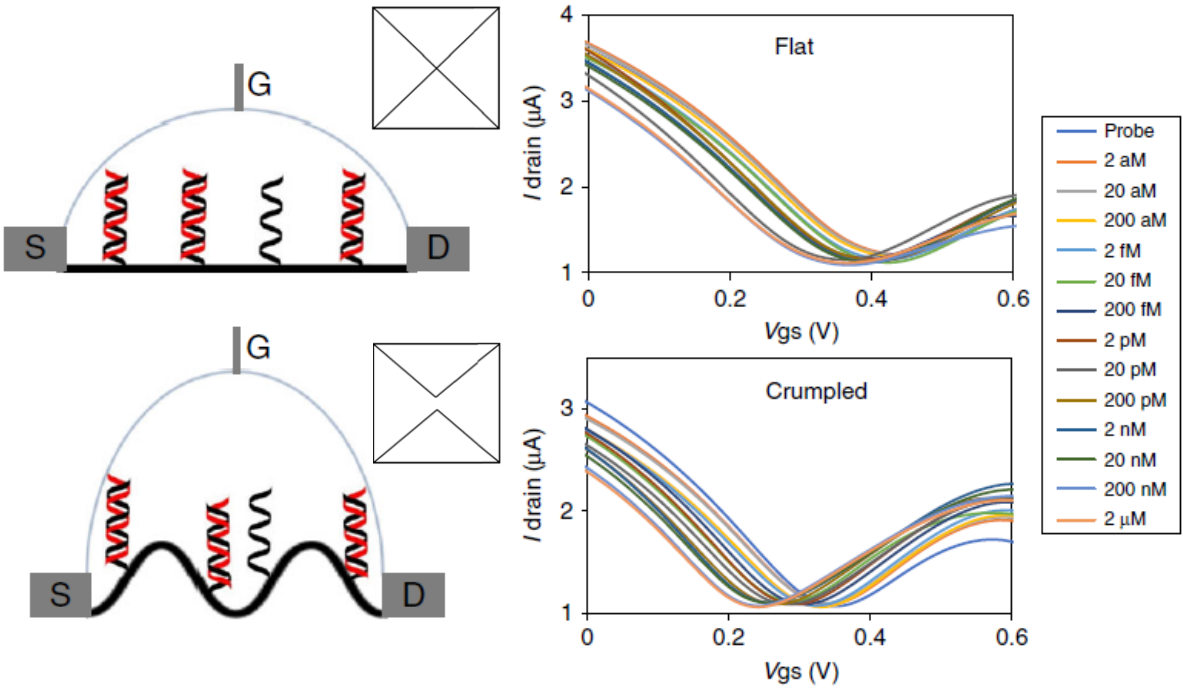

Figure 41. Scheme of the flat (top) and crumpled (down) graphene sensor and their respective band gap structure and I-V curve. Adapted from Hwang et al. 2020.[188]

Aptamer-modified graphene FETs have been successfully studied for biomolecule recognition based on electric variation in the semiconductor channel. For small molecules, the binding between aptamer and analyte results in the conformational change of the charge aptamer, hence, in a shift in the CNP. A modified pyrene-aptamer was used as selective sensor for ATP.[189] Aptamer can also be attached directly to the graphene surface. The variation in the graphene FET drain current was study for immunoglobulin E sensing.[190] The use of aptamers and short linkers allows a high sensitivity since the reaction happens close to the graphene surface.[191] Besides, aptamers could be used in the recognition of large molecules, such as proteins. For example, a selective aptamer for Hemagglutinin (HA) which is a protein biomarker of H1N5 avian influenza virus, was used in the development of a FET sensor in serum chicken.[192] The attached charged macromolecule induces an ion rediffusion which is translated in a change in the measured potential.[193]

Enzymes can be also bound to the FET channel surface. After the enzymatic reaction, the concentration change of the analyte or the corresponding product modulate the FET characteristics allowing analyte detection. They have used for glucose and neurotransmitter sensing. The monitorization of glucose level is highly desirable because it is associated with diabetes, hypoglycemia, and certain other diseases. A FET device composed of a graphene monolayer modified with glucose oxidase as channel showed LODs of 3.3–10.9 mM glucose.[194] The modulation of the channel conductivity occurs by means of n-doping of the graphene

layers due to charge transfer from the enzymatically generated H_2O_2. Detection of neurotransmitters is essential in order to understand how the brain works and to identify neurological diseases.[195] However, it is extremely difficult because they are locally released for truly short periods of time. Garrido and coworkers developed a graphene-based FET using polymer brushes to specifically detect the neurotransmitter acetylcholine.[196] Particularly, the polymer was grown on the graphene component by photopolymerization using the t-butyl methacrylate and N,N-dimethylaminoethyl methacrylate monomers. The first monomer provided the carboxyl groups where the enzyme acetylcholinesterase is chemically bonded, while the second one contributed with pH-sensitive groups which can detect the pH variations produced by the enzymatic degradation of the neurotransmitter to acetate, choline and protons. Thus, the local change of the pH value near graphene produces graphene doping that can be detected and quantified.

The precise detection of the pH value or of differences in the pH value is an important challenge in biosensing since the enzymatic reactions are leading to a local change of the pH. In addition, the pH monitorization is useful for the diagnosis of neural diseases.

The development of graphene FET immunosensors are extremely attractive for point-of-care applications because of the specific antigen-antibody interactions allowing direct or indirect detection methods. However, given the λ_D, the relatively large size of an antibody-analyte complex (9-15 nm) hinders its use in physiological media by a direct method. Therefore, the use of antibody fragments is mandatory.[197] Seo and coworkers have recently developed a graphene-based FET sensor for COVID-19 detection, in which the SARS-CoV-2 spike antibody was conjugated to a noncovalently modified graphene with 1-pyrenebutyric acid N-hydroxysuccinimide.[198] The sensor was able to detect the SARS-CoV-2 virus in different media including clinical samples, transport medium, and cultured virus. Besides, sandwich immunoassays can be implemented on graphene-based FETs.[199] For example, by using a sandwich immunoassay composed by a secondary antibody fragment tagged with a charged protein produced a high current change in graphene when the sandwich is formed (Figure 42).

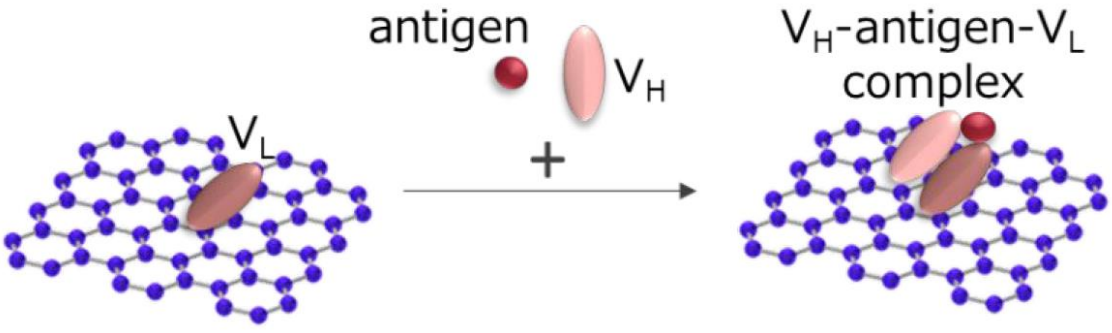

Figure 42. Scheme of the sandwich immunoassay for antigen FET sensor. V_L: antibody fragment attached to the graphene surface and V_H: labeled antibody fragment. Adapted from Kanai et al. 2020.[199]

The detection of electrically active cells is of high importance. Neural diseases are significantly growing in the last decades due to the population ageing. Neuroscientists are looking for technologies that are able to record brain signals because they give crucial information about

neural diseases. Based on this model, diverse research groups have recently developed flexible polyimide SGFET as brain-computer interfaces. The flexible character allows a better contact with the roughness brain surface. With these devices, they were able to record *in vivo* neural activity such as spontaneous oscillatory activity, which has a very low frequency. [200] Until now, there was not possible measure this activity because of the limitation of the current devices. This activity is related to the ions flow that passes through the neurons and can be translate to an extremely low voltages variation.

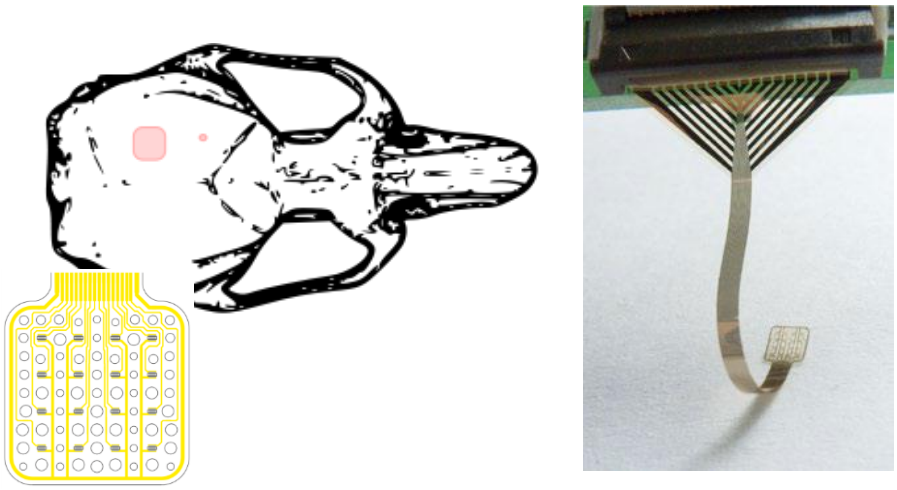

Figure 43. a) Representation of the Solution Gate Field Effect Transistor (SGFET) for in vivo recording in brain rat and b) Image of the neural probe. Adapted from MasVidal-Codina *et* al. 2019.[201]

These transistors exhibit signal-to-noise ratio better to the current platinum one with limit signal above 1kHz. Despite, these new devices are a great step towards a better diagnosis about the growing neuronal diseases, there is a need to improve the interface between the biological environment and the electrical system. For a better understanding of the neuronal processes, such as neurotransmitters or physiological changes in the brain environment, it is necessary the implementation of other sensing capabilities.

1.5.2.2. Diagnostic tools based on Mass Spectrometry.

Laser desorption/ionization (LDI), coupled with time-of-flight mass spectrometry (TOF MS) has become an indispensable analytical tool for the detection and analysis of small molecules, biomolecules, virus, bacteria residing in complex biological systems.[202] The LDI can be assisted by a matrix (matrix-assisted laser desorption/ionization mass spectrometry, MALDI MS which often are organic or inorganic compounds. But one of the main problems that MALDI presents is the matrix interference with molecules with small molecular weight (< 700Da). The matrix is necessary because transfers the energy from the laser to the analyte and reduce the ions fragmentation; however, it introduces background ions that can hinder the analyte signals. Therefore, it is necessary to look for novel strategies to improve the spectrometric analysis.[203] Nanomaterials have been widely developed as efficient assisted matrices for LDI detection of small molecules.[204] Carbon nanomaterials, including GBMs, have been demonstrated as an efficient matrix for MALDI. In particular, graphene has shown a great capacity in MALDI-MS analysis of small molecules due to high surface area, and electronic conductivity, a background-

free mass spectrum in the low molecule weight regions and a high desorption/ionization efficiency. Generally, oxidized carbon materials are the most employed nanostructures in this field because of their easily fragmentability. In 2010, rGO was utilized for the first time as a matrix for MALDI in the detection of nucleosides and amino acids.[205] Recently, GO was coated over the sample and has shown a powerful capability as MALDI matrix to detect more than 200 hundred molecules, including lipids and metabolites, and to perform MALDI-imaging combined with *in situ* mass spectroscopy in mouse brain tissue section (Figure 44).[206]

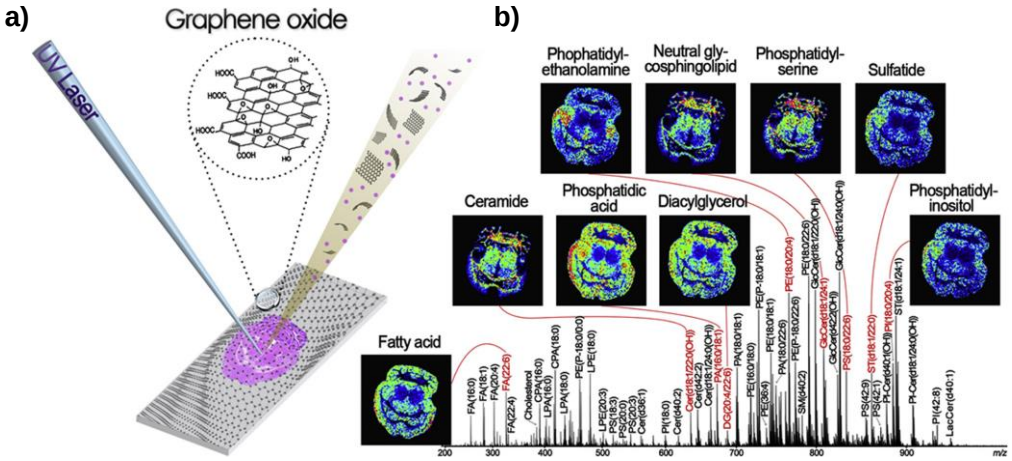

Figure 44. a) General scheme of graphene used as MALDI matrix and b) mass spectrum and ion images of mouse brain horizontal tissue section. Adapted from Zhou *et al*. 2017.[206]

The chemical functionalization of graphene can increase the adsorption capability and selectivity of the corresponding analytes by anchoring functional molecules,. In addition, the large specific surface area provided oriented analyte immmobilization and concomitant pasivation of the surface to avoid unespecific adsorption of contaminants that could interfere in the analysis. In this context, an improvement of the standard MALDI-MS method for the detection of N-glycans released from glycoproteins was reported by using noncovalent functionlized GO via π-π stacking interactions with pyrene derivatives activated as acid chlorides (Figure 45).[207]

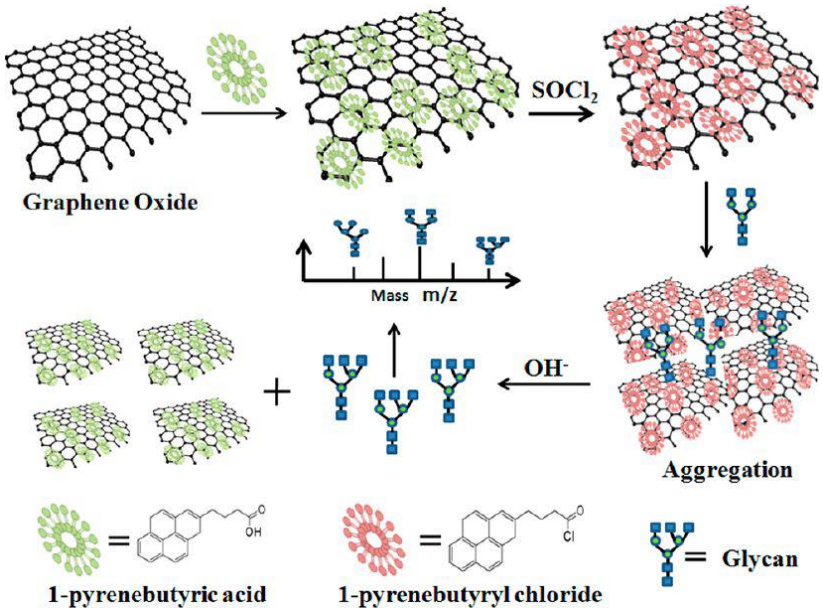

Figure 45. Schematic illustration of the procedure for PCGO preparation and Glycan Enrichment. Adapted from Zhang *et al.* 2013.[207]

The LDI can also be assisted by the surface of substrate materials, namely, surface- assisted laser desorption/ionization (SALDI).The most common approach in matrix-free methods is the use of well-structured materials as support for the sample and at the same time can transfer the energy from the laser to the sample. This strategy is called Surface-Assisted laser desorption ionization MS (SALDI).[208] Currently, the most widely used surfaces are porous silicon,[209] sol-gels which are structures formed by siloxane mixed with metals,[210] porous polymer[211] or the recently use of nanomaterials.[212] Although surfaces composed of graphene has promising applications in SALDI, only few examples have been reported. An rGO paper decorated with graphitic nanospheres as a substrate for matrix-free LDI-MS detection significantly increased the detection limit of diverse molecules compared to commercial products.[213] This carbon-based platform was obtained by pulsed laser irradiation in a selected area of filtrated graphene sheets generating these nanospheres that increased the LOD of diverse towards molecules by over two orders of magnitude compared to the pristine graphene paper. Moreover, the surface hydrophobicity and electric conductivity are enhanced after the laser engineering process.

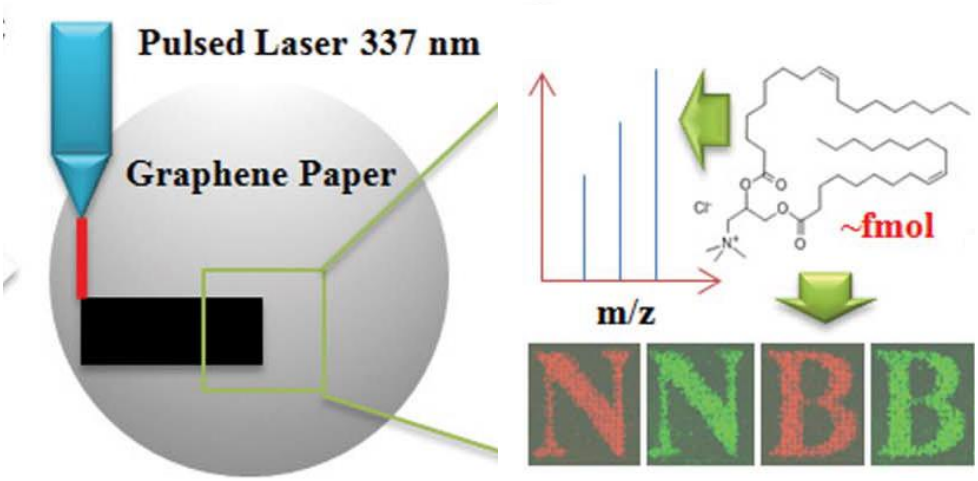

Figure 46. Scheme of the graphene SALDI paper and imaging MS of the pattering surface. Adapted from Qian *et al.* 2013.[213]

Recently, a SALDI platform based on graphene-like monolayer for analysis of diverse small molecules with good LODs of 1 pmol to 10 fmol.[214] The graphenic surface was prepared from self-assembled monolayers of aromatic thiolates on gold on gold by a sequence of irradiative and thermal treatments.

Despite these promising examples, some inconvenient remains, such as aggregation and provide a low shot-to-shot reproducibility. In the work developed by the group of Prof. Jiang based on a 3D printed graphene oxide-doped MALDI target, the doped GO acts as laser absorber and ionization promoter, thus permitting the direct analysis of samples without addition of organic matrix and allowing the reusability of the target for more of 400 successive laser shots (Figure 47).[215]

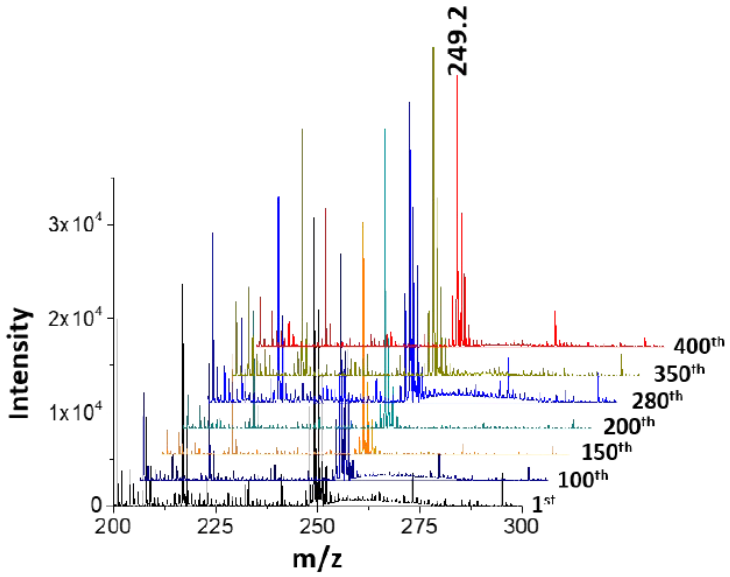

Figure 47. MS spectrum of bisphenol S as model analyte to test the reusability of the 3D printed graphene oxide-doped target. Adapted from Wang *et al.* 2018.[215]

Appendix: Characterization techniques

To the most employed characterization techniques to corroborate chemical modifications of graphene are listed in the following section.

Raman spectroscopy

Within all the possible characterization techniques for CNMs, Raman spectroscopy is the most relevant one due to its sensitivity to the vibration of C-C bonds. The study of inelastic light scattering (the kinetic energy of the particle which impact is not conserved, is transformed or lost) gives us structural information about the defect concentration, stacking of the layers or crystalline size.[216]

All the CNMs, present a similar Raman spectrum as the Figure 48a shows.[219] In particular the Raman spectrum of graphene includes several peaks which are well distinguished and understood, which allow obtaining important spectroscopic information regarding its structure. At ≈1580 cm^{-1} G peak is an in-plane bond stretching vibration mode (a change in the length of a bond) in the honeycomb lattice. It allows for the change in the bond length between all pairs of sp^2 atoms.[217] The D band at ≈1350 cm^{-1}. This band appears when there is scattering between two no equivalent atoms. This can happen near "defects sites" such as a sp^3 type carbon formed due to the attachment of functional groups. Consequently, the ratio I_D/I_G gives us information about the amount of sp^3 type defects is the main tool to semi-quantify the graphene covalent functionalization level of graphene. Finally, the 2D peak at ≈2700 cm^{-1} is a second-order mode of the D band. It is related with the number of layers (Figure 48b) changing in shape and intensity with them.[218]

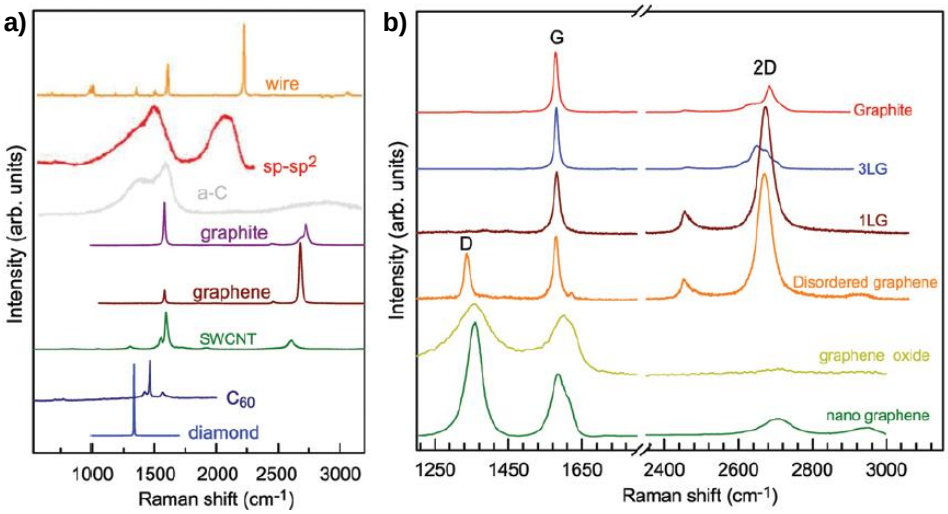

Figure 48. (a) Raman spectra of some carbon allotropes and (b) Raman spectra of GBMs. Adapted from Wu *et* al. 2015.[219]

X-ray photoelectron spectroscopy

X-ray photoelectron spectroscopy (XPS) is a technique that determines the surface chemical composition of the analyzed material. When a solid surface is irradiated under ultra-high vacuum (UHV) conditions with a beam of X-rays, photoelectrons of these surface atoms are

emitted. Simultaneously, the kinetic energy and the energy of the photons are measured. The binding energy can be calculated using the following equation:

$$E_b = E_{hv} - E_k - W_m$$

In this equation, W_m is the work function of the instrument, E_k is the kinetic energy of the electron, $E_{h\nu}$ is the energy of the phonon and E_b is the binding energy of the electron. For each element, the electrons have an identified binding energy; therefore, the elemental composition of the sample can be obtained (Figure 49a).

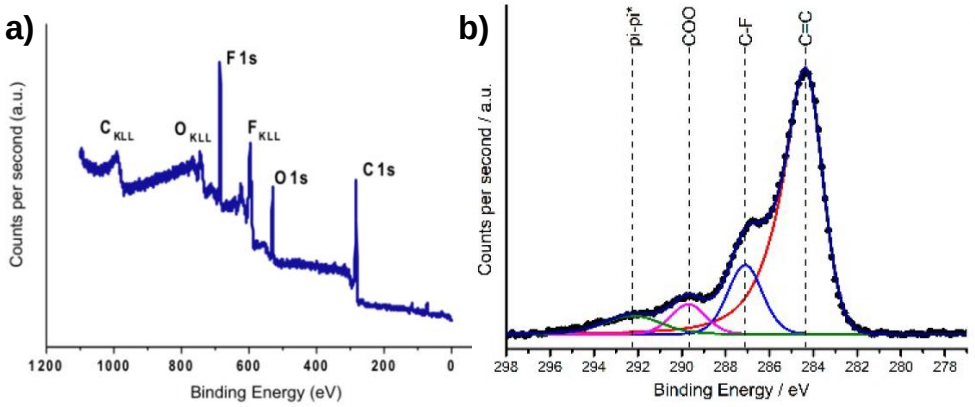

Figure 49. a) Survey of a functionalized graphene with fluorine-containing molecules and b) deconvoluted C1s core level. Adapted from Sulleiro *et al* 2018.[220]

High resolution scan can be performed into specific ranges. With the de-convolution of these regions into different components, information of covalent interaction can be attributed to this new component obtained as we can see in Figure 49b for de C1s region.

Electron Microscopy techniques.

Scanning electron microscopy (SEM) is a technique which gives us high resolution images of the sample topography. An electron beam irradiates the sample surface. Usually, secondary electrons are emitted when these electrons have enough energy to be ejected from the surface, and collected for a detector, displaying an image of the surface topography.[221]

Transmission electron microscopy (TEM), is based on passing an electron beam through the sample, which normally is not more than 100 nm thick. Due to this interaction, the electrons are diffracted, (in function of the electron density of the sample) and detected by a CCD camera to obtain an image with nanometric resolution.

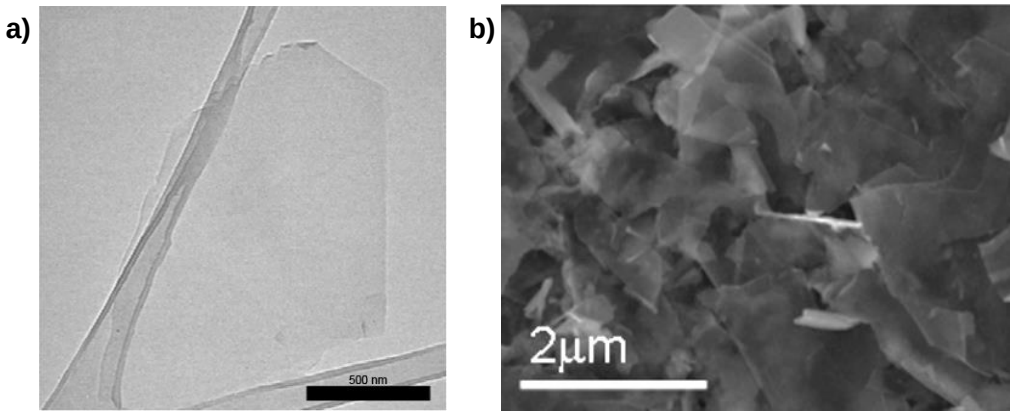

Figure 50. a) TEM image of monolayer grapheme and b) SEM image of few layers graphene. Adapted from Hernandez et al 2008. [222]

Atomic Force Microscopy

In this thesis, Atomic Force Microscopy (AFM) became a powerful technique to determine the surface changes after our different modification. In AFM the sample is sweep with a sharp tip mounted to a cantilever. This interaction leads in a cantilever deflection. The laser beam reflected on the cantilever experiment change and is detected. In this manner a topographic image is obtained. [223] The system is connecting to a piezo driver in order to maintain the force or amplitude constant (in function of the mode, Figure 51).

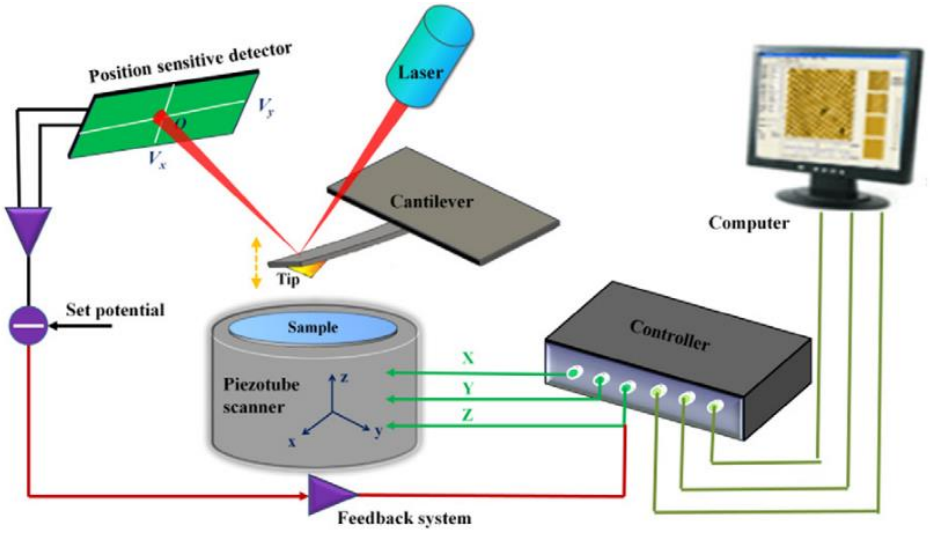

Figure 51. Schematic diagram of Atomic Force Microscope. Adapted from Guo *et* al 2014. [224]

In this thesis 3 different AFM modes were used:

(i) Contact mode: the tip is in contact with the sample surface. The cantilever bending is measured through a laser deflection signal change. The feedback loop, in order to work with constant force, responds by adjusting the tip-sample distance. This mode has the disadvantage that both sample and tip may suffer damage.

(ii) Tapping mode: In this mode, the cantilever oscillates at a frequency determined for the tip. The amplitude is constant due to the feedback loop, so the changes in the frequency give us information about the tip-sample interaction.

(iii) PeakForce tapping mode: It operates in similar way that tapping mode. However, the cantilever oscillates at a frequency below the resonant mode. The tip is periodically tapping the sample (pNewton interactions). Thus, in each tapping cycle, a different force curve is measured, which lead to a higher resolution image. In this case, force is measured directly for the deflection of the cantilever.[225]

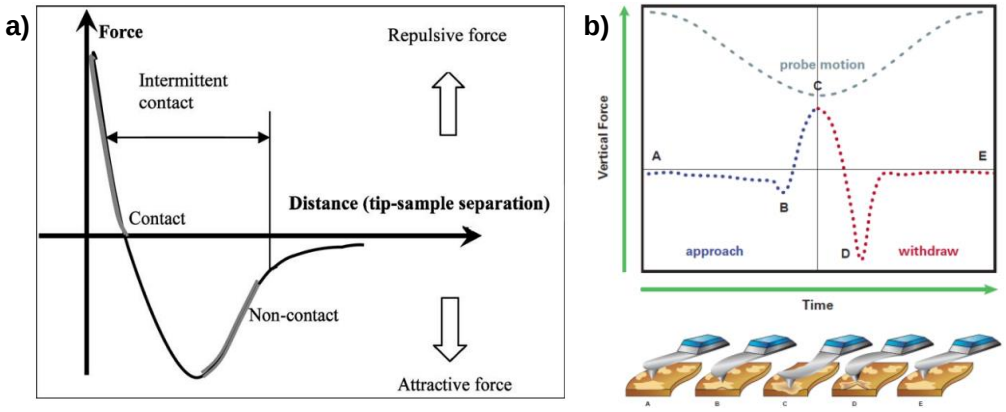

Figure 52. a) Interatomic force variation between tip and sample for tapping mode and b) plot of force and position again time for peakforce tapping mode. Adapted from Jalili *et* al 2004[226].

With this new AFM mode, besides the height and the properties of the material at nanoscale can be studied, such as surfaces forces, mechanical deformation, elastic modulus and energy dissipation.

Matrix-Assisted Laser Desorption/Ionization.

Matrix-Assisted Laser Desorption/Ionization (MALDI) is an ionization method for Mass Spectroscopy (MS). A matrix is mixed with the analyte, to transfer the energy to it, and the resulting crystalized mix is irradiated with a laser beam generating ions. These ions are accelerated, passed through a quadrupole filter. According to the mass-to-charge ratios [m/z] values, they have different times of flight (TOF), thus the ions are separated, and they reach the detector.

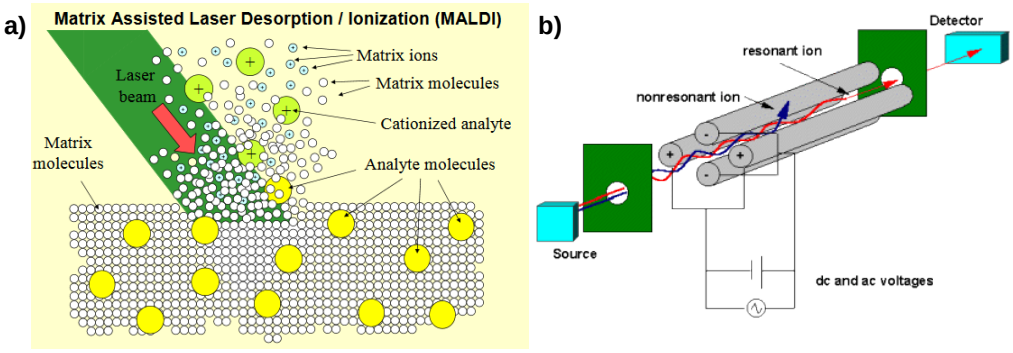

Figure 53. a) Analyte/matrix ionization process and b) quadrupole filter Adapted from Bruker.[227]

There are several factors to take in account to choose the most suitable matrix, but it mainly depends on the type of compounds you want to analyze. The matrix must have a high desorption/ionization efficiency of the laser and might contribute to the vaporization of the sample. The most common matrices are 2,5-dihydroxybenzoic acid (DHB) for detection of low-weight molecules and 3.5-dimethoxy-4hydroxycinnamic acid (sinapic acid) for high-weight molecules like proteins.[228] However, new matrixes are constantly being added as well as matrix-free systems based on surface assistance. As mentioned previously, graphene derivatives can be used as MALDI matrix and as SALDI or SELDI support. This point has been one of the main chapters of this thesis.

Contact Angle.

Wetting solid surface with liquid is a classical way to understand the nature of a material. When a drop of a solvent is put in contact with a flat solid surface and the liquid does not wet the solid completely, a Young's equilibrium angle θ is formed. For a polar solvent like water, if this angle (called contact angle) is larger than 90°, the surface is considered hydrophobic. Otherwise, if the angle formed is smaller than 90°, the surface is considered hydrophilic.[229] In the image 54, both formed contact angles are hydrophilic; however, the first example is considered more hydrophilic than the second one. With this method, we can study hydrophobic changes on surfaces after chemical or physical treatments.

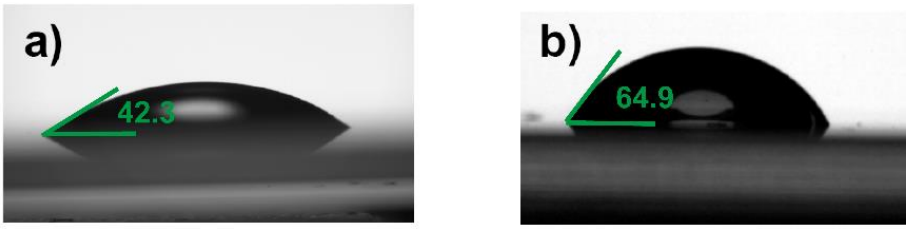

Figure 54. Contact angle for two hydrophilic surfaces.

2. RESULTS AND DISCUSSIONS

2. Results and discussions

2.1. Aim of the work

The use of CVD graphene has been widely studied in both electronic and sensor fields as shown along the previous introduction. Moreover, the chemical functionalization of graphene allows to introduce other functionalities and to increases the adsorption capability of functional biomolecules and tuning its properties.

A solvent cleaning procedure of CVD graphene transistors was investigated. This approach showed evidences of the chemical doping reduction as well as noise levels typically associated to polymers residues after each of the photolithography processes.

In this thesis, diverse routes for the functionalization CVD graphene have been studied in different surfaces and substrates in order to develop organic interfaces that will be useful for the recognition of biomolecules.

Particularly, the development of a covalently functionalized graphene sensing platform, such as graphene Solution-Gated Field Effect transistors (graphene-SGFET), was addressed to introduce carboxylic groups as "anchor points", which will be used to link a selective aptamer for the thrombin recognition.

In addition, taking advantage of the high desorption/ionization efficiency of graphene, several modified CVD graphene-based glycan arrays were manufactured on different substrates, including ITO and bare glass, as potential sensing platforms. The obtained graphene-based arrays were able to detect carbohydrate-lectin interactions, which are involved in a plethora of biological process, by LDI-MS analysis.

2.2. Chemical modification of graphene-based transistors for biosensing applications

The following research has been performed in the framework of the Graphene Flagship Project, which is the European Union's biggest scientific research initiative. In particular, our group is involved in the work package entitled *Biomedical Technologies* that aims at the development of implants and therapeutic elements for specific clinical outcomes in neurology, ophthalmology and surgery to design the future generation of medical implants. This initiative is composed by 145 groups and partners, from 21 different countries. This research has been developed in collaboration with the Biomedical Application Group headed by Prof. Rosa Villa in the *Centro Nacional de Microelectronica* in Barcelona.

In the remainder of this discussion, the nomenclature introduced by Criado and coworkers[72a] has been applied (Figure 55) to clearly differentiate the type of support substrate of graphene and the functional group to which graphene is covalently linked when is required.

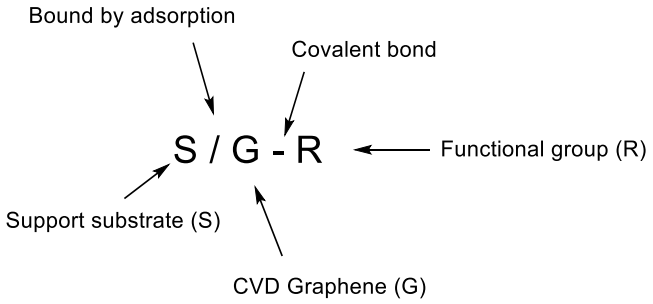

Figure 55. Nomenclature adopted for functionalized graphene on a substrate.

In recent years, the amount of people who suffer neurological disorders such as stroke, encephalitis, Alzheimer's disease, epilepsy or Parkinson, have been increased due to the high life expectancy and the reduce of the fertility, which results in population aging and is estimated to increase in years to come.[230] For this reason, there is a significant interest in the study about the brain for diagnosis and therapy. Graphene-based devices have been one of the most promising material candidates for neural monitoring due to the remarkable electronic properties of graphene.[61,201] In addition, the graphene flexibility can also improve the interaction of the device with the neuronal tissue.[231]

In particular, the goal of our work is to develop and provide design rules for an *in vivo* sensing platform for novel diagnosis and treatments, which can be applied for future neural flexible probes based on graphene (*e.g.* graphene microtransistor array on polyimide, Figure 56). The final implants will use the modified graphene as component to monitor and influence the nervous system. These devices will consist in microelectrode arrays of g-SGFETs, which particularly allows measurements in aqueous systems.[232] With this purpose, the generation of interfaces on this kind of devices has been addressed for an optimal recognition capability through graphene modifications that allows to introduce receptor anchor sites or new functionalities.

However, the development of reproducible measures is required for standardization and thus commercialization. Hence, the purest and cleanest graphene is needed in order to have the

minimum impurities that could affect the reproducibility of the measurements. In this context, we have firstly studied a cleaning method for graphene as transistor component to obtain the best device performance. Then, the implementation of sensing capacities to GFET has been tackled by chemical modification.

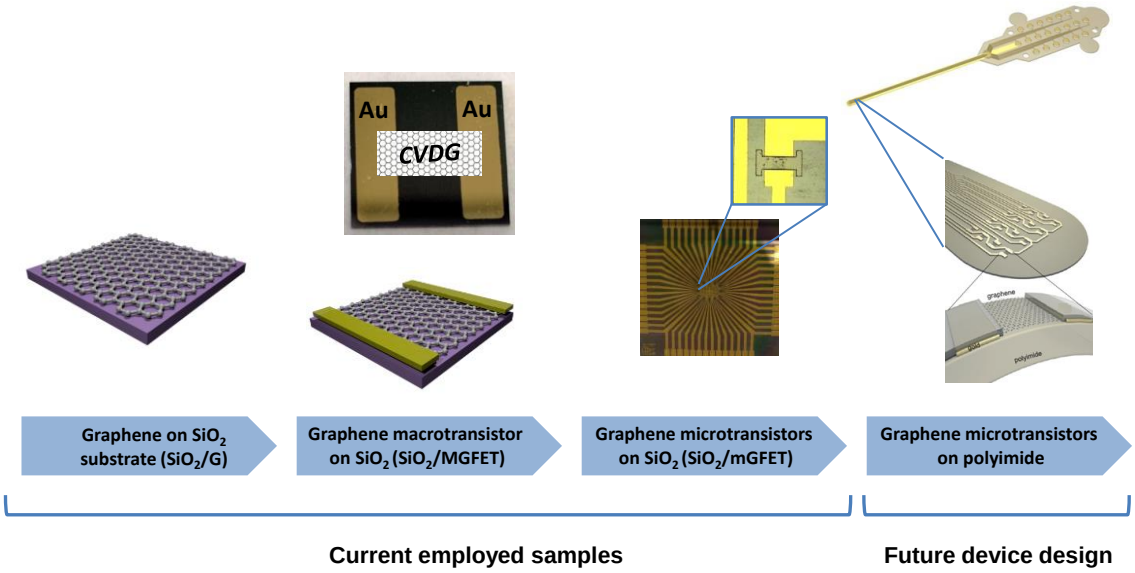

Figure 56. Scheme of the different architectures used in the developed of the sensing platform.

For these purposes, different CVD graphene samples have been used. As first approach towards novel flexible *in vivo* sensing implants (e.g. graphene microtransistors on polyimides, Figure 56), we have focused on simple architectures, such as CVD graphene on SiO_2 substrate (SiO_2/G, 1 x 1 cm); individual CVD graphene macrotransistors (SiO_2/MGFET), which are composed of two gold electrodes to connect to the measurement setup, and a graphene ribbon of 1.0 x 0.5 cm on SiO_2; and chips (SiO_2/mGFET) composed of forty-eight CVD graphene microtransistors array. Particularly, this array is made of different layers as shown in Figure 57. Each microtransistor possesses a 50 μm graphene ribbon as semiconductor on SiO_2. Given that the electrical characterization is performed in aqueous solution, the protection of the metal tracks is mandatory to avoid short circuit. Thus, an epoxy polymer (SU-8) passivation layer was done on the electrodes.[233]

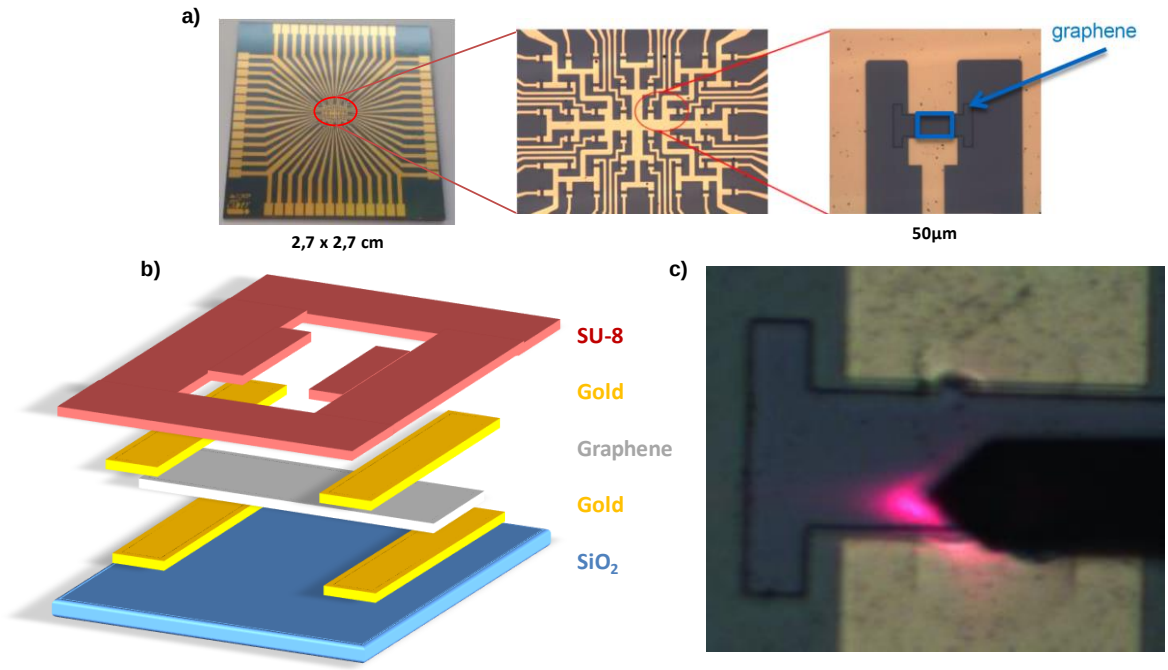

Figure 57. a) SiO_2/mGFET at different magnifications, b) device layers and c) optical image of an individual CVD graphene microtransistor.

In the following studies, these samples have been employed for different purposes. SiO_2/G and SiO_2/MGFET have been used to find the optimal conditions since the large dimension of graphene allows complete surface analysis by different techniques. In addition, SiO_2/MGFET offered the possibility to obtaining a preliminary electronic characterization. Then, the SiO_2/mGFET has been mainly used to precisely characterize the electronic properties of graphene due to the high data generated for one sample. However, the surface analysis of graphene in this chip is limited due to the low dimension of the graphene component (50 nm).

2.3. Effect of solvent in CVD graphene processed devices

The two types of devices SiO_2/MGFET and SiO_2/mGFET were employed for evaluating the effectivity of diverse solvents to remove polymer residues from the graphene surface as post-lithographic cleaning process. The two graphene-based devices were built using a clean-room process, minimizing any contamination on the graphene surface to obtain an excellent performance. They were manufactured by a sequential layer-by-layer deposition using different photolithography steps to define the shape of each layer (Figure 58). Photolithography consists of defining a pattern from a photomask by illumination the sample with UV-light to a photosensitive surface to enable the deposition of a new material.[234]

In this kind of fabrication process, various polymers were used that can introduce some contamination in the semiconducting material. Graphene as effective semiconductor in FETs is extremely sensitive to the retained contamination. The polymer residues can introduce chemical doping species, can reduce carrier mobility and can degrade the signal to noise ratio. For SiO_2/mGFET, three different polymers were used in this device fabrication. PPMA and AZ5214E (Clariant, Germany; Figure 58 step 3) were used in the graphene transfer steps to provide mechanical stability once graphene is delaminated, and an epoxy polymer (SU-8, Figure 58 step

6) to passivate the metal tracks. However, SiO_2/MGFET fabrication was based on CVD graphene transfer, i.e. graphene in contact with PMMA, while only AZ5214E is used for patterning the graphene macrotransistor channel. Since alternative microfabrication technology is not currently identified, a solution based on post-lithography cleaning processes has been evaluated.

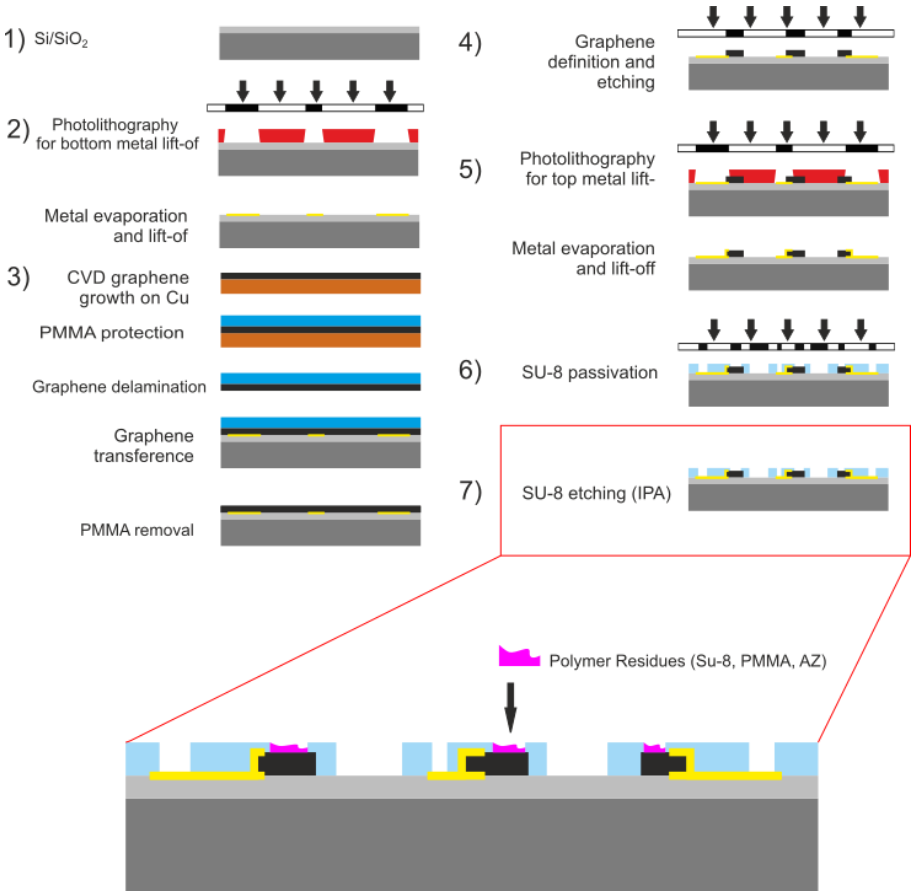

Figure 58. Graphene field effect transistor manufacturing process. Adapted from Masvidal 2016.[235]

Along our chemical processes of graphene, an unexpected tendency was observed in the graphene electrical properties when THF was presented during chemical processes (Figure 111). For that reason, the solvent cleaning influence on the electronic performance of GFET was then discussed.

Polymer solubility involves many different parameters such as solvent diffusion and chain disentanglement. To select with precision the most suitable solvent for polymer removal by wet cleaning process, both thermodynamic and kinetic considerations must be taken. Hildebrand and Hansen solubility parameters, which are interpreted in terms of molecular interactions, are the most preferred methodologies to calculate the best solvent (or mixture of them), according to three main characteristics: polar, dispersive and hydrogen bonding interactions between solvent and polymer. On the other hand, kinetic mechanisms also play an important role in the polymer dissolution process, as only favorable interactions do not guarantee an effective dissolution. Due to the fact that the solvent aggression begins by pushing the more superficial rubbery polymer into the solvent, and with the time, a larger dilute upper layer is pushed into the solvent, further penetration of the solvent into the solid increases the solubility.[236] For

instance, Miller Chou *et al.* reported that the dissolution rate of the polymer chains decreases with increasing solvent molecular size because it is limited by the solvent molecules penetration.[237] According to this affirmation, MeOH should be the most suitable solvent. However, it has been reported that some polymer films crack in MeOH.[238] This event could affect the device architecture and performance. As an alternative to MeOH, a mixture of acetone and isopropanol is routinely employed in some intermediate steps of the microprocessing sequences without reported cracking. However, acetone tends to leave many organic residues and isopropanol cannot always penetrate to remove them all.

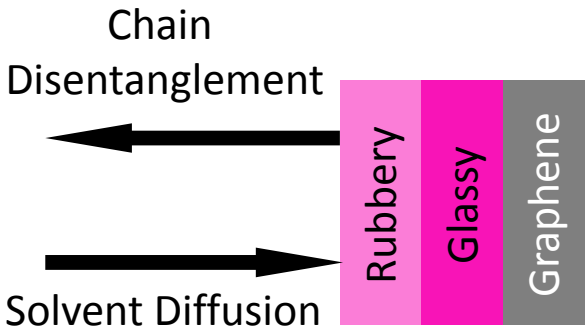

Figure 59. Schematic one-dimensional solvent diffusion and polymer dissolution. Adapted from Narasimhan *et* al. 1998.[236]

As mentioned above, the commercial polymer materials PMMA, AZ, and SU-8 polymers were used in the fabrication process of our graphene-based devices. Since specific information for AZ and SU-8 polymers was not available, the information of structurally similar polymers such as Amberol F7 and Araldi was respectively used. Thus, the indicative solubility parameters of the polymers employed have the following values: δ_{PMMA} = 19.0 $MPa^{1/2}$, $\delta_{Amberol\ F\text{-}7}$ = 19.0 $MPa^{1/2}$ and $\delta_{Araldit}$ = 21.0 $MPa^{1/2}$.[239] Accordingly, EtOH and THF were specifically selected as cleaning polymer agents. They, both, present acceptable solubility parameters for the target polymers (δ_{EtOH} = 26.0 $MPa^{1/2}$, δ_{THF} = 18.6 $MPa^{1/2}$) and have low molecular weights.[240] Moreover, the two solvents are volatile and easy to remove. While THF is considered to be one of the most efficient universal solvents, EtOH can be preferred for industrial applications, as it is non-toxic and more environmentally friendly.

For evaluating the effect of these two solvents for cleaning graphene surface of polymer residues in g-SGFET, the two graphene devices SiO_2/MGFET and SiO_2/mGFET were employed. Firstly, the large area graphene SiO_2/MGFET allowed a physic-chemical characterization of the graphene surface, to understand the solvent effect in the residues from PMMA and AZ. In particular, the polymer solvation was assessed by extended and local surface characterization techniques. Then, the assessment of SiO_2/mGFET permitted a refined studied of the effect of the three polymer residues, including SU8, based on its electrical performance, in terms of charge neutrality point (CNP), transconductance and noise levels.

The presence of polymer residues before and after the cleaning process in SiO_2/MGFET samples was determined by XPS, AFM and Raman spectroscopy. XPS analysis provided evidence of the

polymer contamination in relation to the chemical bond spectra obtained from the graphene surface. Pristine suspended graphene would show a single XPS emission band corresponding to the C=C core level binding energy which is found at 284.70 eV.[241] For transferred graphene supported on for example SiO_2 wafer, the XPS spectrum also contains the substrate relate contributions since the probe depth of XPS is greater than the graphene film thickness. In addition, oxygen-containing carbon groups such as C-O and C-O-C (≈ 286 eV), C=O (≈ 287.5 eV) and O-C=O (≈ 289 eV) appears due to amorphous carbon and polymer contamination. Figure 60c shows a typical C1s core level spectrum of a SiO_2/MGFET. The presence of oxygenated groups indicates that polymer contamination, from PMMA and AZ employed during transfer and patterning, respectively, is present. The initially higher area of O-C=O groups is an indication that contamination correspond to PMMA residues, as it can be clearly understood from the reference spectrum of a PMMA film as compared to AZ reference spectrum (Figure 60a and b, respectively). However, the absence of high oxygen-content components as diagnostic signal in C1s core level for AZ hinders the detection of this polymer by XPS.

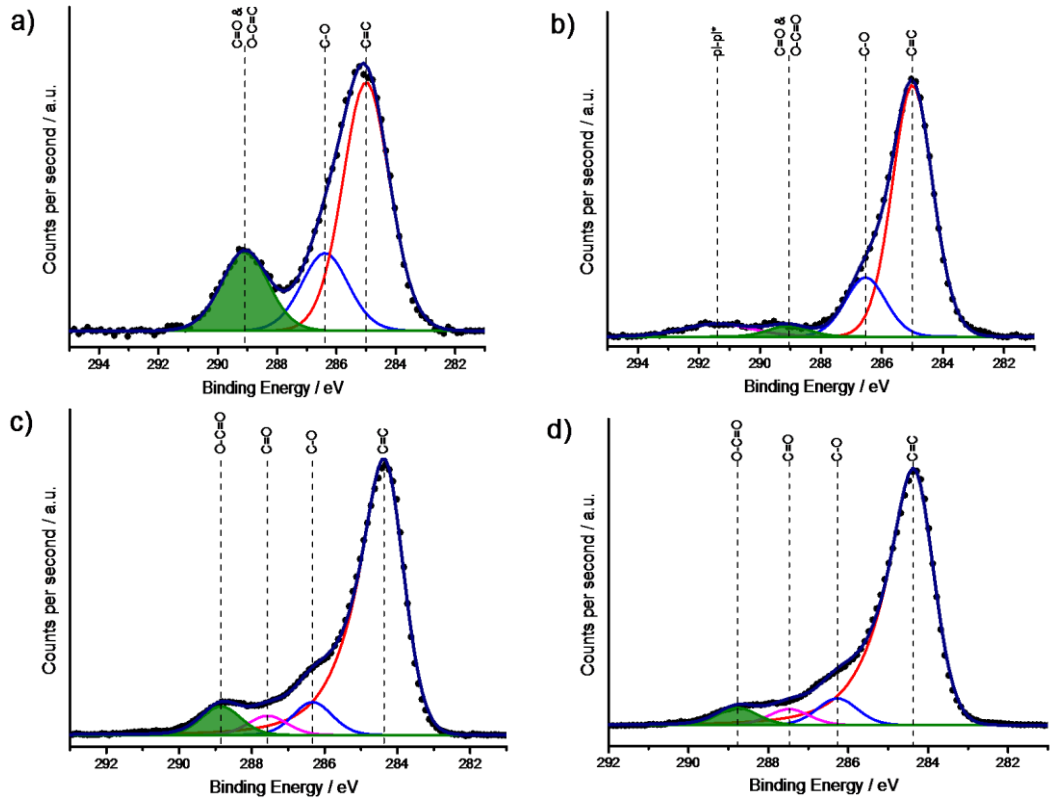

Figure 60. Deconvoluted C1s Core levels for a) PMMA, b) epoxi resin AZ, SiO_2/MGFET c) before treatment and d) after 120′ EtOH cleaning process.

Then the cleaning treatments of SiO_2/MGFET with EtOH and THF were performed at different times, 10 and 120 minutes. Considering the C/O/Si atomic percentages before and after the solvent step fully supports that an effective removal of certain amount of polymer residues is obtained (Table 1). A reduction of atomic percentage of carbon is obtained for all treatments

and that it can be attributed to both applied solvents. More detailed data was obtained from the XPS-curve fitting of the C1s core levels. For the EtOH- treated substrates, a reduction in the O-C=O component, was observed (≈ 2.5 %, Table 1). This decrease in the carboxylic groups implies an elimination of the polymer. For the THF- treated substrates, the decrease in the O-C=O component cannot be established because the initial amount of this specie was originally lower. The amount of polymer residue can vary from batch to batch but also among samples of a same batch.

Table 1. C/O/Si atomic percentages before and after the solvent treatments

Treatment (Solvent/time)	Before			After			Δ (before-after)		
	C/at%	**O/at%**	**Si/at%**	**C/at%**	**O/at%**	**Si/at%**	**C/at%**	**O/at%**	**Si/at%**
EtOH/10 min	54.85	27.61	17.54	50.59	28.18	21.24	4.36	-0.57	-3.7
EtOH/120 min	49.13	30.87	20.00	42.83	32.44	24.47	6.30	-1.57	-4.73
THF/10 min	64.34	19.84	15.83	60.85	22.23	16.92	3.49	-2.39	-1.09
THF/120 min	55.89	24.80	19.31	53.00	26.34	20.66	2.89	-1.54	-1.35

The presence of polymer contamination and the subsequent effect of EtOH and THF solvation were also confirmed by the AFM results. The contamination consists of an ultrathin molecular layer on top of the graphene, but polymer rests in the form of nanometers particles can also be obtained. As reflected the AFM images in Figure 61a and c, the highly rough surface of graphene is indicative of the polymer residues in the form of spots. They were found in all processed samples, with a heterogenous distribution and density. As for the solvent cleaning, apparent topography changes were observed for both EtOH and THF, without significant differences on time duration. Changes in the morphology roughness were measured by AFM before and after solvent treatment as a parameter of cleaning.

Table 2. Percentage of reduction in the traceable XPS peak, AFM roughness and macroscopic damage observed optically for the different solvents at different times for SiO_2/MGFET.

Chemical Solvent	**Solvation time (min)**	**Δ Area$_{O-C=O}$ (%)**	**Δ Roughness (%)**	**Macroscopic Damage**
EtOH	10	-2.56	-0.37	None
EtOH	120	-2.61	-1.89	None
THF	10	-0.68	-0.80	Detachment
THF	120	-1.02	-0.77	Detachment

The Root mean square roughness (RMS roughness) values were calculated considering the root mean square of graphene surfaces according to the *Equation 1*.[242] Where L is relative length of the profile and $Z(x)$ is the function that describes the surface profile analyzed in terms of height (Z) and position (x) of the sample over the evaluation L. RMS roughness of a surface is similar

to the roughness average (R_a), but while the Roughness average takes in account the irregularities over the mean line, RMS roughness obtains more information distinguished between peaks and valley.

$$RMS = \sqrt{\frac{1}{L}\int_0^L |Z^2(x)|\, dx} \qquad \textit{Equation 1.}$$

A reduction of RMS values was obtained for both solvents without significant differences on time duration (Figure 61 and Table 2), which suggests a removal of the surface coverage of these polymers. In particular, a clear removal of the single spots was observed (Figure 61). In addition, nanometer size defects as holes or cuts were also revealed, while macroscopic detachment tended to proliferate more when THF was used as a solvent.

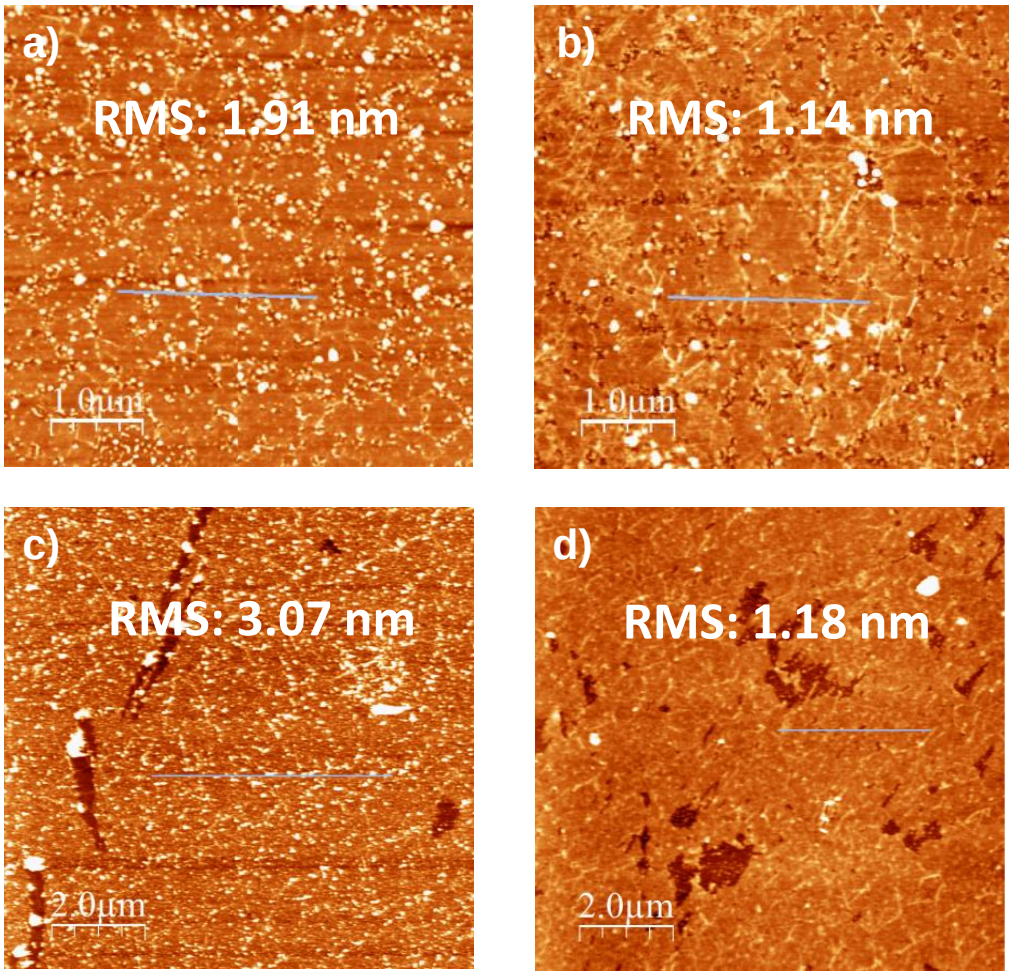

Figure 61. AFM image a) before and b) after cleaning process with THF 2h and c) before and d) after cleaning process with EtOH 2h. RMS value were measured avowing the scratches areas.

Histograms of height were obtained from the AFM images in order to estimate the nanometer size polymer residues in terms of this parameter. The histogram analysis showed a particles size from 2 nm to 10 nm in height (Figure 62). After cleaning, a reduction of roughness values was obtained for all, quantitatively, down to about 1 nm.[243] However, the THF cleaning process for 10 min, the height was increased possibly due to some detachment areas. Optical damage was also detected when THF was used (Table 2). The graphene detachment produced during the THF treatment could be ascribed to mechanical damage of the polymer during its dissolution.[244]

Ouano *et al*. reported that the dissolution of PMMA in THF produced a fast polymer crazing due to the joint action of high diffusion rates and slower swelling.[245] Therefore, a catastrophic polymer fracture results when the internal pressure accumulates faster than the glassy matrix is able to relax through gradual swelling. A similar process may occur in our case during the THF cleaning, in which the polymer fractures could compromise the physical integrity of the graphene film.

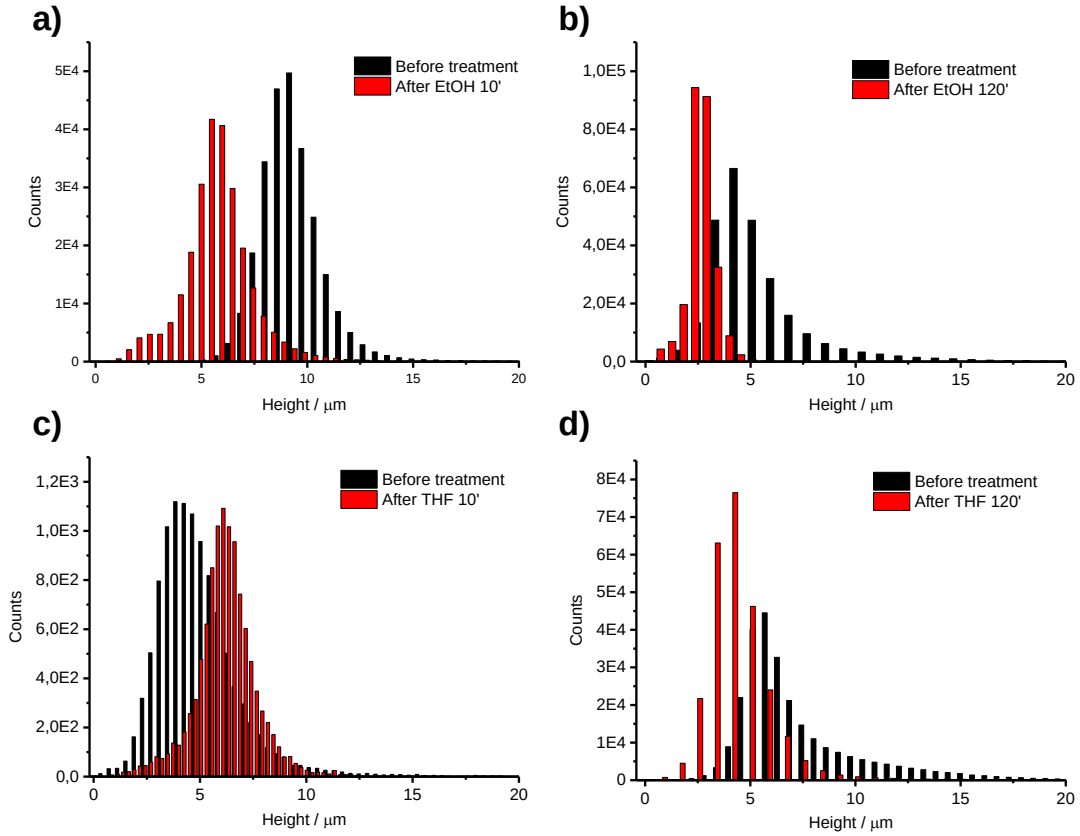

Figure 62. Histograms obtained from the AFM images for SiO_2/MGFET before and after treatment with EtOH for a) 10 min and b) 120′ and with THF c) 10 min and d) 120′.

Raman spectroscopy exhibited that the structural characteristics of graphene were not significantly affected by any of the two solvent treatments. According to Raman scattering information, the CVD graphene consists in mainly single layer graphene with some defects or limited domain size, distributed in the order of a few microns range (*e.g.* I_D/I_G = 0.25, 532nm, Figure 63).

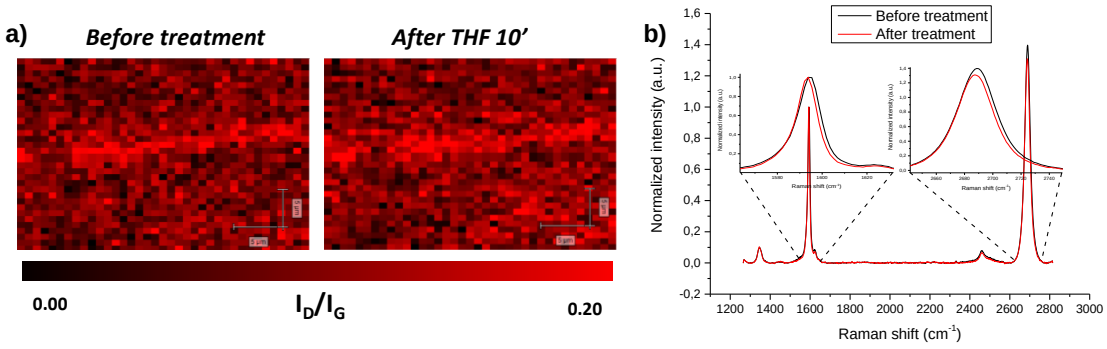

Figure 63. a) Raman mapping of the D band intensity in 30x25 μm² area and b) averaged Raman spectra (≈1000 single-point spectra, λ_{exc} = 532nm) before and after cleaning process of SiO_2/MGFET with THF 120 min

The presence of the three possible polymer residues and, then, the removal effectiveness of the selected solvents was evaluated by a deep analysis of the graphene SGFET electrical characteristics in SiO_2/mGFET.

The electrochemical evaluation of microtransistor array was performed in the GFET cell (Figure 64). SiO_2/mGFETs were placed in a cell which is composed of four gold arrays of 12 contacts which are in touch with the gold electrodes (source and drain). To perform the measurements, 600 μL of the PBS 10 mM solution was deposited in the cavity of the cell and then the system was connected to the set-up to record the corresponding signals (Figure 65). After characterization, the probes were removed from the cell, cleaned with distilled water and dried.

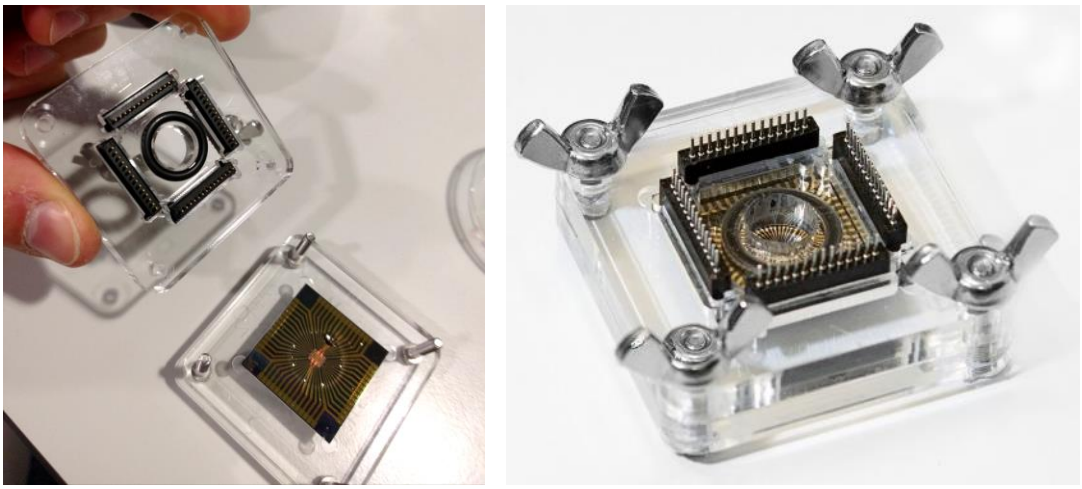

Figure 64. Biosensing platform in the GFET cell.

The set-up (Figure 65) to perform the measurements is composed by a Printed Circuit Board (PCB) connected to a Data Acquisition Card (DAQ Card), which digitalizes and transmits to a computer the analog signal and allow the measurement of 24 transistors of each probe and the Direct Current (DC) source that polarize the operational amplifiers from the PCB. A voltage sweeps from 0 to 0.4V is used and, immersed in the solution, Ag/AgCl was used as reference electrode (gate).

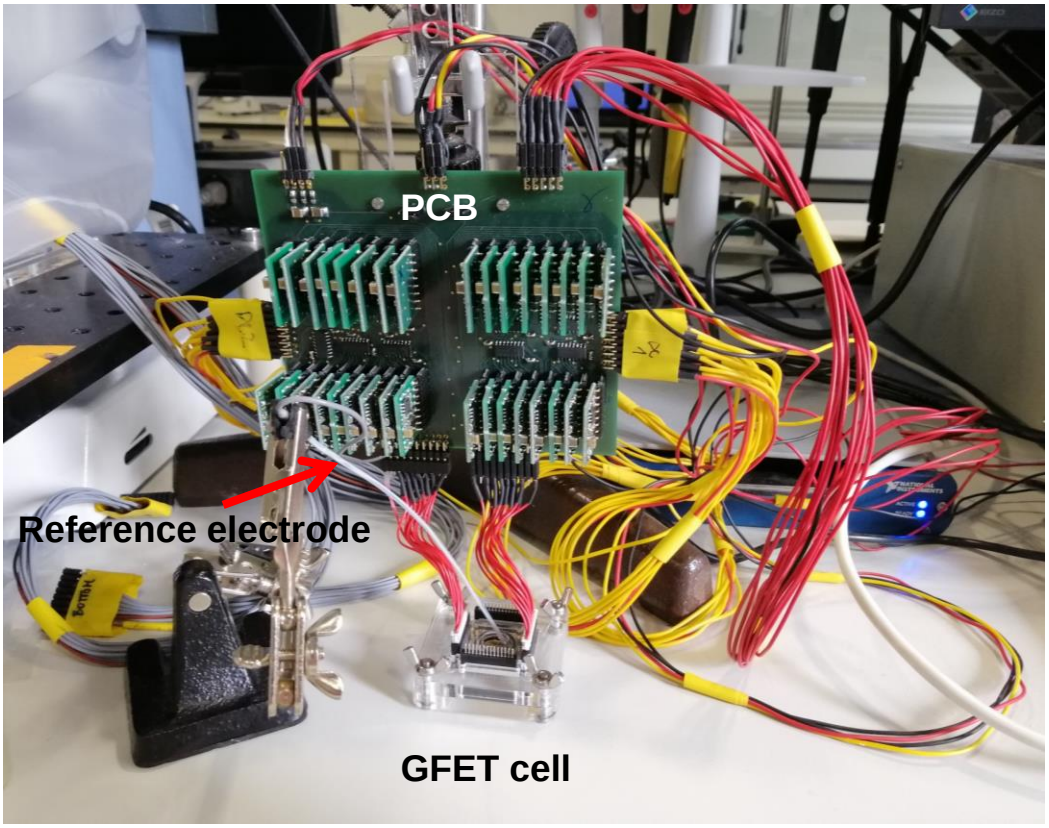

Figure 65. Image of the GFET cell connected to the PCB.

For these experiments, the electrical characterization of SiO_2/mGFET based on the evaluation of the superficial charges changes was acquired from a current-voltage curve (*I-V* curve). As its name suggests, *I-V* curve exhibits the relationship between the current flowing through the electronic device and the applied voltage across its electrodes. In particular, the *I-V* curve studied is defined by drain-source current (*Ids*) when different gate-source voltages (*Vgs*, (-0.2) - 0.5 V) are applied for a fixed drain-source voltage (*Vds*, 0.1 V). This curve can be used as a tool to determine the following parameters: (1) the charge neutrality point (CNP or V_{CNP}), which corresponds to the *Vgs* at the minimum *Ids* current, and (2) transconductance (g_m) that is defined as the facility to pass an electric current through a conductor.

For pure graphene, its valence and conduction bands meet in a single point called as Dirac Point (U_D); therefore, Fermi level lays at U_D.[61] The *Vgs* where Fermi Level reaches the U_D is the CNP, in which there are no carriers (holes or electrons) to contribute the electronic transport. But the Fermi level can be shifted from U_D applying a *Vgs* due to the increase of the carrier concentration that contributes to the charge transport. In a similar manner, external charges, such as impurities, derived groups from chemical functionalization or recognized analytes when the device is using as sensor, can also shift the Fermi level. Thus, CNP can be employed to evaluate graphene doping, graphene functionalization and as sensing mechanism.[200]

To know the sensitivity of transistor, g_m is calculated (*Equation 2*). Transconductance is ratio of output *Ids* with respect to the change in the input *Vgs*. Therefore, g_m will quantify how sensitive the device current is with respect to the device voltage.

$$g_m = \left.\frac{dI_{ds}}{dV_{gs}}\right|_{V_{ds}} \qquad \textit{Equation 2.}$$

In addition, in order to study the transistor noise, root-mean-square Voltage noise-dependence (*Vrms*) is also analyzed. *Vrms* correlates the intrinsic noise current Ids^{rms} (integrated current noise over the frequency bandwidth) with its g_m.[246] This parameter will be also related to the sensitivity of the device.

$$V_g^{rms} = \frac{I_{ds}^{rms}}{g_m} \qquad \textit{Equation 3.}$$

Accordingly, the effects of THF and EtOH in SiO_2/mGFET were evaluated in terms of *Vrms*, CNP and g_m. It is worth noting that the time duration of the treatment was not considered in the following study because no significant differences were found for the SiO_2/MGFET cleaning. The *I-V* and the *Vrms* were firstly studied in order to see the changes in the device performance. The average variation was acquired from the 48 graphene microtransistors of SiO_2/mGFET. The Figure 66 shows how *Vrms* decreases for the treatment with EtOH and increase with THF. In fact, we can observe how the standard deviation significantly decreased after the EtOH cleaning due to its efficient polymer removal, which led to a homogeneous performance of the microtransistors set (Figure 66a). The increment of the noise after the THF process might occur because of the low graphene damage that the AFM images previously showed in SiO_2/MGFET (Figure 66b).

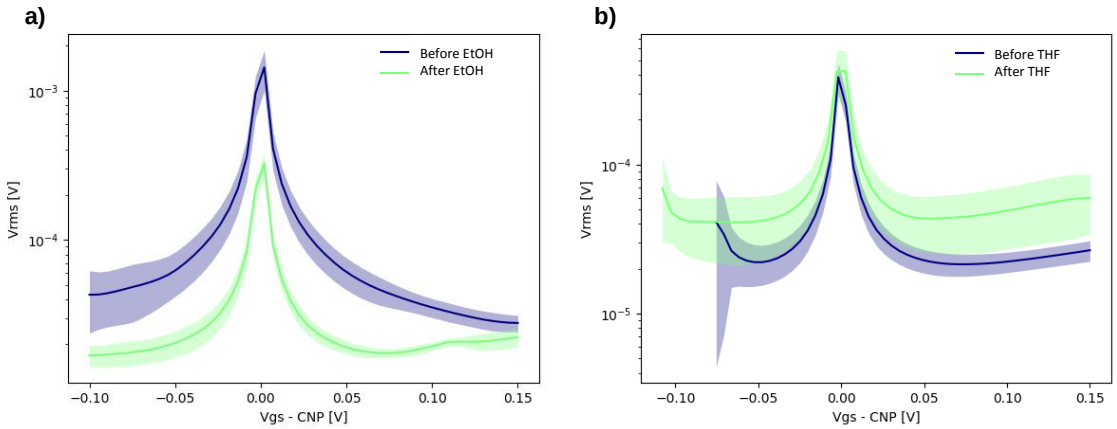

Figure 66. *Vrms* curves before(blue) and after (green) the cleaning process in a) SiO_2/mGFET-(EtOH) 1h and b) SiO_2/mGFET-(THF) 2h.

The *I-V* curves can give information related to the SiO_2/mGFET performance. Particularly, the shift in the CNP can be associated to the graphene doping.[179] For that reason, the amount of polymer residue removed could be detected as function of the shift in the current voltage minimum. For both solvents, a significant shift to in the CNP was observed (Figure 67 and Table 3) which implies the loose of n-type doping of graphene. Therefore, these results can be interpreted as removal of removing of negatively charged and/or polar polymer residues which allowed n-type conduction. For the samples where EtOH was used as cleaning agent, the CNP was shifted from 0.35 to 0.15 V (Figure 67a) while for the corresponding samples in which THF

was used the CNP was shifted from 0.20 to 0.10 V (Figure 67b). Nevertheless, a little decrease in the *Ids* was observed after treatment with THF, possibly, due to small graphene damages.

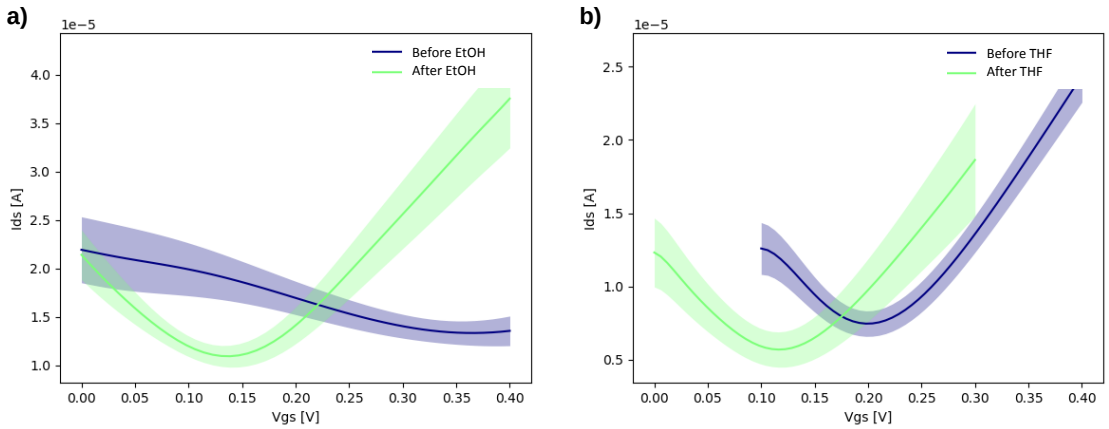

Figure 67. I-V curves before(blue) and after (green) the cleaning process for a) m-EtOH 1h and b) m-THF 2h.

Table 3. SiO_2/mGFET CNP before and after cleaning process with EtOH and THF.

Solvent	CNP (V)	
	Before	*After*
EtOH	0.35	0.15
THF	0.20	0.10

In summary, conventional solvents used in silicon microfabrication are generally inefficient in the case of graphene. Alternatively, THF and EtOH have been studied as candidate options. Despite its undeniable capability for polymer cleaning/solving, THF may compromise graphene integrity due to a possible fast polymer crazing. But EtOH has demonstrated to be highly effective for reducing the residues on the surface of graphene after microfabrication steps such as photolithography. EtOH efficiency is not dependent on the residues thickness/amount and as it is easy adaptable at wafer scale. Therefore, EtOH is a promising candidate to be included as a necessary material in the regular cleaning procedures for microfabrication of graphene electronic devices.

2.4. CVD graphene modification for biosensing implementation.

Chemical modification of graphene materials is a mandatory step in the production of biosensors for the attachment of the recognition elements when needed. In order to implement biosensing capacity to GFET as potential *in vivo* sensing implants, different chemical modifications of CVD graphene will be explored to introduce carboxylic groups (Figure 68). This chemical specie was selected because, on the one hand, when it is closely attached to graphene surface, it introduce pH sensing capability since produces charge density changes depending on the proton concentration in solution.[247] *In vivo* monitorization of pH variations in nerve tissue has a significant interest for diagnosis of neural diseases as epilepsy. This is due to the fact generalized epileptic seizure produces local hypoxia, which generates lactic acidosis

during the seizures.[248] These episodes may be result of excessive and abnormal activity in the brain cortex and the molecular mechanisms that terminate seizures remain unknown. On the other hand, carboxylic functional groups will work as "anchor point" for the development of a different sensing platform. Hence, the introduction in a second step of a NH_2-aptamer as receptor allows a selectively sensing of the corresponding biomolecule. However, diverse restrictions are present for SGFETs. The structural integrity of graphene should be maintained to preserve its remarkable electronic properties. In addition, due to the layer by layer composition of the final device with polymers (Figure 58), the proposed chemical modification strategy should be performed under mild reaction conditions, in terms of temperature and compatible solvents.

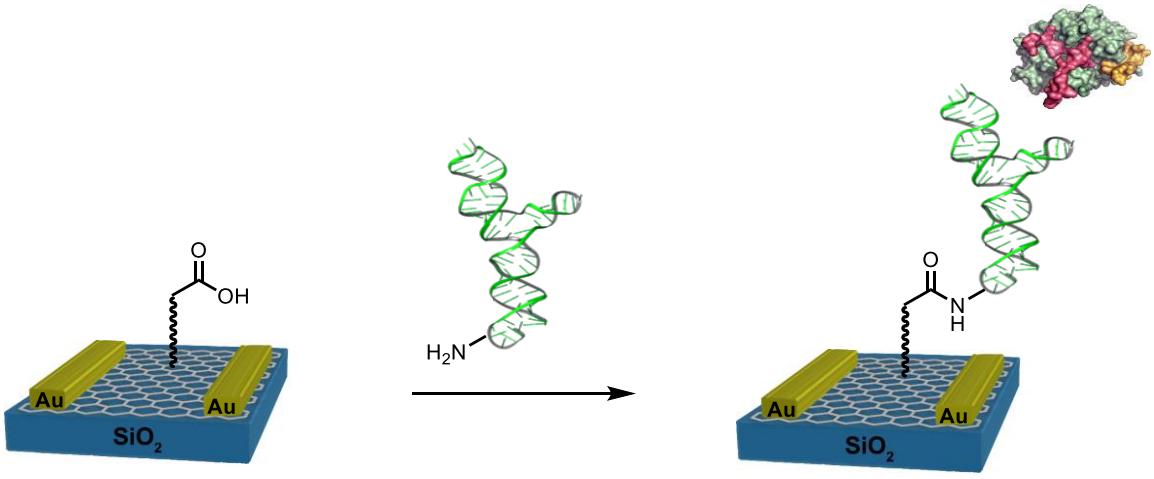

Figure 68. General scheme of the CVD graphene modification for GFET biosensing platform.

2.4.1. Chemical modification of CVD graphene with carboxylic groups for biosensing.

For the introduction of carboxylic groups, two different strategies were proposed. Both are based on the most studied covalent functionalization of CVD graphene, the radical reaction *via* diazonium salt decomposition. The first strategy is based on a one-step modification with the *p*-(carboxymethyl) phenyl radical **18** (Figure 69, blue, *strategy 1*). The advantage of this modification is the creation of stable and short linkers, which can anchor the receptor near the graphene surface, allowing a better sensitivity for the EDL. The second modification strategy consists in a two-steps approach: firstly, a covalent functionalization with 3,4-bis(octadecyloxy) radical **19** (Figure 69, red, *strategy 2*). Then the introduced aliphatic chains non-covalently interact with the lipidic bidentate molecule **20** carrying the carboxylic group. This methodology provides a potential recyclable interface for biomolecule sensing because of the weak interaction between alkyl chains as it could be overcome with the use of specific solvents. However, the long alkyl chains as linker of the recognized biomolecule could reduce the sensitivity of the transistor.

As mentioned above, different limitations must be considered to decide the optimal reaction conditions. Both functionalization strategies are based on covalent modifications, thus defects will be introduced in graphene to preserve its electronic properties. Therefore, the functionalization degree must be controlled. In addition, the passivation polymer SU-8 presented in the final device is not compatible with many common organic solvents, and the

layer by layer device does not allow the use of high temperatures because of possible detachments.

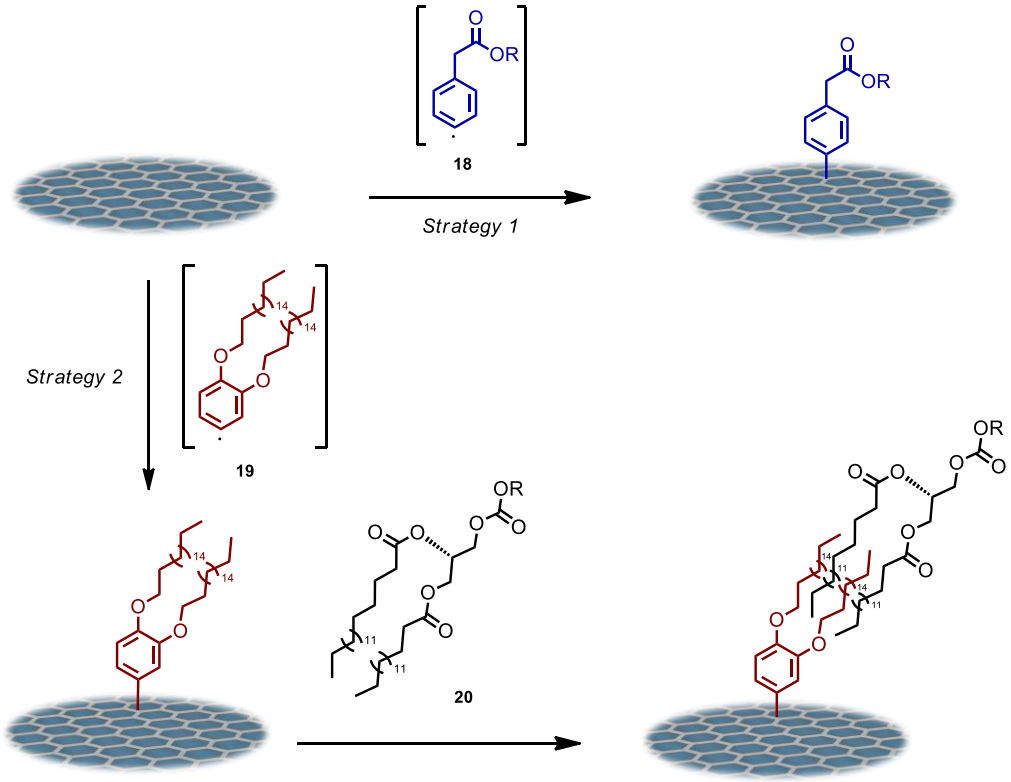

Figure 69. Scheme of the two different functionalization strategies to introduce the carboxylic "anchor point" groups.

The reactivity of diazonium salts with graphene has been widely studied. Due to the high reactivity of the generated radical species, olygomers are formed over the surface attached molecules for both approaches. In principle, this could be a disadvantage since the created oligomer layer on graphene could be longer than the Debye length; consequently, the carboxylic groups would be beyond the effective solution region. However, a moderate olygomerization would allow the introduction of several carboxylic groups per one sp^3 carbon atom generated (Figure 80). Thereby, the graphene structure would not highly modify with a large number of functional groups in the effective solution region.

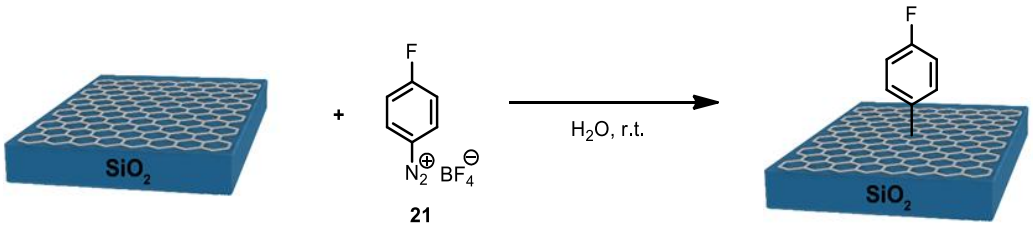

Figure 70. Scheme of the SiO_2/G-(*p*-(F) Ph) reaction.

As both modification strategies are based on diazonium salt reactions, the reactivity of SiO_2/G was firstly studied with **21**. In this manner, the use of **21** allows the detection of F atoms as diagnostic signal in the chemical composition of graphene. The modified sample SiO_2/G-(*p*-(F)Ph) was characterized by Raman spectroscopy (Figure 71a and b) and XPS analysis (Figure

71c and d). Raman spectra showed an increase in the number of defects ($\Delta(I_D/I_G)$ = 0.14). The average spectra were obtained from the representative region Raman mapping (30 x 20 μm² ≈ 1500 points spectra) before and after modification. Besides, the atomic composition of SiO_2/G-(*p*-(F)Ph) by XPS analysis showed fluorine atoms that were not present in the pristine material. These experimental evidences confirmed the successful functionalization of SiO_2/G.

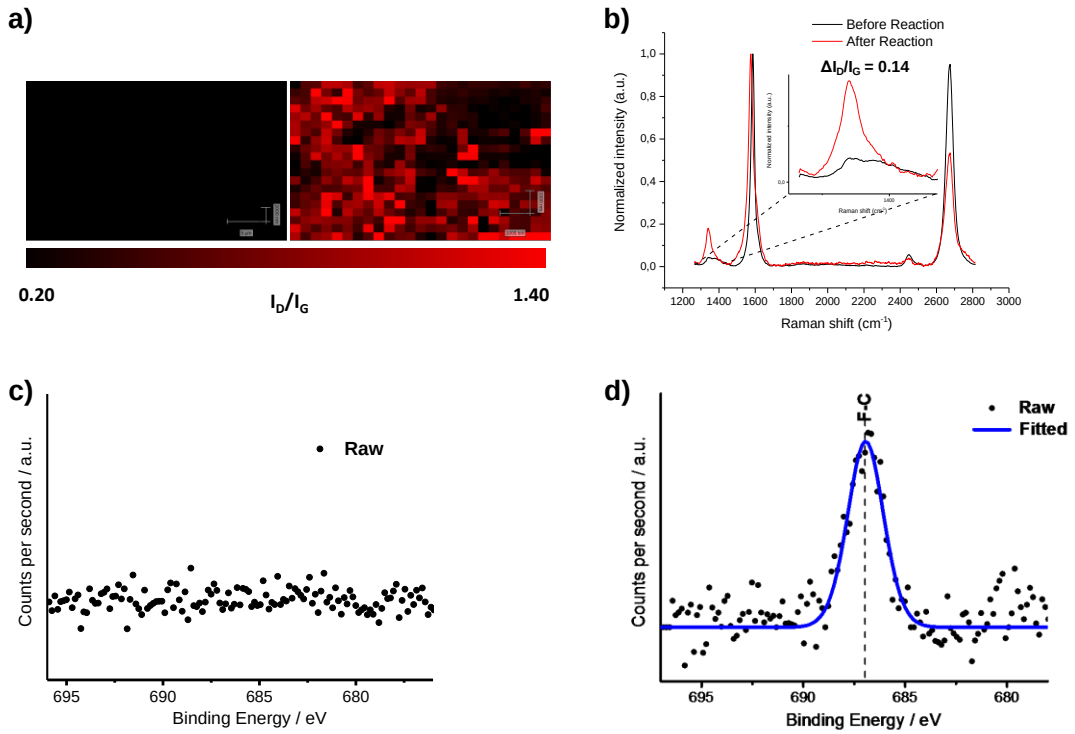

Figure 71. a) Raman mapping of the D band intensity in 30x20 μm² area and b) averaged Raman spectra (≈1500 single-point spectra, λ_{exc} = 532nm) before and after reaction. F1s core level in XPS analysis of the reaction regarding the presence of F c) before and d) after reaction.

After confirming the functionalization on a basic substrate, we applied the reaction conditions for our strategies. Thus, SiO_2/MGFET was chemically modified (Figure 56). This device was useful to fully characterized the chemical modification due to the large dimensions of the graphene surface, which is mandatory for the key characterization technique XPS. On the other hand, SiO_2/MGFET can be connected to the set-up to perform a preliminary evaluation of the electronic properties of graphene. As mentioned before, the modification was performed through the decomposition of the corresponding diazonium salts **24** and **23** (*strategies 1* and *2*, respectively). The high solubility of 2-(4-aminophenyl)acetic acid in aqueous solution allowed the synthesis of the stabilized aryldiazonium ion[249] for the *ex-situ* generation of the radical in aqueous conditions. However, due to the low solubility in organic common solvents and water of the aniline **22**, the synthesis of the corresponding stabilized aryldiazonium salt was challenging. Thus, the generation of the radical was performed *in-situ* from the aniline.

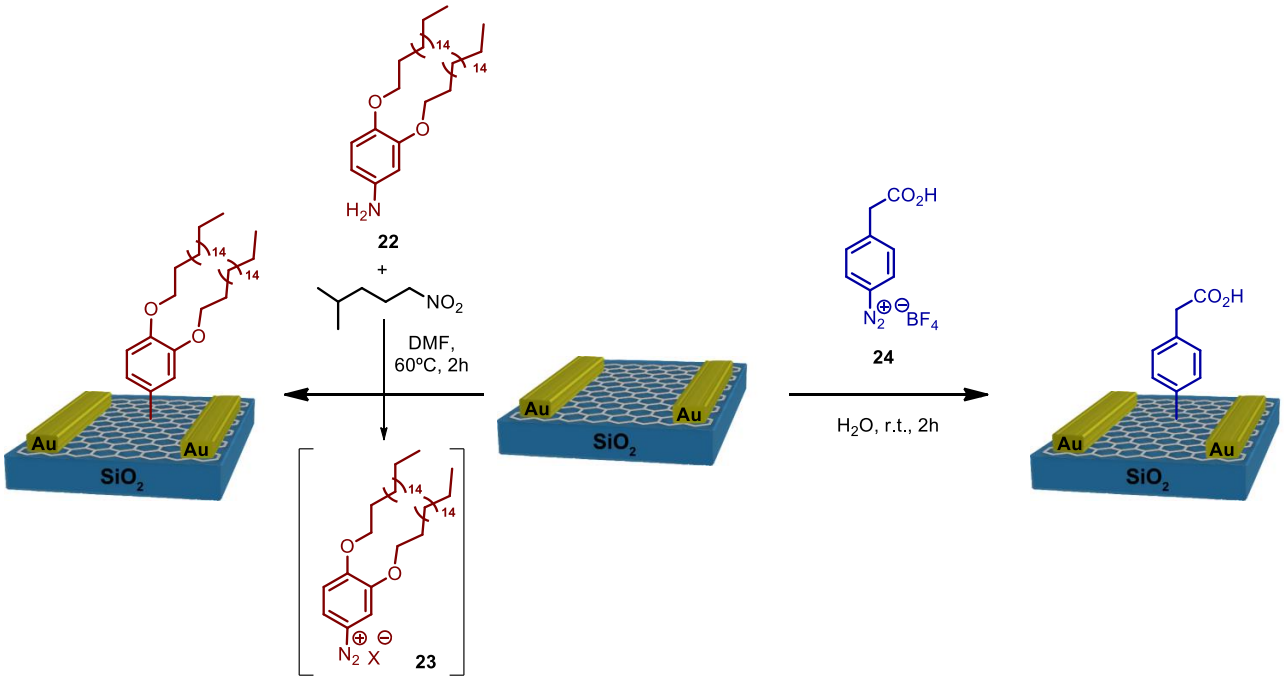

Figure 72. General scheme for the *p*-(CH_2CO_2H)Ph (blue) and 3,4-($C_{18}H_{37}O$)$_2$Ph (red) covalent modification.

The synthesis of **22** was performed through the following synthetic steps. In general, the *in situ* formation of aryldiazonium species from the corresponding anilines and its subsequent thermal decomposition initiated by isoamyl nitrite has been proved as useful tool to functionalize carbon-based nanomaterials.[250] Thus, the aniline **22** was synthetized by the di-alkylation of nitrocathecol (**25**) to obtain the bis(octadecyloxy) compound **27**, followed by the reduction of the nitro group to obtain 3,4-bis(octadecyloxy)aniline (**22**).

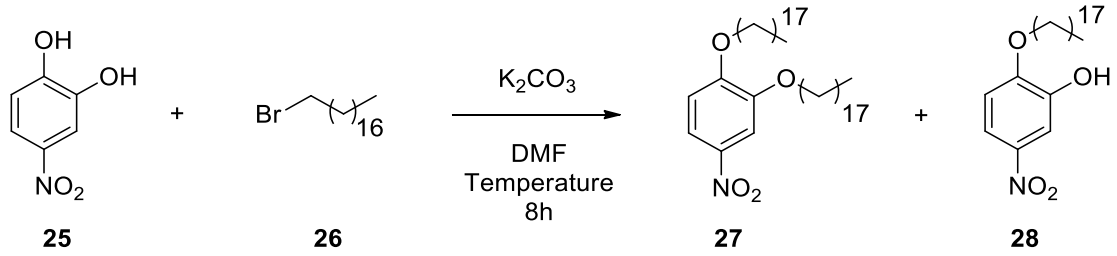

Figure 73. General scheme for the reaction between 25 and 26 for different conditions.

For the dialkylation of **27** different reaction conditions were performed. Firstly, the alkylation of **25** was performed at low concentration in DMF. The employment of solution 0.13 M using an excess of 1-bromooctadecane (**26**) and K_2CO_3 to increase the oxygen nucleophilic character. However, after purification by flash chromatography, the isolated compound results in the monosubstituted alkoxy adduct **28**. For that reason, it was necessary to increase the concentration and temperature to 0.25 M and 150 ºC, respectively.[251] By using these new conditions, **27** was obtained in 87% yield.

Table 4. Condition for the synthesis optimization of X.

Entry	25 Concentration (M)	Temperature (°C)	Obtained product	Yield (%)
1	0.13	90	**28**	79
2	0.25	150	**27, 28**	87

Then **27** was reduced under H_2 atmosphere using Pd/C as catalyst.[252] The synthesis of **22** is fully described in the section dedicated to experimental details as well as the Nuclear Magnetic Resonant (NMR) spectra and High-Resolution Mass Spectroscopy (HR-MS) of the synthetized molecules.

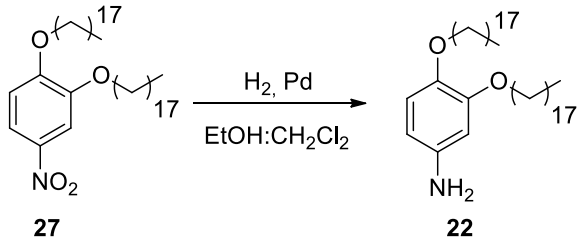

Figure 74. Synthesis of the 3,4-bis(octadecyloxy)aniline (22).

With the aniline **22** and the diazonium salt **24** in hands, the two modification strategies were performed to the SiO_2/MGFET devices. To monitor the chemical modification of graphene, Raman spectroscopy and AFM were employed. The covalent functionalization using **24** was performed in water at room temperature for *strategy 1*. However, when water was use in the *strategy 2*, the functionalization did not proceed because of solubility problems. In order to improve the solubility of this compound, different solvents were used for the functionalization of CVD graphene with **22** being dimethylformamide (DMF) the best option. In addition, the increment of temperature to 60 °C was needed. Raman spectroscopic measurements (Figure 75) showed for both strategies, an increase of the D band intensity respect to the G band ($\Delta(I_D/I_G)$) of 0.12 and 0.31 for the modified SiO_2/MGFET-(*p*-(CH_2CO_2H)Ph) and SiO_2/MGFET-(3,4-($C_{18}H_{37}O$)$_2$Ph) samples, respectively. The increment of the D band is associated to sp^3 hybridization of carbon after the covalent modification of the sp^2 carbon atoms of graphene.

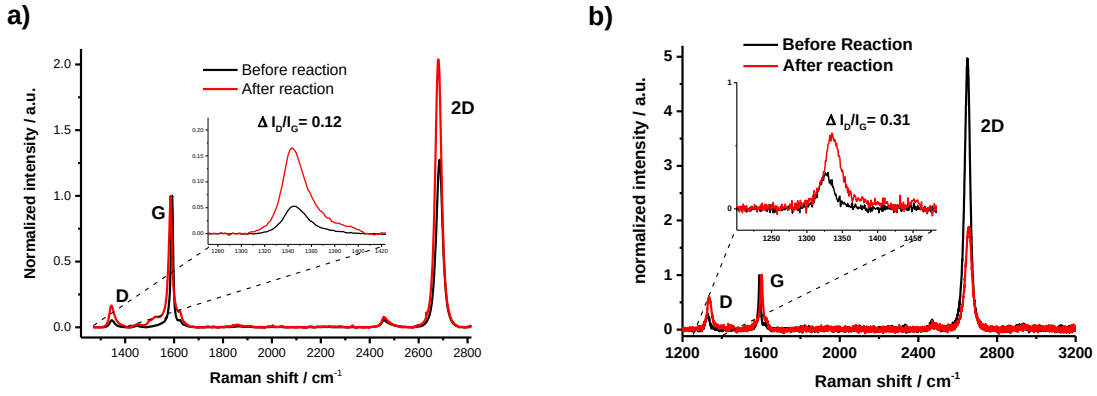

Figure 75. Average Raman spectra before (black) and after (red) covalent functionalization for a) SiO_2/MGFET-(*p*-(CH_2CO_2H)Ph) and b) SiO_2/MGFET-(3,4-($C_{18}H_{37}O$)$_2$Ph).

Results and discussion

To evaluate the impact of the functionalization and particularly the presence of possible olygomers in graphene, the surface topographies were inspected by AFM. Figure 77 shows the AFM images of SiO_2/MGFET before and after the covalent modification approaches. Figure 77a and e exhibited the characteristic graphene wrinkles derived from different factors during the transfer procedure such as solvent trapping, edge instabilities, interatomic interactions, etc.[253] After functionalization by *strategies 1* and *2* (Figure 77g and c, respectively), they showed topographic changes. The AFM height profiles showed a variation from 1.0 to 3.0 nm and from 1.5 to 8.0 nm for SiO_2/MGFET-(3,4-($C_{18}H_{37}O)_2$Ph) and for SiO_2/MGFET-(*p*-(CH_2CO_2H)Ph), respectively.

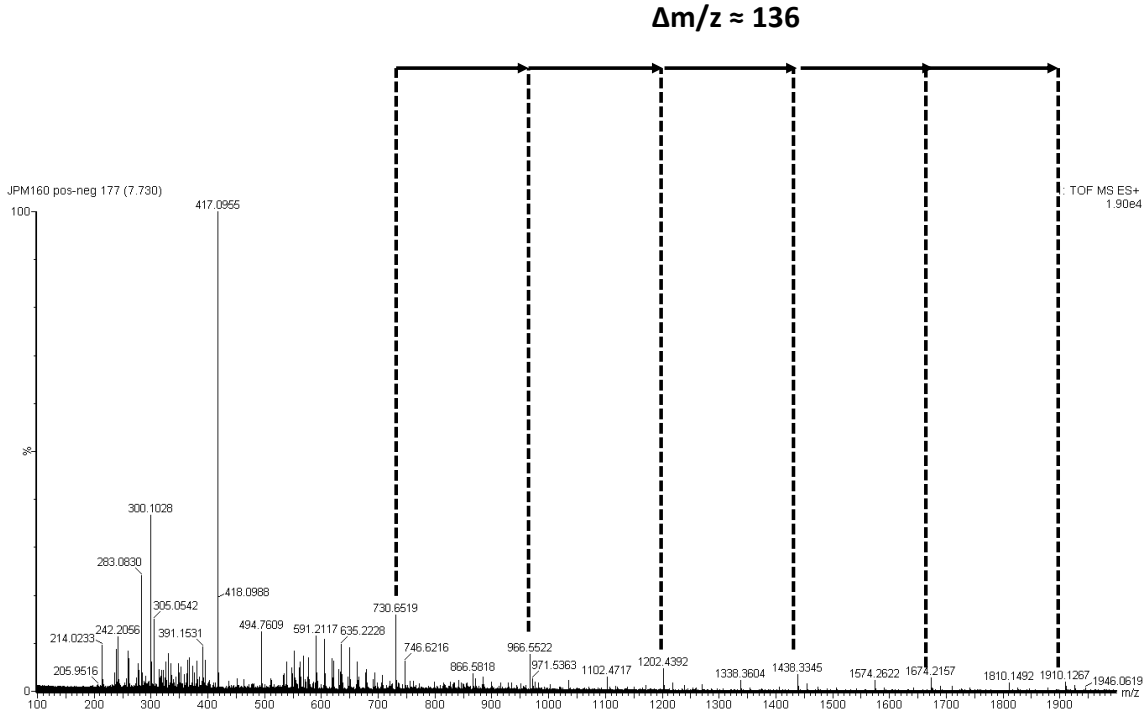

Figure 76. Mass spectroscopy (ES+) mode (m/z 100-2000) Background of the obtained residue.

Presumably, the reaction with **24** allowed a higher polymerization due to a lower steric hindrance and the easier accessibility of the corresponding radical to the *meta* position and to the α-CH_2 of the carboxyl group. Despite the structure of the generated oligomers on the graphene surface was not obtained (different attempts of characterization of SiO_2/MGFET, SiO_2/G and Cu/G by MALDI failed), the positive electrospray ionization mass spectroscopy (ES+) of the obtained residue in the reaction mixture showed a repetitive difference pattern of 136 m/z from 100 to 2000 m/z, which could correspond to 2-phenylacetic acid (Figure 76). This experimental evidence suggested the formation of olygomers during the modification process (Figure 80b).

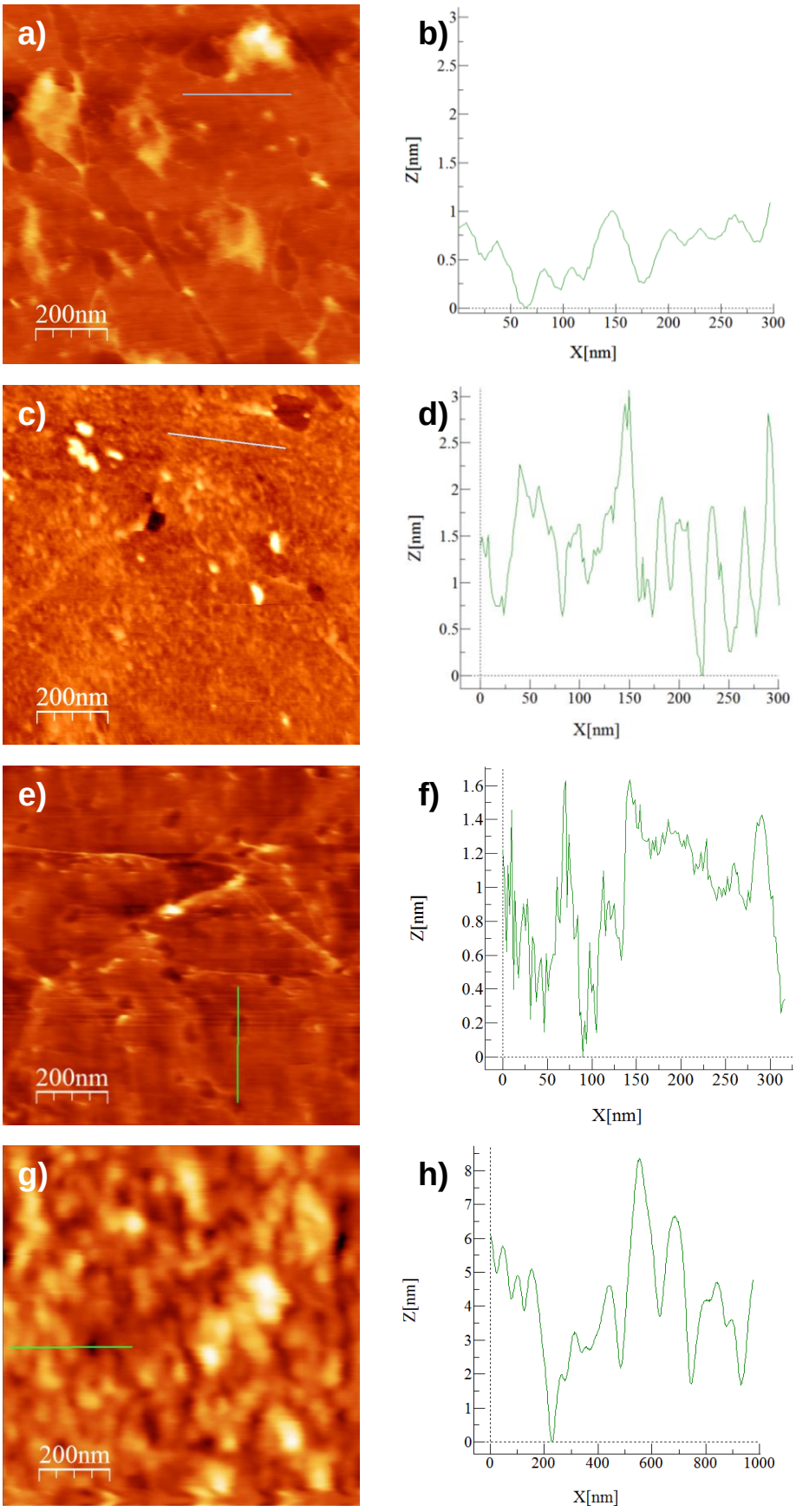

Figure 77. AFM images for SiO_2/MGFET-(3,4-($C_{18}H_{37}O$)$_2$Ph) a) before and c) after reaction and for SiO_2/MGFET-(*p*-(CH_2CO_2H)Ph) e) before and g) after reaction. AFM height profiles (blue and green lines in a, c and e, g respectively) for SiO_2/MGFET-(3,4-($C_{18}H_{37}O$)$_2$Ph) b) before and d) after reaction and for SiO_2/MGFET-(*p*-(CH_2CO_2H)Ph) f) before and h) after reaction.

Results and discussion

Covalent functionalization alters the electronic properties of graphene because of the introduction of defects associated with sp^3 hybridization that disrupts its aromatic structure. Thus, before proceeding with the sensing performance, the evaluation of the electronic properties of graphene after modification was studied. For that reason, the parameters CNP and g_m were evaluated from the *I-V* curve (Figure 78). As mentioned above, *Ids* is obtained as function of the applied *Vgs* for a fixed *Vds*. As shown Figure 78a, the *I-V* curve of SiO_2/MGFET-(*p*-(CH_2CO_2H)Ph) presented a low decrease in the *Ids* after the modification, *i.e.* less intensity between source and drain. However, no change in CNP value was detected, so the Fermi level was not altered. As defined in *Equation 2*, g_m can be obtained by deriving *Ids* with respect to *Vgs* in the linear ranges. For *strategy 1*, the slopes were similar before and after modification so, the g_m was not significantly affected. For SiO_2/MGFET-(3,4-($C_{18}H_{37}O$)$_2$Ph), although there was not a significant change in the *Ids*, the CNP showed a higher shift from 0.5 to 0.2 after covalent modification (Figure 78b); in addition, the g_m significantly decreased since differences in the slopes are observed. However, the evaluation of CNP and *gm* after *strategy 2* modification concludes that the devices was further affected compared to the *strategy 1*., the two chemical approaches were suitable to be implemented in the next architecture of the biosensing devices with acceptable graphene properties, being more affected the device obtained by *strategy 2*.

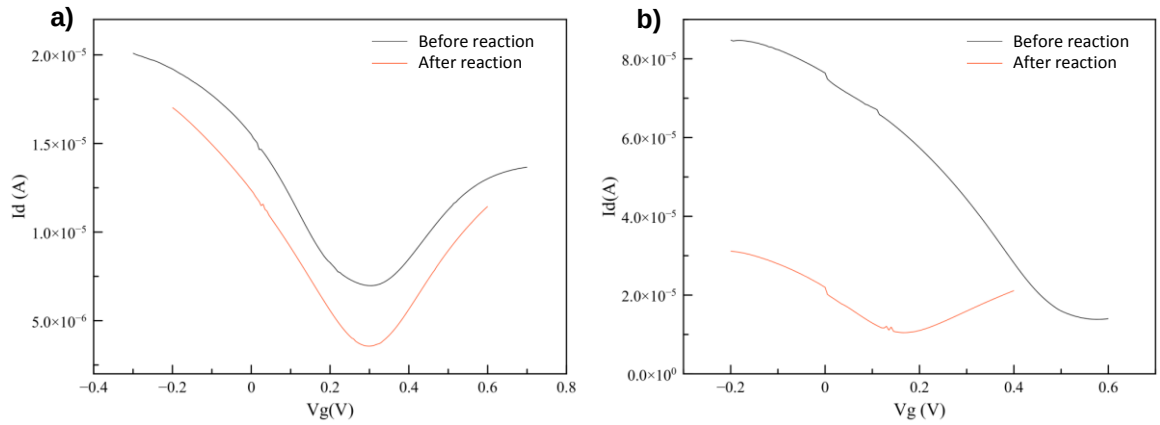

Figure 78. I-V curves for a) SiO_2/MGFET-(*p*-(CH_2CO_2H)Ph) and b) SiO_2/MGFET-(3,4-($C_{18}H_{37}O$)$_2$Ph) before (red) and after reaction (blue).

The covalent modification approaches were subsequently performed in the microtransistors arrays. The optimal reaction conditions developed for SiO_2/MGFET were applied for the modification of graphene in SiO_2/mGFET. To monitor the modification of the graphene devices, Raman spectroscopy and AFM were employed. It is noteworthy that the graphene surface of SiO_2/mGFET was not able to be analyzed by XPS because of the low dimension of the graphene component (Figure 57). As shown in Figure 79, the modified SiO_2/mGFETs though *strategies 1* and *2* exhibited a slight increment of the I_D/I_G ratio ($\Delta(I_D/I_G)$ = 0.07 for both reactions, this spectroscopic data was obtained from ~1000 single-point spectra).

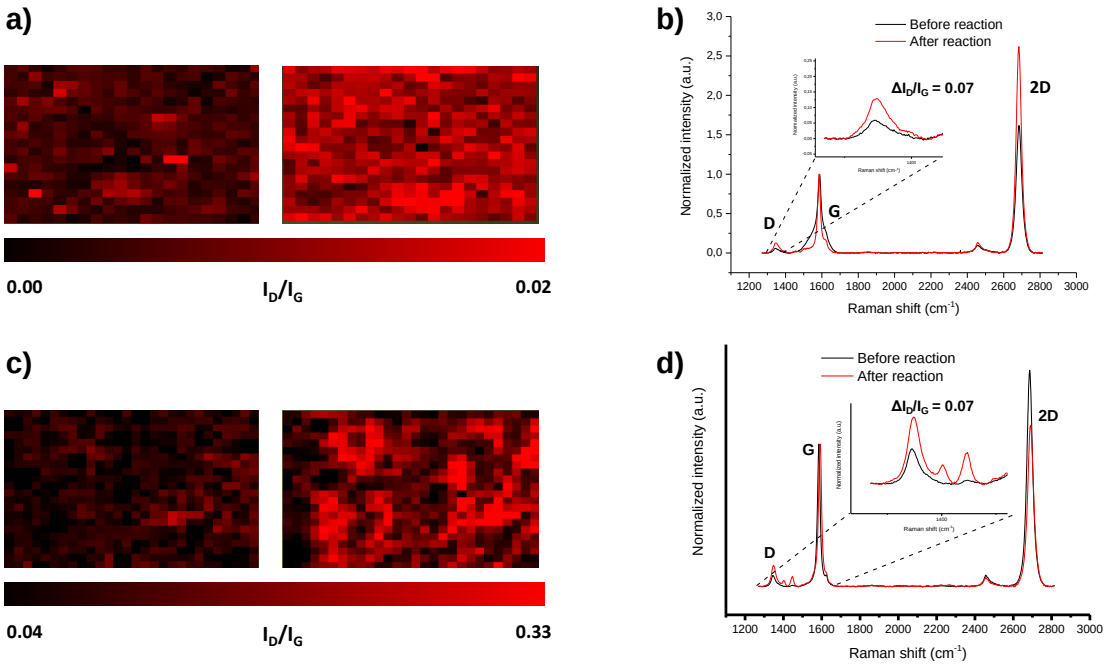

Figure 79.) Raman mapping of the D band intensity in 30x20 μm² area for a) SiO_2/mGFET-(3,4-($C_{18}H_{37}O)_2$Ph) and c) SiO_2/mGFET-(*p*-(CH_2CO_2H)Ph) before and after reaction. Averaged Raman spectra (≈1000 single-point spectra, λ_{exc} = 532nm) for a) SiO_2/mGFET-(3,4-($C_{18}H_{37}O)_2$Ph) and c) SiO_2/mGFET-(*p*-(CH_2CO_2H)Ph) before and after covalent modification.

Unexpectedly, the Raman spectra of graphene for SiO_2/mGFET-(*p*-(CH_2CO_2H)Ph) exhibited additional bands at 1402 and 1446 cm^{-1} (Figure 80a). These bands can be assigned to the vibration modes of the oligomers which remain (covalently or non-covalently) attached to the graphene surface (Figure 80b).[97] Particularly, the most probable assignment of ~1400 cm^{-1} bands is related to the scissor-vibration (bending mode) of the CH_2 group in phenylacetic derivatives.[254] These species were a double-edged sword: on the one hand, several carboxylic groups are introduced for each hybridized sp^3 carbon atom of graphene; therefore, the electronic behavior of the device will be mildly affected for an acceptable number of introduced anchor points. However, the dimension of formed oligomers would compromise the sensing performance exceeding the Debye length when the receptor is anchored (*i.e.* the dispersion of the ions are far from the influencer region, so the recognized analyte will not have influence in the measures).

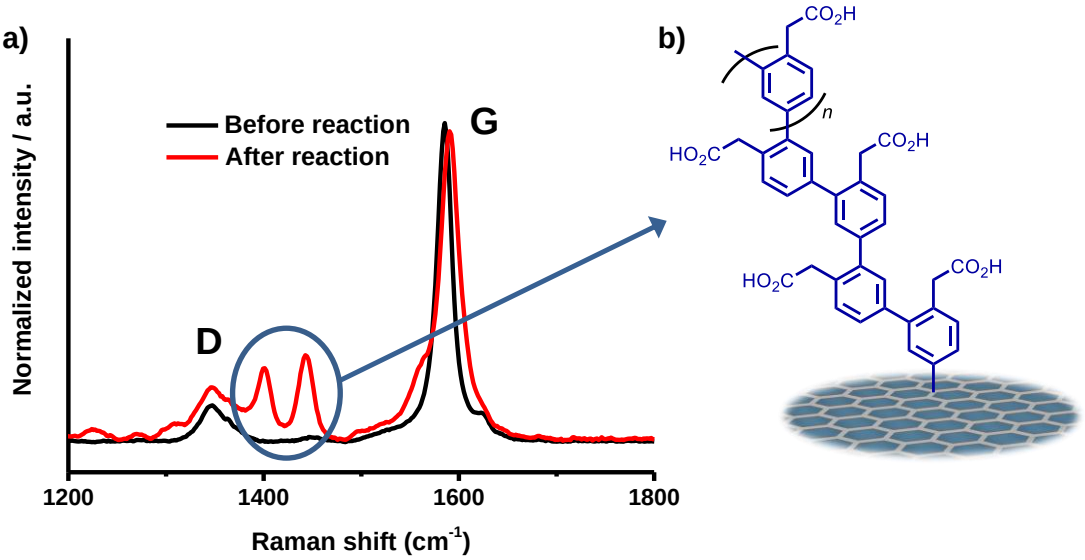

Figure 80. a) Average Raman spectra before (black) and after (red) for SiO_2/mGFET-(*p*-(CH_2CO_2H)Ph) c with extra bands and b) proposed structure of the oligomer formed

The impacts of the functionalization in SiO_2/mGFET-(*p*-(CH_2CO_2H)Ph) and the presence of possible olygomers on the graphene surface was also studied by AFM. Figure 81 shows the AFM images of SiO_2/mGFET before and after the covalent modification by *strategy 1*. After functionalization (Figure 81 d-e), the graphene surface showed topographic changes that can be interpreted as the appearance of small granules. The AFM height profiles showed a variation from 3.0 to 10 nm approximately. As mentioned, the reaction with **24** allowed high polymerization due to a lower steric hindrance and the easier accessibility of the corresponding radical to the *meta* position and to the α-CH_2 of the carboxyl group.

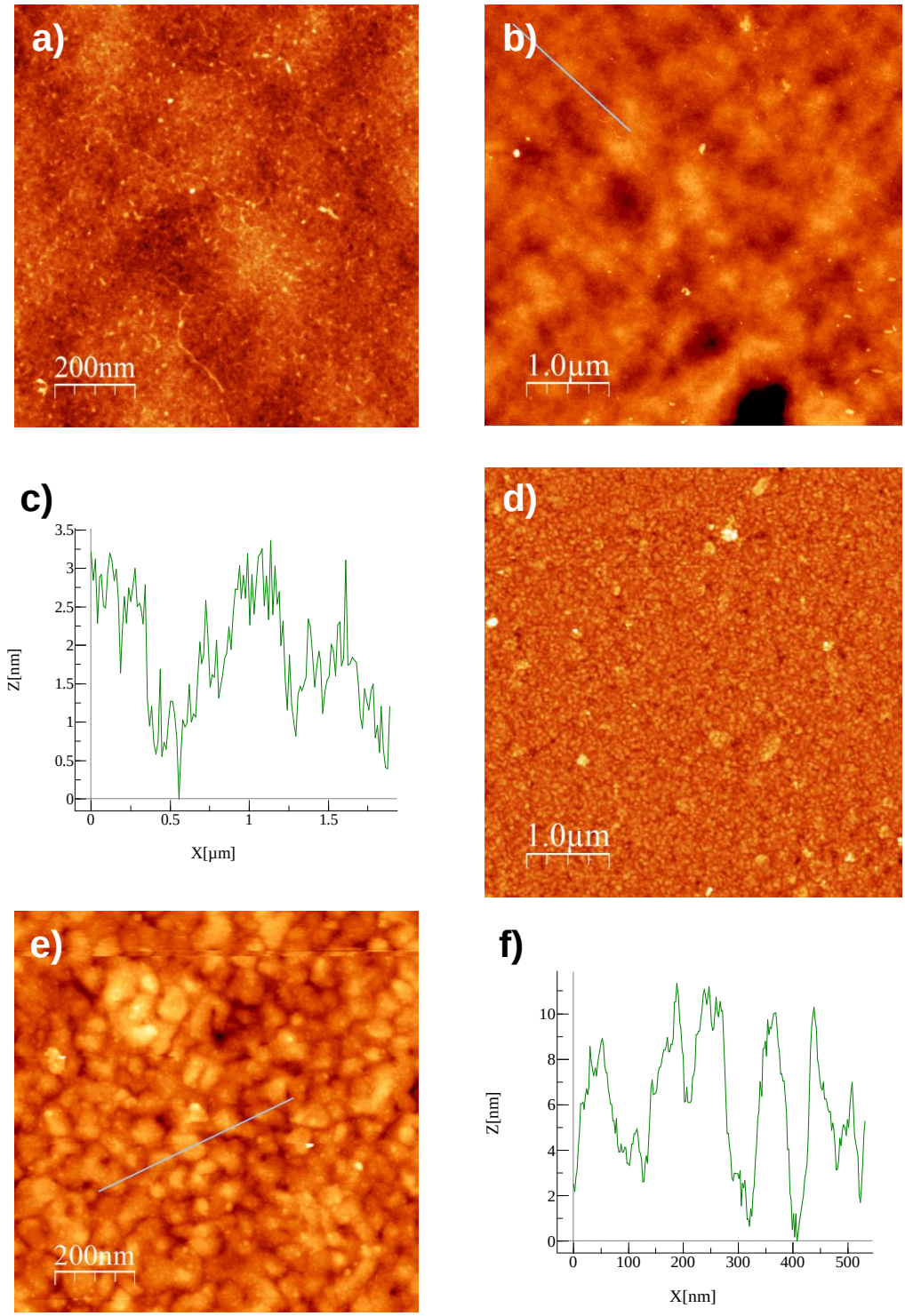

Figure 81. AFM images for SiO_2/mGFET-(*p*-(CH_2CO_2H)Ph) a, b) before and d, e) after chemical functionalization at different magnifications. AFM height profiles c) before and f) after chemical modification (blue lines in b and e images respectively).

Presumably, the detection of the high concentration of oligomers is related to the variations in the graphene reactivity. Particularly, the reactivity of CVD graphene on surfaces is influenced by mechanical strain and the charge doping, thus it strongly depends on the support substrates and possible absorbates in the interlayer.[100] In this context, the employment of a SiO_2 with different nature in SiO_2/mGFET respect to SiO_2/MGFET, which was necessary for an optimal device performance, could alter the CVD graphene reactivity. Thereby, the new SiO_2 substrate

could introduce changes in the graphene structure (such as different adsorbates) decreasing the graphene reactivity. Consequently, it would make more affordable the formation of oligomers on graphene, instead of the reaction between radical and graphene. But further research is essential to understand the effect of contaminants in the CVD graphene functionalization. In order to avoid the highly generated oligomers, reaction parameters such as temperature, concentration and addition rate of radical precursor, were modified. After the graphene characterization by Raman spectroscopy, the slow addition of **24** was the key factor that resulted in a non-detection of oligomers. As expected, the controlled addition of **24** avoids a high concentration of the generated radical, hindering the reaction with itself and other species present in solution. This experimental evidence suggested a similar functionalization to the previously obtained with SiO_2/mGFET.

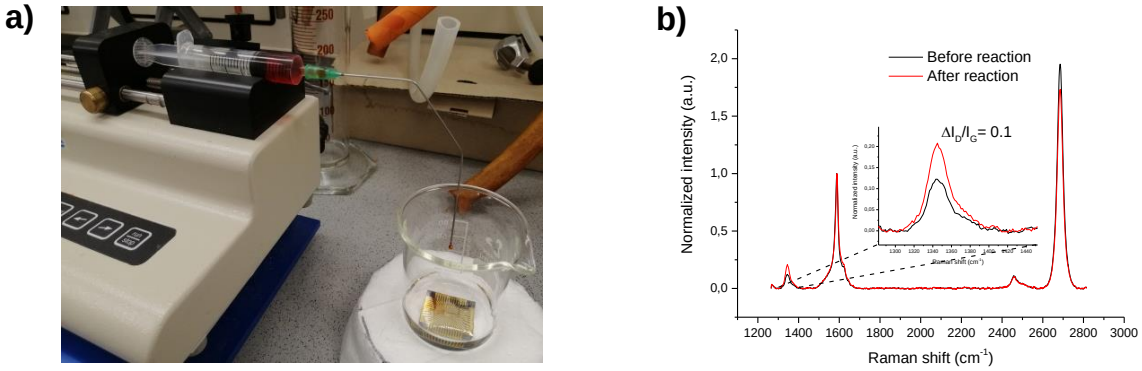

Figure 82. a) Image of the slow addition set-up b) Average Raman spectra for SiO_2/mGFET-(*p*-(CH_2CO_2H)Ph) before (black) and after (red) covalent functionalization using the slow addition instrument.

Once *strategy 1* was optimized, the electronic behavior of modified SiO_2/mGFETs by the two proposed modification approaches was evaluated. Particularly, *I-V* curves and *Vrms* characterization were performed for SiO_2/mGFET-(*p*-(CH_2CO_2H)Ph) and SiO_2/mGFET-(3,4-($C_{18}H_{37}O$)$_2$Ph) (Figure 83). It is worth noting that the average data was acquired from the individual 48 graphene microtransistors for each device.

As with the electronic characterization of SiO_2/MGFET-(*p*-(CH_2CO_2H)Ph) (Figure 78), the impact of the functionalization for SiO_2/mGFET-(*p*-(CH_2CO_2H)Ph) was not significant (Figure 83a), because a low decrease in the *Ids* and a low shift of 0.05 V for the CNP after modification were detected. Besides, there was an increase of g_m, which suggested a possible residues removal during the functionalization process by solvent effects. In addition, *Vrms* has no value changes. Nevertheless, this functionalization is suitable for the electronical device performance for biosensing.

Concerning SiO_2/mGFET-(3,4-($C_{18}H_{37}O$)$_2$Ph), *strategy 2* disrupted the electronical properties of graphene (Figure 83b). The *I-V* curve was flattened after functionalization, CNP shifted notably (≈ 0.2 V, out of the range) and the *Ids* showed a significant decrease. In addition, *Vrms* was remarkably increased. Presumably, these deep changes occurred because of the mandatory use of DMF to partially solubilize **22**. DMF was not compatible with the passivation layer of cured SU-8 polymer, even in short periods of reaction time (5 minutes), although macroscopic damage

of the device has never been observed. This approach has proven to be invalid for the manufacture of the envisioned biosensing platform device.

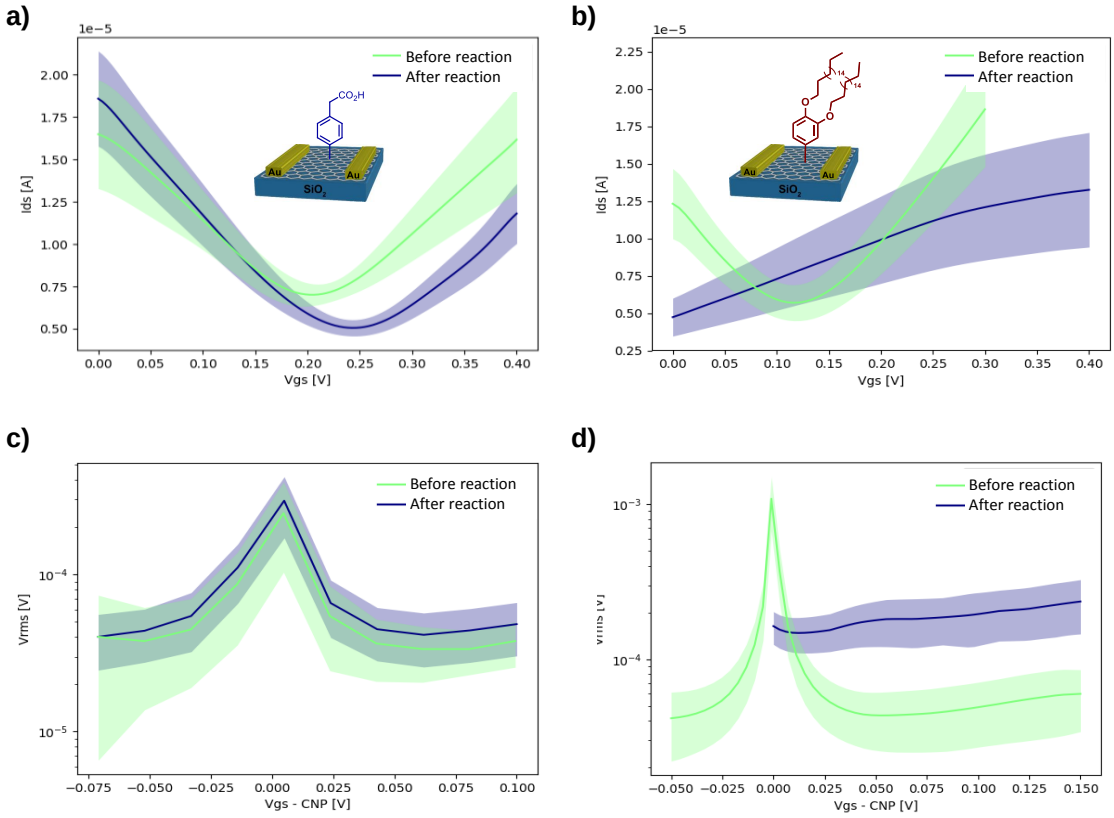

Figure 83. I-V curves for a) SiO_2/mGFET-(*p*-(CH_2CO_2H)Ph) and b) SiO_2/mGFET-(3,4-($C_{18}H_{37}O$)$_2$Ph) and *Vrms* curves for a) SiO_2/mGFET-(*p*-(CH_2CO_2H)Ph) and b) SiO_2/mGFET-(3,4-($C_{18}H_{37}O$)$_2$Ph) before (green) and after functionalization (Blue).

2.4.2. Modified CVD graphene in FET aptasensors for thrombin detection.

Generally, pH response of the graphene is attributed to residual surface functionalities.[255] Defect-free graphene might be no sensitive to pH changes, since the graphene pH sensitivity is given by the terminal polar or charged groups on the graphene surface. These groups increase the surface charge of graphene making it responsive towards pH variations. Thus, the pH sensing capability in a solution-gated transistor will be reflected in the CNP changes.

In order to evaluate the pH sensitivity of our samples, two SiO_2/mGFETs were electrically characterized before and after the chemical modification (SiO_2/mGFET-(*p*-(CH_2CO_2H)Ph)). For this purpose, the corresponding transistors were incubated in a set of PBS solutions with decreasing pH values from ≈ 9.5 to 2.5. As a result, all the samples showed pH response reflected in the CNP changes (Figure 84a).

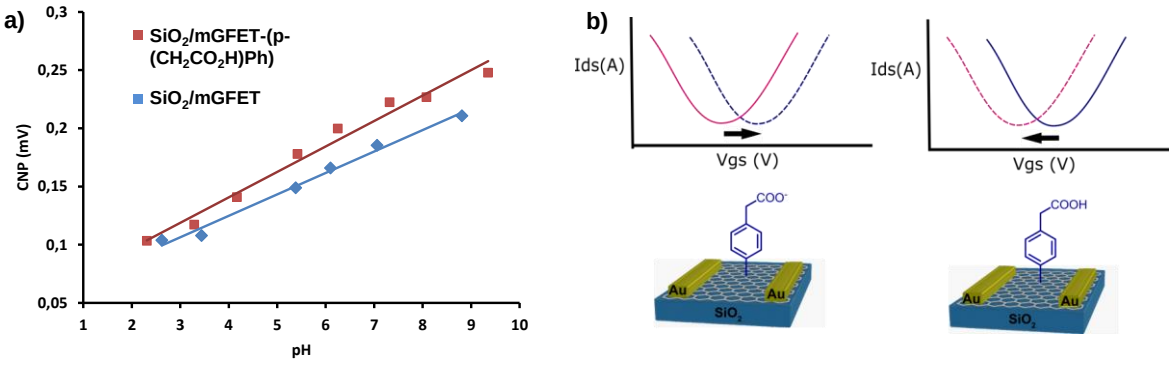

Figure 84. a) SiO_2/mGFET-(*p*-(CH_2CO_2H)Ph) CNP variation in function of pH before and after functionalization b) Influence of the pH in the CNP.

Particularly, the sensitivity differences of different SiO_2/mGFET-(*p*-(CH_2CO_2H)Ph) samples directly depended on the number of introduced defects (Table 5). The pH sensing capability of the non-modified samples (before functionalization, Entry 1 and 3) is attributed to the defects created during the synthesis and/or the residues derived from the transfer process. And the improved sensitivity of the modified transistors (Entry 2 and 4) is assigned to the introduced phenylacetic moieties. Indeed, the pH sensitivity linearly depended on the number of defects in terms of the spectroscopic parameter $\Delta(I_D/I_G)$. Thus, for Entry 2 and 4 m-*p*-(CH_2CO_2H)Ph samples, the increment of defects (10 and 29 % of I_D/I_G increased, respectively) resulted in a similar increment of sensitivity (9 and 22 % of slope increase, respectively). Besides, regardless of the chemical modification, the higher was the number of defects, the higher is the sensitivity. Therefore, the functionalization of graphene with phenylacetic moieties can be considered as an effective and controllable chemical procedure to improve the pH sensing capacity to SiO_2/mGFET devices.

Table 5. Effect of the functionalization degree in the pH sensitivity.

Graphene-SGFET	Entry	**Sensitivity mV/[pH]**	**Slope Increase (%)**	**I_D/I_G**	**I_D/I_G increase (%)**
SiO_2/mGFET	1	0,0140	**9,1**	0,18	**10**
SiO_2/mGFET-(*p*-(CH_2CO_2H)Ph)	2	0,0154		0,20	
SiO_2/mGFET	3	0,0165	**22,5**	0,12	**29,4**
SiO_2/mGFET-(*p*-(CH_2CO_2H)Ph)	4	0,0213		0,17	

After testing our functionalized sensing platform as pH sensor, SiO_2/mGFET-(*p*-(CH_2CO_2H)Ph) was used as sensing platform through the binding of specific bioreceptors on the carboxylic "anchor points". As a probe of concept, our functionalized graphene surfaces were linked with a selective aptamer for thrombin (TBA), which is a proteolytic protein that participates in the

blood coagulation process and it is associated with numerous diseases such as atherosclerosis and stroke. This aptamer was prepared by Dr Ana Aviñó in the Department of Chemical and Biomolecular Nanotechnology (IQAC-CSIC) in Barcelona (Spain).

The preparation of this aptasensor platform involved different manufacturing steps. The covalent attachment of the NH_2-Aptamer was performed through the activation of the SiO_2/mGFET-(*p*-(CH_2CO_2H)Ph) carboxylic group with N-hydroxysuccinimide (NHS) and 1-Ethyl-3-(3-dmethylaminopropyl)-carbodiimide (EDC), followed by the incubation with the selective thrombin aptamer for 12 hours. Afterwards, the free carboxylic binding sites of the graphene were blocked with an ethanolamine solution. After each incubation step, the SiO_2/mGFET-(*p*-(CH_2CO_2H)Ph), located in the chamber (Figure 64), was thoroughly washed to remove the excess of the respective compounds. *i)* It is worth mentioning that there are two main reasons to choose of aptamer instead of antibody. One of them is related with the above-mentioned Debye length. The object attached to the surface must be no longer than the Debye length, because the recognition event must be in the influencer region. The antibody size is generally around 15 nm while the aptamer one is around 3 nm. For an optimal interactions and measurements, PBS solution (1 mM) was used as media for our system. For this PBS concentration the Debye length is 7 nm. So, we can conclude that the use of the thrombin aptamer was suitable for our approach. *ii)* The second reason is related to the regeneration of the aptamer after analysis. This approach will be explained in detail below. The higher structural complexity of the antibody makes harder its recovering by unfolding-folding mechanism.

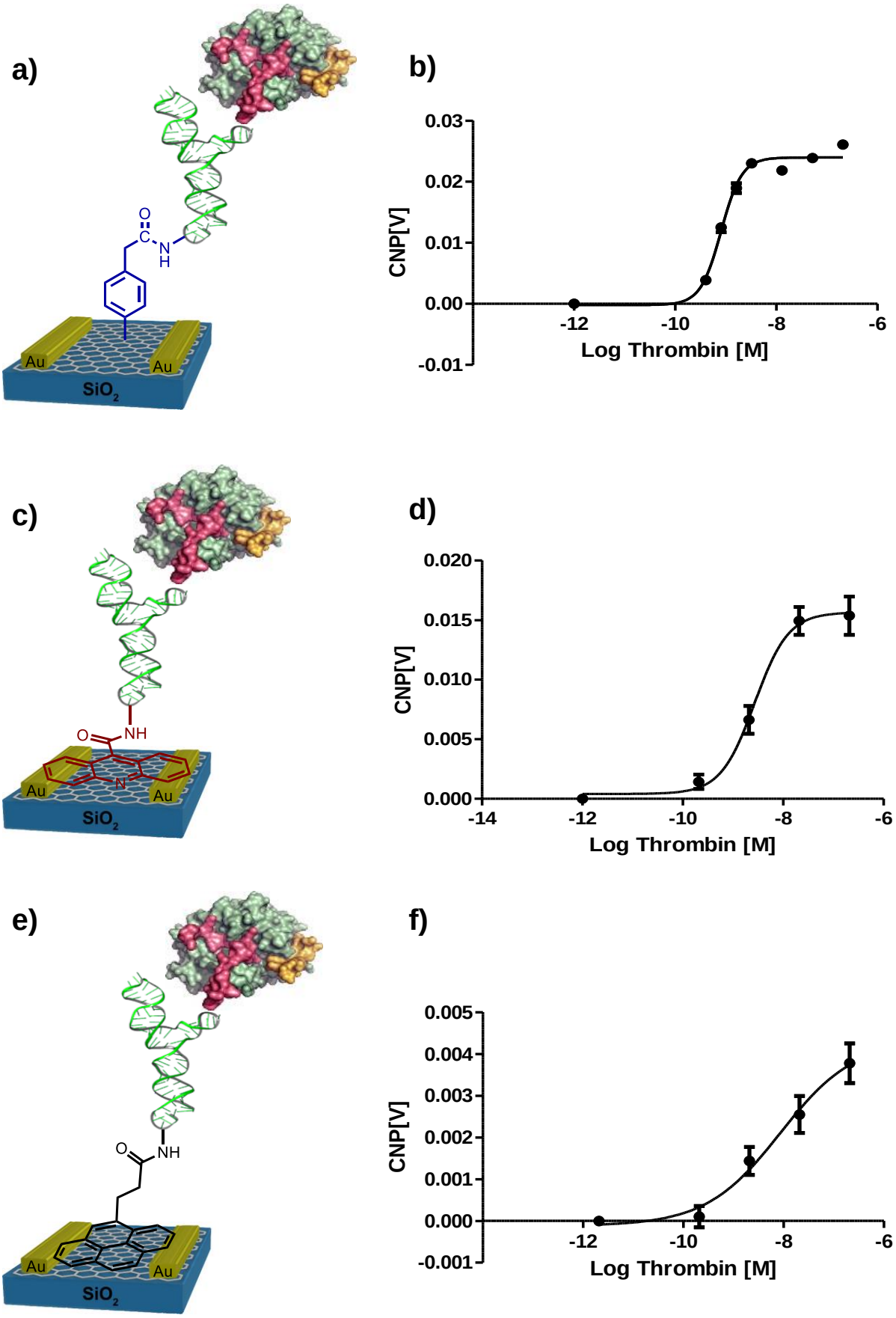

Figure 85. General scheme of the bioconjugated thrombin-aptamer system in a) SiO_2/mGFET-(*p*-(CH_2CO_2H)Ph) c) SiO_2/mGFET-(9-(CO_2H)Acr) and e) SiO_2/mGFET-(4-($CH_2CH_2CO_2H$)py) and affinity curve of the biosensing system for b) SiO_2/mGFET-(*p*-(CH_2CO_2H)Ph), d) SiO_2/mGFET-(9-(CO_2H)Acr) and f) SiO_2/mGFET-(4-($CH_2CH_2CO_2H$)py).

Working in parallel in this project, our collaborators of the Centro Nacional de Microelectronica in Barcelona developed others two modification approaches of graphene to introduce carboxyl groups as "anchor points" based on non-covalent strategies: substituted pyrene (SiO_2/mGFET-(4-($CH_2CH_2CO_2H$)py)) and acridine (SiO_2/mGFET-(9-(CO_2H)Acr) (Figure 85c and e). As shown in table 6, the sensitivity of the method was higher when the covalent functionalization was employed. However, the covalent modification showed a limitation with a lower linear range. Possibly, the creation of the oligomers with a lower height than Debye length in the radical addition introduces higher amount of carboxylic groups in the effective area for each hybridized sp^3 C atom of graphene (*i.e.* higher amount of aptamers) whereas with the π-π approaches the amount of aptamers should be lower because of the early saturation of the surface does not allow the introduction of too many carboxylic groups. For that reason, the sensitivity of the covalent approach is higher (15.7 mV/[M]). However, this high number of aptamers could result in a masking for the next thrombin attached.In addition, the olygomerization observed by AFM analysis could compromise the Debye length, resulting in an earlier saturation of the transducer signal.

Table 6. Electrical characterization of graphene functionalization for bioconjugated thrombin.

Functionalization	Sensibility mV/[M]	RSD(%)	n	Linear Range[nM]
SiO_2/mGFET-(*p*-(CH_2CO_2H)Ph)	15.7	20	10	0.4 - 3
SiO_2/mGFET-(4-($CH_2CH_2CO_2H$)py)	1.1	25	10	0.2 - 200
SiO_2/mGFET-(9-(CO_2H)Acr)	6.3	27	18	0.2 - 20

The high hydrophobic surface area of graphene facilitates a great density of captured biomolecules.[256] For that reason, we decided to study the influence of the aptamer approach against the unspecific adsorption of the thrombin protein. For that purpose, the non-covalent approach was employed due to its high linear range in the thrombin detection. Thus, two different control experiments were performed: i) The incubation of the sensor with BSA protein after the thrombin aptamer attachment (*control experiment 1*). ii) The incubation of the graphene surface with thrombin in the absence of the aptamer (*control experiment 2*). In the Figure 86, the sensing evaluation of SiO_2/mGFET-(4-($CH_2CH_2CO_2H$)py) sensor and the two control samples were plotted. In both control experiments, the CNP value changes of graphene were minimum compared to the functionalized m/G.

On the one hand, the *control experiment 1* showed the high selectivity of the thrombin aptamer. On the other hand, the *control experiment 2* demonstrated that nonspecific thrombin adsorption was not occurring or was not interfering with the measurable signal. Therefore, the bioconjugation step with aptamer is mandatory in the sensor manufacturing.

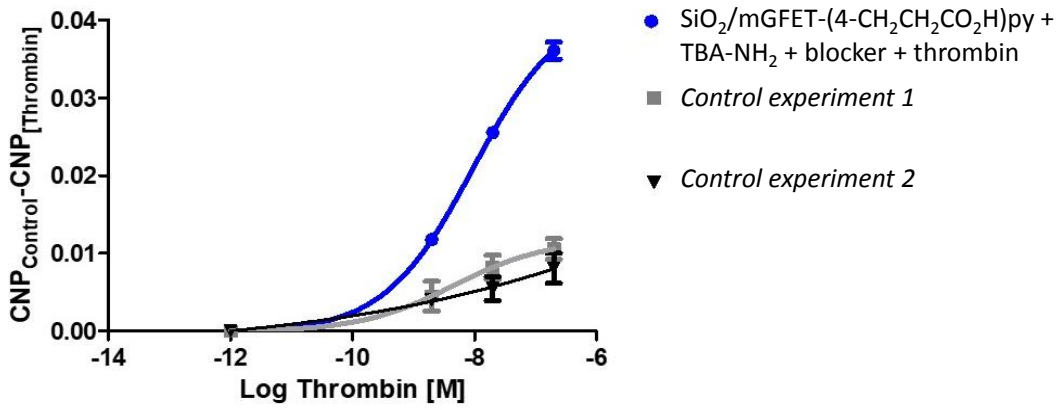

Figure 86. Unspecific adsorption for the sensing platform functionalized with pyrene. ***Control experiment 1*****: SiO_2/mGFET-(4-$CH_2CH_2CO_2H$)py + TBA-NH_2 + blocker + BSA.** ***Control experiment 2*****: SiO_2/mGFET-(4-$CH_2CH_2CO_2H$)py + blocker + thrombin.**

The regeneration of the developed biosensors was evaluated. For the development of this kind of aptasensor there are two possible strategies for the incubation of the corresponding biomolecules.[257] For this study, the *overlay method* was chosen because it is not required the protein-aptamer unbinding between each incubation step. Hence, the corresponding protein (thrombin or BSA) solution with x concentration was incubated on the sensing platform and the analyte is selectively recognized for the aptamer. After the corresponding measurements, a $10x$ concentration solution was incubated without removing the protein attached in the previous incubation step. However, this approach would not be interesting for a commercial device due to non-recyclable ability of sensing platform. For that reason, approaches that allowed the unbinding of the protein with the aptamer were tackled. For this purpose, the denaturalization of the aptamer is necessary to remove the conjugated thrombin followed by the aptamer folding. Based on previous results,[258] we tested two different regeneration processes. One of them involves the use of moderately high temperature, immersing one chip in water at 80 °C for 5 minutes.[259] The second one involves basic pH, by immersing the device in a 10 mM NaOH solution for 20 minutes.[260] For both regeneration processes, the samples were incubated with PBS in order to recover the aptamer structure. However, the sensing capacity that they showed before the aptamer denaturalization was not recovered. Therefore, for the good future of this project will be necessary the improvement of the suitability regeneration processes.

In summary, a graphene biosensing platform was functionalized with carboxylic groups in order to link a specific bioreceptor. To this end, the optimization through different device architectures was required. The sensing properties were implemented in a GFET by two different approaches: on the one hand, the improvement of pH sensing capacities was achieved by the chemical incorporation of carboxylic groups on the graphene surface. On the other hand, a selective protein sensing by binding specific aptamers on graphene was carried out. In addition, we demonstrated that the covalent modification is promising for the proposed sensing implementation. Indeed, the covalently functionalized graphene device showed sensing capability with higher sensitivity than other chemical approaches. However, special attention should be paid in further research for a better control of the graphene functionalization to overcome the short linear range of the detection. Thus, these results pave the way to novel

biosensors, as for example sensing implants for cortex *in vivo* sensing to monitor neurotransmitters concentrations, which are related to different neural diseases.

2.5. Mass spectrometry of Carbohydrate-Protein Interactions on a Glycan Array Conjugated to CVD graphene Surfaces.

Carbohydrates, along with nucleic acids, proteins and lipids, are the fundamental macromolecules that constitute the cells. They participate in numerous cellular processes and encode a large amount of information due to their structural diversity. The cell surface is covered in a dense layer of carbohydrates called glycocalix. In this layer carbohydrates are found to form glycoconjugates, such as glycoproteins, glycolipids or proteoglycans. The expression of glycosylated macromolecules is specific to each cell or tissue type and can be altered by their stage of development or differentiation. The glycosylation profiles of cells also vary in various pathologies. Therefore, abnormal glycosylation patterns can be used as biomarkers for cancer or autoimmune diseases. The set of proteins that specifically recognizes carbohydrates are called lectins. C-type lectins are an important family of receptors that are expressed on the surface of dendritic cells. They are capable of specifically recognize carbohydrates which pathogens express on their surface.

Mass spectrometry (MS) is a valuable tool for functional genomic, and glycomic studies. In particular, the combination of MS with microarrays is a powerful technique for analyzing the activity of carbohydrate processing enzymes and for the identification of carbohydrate-binding proteins (lectins) in complex matrices. On the other hand, graphene exhibits high desorption/ionization efficiency and good conductivity, specifications of a high-performance component for MALDI platforms.[205-207,213-215] Besides, the chemical functionalization of graphene increases the adsorption capability of functional biomolecules (e.g. receptors), resulting in very stable interfaces.

Graphene can be covalently or non-covalently modified by a range of functional groups. The activation of graphene with reactive groups has the advantage of providing oriented analyte immobilization and concomitant passivation of the surface to avoid unspecific adsorption of contaminants that could interfere in the analysis.[261] As mentioned in the introduction, there are few examples referring to graphene derivative-coated surfaces for SALDI-MS, but all based on GO derivatives.[213-215] The GO doped in the target plate act as laser absorber and ionization promoter, consequently permitting the direct analysis of samples without addition of an organic matrix. However, current substrate is far from ideal in terms of stability, reproducibility and effective functionalization; thus, improved performance with new materials is required.

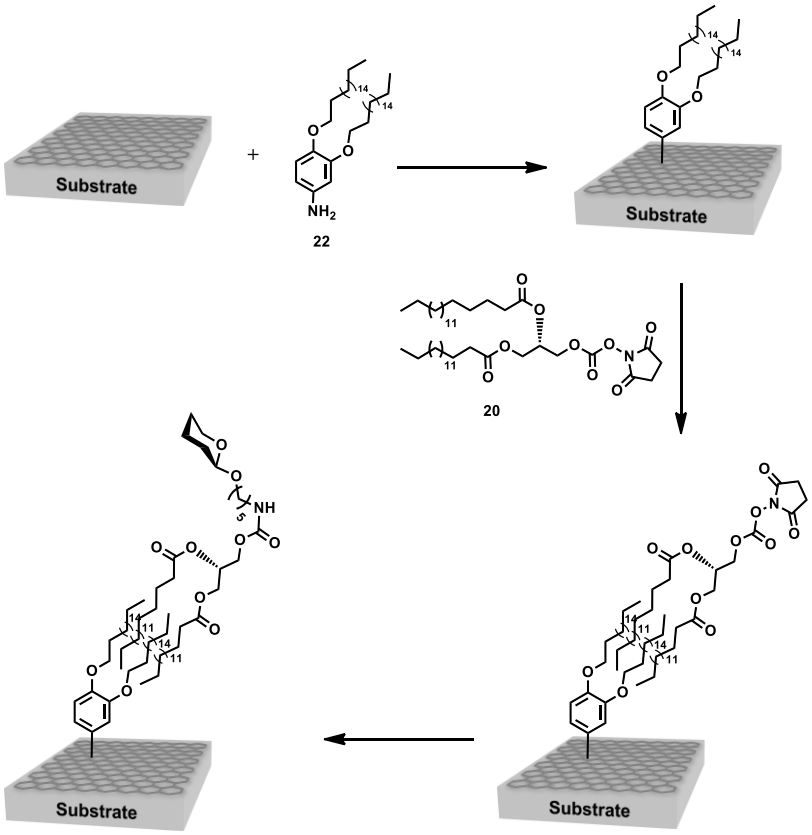

Figure 87. General scheme of the functionalization of CVD graphene substrates of the Lectin-Glycan array platform.

For that purpose, CVD graphene is a promising but largely unexplored candidate in this area. The CVD graphene presents higher conductivity and electron mobility,[59] which is required for MS detection, than GO. In addition, it presents high transparency to detect interactions *via* fluorescence readout. Taking advantage of the properties of CVD graphene, we developed several modified CVD graphene-based glycan microarrays on different transparent substrates (Figura 84), including: (1) conductive ITO-coated glass (ITO/G) and (2) non-conductive bare soda lime glass slides (Glass/G), as potential sensing platform for carbohydrate-lectin interaction. The detection of these interactions is of great interest because they are involved in a plethora of biological processes.[262] The glycan arrays were fully characterized by MALDI-MS analysis and, in some cases, optical microscopy. This research has been developed in collaboration with the company Graphenea S.L. and the Glycotechnology Lab headed by Dr. Niels Reichardt in CICbiomaGUNE (Spain).

2.5.1. Functionalization of CVD graphene

In order to develop the envisioned microarray, *strategy 2* described in previous sections was used (see 2.2.1.). Thus, the functionalization of graphene microarray was based on the formation of a hydrophobic bilayer *via* the combination of covalent and non-covalent modification of graphene (Figure 87). Initially, the graphene surface was covalently functionalized with stearyl alkoxide-substituted aniline derivative **22** *via* a diazonium salt reaction generated *in situ* and further modified by hydrophobic interactions with the N-hydroxysuccinimide (NHS) activated bidentate 1,2-*sn*-dipalmitoyl glycerol **20**. Onto this NHS activated hydrophobic bilayer, amine-

containing ligands can be robotically printed and immobilized as highly stable carbamates. In addition, the terminal reactivity of the bidentate linker might be easily changed to azide, alkyne[263] or amine groups to accommodate other ligand types. Hereupon, *p*mol amounts of 5-amino-penty modified carbohydrates were spatially arrayed on the different surfaces, generating micrometer sized spots of the immobilized carbohydrates. The non-covalent approach through the aliphatic chains allows a good desorption/ionization reversibility which is required for an effective mass detection of the immobilized analytes.

The CVD graphene used in the development of this project was provided by the company Graphenea S.L. For that reason, it was necessary the study of the reactivity for this CVD graphene. As a proof of concept, we have firstly studied the covalent modification of CVD graphene on SiO_2 (SiO_2/G-(3,4-($C_{18}H_{37}O)_2$Ph)) as common and commercially available support substrate (Figure 88). It is an ideal substrate for this study because, as mentioned in the introduction, can increase the reactivity of CVD graphene due to the polar and charged group in the interlayer. In particular, the diazonium salt **23** was generated *in situ* from the mentioned aniline **22** (Figure 72). As in the previous section, the reaction was performed in DMF at 60 °C due to the low solubility of the compound. In order to characterize the modified graphene surface, different techniques were used: Raman spectroscopy and AFM.

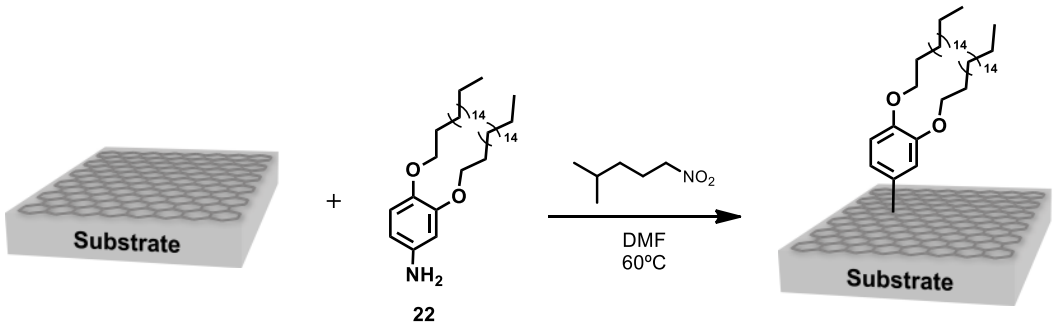

Figure 88. General scheme of the S/G-(3,4-($C_{18}H_{37}O)_2$Ph) functionalization of graphene surfaces.

SiO_2/G-(3,4-($C_{18}H_{37}O)_2$Ph) was characterized by Raman spectroscopy. The main distinction was observed on the D band (≈1350 cm^{-1}) intensity that denotes a slightly increment. This increment might be explained by the formation of sp^3 carbon defects in the graphene structure (Figure 89). Raman analysis has shown a slight increase in the number of defects ($\Delta(I_D/I_G)$ = 0.05). The average spectra were obtained from the representative region Raman mapping (30 x 20 μm^2 ≈ 1500 points spectra) before and after modification.

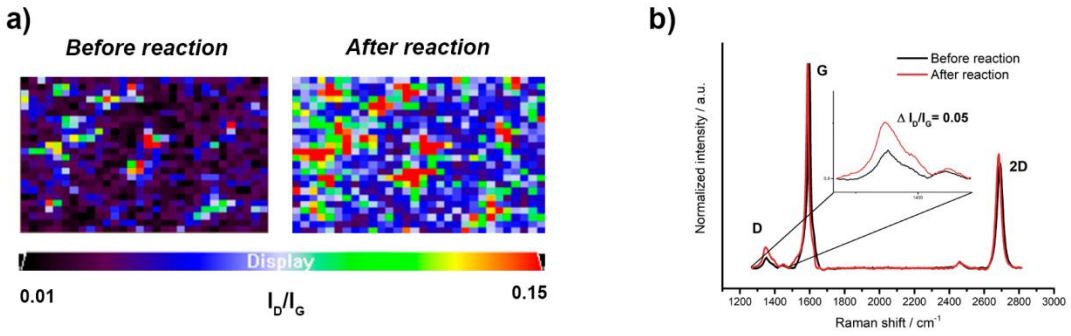

Figure 89. a) Raman mapping of the D band intensity (30 x 20 μm²), and b) average Raman spectra for SiO_2/G-(3,4-($C_{18}H_{37}O)_2$Ph) before (black) and after (red) covalent functionalization.

In addition to the Raman analysis, the AFM study showed significant topographical changes in the graphene surface (Figure 90). Thanks to the flat character of SiO_2 was easily observed the graphene changes by this technique. Before the modification, graphene surface showed the typical wrinkles because of solvent trapping, edge instabilities, interatomic interactions etc.[253] After the functionalization, the obtained image showed an increase in the roughness. High nucleation spots are clearly observed in the Figure 90b. Probably, it was produced by the well-known oligomers derived from the generated phenyl radicals.[95] Therefore, the proposed covalent modification of graphene allows a high introduction of the desire molecule without the significant disruption of the intrinsic properties of CVD graphene because of the oligomer formation. It is worthy to mention that due to the high degree of radical generation and oligomers in the solution media, the use of hot toluene was necessary to clean the substrate because of the low solubility these byproducts.

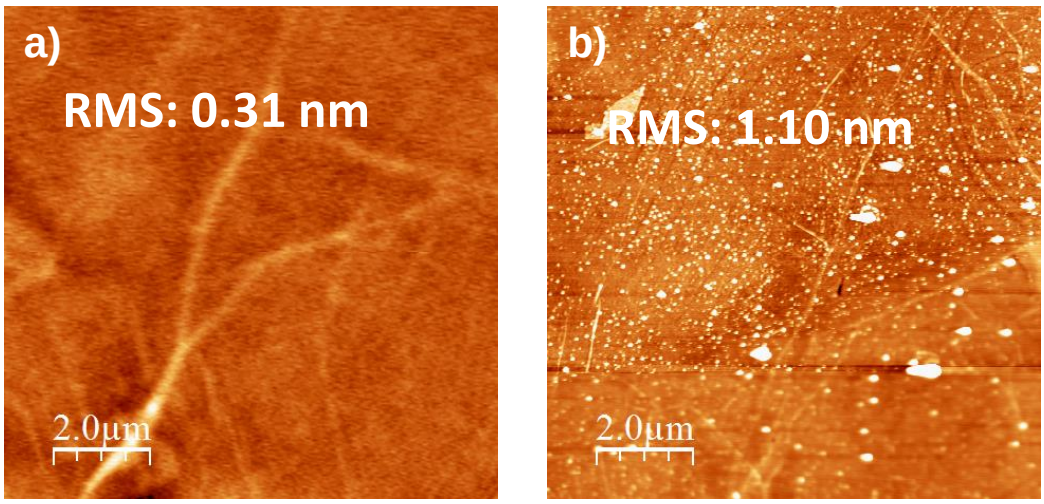

Figure 90. AFM images of SiO_2/G a) before and b) after reaction.

After confirming the covalent modification of CVD graphene on a generic substrate, the preparation of the different graphene-based microarrays were addressed on (1) conductive ITO-coated glass (ITO/G) and (2) non-conductive bare soda lime glass slides (Glass/G as support platforms. Consequently, the two substrates were covalently functionalized using the reaction conditions described above for SiO_2/G-(3,4-($C_{18}H_{37}O)_2$Ph (Figure 88). Then the modified samples were fully characterized by Raman spectroscopy, XPS analysis, water contact angle

measurements and AFM. Firstly, the ITO/G samples were modified under the reaction conditions described above for SiO_2/G-(3,4-($C_{18}H_{37}O$)$_2$Ph. However, the samples were not successfully modified according to the increment of defects after reaction ($\Delta(I_D/I_G)$) in the averaged Raman spectra from ≈1000 single-point spectra in a 30 x 20 μm² area (Figure 91).

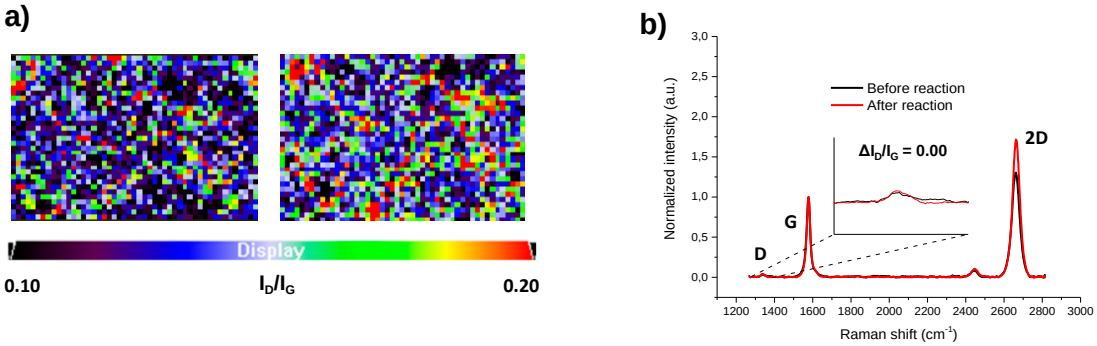

Figure 91. a) Raman mapping of the D band intensity in 30x20 μm² area and b) averaged Raman spectra (≈1000 single-point spectra, λ_{exc} = 532nm) ITO/G-(3,4-($C_{18}H_{37}O$)$_2$Ph) before and after covalent modification (2 mM).

For this reason, we decided to increase the concentration of **22** from 2 to 8 mM. Then, similar Raman mapping studies of ITO/G-(3,4-($C_{18}H_{37}O$)$_2$Ph) after modification showed an increment of D and D' band at 1350 and 1615 cm^{-1}($\Delta(I_D/I_G)$ = 0.06, Figure 92a and b). Once again, the increment of the defects according to the Raman is not high compared to similar diazonium salt reactions, presumably, because of the steric hindrance that attached oligomers produced. Then the obtained reaction conditions were transfer to the Glass/G modification. Although the Raman spectroscopic analysis showed a lower functionalization degree in terms of the increment of the number of defects ($\Delta(I_D/I_G)$ = 0.01, Figure 92c and d). Nevertheless, the Raman mapping showed hot functionalized spots, probably caused by the high glass roughness and heterogeneity of the bare glass surface, which generate these high reactivity regions.[107] For that reason, it was decided continue with this surface for this experiment despite the low functionalization degree in the Raman average.

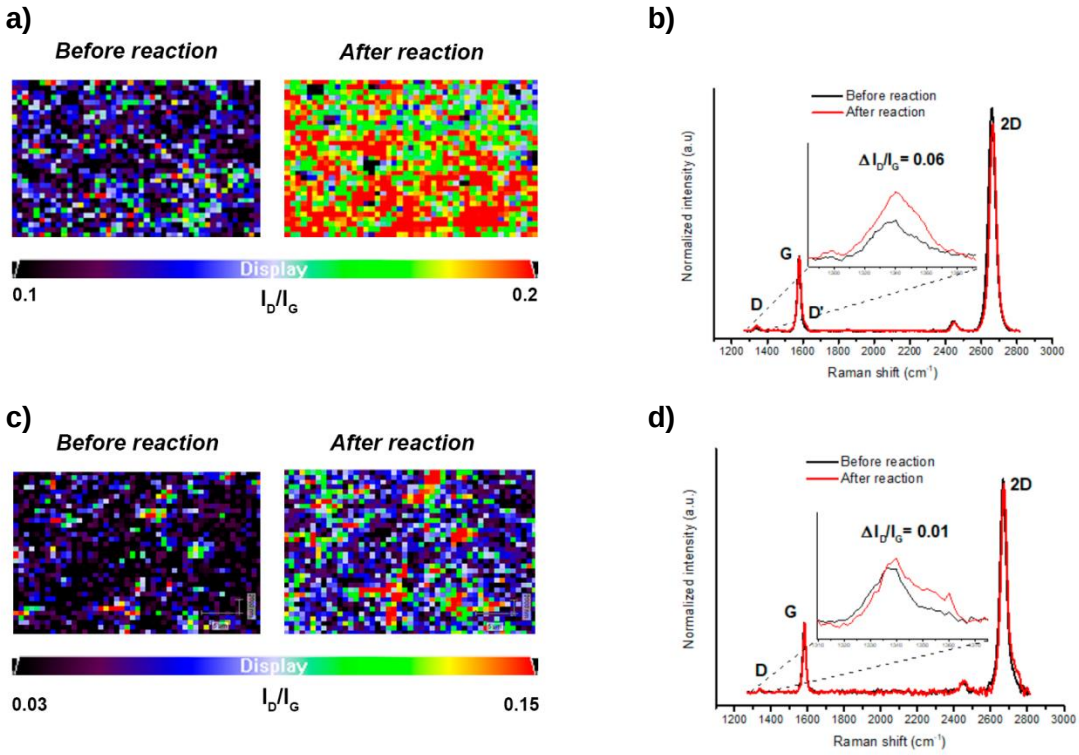

Figure 92. a, c) Raman mapping of the D band intensity in 30x20 μm² area and b, d) averaged Raman spectra (≈1000 single-point spectra, λ_{exc} = 532nm) before and after on a, b) ITO/G-(3,4-($C_{18}H_{37}O)_2$Ph) and c, d) Glass/G-(3,4-($C_{18}H_{37}O)_2$Ph) (8mM).

In addition, the XPS analysis of the graphene surface was performed to provide evidence of the graphene functionalization studying the chemical composition of the sample before and after covalent reaction. The XPS analysis showed an increase of atomic carbon concentration after functionalization (Table 7).

Table 7. Atomic percentage of S/G-(3,4-($C_{18}H_{37}O)_2$Ph) substrates before and after chemical modification.

Sample		Atomic %	
		C1s	***O1s***
ITO/G-(3,4-($C_{18}H_{37}O)_2$Ph)	***Before reaction***	62.63	37.37
	After reaction	74.17	25.83
Glass/G-(3,4-($C_{18}H_{37}O)_2$Ph)	***Before reaction***	56.55	43.45
	After reaction	65.54	34.46

Focusing on the atomic carbon composition, pristine graphene substrates showed a C1s core level composed of a graphenic C=C asymmetric component (284.37 eV) and the oxygenated carbon groups such as C-O and C=O components (≈ 286 and ≈ 288 eV, respectively; Table 8). However, after covalent functionalization, C=C/C-C component significantly increased (9.2 and 20.5% for ITO/G-(3,4-($C_{18}H_{37}O)_2$Ph) and Glass/G-(3,4-($C_{18}H_{37}O)_2$Ph), respectively), because of the introduction of the dialkoxyphenyl moieties.

Table 8. C1s components for CVD graphene on ITO coated glass and bare glass before and after chemical modification.

Sample	C1s Component	Before Reaction		After Reaction	
		Binding energy (eV)	*Area (%)*	*Binding energy (eV)*	*Area (%)*
Glass/G-(3,4-($C_{18}H_{37}O$)$_2$Ph)	C=C/C-C	284.37	82.0	284.37	91.8
	C-O	286.49	7.8	285.28	4.4
	C=O	288.57	8.3	286.70	1.6
	O-C=O	289.99	2.0	288.42	1.5
	pi-pi*	-	-	290.78	0.8
Glass/G-(3,4-($C_{18}H_{37}O$)$_2$Ph)	C=C/C-C	284.37	64.0	284.37	84.5
	C-O	285.27	12.5	285.28	7.2
	C=O	286.54	10.3	286.70	5.6
	O-C=O	288.61	8.1	288.42	1.6
	pi-pi*	290.67	5.2	290.78	1.1

In addition, the surface morphology was study by AFM after functionalization and a thorough washing process. The AFM images of functionalized ITO/G (Figure 93a and c) suggested the existence of an amorphous layer on the surface composed by a significant fraction of aryl oligomers. Comparing with the flat character of the SiO_2, ITO presents the characteristically superimposed sheets.[264] For that reason, it is not possible to observe the typical graphene wrinkles. Before the functionalization, the AFM images suggested a quite flat ITO sheets (≈ 3.3 nm). After the covalent modification, the molecules introduced led to an increase of in the height morphology (≈ 5.5 nm) and visible vesicles of 30 nm are observed derived from the oligomer creation (Figure 93c). However, the topography studied by AFM for functionalized graphene on bare glass was not conclusive owing to the higher roughness and low quality of the glass substrate (Figure 93e).

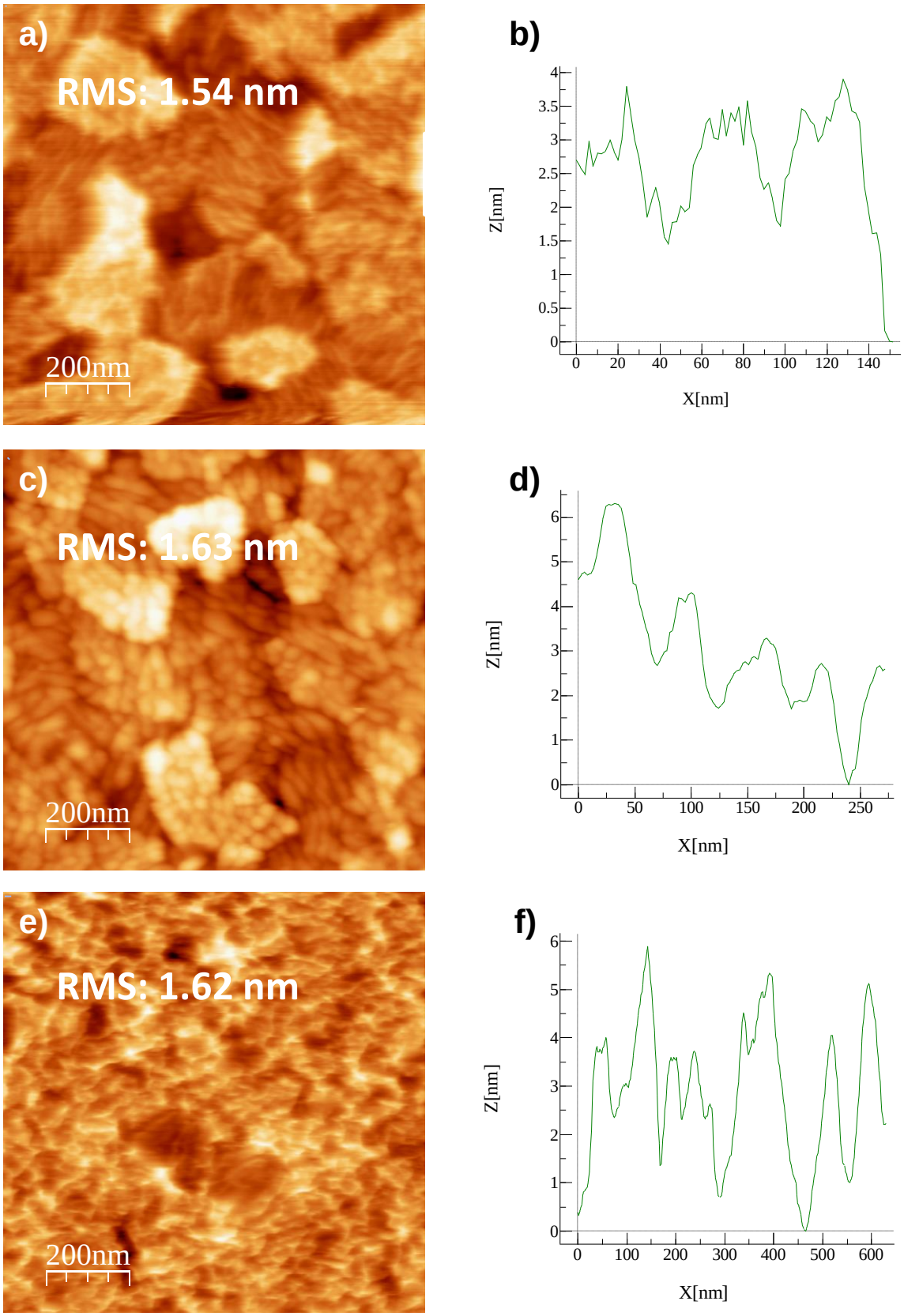

Figure 93. AFM images of a) CVD graphene on ITO-coated glass, c) ITO/G-(3,4-($C_{18}H_{37}O$)$_2$Ph) and e) Glass/G. AFM height profiles (blue line) of ITO/G-(3,4-($C_{18}H_{37}O$)$_2$Ph) b) before and d) after reaction and f) height profile of CVD graphene on Glass/G.

In order to determine the influence of the functionalization on the surface hydrophobicity, the water contact angle was measured for the different samples. Thereby, the water contact angle on functionalized ITO/G (Figure 94b and c) increased with respect to the pristine material (from 64.9 to 73.1°), confirming the presence of the alkyl chains. Nevertheless, the water Glass/G contact angle measurements showed a decrease of hydrophobicity after the covalent modification (Figure 94e and f), probably caused by the heterogeneity of the glass surface. Overall, the characterization of CVD graphene on bare glass was quite challenging, due to its poorer surface characteristics compared to ITO coating.

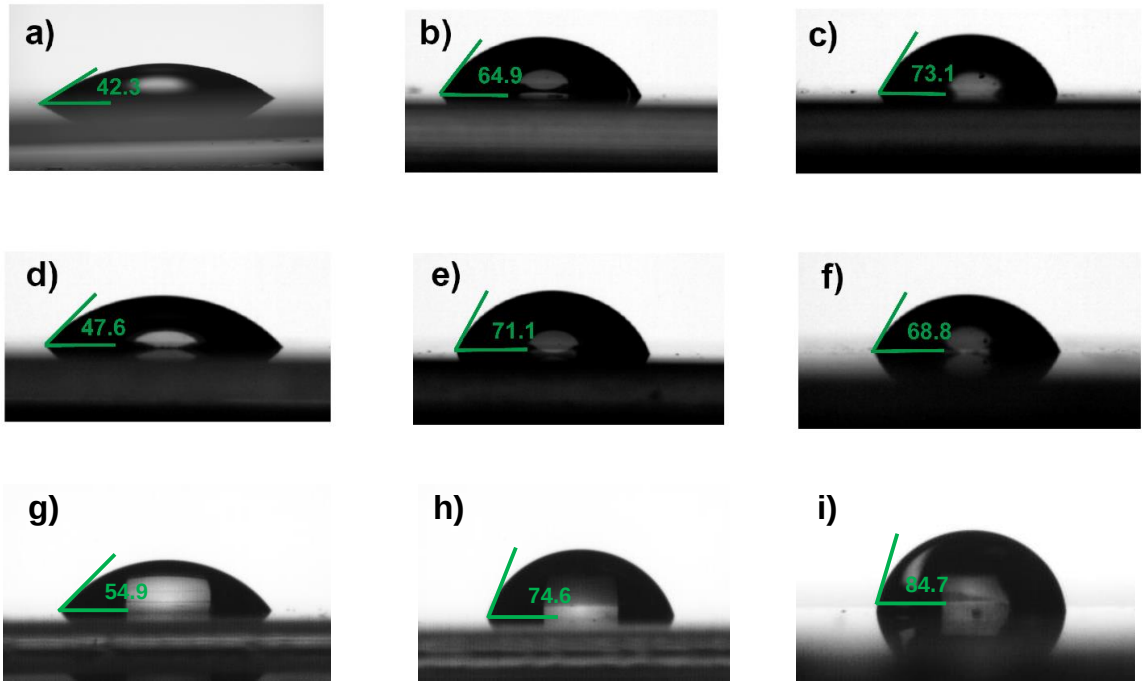

Figure 94. Contact angles of a) ITO-coated glass treated with piranha solution, b) ITO/G, c) ITO/G-(3,4-($C_{18}H_{37}O$)$_2$Ph), d) bare glass treated with piranha solution, e) Glass/G, f) Glass/G-(3,4-($C_{18}H_{37}O$)$_2$Ph), g) quartz treated with piranha solution, h) Quartz/G and i) Quartz/G-(3,4-($C_{18}H_{37}O$)$_2$Ph).

As an alternative for a non-conductive substrate with higher quality than the used bare glass, CVD graphene was deposited on quartz (Quartz/G) surface and the radical reaction was subsequently performed on it. The characterization by Raman (Figure 95) showed a higher increase in the ratio I_D/I_G compared with the previous experiment on Glass/G ($\Delta(I_D/I_G) = 0.07$) after the covalent modification in DMF.

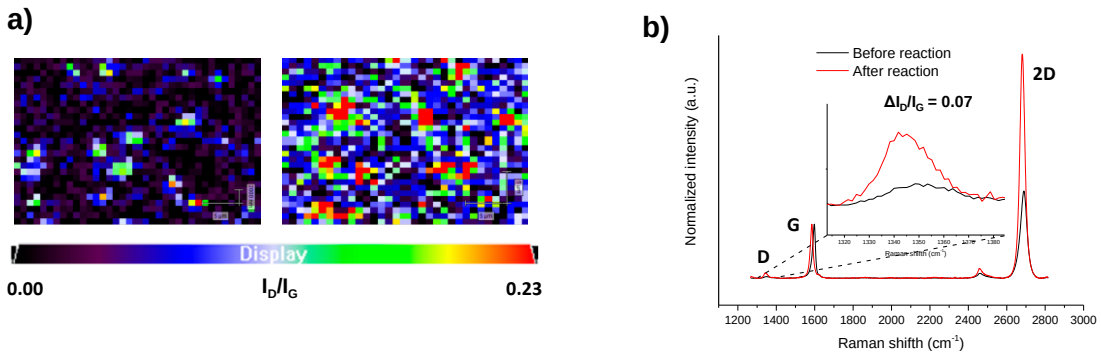

Figure 95. a) Raman mapping of the D band intensity (30 x 20 μm²), and b) average Raman of Quartz/G-(3,4-($C_{18}H_{37}O$)$_2$Ph) spectra before (black) and after chemical modification (red).

For this highly flat surface, the AFM study showed the expected wrinkles for graphene before functionalization and once again, vesicles due to the oligomers generation after the modification with the radical 19 (Figure 96a and c). As well as an increase in the surface height was observed (Figure 96b and d). The water contact angle analysis for Quartz/G-(3,4-($C_{18}H_{37}O$)$_2$Ph) was also enhanced (from 74.6 to 84.7, Figure 94h and i) according to the expected result for this high-quality surface material. However, during the water contact angle analysis in water graphene detachment was observed because of the poor adsorption of graphene on Quartz. The use of aqueous solution in the array fabrication and in the final application is mandatory; therefore, the employment of Quartz/G was discarded.

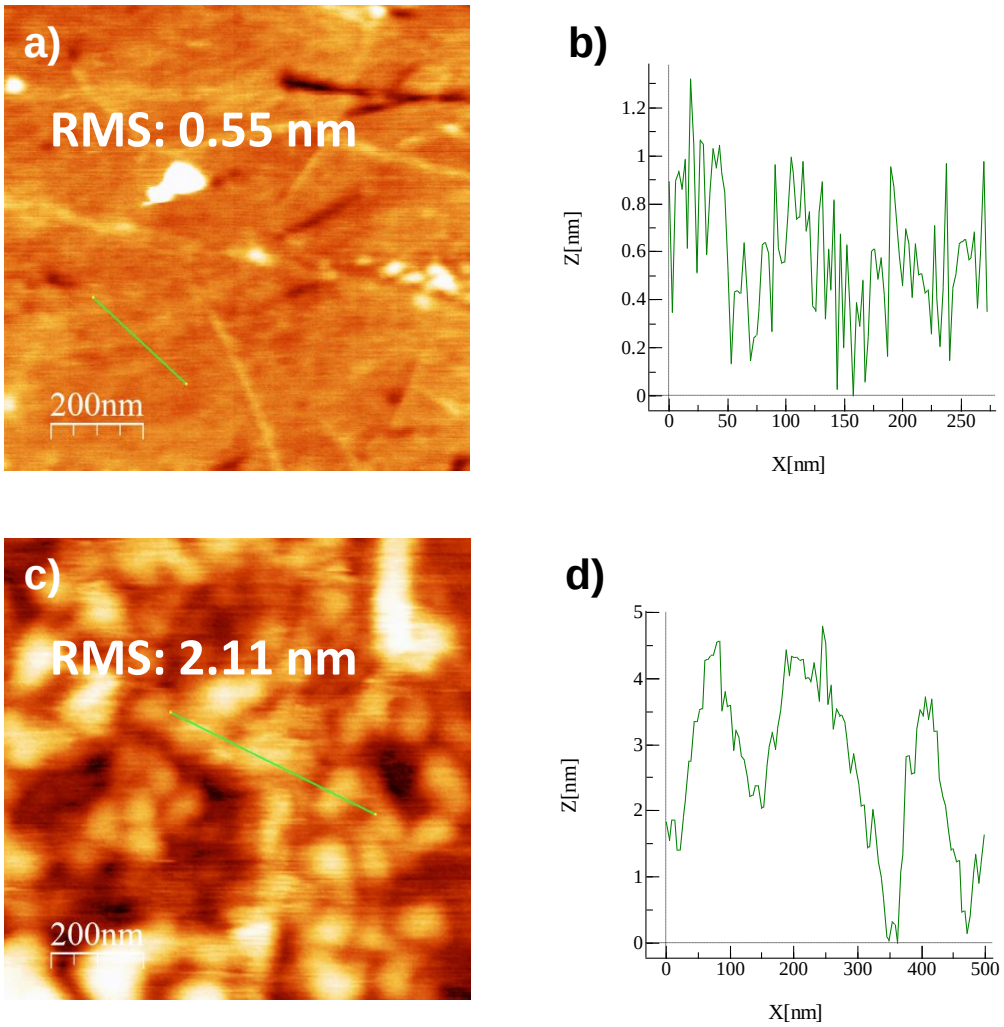

Figure 96. AFM images of Quartz/G a) before and c) after functionalization. AFM height profiles (green line) of Quartz/G b) before and d) after functionalization.

2.5.2. Interface generation on CVD graphene for detection of carbohydrates-lectin interactions

After the covalent modification of CVD graphene, the immobilization of N-hydroxysuccinimide (NHS) activated bidentate 1,2-*sn*-dipalmitoyl glycerol linker (**20**) was carried out onto ITO/G and glass/G modified substrates. To evaluate the adsorption of the lipidic bidentate linker **20**, MALDI-TOF MS after matrix deposition was performed. The immobilization was clearly confirmed on both CVD graphene-based substrates by the detection of **20** (*m/z* 732.50 $[C_{35}H_{68}O_5+Na]^+$).

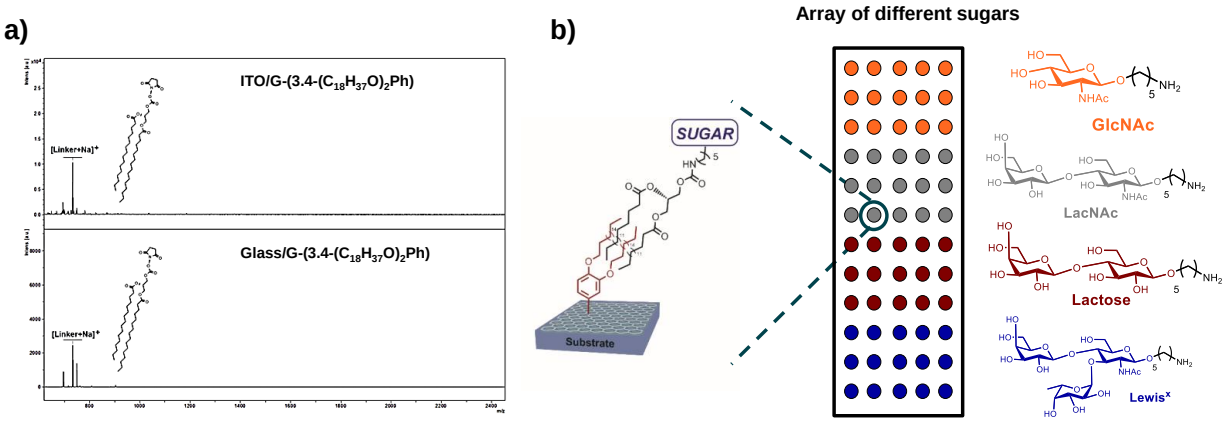

Figure 97. a) MALDI-TOF spectra of bidentate linker on ITO/G-(3,4-($C_{18}H_{37}O$)$_2$Ph) (top) and on Glass/G-(3,4-($C_{18}H_{37}O$)$_2$Ph) (bottom); *m/z* 732.50 [$C_{35}H_{68}O_5$+Na]$^+$ b) General scheme of the sugar microarray.

The activation of the surface with reactive NHS groups permitted the immobilization of amine containing biomolecules. Then, as a proof of concept, the solutions of four different 5-aminopentyl modified carbohydrates (Figure 97b): N-acetyl-D-glucosamine (GlcNac), N-acetyl-D-lactosamine (LacNac), lactose (Lac) and Lewis^x trisaccharide (Le^x), were robotically dispensed on both NHS activated substrates using a robotic piezoelectric spotter (50 μM, Figure 98a). The non-reacted NHS groups were quenched by the immersion of the substrates in ethanolamine solution. Each spot contains *p*mol amounts of each carbohydrate in 50 μM concentration forming subarrays of four different carbohydrates, and five replicates were printed for each carbohydrate. Thus, carbohydrate structures are spatially organized and immobilized creating a sugar microarray (Figure 97b). The created hydrophobic bilayers showed high stability for ITO/G-(3,4-($C_{18}H_{37}O$)$_2$Ph) and for Glass/G-(3,4-($C_{18}H_{37}O$)$_2$Ph) surfaces during aqueous washings, in which the excess of buffers and reagents in the printing solutions could be removed by a simple washing procedure. However, as it was advanced above, the superficial tension of aqueous solution resulted in the detachment of graphene from the particularly flat quartz surface of the functionalized Quartz/G-(3,4-($C_{18}H_{37}O$)$_2$Ph) (Figure 98c).

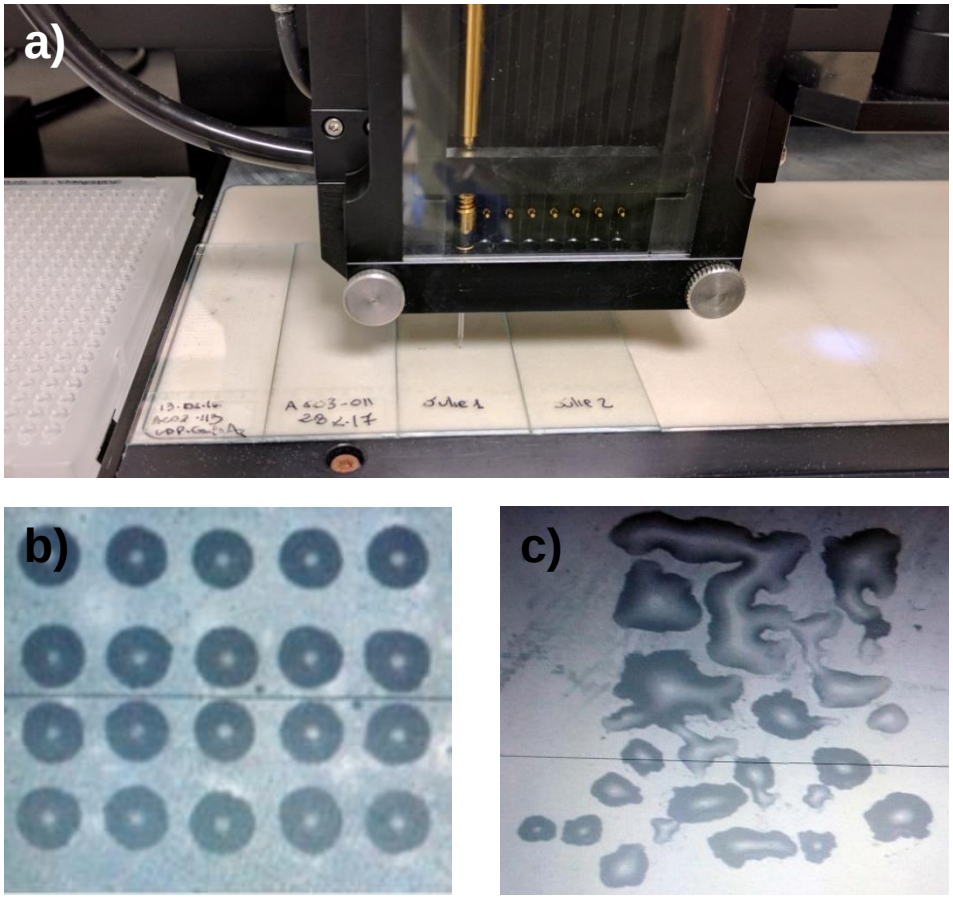

Figure 98. a) Robotic piezoelectric spotter, optical image of the sugar printed on a) glass and b) quartz after the aqueous washing.

The successful immobilization of the carbohydrates was monitored by MALDI-TOF MS after matrix deposition. By this monitorization, the performance of the prepared arrays could be evaluated. Under laser irradiation, the hydrophobic bilayer is disrupted allowing the detection of carbohydrates coupled to bidentate linker on individual spots. For an accurate comparison of the different CVD graphene substrate performance, all spectra were recorded under identical laser settings and power conditions and a sum of 500 shots was acquired in each spectrum. Both ITO/G-(3,4-($C_{18}H_{37}O$)$_2$Ph) and Glass/G-(3,4-($C_{18}H_{37}O$)$_2$Ph) showed similar performance in the analysis of immobilized carbohydrates (Table 9). Clean mass spectra with high ion intensity and good signal to noise ratio were obtained from individual spots (Figure 99). The functionalized CVD graphene did not show interference or additional signal of matrix background that could avoid the detection of the desired species. It is well known the characteristically artifacts of CNMs usually are produced and could mask the small molecules signals.[265] For the modified CVDG graphene, these artifacts were not present even with laser fluence higher than 50%. The MALDI spectra were acquired using low laser fluence (30%) due to the remarkable desorption/ionization capability of the created interface.

Table 9. MS detection of different immobilized carbohydrates using APTES modified ITO (lacking CVDG coating) and CVDG coated bare glass slides.

Carbohydrate	m/z $[M+Na]^+$	ITO/APTES		Glass/G-(3,4-($C_{18}H_{37}O)_2$Ph)		ITO/G-(3,4-($C_{18}H_{37}O)_2$Ph)	
		Peak intensity	S/N	Peak intensity	S/N	Peak intensity	S/N
GlcNAc	923.65	3483	598.9	5292	736.4	6372	642.7
LacNAc	1085.71	2846	386.0	2016	385.3	7452	783.0
Lactose	1044.68	6275	964.4	1577	276.2	23014	1911.9
Le^x	1231.76	3189	526.7	2789	417.1	2783	271.2

In addition, the performance of Glass/G-(3,4-($C_{18}H_{37}O)_2$Ph) and ITO/G-(3,4-($C_{18}H_{37}O)_2$Ph) microarrays were compared with the previously described hydrophobic coated ITO-based microarrays reported by Niels and coworkers.[266] This non-graphene array was prepared by the Silanization with 3-aminopropyltriethoxysilane (APTES) of ITO-coated glass slides and the subsequent coupling of NHS-activated stearic acid for the immobilization of the amine containing carbohydrates. Both CVD graphene slides showed a similar performance, in terms of S/N and peak intensity, as the non-graphene APTES modified ITO (Table 9 and Figure 99). Therefore, functionalized CVD graphene could become an alternative in carbohydrate microarray fabrication.

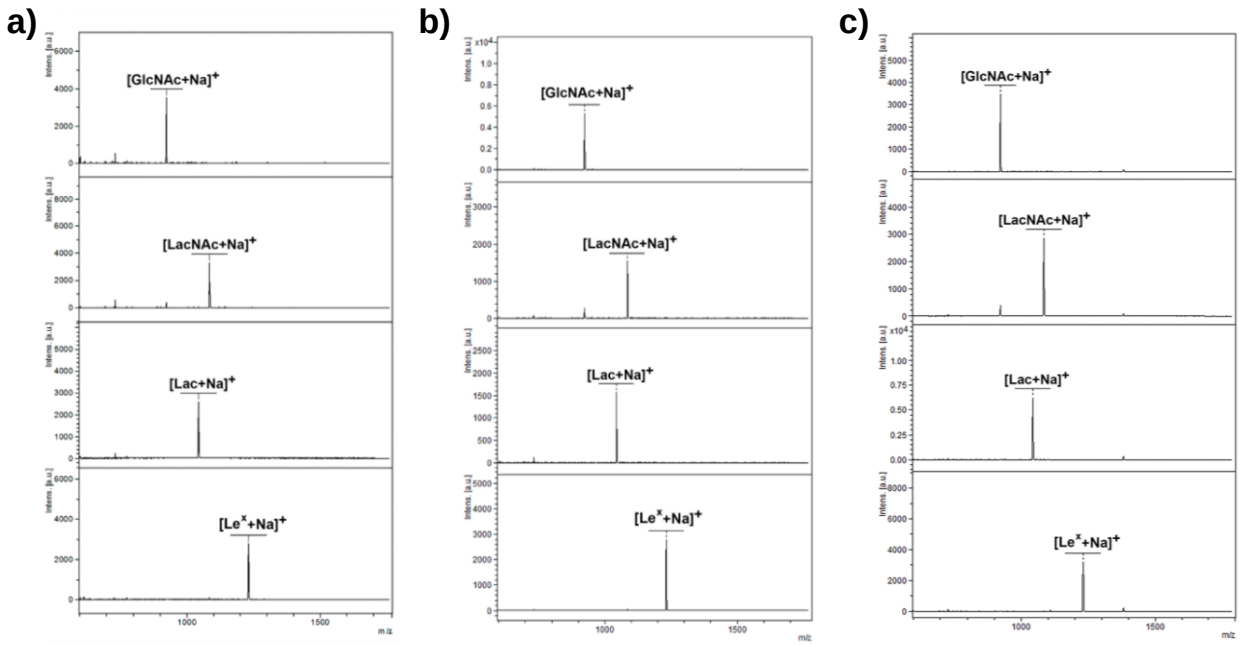

Figure 99. Mass spectra of carbohydrates immobilized a) on ITO/G-(3,4-($C_{18}H_{37}O)_2$Ph) and b) on Glass/G-(3,4-($C_{18}H_{37}O)_2$Ph) and c) ITO/APTES microarrays by MALDI-TOF using DHB as matrix.

The capacity of CVD graphene as surface for SALDI-MS was evaluated for the first time. In particular, the detection of the four immobilized carbohydrates on chemically modified graphene under matrix-free conditions was studied on bare-glass and ITO coated glass substrates (Figure 100). The four carbohydrates immobilized on glass/CVDG microarrays were efficiently detected (Figure 100a). However, the SALDI-MS performance of ITO/G-(3,4-($C_{18}H_{37}O$)$_2$Ph) was unexpectedly less sensitive (Figure 100b). Indeed, only lactose and GlcNAc were detected. To obtain a proper detection using ITO coated glass substrates, the carbohydrate concentration had to be increased from 50 μM to 0.1 mM (Figure 100c). This extraordinary difference between ITO/G-(3,4-($C_{18}H_{37}O$)$_2$Ph) and glass/G-(3,4-($C_{18}H_{37}O$)$_2$Ph) as SALDI platform can be explained by the more efficient absorption of graphene on a flat ITO surface that can hinder the graphene fragmentability under laser irradiation, which is directly related to the desorption/ionization capacity. However, further studies are needed for a better interpretation of this exhibited results. Thus the role of CVD graphene as a SALDI platform was successfully performed for the first time.

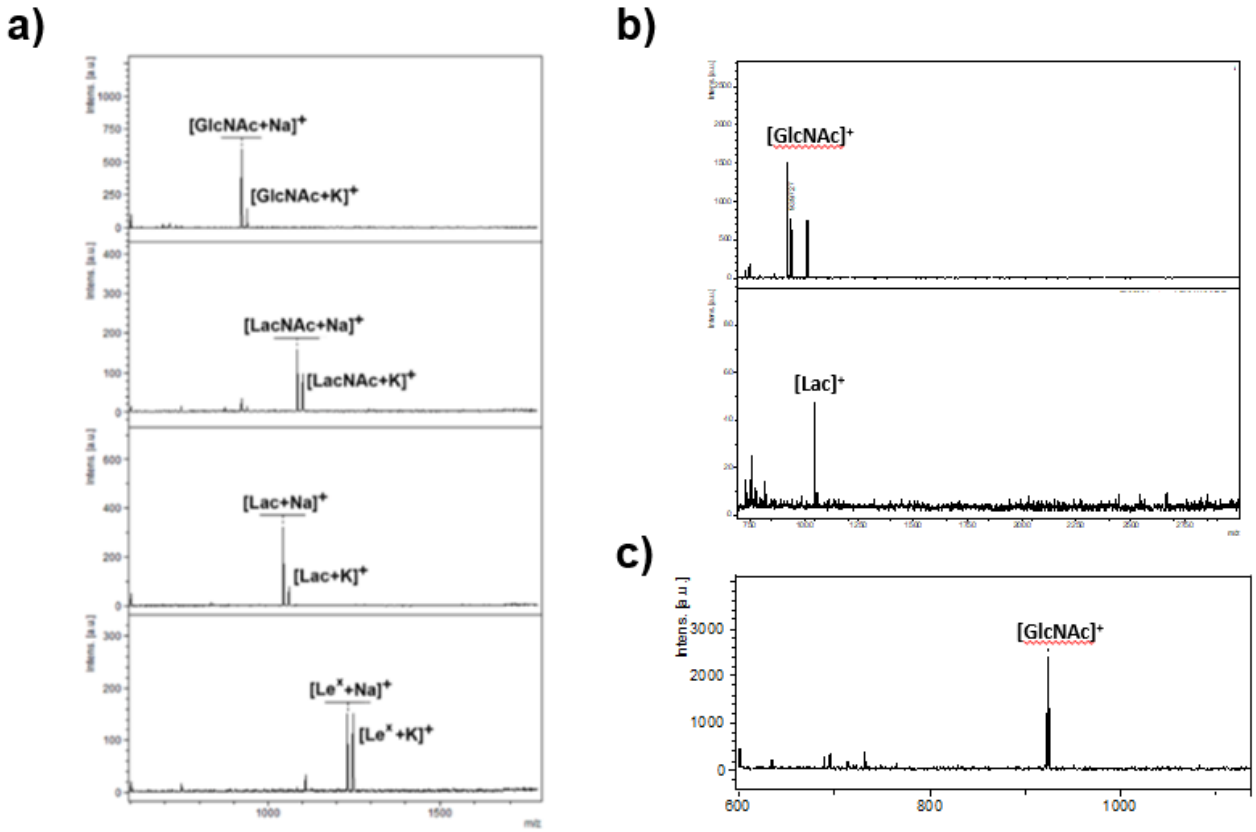

Figure 100. Mass spectra of carbohydrates immobilized on a) Glass/G-(3,4-($C_{18}H_{37}O$)$_2$Ph) and b) ITO/G-(3,4-($C_{18}H_{37}O$)$_2$Ph) microarrays by SALDI at 50 μM. c) Mass spectra of carbohydrates immobilized on ITO/G-(3,4-($C_{18}H_{37}O$)$_2$Ph) microarray by SALDI at 100 μM.

Since graphene surfaces show high hydrophobicity and their interaction with phospholipids has been previously described,[267] the assay performance for graphene surfaces was also evaluated with the bidentate activated linker **22** directly immobilized on the non-chemically functionalized CVD graphene surface. The recorded MS spectra under identical conditions

showed that the direct neoglycolipid immobilization on graphene surface produced spectra with far lower S/N and spectral quality than the spectra obtained from covalently modified graphene (Table 10), which had been hydrophobically derivatized with the dialkoxy aniline ligand **22**.

Table 10. MS detection of different immobilized carbohydrates using CVD graphene-based substrates with and without chemical functionalization by MALDI-TOF.

Carbohydrate	*m/z* $[M+Na]^+$	ITO/G-(3,4-$(C_{18}H_{37}O)_2Ph$)		ITO/G		Glass/G-(3,4-$(C_{18}H_{37}O)_2Ph$)		Glass/G	
		Peak intensity	***S/N***	***Peak intensity***	***S/N***	***Peak intensity***	***S/N***	***Peak intensity***	***S/N***
GlcNAc	923.65	3525	292.1	306	88.4	5292	736.4	162	30.4
LacNAc	1085.71	3281	743.5	174	44.3	2016	385.3	314	70.5
Lactose	1044.68	2587	365.0	345	71.2	1577	276.2	282	68.2
Le^x	1231.76	2783	271.2	483	117.8	2789	417.1	195	41.1

This experimental evidence concludes that the covalent hydrophobic modification of the graphene layer, although does not affect substantially the hydrophobic properties of the material, can lead to a higher loading of the bidentate linker 22 and consequently to an increase in the loading of immobilized carbohydrates. Therefore, the chemical modification of CVD graphene is mandatory for the manufacture of the described carbohydrate microarrays.

2.5.3. Optical and Mass Spectrometry detections of carbohydrate-lectin interactions

Lectins are proteins that recognize specific structural elements of carbohydrates with high selectivity, acting as translators of the information encoded by carbohydrates on the cell surface or in extracellular proteins. They are widespread in all living organisms, from bacteria to mammals and display numerous biological functions, in cell-cell communication, fertilization and immune response, e.g. through the recognition of foreign carbohydrates presented in colonizing pathogens.[268]

The detection of carbohydrates-lectin interactions by mass spectrometry was carried out.[269] In particular, the array prepared on Glass/G-(3,4-$(C_{18}H_{37}O)_2Ph$) was incubated with lectin *Auleria aurantia* (AAL) solution. AAL is isolated from orange peel fungus and recognizes L-fucose, with a broad specificity towards different linkages (α-1,2; α-1,3; α-1,4; α-1,6). This lectin is commonly employed as a tool in the isolation and characterization of fucosylated glycoproteins, which are often overexpressed in different types of cancers.[270] By MALDI-TOF MS, the incubated platform thus showed the detection of a peak at *m*/*z* = 33691 Da $[AAL]^+$[42], which corresponds to the monomeric lectin, exclusively on spots of immobilized Le^x carbohydrate (Figure 101d).

In addition, carbohydrate microarrays were extensively employed as high throughput screening tools for the characterization of these proteins. Commonly, carbohydrate-lectin interactions on microarrays are quantified *via* the emitted fluorescence of the adhered labeled lectins after a washing step to remove non-binders. It is well documented that graphene can quench fluorescent dyes *via* FRET with high efficiency.[169] In fact, bioassays based on the quenching and subsequent recovery of the fluorescence on graphene has been developed to study carbohydrate-lectin interactions.[271] We hypothesized that the hydrophobic bilayer constructed on CVD graphene-based microarrays could provide enough distance to avoid FRET based quenching of the dyes allowing fluorescence measurements on these surfaces. To verify this hypothesis, we incubated CVD graphene carbohydrate microarrays with fluorescently labeled lectin AAL (AAL-555). After incubation with AAL-555, the Glass/G carbohydrate microarray was washed and scanned in a microarray scanner. Figure 101c shows the superimpose image of printed drops and the fluorescence emission of AAL-555 measured by microarray scanner. A fluorescence signal was only observed for the spots corresponding to the immobilized **Le**^{x} carbohydrate, which was the only fucosylated structure on the array.

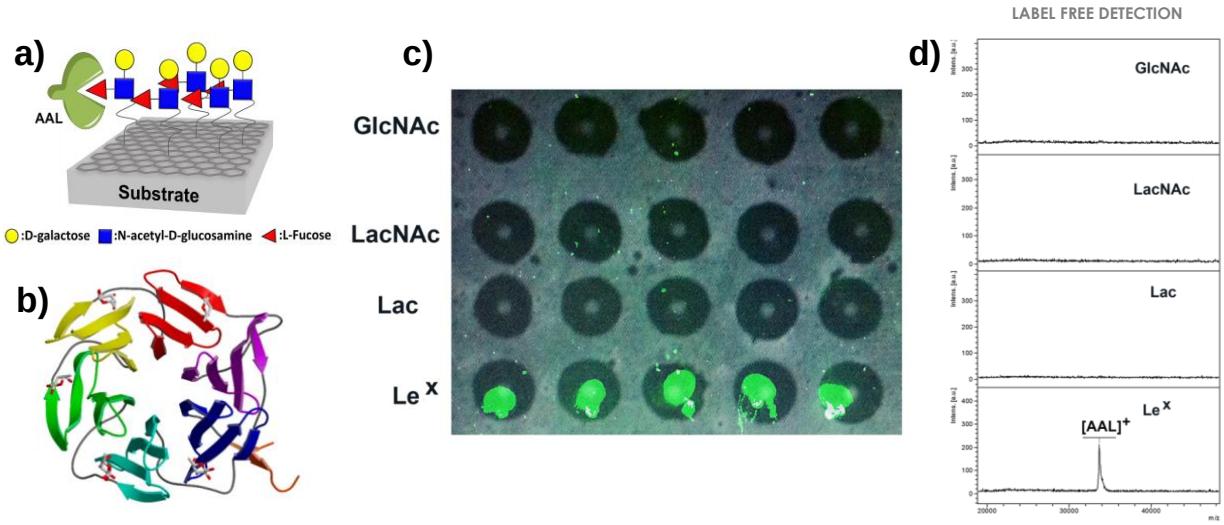

Figure 101. Detection of carbohydrate binding proteins (lectins) on CVD graphene microarrays. a) Schematic representation of Auleria *aurantia lectin* (AAL) binding towards fucosylated Le^{x} structure, b) structure of the mentioned protein, c) fluorescence detention of AAL-555 binding towards Le^{x} and d) detection of AAL binding towards Le^{x} by MALDI-TOF mass spectrometry.

As summary, we have developed MS active CVD graphene carbohydrate microarrays on a variety of support materials. It was based on the formation of a hydrophobic bilayer on chemically modified graphene by the construction of NHS active surfaces on CVD graphene. The presence of the bilayer was required for an effective mass detection of the immobilized analytes. Low cost materials such as bare microscope glass slides were enough as surface for CVD graphene deposition and the subsequent functionalization for the preparation of microarrays without the need of an ITO adhesive layer.

Results and discussion

The developed surfaces are suitable for LDI-MS analysis. CVD graphene behaved as anchoring platform on ITO and as conductive surface on bare glass substrates for SALDI. Likewise, it was established the crucial role of chemical functionalization for the manufacture of CVD graphene carbohydrate microarrays and might be further studied for the immobilization and sensing of other biomolecules such as proteins, peptides or DNA.

2.6. Conclusions

Conventional solvents used in silicon microfabrication processing are generally inefficient in the case of graphene. Alternatively, THF and EtOH have been considered as candidate options. Despite its undeniable capability for polymer cleaning/solving, THF is extremely dependent of the type of residue; therefore, its use may compromise graphene integrity. Differently, EtOH has demonstrated to be extremely effective for reducing the residues on the surface of graphene after microfabrication steps such as photolithography. EtOH solvent capability is basically independent of the residues thickness, and as it is easily adaptable at wafer scale and is highly compatible with microfabrication technologies, it is validated to be included as a necessary material in the regular cleaning procedures in the microfabrication of graphene electronic devices.

Besides, the generation of graphene biointerfaces was suitable for their use in electronic devices. For that purpose, graphene transistors were functionalized with carboxylic groups as "anchor" point to link biomolecules. It was performed an optimization process through different chemical modification strategies. With this first modification (*strategy 1*) two different sensing capabilities were implemented in the devices. The introduction of the carboxylic group allows an improvement in the pH-current variation. In addition, recognition of biomolecules trough the introduction of a thrombin-aptamers showed sensing capability with good sensitivity. These results open a great amount of possibilities for cortex *in vivo* sensing and the detection of neurotransmitters and the diseases related with them.

We have studied the preparation of MS active CVD graphene carbohydrate microarrays on a variety of support materials. The construction of NHS active surfaces on CVD graphene was based on the formation of a hydrophobic bilayer on chemically derivatized graphene. The presence of the bilayer was required for an effective mass detection of the immobilized analytes. Low-cost materials such as uncoated microscope glass slides were sufficient as surface for CDVG deposition and the subsequent functionalization for the preparation of microarrays without the need of an ITO adhesive layer.

The potential of CVD graphene as a performance component for LDI-MS analysis is reported for the first time. In particular, CVD graphene behaved as anchoring platform on ITO and as conductive surface on bare glass substrates for SALDI. Likewise, the crucial role of chemical functionalization for the manufacture of CVD graphene carbohydrate microarrays was established. We speculate that this methodology might be further expanded with the immobilization of other biomolecules such as DNA, peptides or proteins for the development of LDI-MS-based assays.

3. EXPERIMENTAL DETAILS

3. Experimental details

Comercial reagents and solvent were purchased from different commercial companies and they were used as received without further purification.

CVD graphene substrates were provided by Graphenea S. L. (Donostia, Spain) and by the Instituto de Microelectrónica de Barcelona IMB-CNM (CSIC), Universidad Autónoma de Barcelona, (Bellaterra, Spain).

3.1. Materials and techniques

NMR

All NMR spectra were acquired at Bruker 500 MHz instrument. The spectra were processed with MestReNova software version 7.1.1-9649.

FTIR

Fourier-transformation Infrared spectroscopy (FTIR, Nicolet 6700 Thermo) spectra were measured with KBr flake. The spectra were processed with Microsoft Excel 2010.

Raman spectroscopy

Raman spectra were recorded with a Renishaw Invia Raman microscope equipped with a 532 nm wavelength laser, a lens-based spectrometer with 1800 gr/mm grating and a Peltier-cooled front-illuminated CCD (1024 px x 532 px). 4.4 Wire software was used to data analysis, processing and presentation

XPS

XPS measurements were performed in a SPECS Sage HR 100 spectrometer with a nonmonochromatic X ray source of Aluminum with a Kα line of 1486.6 eV energy and 300 W. XPS measurements were performed on a SPECS Sage HR 100 spectrometer with a nonmonochromatic X ray source of Aluminium with a Kα line of 1486.6 eV energy and 300 W. XPS data was fitted using CasaXPS 2.3.16 PR 1.6 software.

AFM

Surface topologies of slides were characterized by atomic force microscopy (AFM; JPK NanoWizard II) in intermittent contact tapping mode and contact mode using a tapping etched silicon probe (TESPA-V2) with a 0.01 – 0.025 Ω/cm antimony (n) doped Si, rectangular 3.8μm thick cantilever with a nominal resonant frequency, spring constant, length, and width of 320 kHz, 42 N/m, 123 μm, and 40 μm respectively. For the taping force measures an AFM DIMENSION ICON was employed using a Nanoscope V Bruker controller.

The obtained AFM-images were analyzed in WSxM 5.0 Develop 7.0 and NanoScope Analysis 1.9.

Spotter

Microarrays were printed employing a robotic piezoelectric SciFLEXARRAYER spotter S11 (Scienion, Berlin, Germany). Fluorescence measurements were performed in Agilent G265BA microarray scanner system (Agilent Technologies, Santa Clara, USA). Quantification was performed with ProScanArray® Express software (Perkin Elmer, Shelton, USA).

Contact angle

Static contact angle measures were performed at Drop Shape Analysis System KRUSS, DSA 100 v 1-19. To evaluate the angles, DSA 3 v 1.6-02 software were used.

MALDI-TOF

Mass spectra were recorded on Bruker Ultraflextreme III TOF mass spectrometer equipped with a pulsed Nd:YAG laser (λ= 355 nm) and controlled by FlexControl 3.3 software (Bruker Daltonics, Bremen, Germany). Acquisitions (total of 5000 shots) were carried out in positive reflector ion mode with a pulse duration of 50 ns, a 40 frequency of 1000 Hz, a laser fluence of 30%, and the following laser focus settings: offset = 0%, range = 100%, and value = 9.5%. The m/z range was chosen according to the mass of the sample. The accumulated spectra were then process with FlexAnalysis v3.3 software. For calibration of mass spectra INTAVIS peptide calibration standard mixture II was employed.

MANUFACTURING OF GRAPHENE DEVICES

SiO_2/mGFET was manufactured by applying a conventional lift-off process using the image reversal photoresist AZ5214E (Clariant, Germany) to a four-inch silicon wafer (Figure 58) covered with thermal SiO_2. The bottom metal layer was a thermally evaporated Ti/Au, 10/100 nm in thickness. The GFET active areas were defined by means of an oxygen-based reactive ion etching based on a patterned AZ5214E resist mask. The patterning process of the top metal layer is like bottom metal contact patterning with a Ni/Au, 20/200 nm thick film. SU-8 resist was employed as the passivation layer of the graphene GFETs. Product SU-8 2005, from MicroChem is an epoxy-based negative photoresist, which was patterned to passivate the metal leads while defining the graphene channel and metal contacts openings. The simpler device SiO_2/MGFET was fabricated by a single photolithography step using AZ mask and reactive ion etching, like the microtransistor array. Gold electrical contacts were patterned on top of transferred graphene by using a shadow mask (i.e. no resist involved).

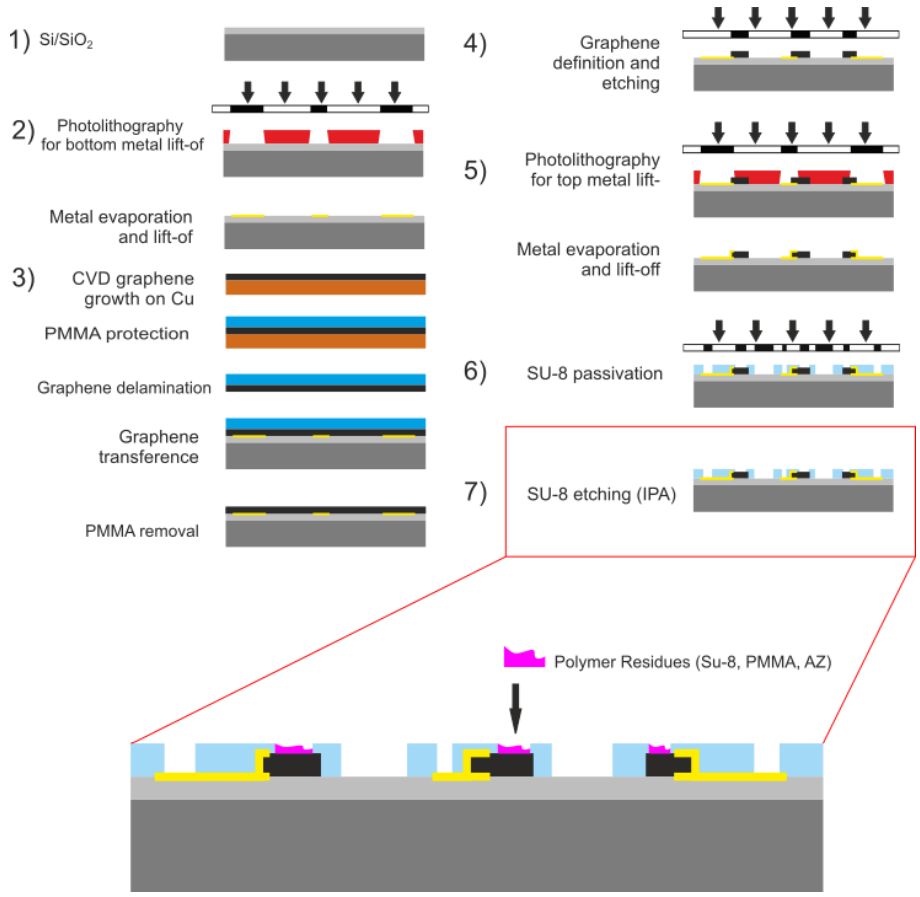

Figure 102. Graphene field effect transistor manufacturing process. Adapted from Masvidal 2016.[272]

3.2. Synthesis of compounds

3.2.1. Synthesis of 4-nitro-1,2-bis(octadecyloxy)benzene (27):

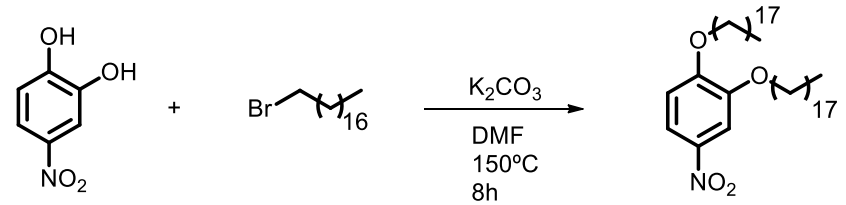

25 **26** **27**

A mixture of nitrocathecol **25** (1.00 g, 6.45 mmol), 1-bromooctadecane **26** (5.14 g, 15.48 mmol) and anhydrous K_2CO_3 (2.67 g, 19.35 mmol) in DMF (25.8 mL) was heated at 150 °C for 12 h. After cooling, the mixture was diluted with satd. NH_4Cl solution (500 mL) and extracted with CH_2Cl_2 (3x200 mL). The organic phase was evaporated under reduced pressure. The residue was purified by column chromatography (SiO_2; 2:1 petroleum ether/dichloromethane) to obtain 4-nitro-1,2-bis(octadecyloxy)benzene (**27**, 3.71 g, 5.6 mmol, 87%) as a yellow solid. ^{1}H NMR (500 MHz, $CDCl_3$) δ 7.87 (dd, *J* = 8.9, 2.6 Hz, 1H), 7.72 (d, *J* = 2.6 Hz, 1H), 6.87 (d, *J* = 8.9 Hz, 1H), 4.07 (m, 4H), 1.90 – 1.81 (m, 4H), 1.51 – 1.44 (m, 4H), 1.36 – 1.25 (m, 56H), 0.88 (t, *J* = 6.9 Hz, 2x3H) ppm. ^{13}C NMR (125 MHz, $CDCl_3$), δ: 154.7 (C), 148.7 (C), 141.2 (C), 117.6 (CH), 111.0 (CH), 108.6 (CH), 69.5 (CH_2), 69.4 (CH_2), 32.0 ($2CH_2$), 29.7 ($14CH_2$), 29.69 ($2CH_2$), 29.63 ($3CH_2$), 29.62 (CH_2), 29.39 ($2CH_2$), 29.38 (CH_2), 29.35 (CH_2), 29.0 (CH_2), 28.9 (CH_2), 26.0 (CH_2), 25.9 (CH_2), 22.7 ($2CH_2$), 14.12 ($2CH_3$). HRMS (ES+) for $C_{42}H_{77}NO_4Na$ $[M+Na]^+$, calculated: 682.5750, found: 682.5751.

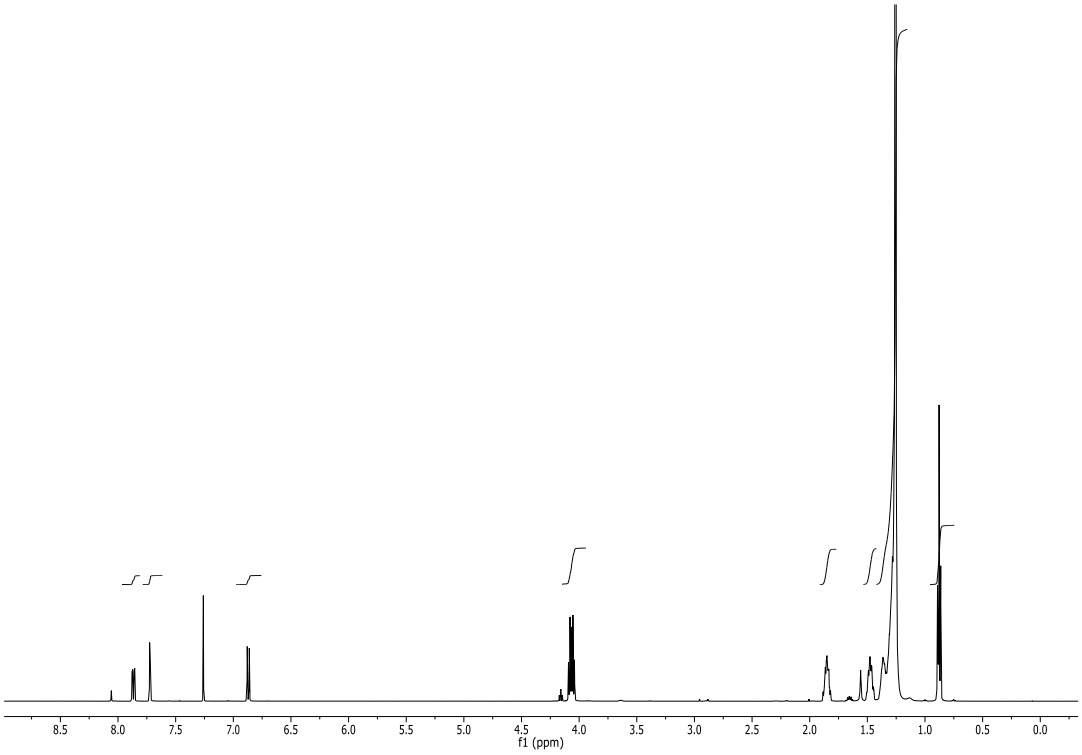

Figure 103. ^{1}H NMR spectrum (500 MHz, $CDCl_3$-d_1) of 27.

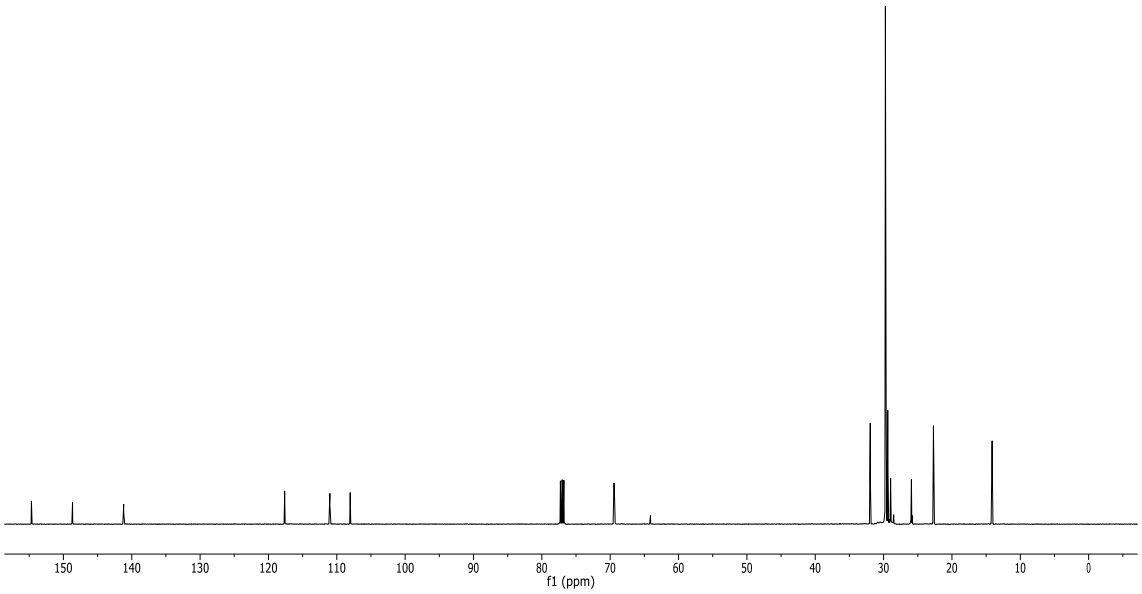

Figure 104. ^{13}C NMR spectrum (125 MHz, $CDCl_3$-d_1) of 27.

3.2.2. Synthesis of 3,4-bis(octadecyloxy)aniline (22)*:*

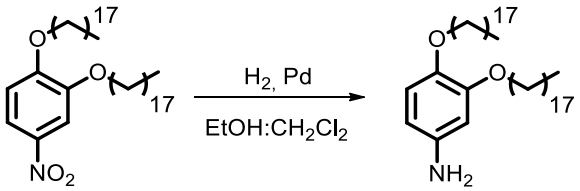

28 **22**

4-nitro-1,2-bis(octadecyloxy)benzene **28** (3.71 g, 5.6 mmol) was added in a round-bottom flask with a mix of CH_2Cl_2:EtOH (600 mL). Then the catalyst Pd/C was added. Solvent was deoxygenated under vacuum and H_2 was insufflated (3 cycles). The reaction was stirred under H_2 atmosphere overnight. The mixture was filter over Celite®, and the liquid phase was evaporated under reduced pressure to obtain 3,4-bis(octadecyloxy)aniline (**22**, 3.36 g, 5.3 mmol, 94%) as a pink solid. ^{1}H NMR (500 MHz, $CDCl_3$), δ 6.73 (d, *J* = 8.4 Hz, 1H), 6.30 (d, *J* = 2.6 Hz, 1H), 6.20 (dd, *J* = 8.4, 2.6 Hz, 1H), 3.93 (t, *J* = 6.6 Hz, 2H), 3.89 (t, *J* = 6.7 Hz, 2H), 1.83 – 1.76 (m, 2H), 1.76 – 1.70 (m, 2H), 1.50 – 1.39 (m, 4H), 1.25 (bs, 65H), 0.88 (t, *J* = 6.9 Hz, 2x3H). ppm. ^{13}C NMR (125 MHz, $CDCl_3$), δ: 150.6 (C), 141.9 (C), 141.2 (C), 117.3 (CH), 106.8 (CH), 102.7 (CH), 71.0 (CH_2), 69.0 (CH_2), 31.9 ($2CH_2$), 29.7 ($18CH_2$), 29.8 ($6CH_2$), 29.4 ($2CH_2$), 26.1 ($2CH_2$), 22.7 ($2CH_2$), 14.1 ($2CH_3$) ppm. HRMS (ES+) for $C_{42}H_{80}NO_2$ $[M+H]^+$ calculated: 630.6111, found: 630.6088.

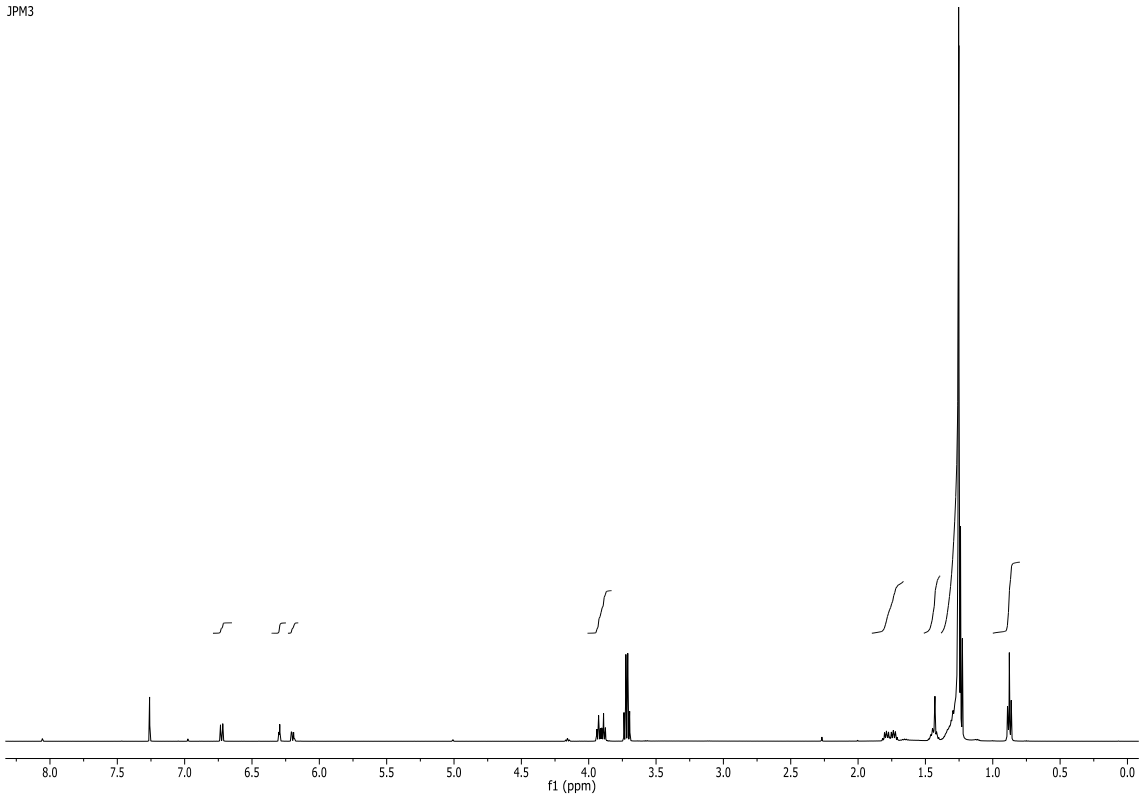

Figure 105. ^{1}H NMR spectrum (500 MHz, $CDCl_3$-d_1) of 22.

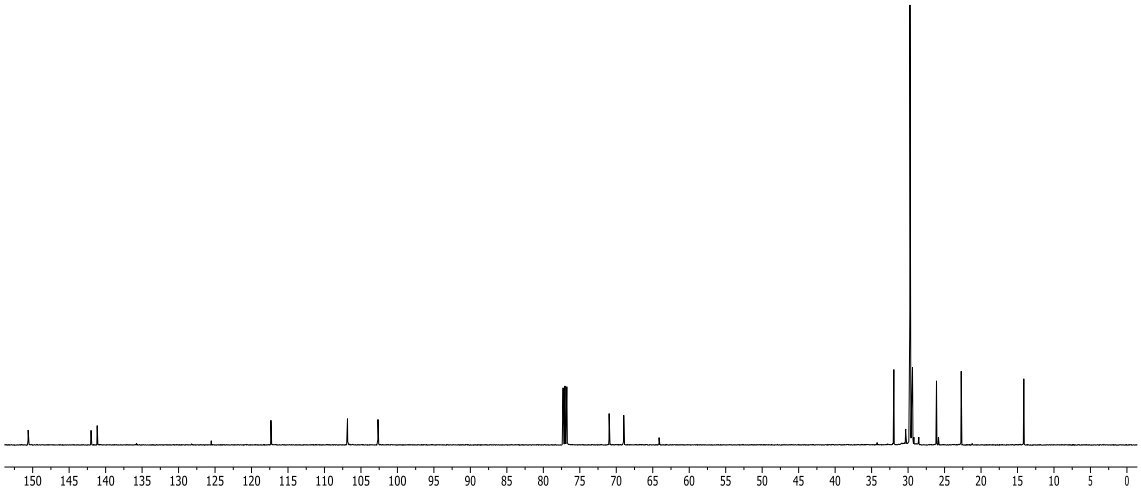

Figure 106. ^{13}C NMR spectrum (125 MHz, $CDCl_3$-d_1) of 27.

3.2.3. Systhesis of 4-(carboxymethyl)benzenediazonium tetrafluoroborate (24)*:*

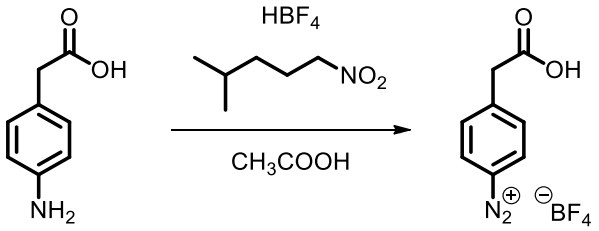

29 **24**

2-(4-aminophenyl)acetic acid (**29**, 500 mg, 3.3 mmol) and HBF_4 (1.5 mL, 24 mmol) was dissolved in acetic acid (70 mL). A solution of isoamylnitrate (1.4 mL, 3.75 mmol) in acetic acid (35 mL) was dropwised to the first mix and it was stirred for 15 min at r.t.. Cold EtOH (30 mL) was added to quench the reaction and the flask was stored in the -20 °C freezer overnight. The mix was then filtered in Millipore 0.1 μm and washed three time with cold EtOH (20 mL). The crystals were dried under vacuum to obtain 4-(carboxymethyl)benzenediazonium tetrafluoroborate (**24**, 738 mg, 3 mmol, 89%) as a yellow solid. ^{1}H NMR (500 MHz, $CDCl_3$) δ 8.44 (d, *J* = 8.9 Hz, 2x1H), 7.80 (d, *J* = 8.9 Hz, 2x1H), 3.94 (s, 2H) ppm.

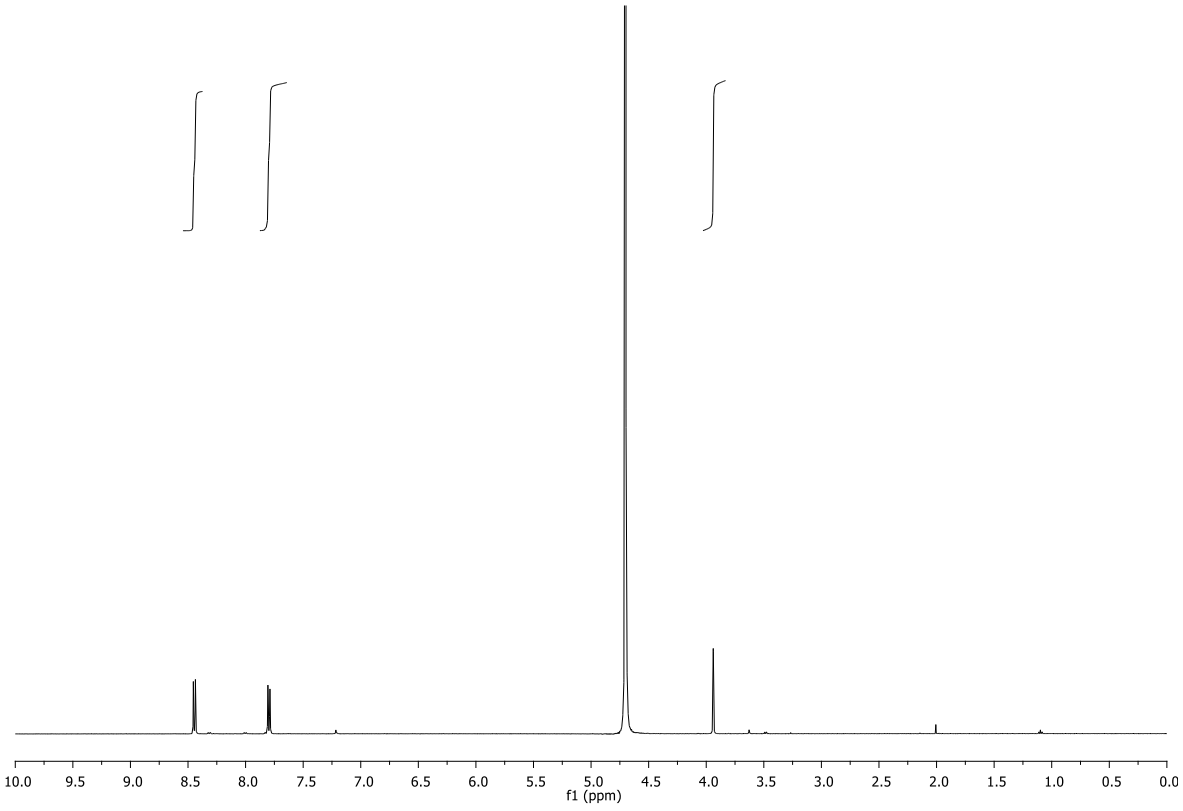

Figure 107. ^{1}H NMR spectrum (500 MHz, $CDCl_3$-d_1) of 24.

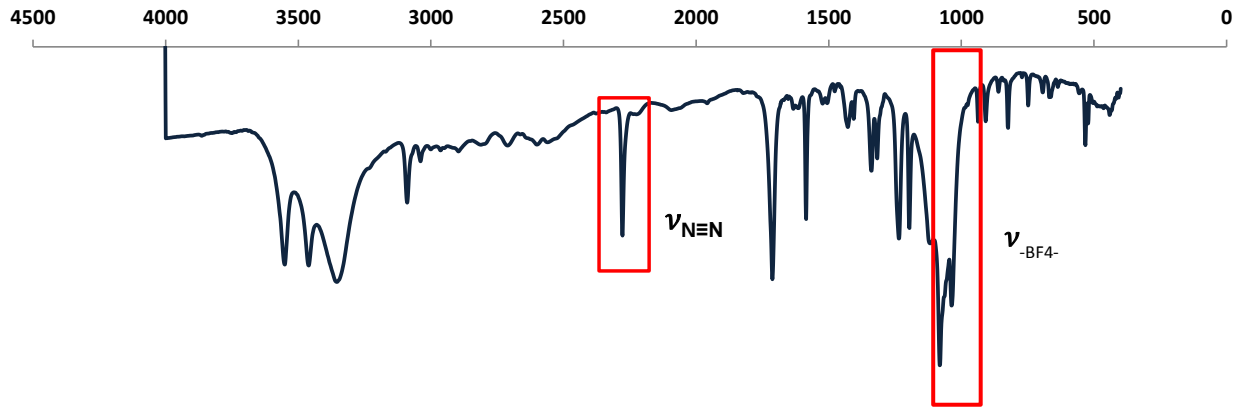

Figure 108. IR spectrum of 24.

3.2.4. Systhesis of 4-(carboxymethyl)benzenediazonium tetrafluoroborate (21)*:*

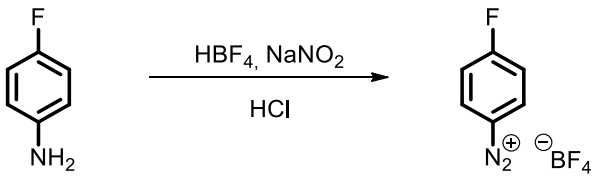

30 **21**

A mix of 4-fluoroaniline (**30**, 2,76 g, 0.025 mol) in HCl (35 wt%, 7.5 mL) and cooled to 0ºC. A solution of $NaNO_2$ (2.07 g) in H_2O (6 mL) was slowly added while stirring for one hour at 0ºC. HBF_4 (48wt%, 7.5 mL) was added and after two hours a white precipitated was isolated by filtration and washed with cold diethylether to obtain fluorobenzenediazonium tetrafluoroborate (**21**, 3.50 g, 16.7 mmol, 67%) as a yellow solid. ^{1}H NMR (500 MHz, DMSO) δ 8.82 (dd, *J* = 9.2, 4.5 Hz, 2H), 7.90 (m, 2H) ppm.

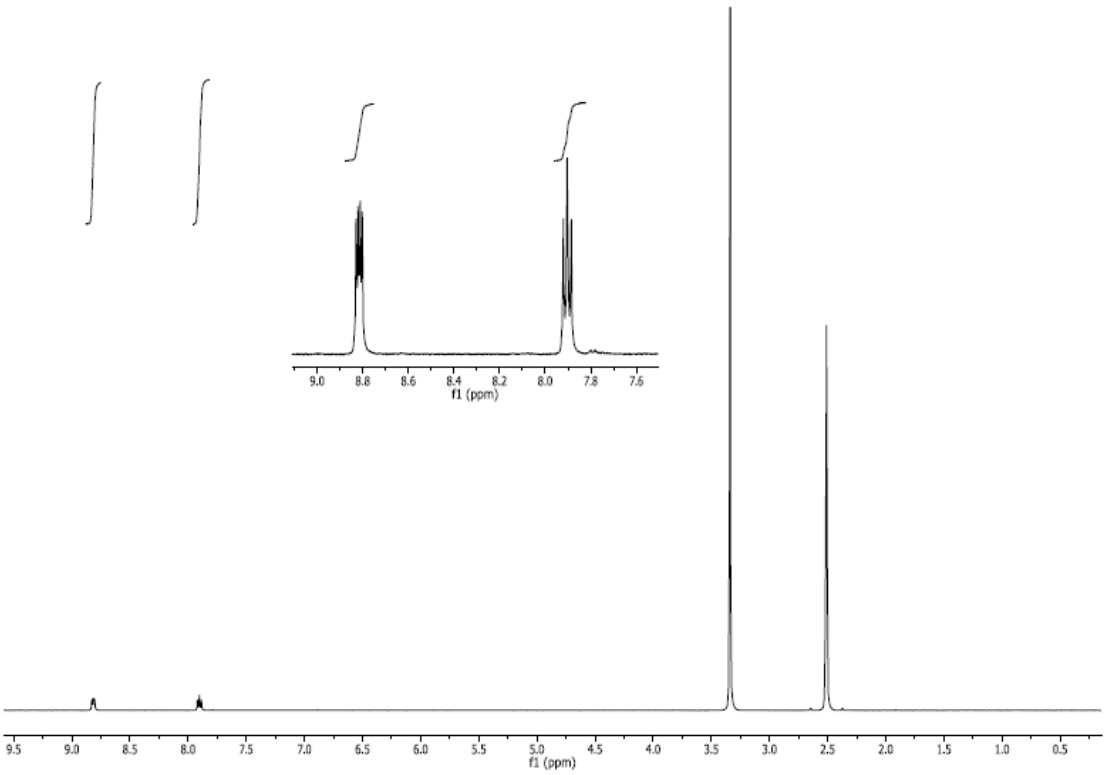

Figure 109. ^{1}H NMR spectrum (500 MHz, DMSO-d_6) of 21.

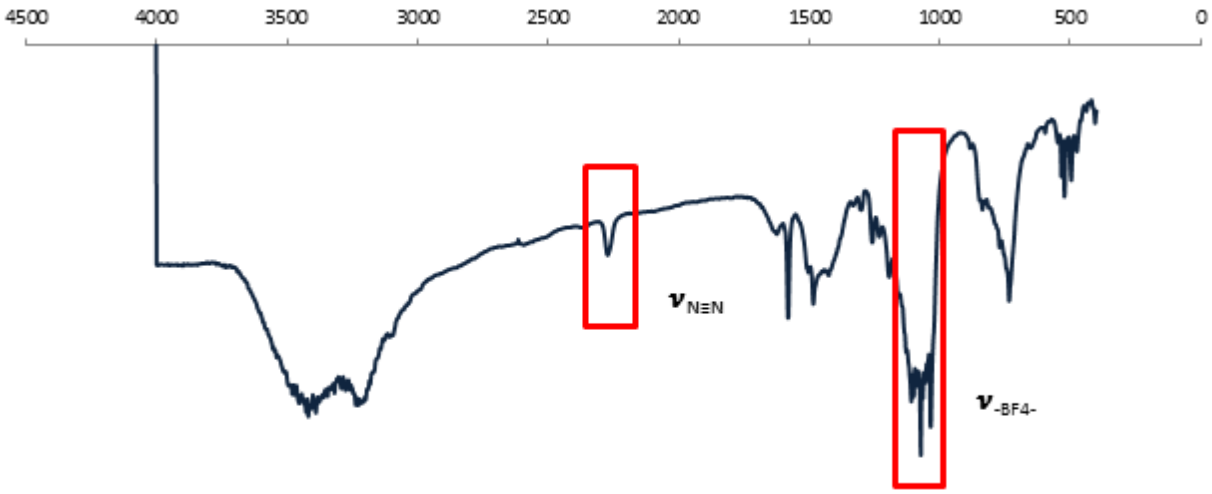

Figure 110. IR spectrum of 21.

3.3. Cleaning protocol

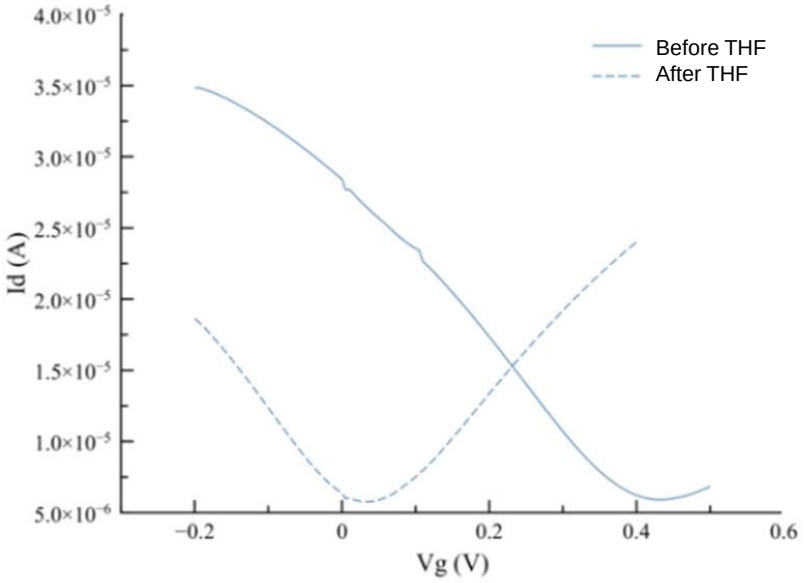

Figure 55. THF treated SiO_2/MGFET *I-V* curve.

3.3.1. *Cleaning protocol of SiO_2/MGFET with EtOH for 10 min:*

The SiO_2/MGFET was cleaned by immersion in a glass beaker with 50 mL of EtOH for 10 minutes. After the corresponding time, the substrate was taken from the solvent and dived 3 times x1 second in distilled water and dried with nitrogen. **Δ RMS roughness:** -0.37 nm**, Δ atom % (O-C=O):** -2.56.

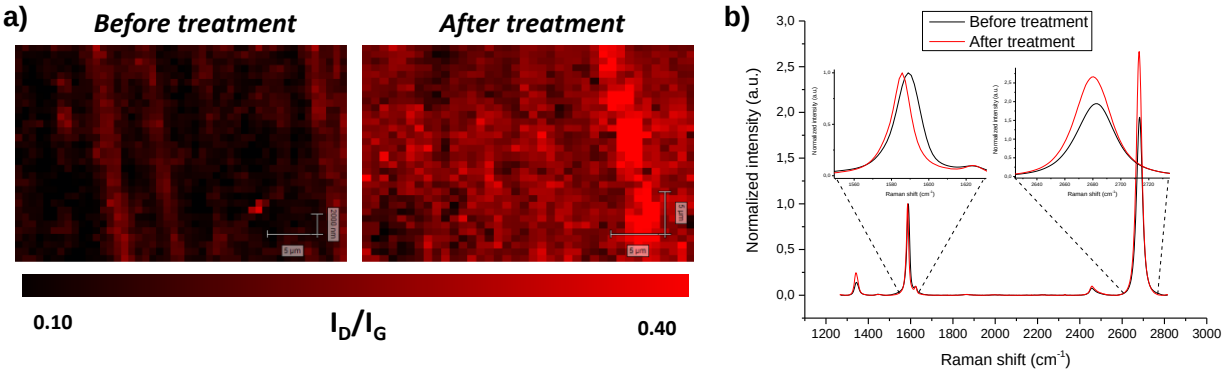

Figure 112. a) Raman mapping of the D band intensity in 30x25 μm² area and b) averaged Raman spectra (≈1000 single-point spectra, λ_{exc} = 532nm) before and after cleaning process of SiO_2/MGFET with EtOH 10 min.

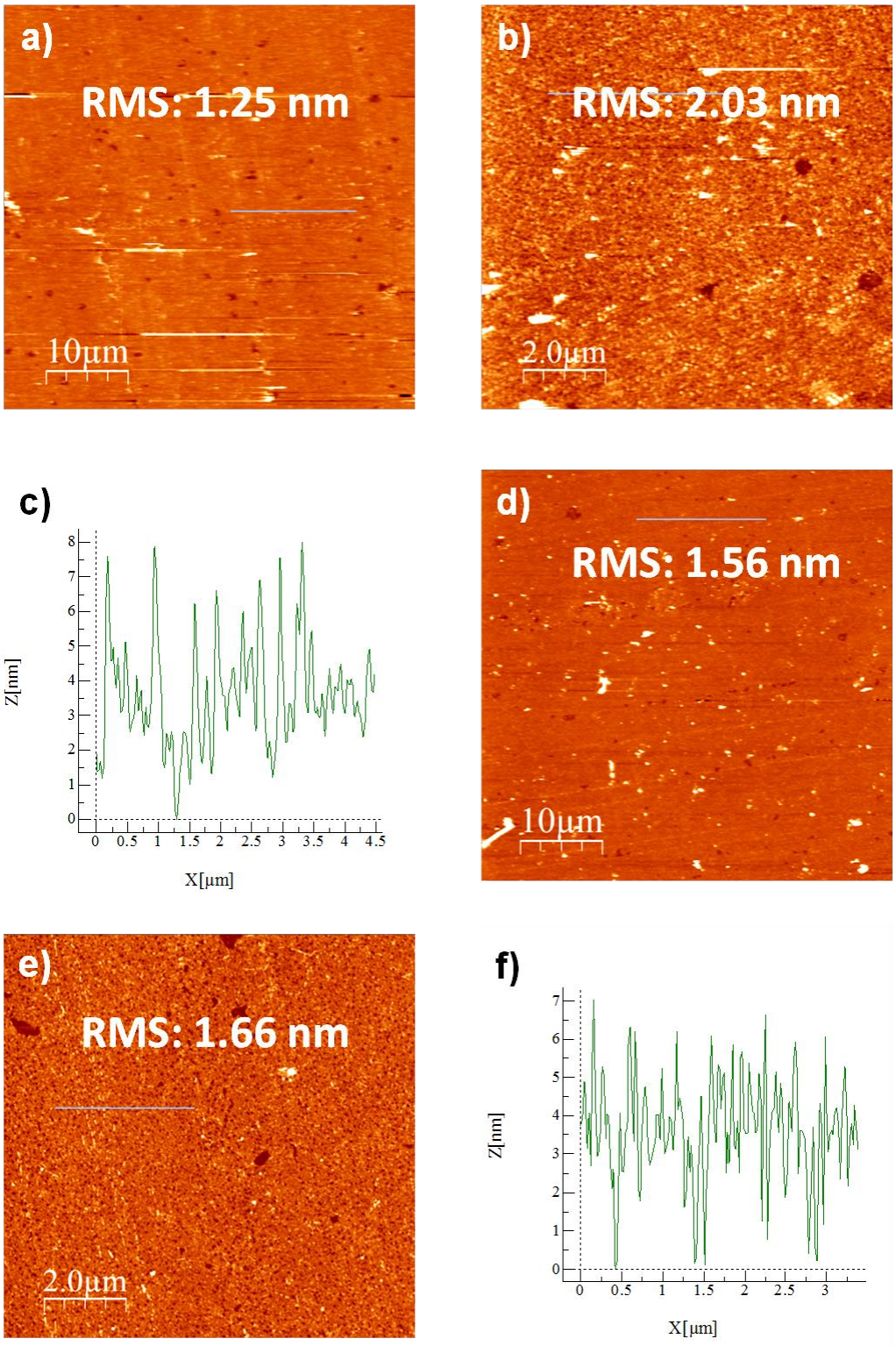

Figure 113. AFM images of SiO_2/MGFET a, b) before and d, e) after cleaning process with EtOH 10 min at different magnifications. AFM height profiles c) before and f) after cleaning process with EtOH 10 min (blue lines in b and e images respectively).

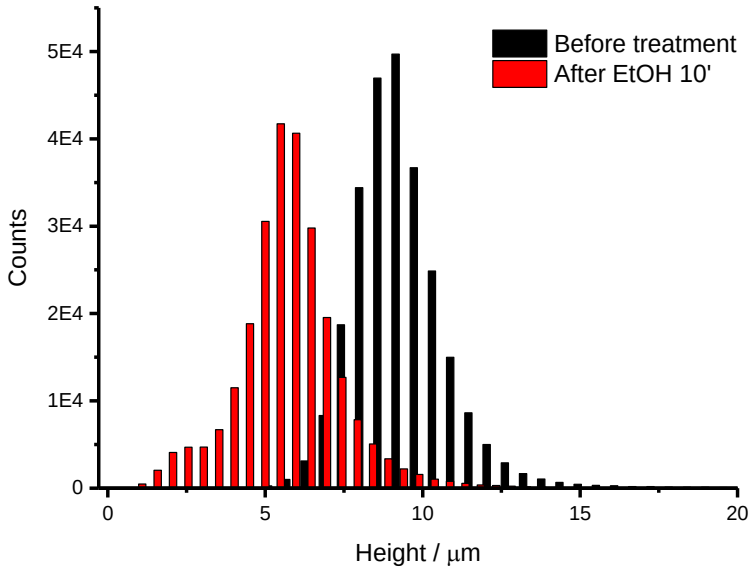

Figure 114. Histogram obtained from the AFM images for SiO_2/MGFET before and after treatment with EtOH 10 min.

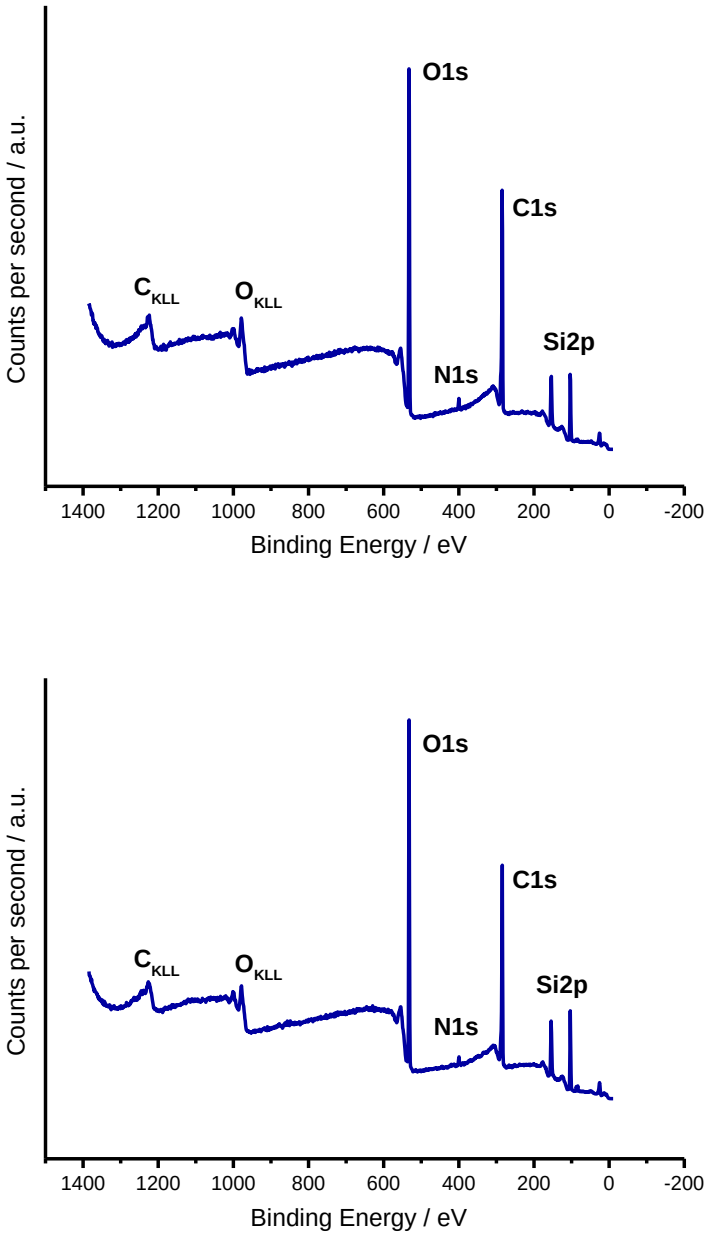

Figure115. Survey XPS spectra of SiO_2/MGFET before (top) and after (bottom) cleaning process with EtOH 10 min.

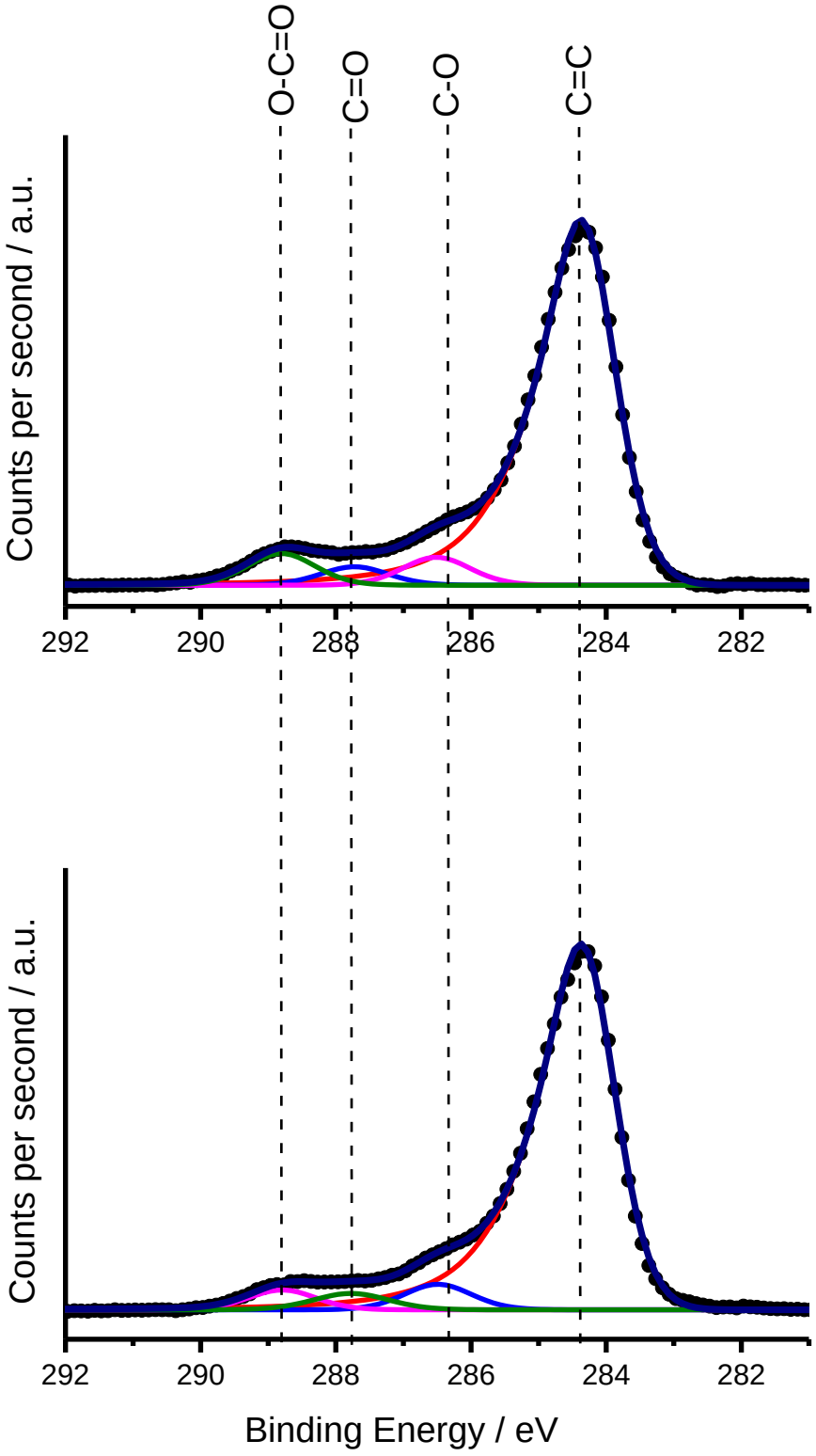

Figure 116. Deconvoluted C1s core level spectra of SiO_2/MGFET (top) before and (bottom) after cleaning process with EtOH 10 min.

Table 11. C/O/Si atomic percentages before and after the solvent treatment with EtOH 10 min.

Treatment (Solvent/time)	Before			After			Δ (before-after)		
	C/at%	**O/at%**	**Si/at%**	**C/at%**	**O/at%**	**Si/at%**	**C/at%**	**O/at%**	**Si/at%**
EtOH/10 min	54.85	27.61	17.54	50.59	28.18	21.24	4.36	-0.57	-3.7

Table 12. Atomic percentages of the C1s component and AFM roughness before and after cleaning process of SiO_2/MGFET with EtOH 10 min.

Treatment (Solvent/time)	BEFORE				AFTER				Δ (before-after)		
	XPS analysis			AFM roughness (nm)	XPS analysis			AFM Roughness (nm)	C1s component	Δ atom percentage	Δ Roughness (nm)
	C1s component	Position / eV	Atomic / %		C1s component	Position / eV	Atomic /%				
EtOH/10 min	*C=C*	284.37	82.23	2.03	*C=C*	284.37	85.08	1.66	*C=C*	**-2.85**	**0.37**
	C-O	286.51	6.36		*C-O*	286.49	5.99		*C-O*	0.37	
	C=O	287.73	4.20		*C=O*	287.78	4.27		*C=O*	-0.07	
	O-C=O	288.81	7.22		*O-C=O*	288.79	4.66		*O-C=O*	**2.56**	
	*Pi-pi**	-	-		*Pi-pi**	-	-		*Pi-pi**	-	

3.3.2. *Cleaning protocol of SiO_2/MGFET with EtOH for 120 min:*

The SiO_2/MGFET was cleaned by immersion in a glass beaker with 50 mL of EtOH for 120 minutes. After the corresponding time, the substrate was taken from the solvent and dived 3 times x1 second in distilled water and dried with nitrogen. **Δ RMS roughness:** -1.89 nm**, Δ atom % (O-C=O):** -2.61.

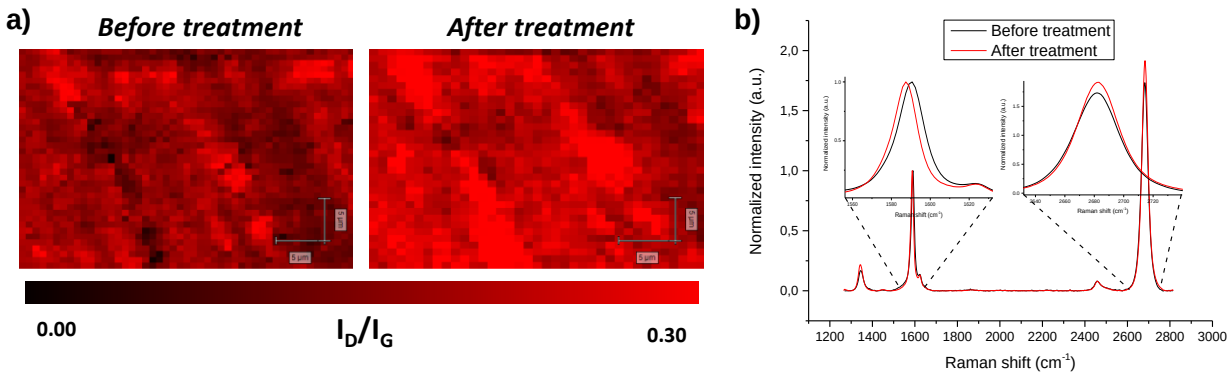

Figure 117. a) Raman mapping of the D band intensity in 30x25 μm² area and b) averaged Raman spectra (≈1000 single-point spectra, λ_{exc} = 532nm) before and after cleaning process of SiO_2/MGFET with EtOH 120 min.

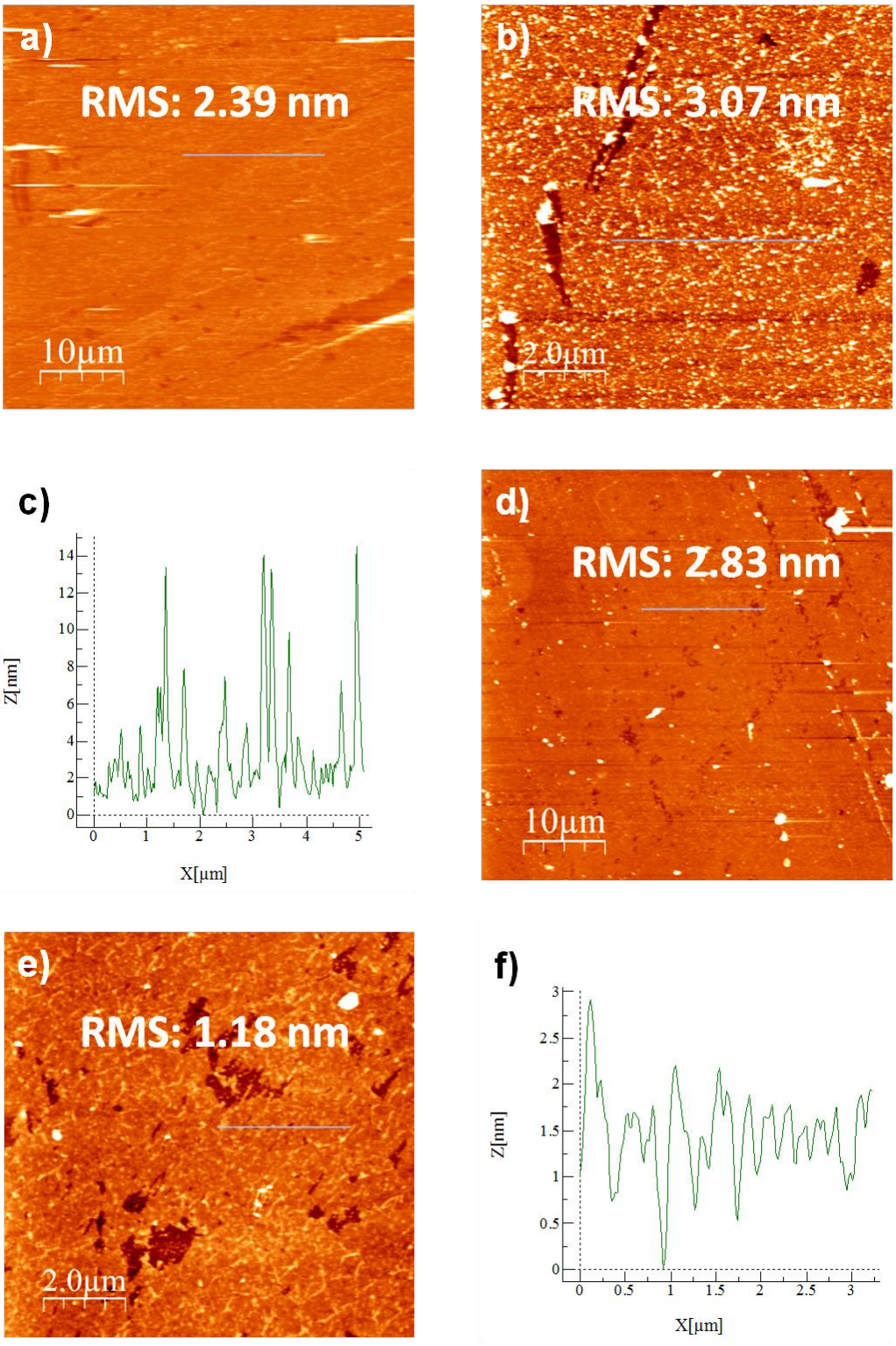

Figure 118. AFM images of SiO_2/MGFET a, b) before and d, e) after cleaning process with EtOH 120 min at different magnifications. AFM height profiles c) before and f) after cleaning process with EtOH 120 min (blue lines in b and e images respectively).

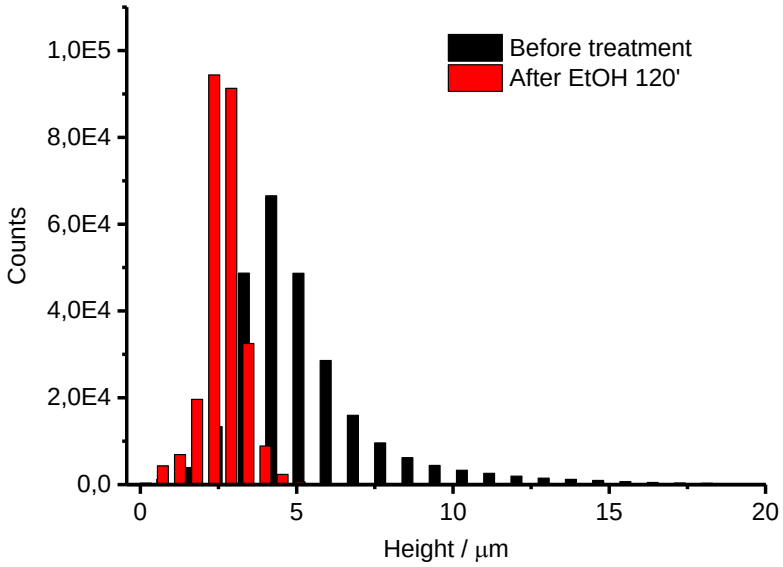

Figure 119. Histogram obtained from the AFM images for SiO_2/MGFET before and after treatment with EtOH 120 min.

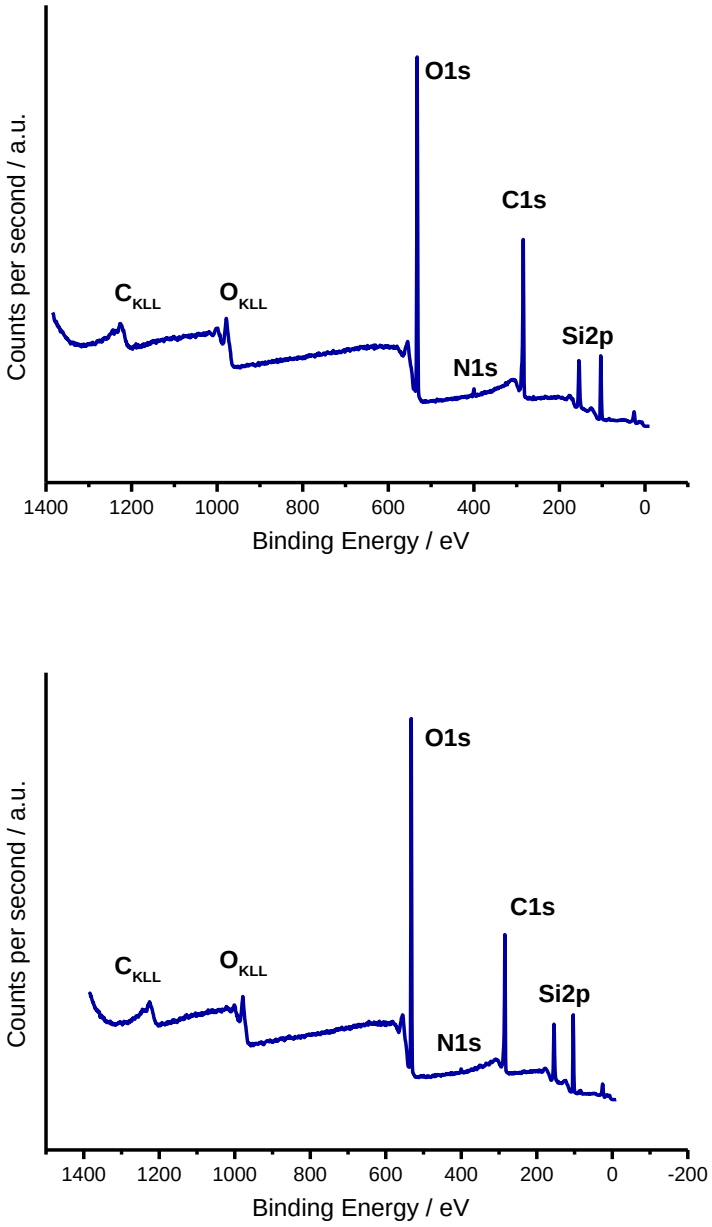

Figure 120. Survey XPS spectra of SiO_2/MGFET before (top) and after (bottom) cleaning process with EtOH 120 min.

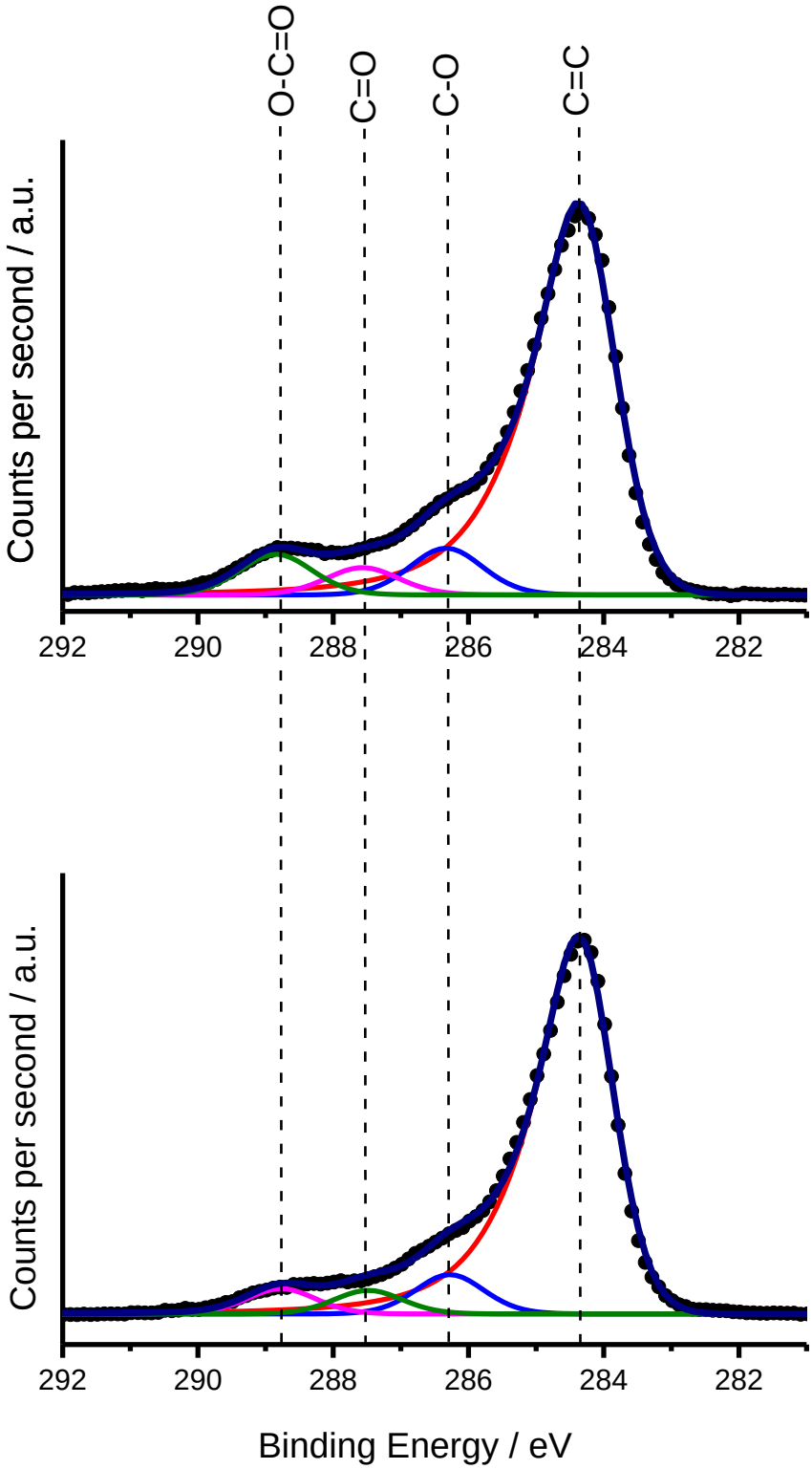

Figure 121. Deconvoluted C1s core level spectra of SiO_2/MGFET (top) before and (bottom) after cleaning process with EtOH 120 min.

Table 13. C/O/Si atomic percentages before and after the solvent treatment with EtOH 120 min.

Treatment (Solvent/time)	Before			After			Δ (before-after)		
	C/at%	**O/at%**	**Si/at%**	**C/at%**	**O/at%**	**Si/at%**	**C/at%**	**O/at%**	**Si/at%**
EtOH/120 min	49.13	30.87	20.00	42.83	32.44	24.73	6.30	-1.57	-4.73

Table 14. Atomic percentages of the C1s component and AFM roughness before and after cleaning process of SiO_2/MGFET with EtOH 120 min.

Treatment (Solvent/time)	BEFORE				AFTER				Δ (before-after)		
	XPS analysis			AFM roughness (nm)	XPS analysis			AFM Roughness (nm)	C1s component	Δ atom percentage	Δ Roughness (nm)
	C1s component	Position / eV	Atomic / %		C1s component	Position / eV	Atomic /%				
EtOH/120 min	*C=C*	284.37	77.21	3.07	*C=C*	284.37	80.93	1.18	*C=C*	**-3.72**	**1.89**
	C-O	286.33	9.29		*C-O*	286.28	8.51		*C-O*	0.78	
	C=O	287.57	5.42		*C=O*	287.48	5.09		*C=O*	0.33	
	O-C=O	288.85	8.08		*O-C=O*	288.77	5.47		*O-C=O*	**2.61**	
	*Pi-pi**	-	-		*Pi-pi**	-	-		*Pi-pi**	-	

3.3.3. *Cleaning protocol of SiO_2/MGFET with THF for 10 min:*

The SiO_2/MGFET was cleaned by immersion in a glass beaker with 50 mL of THF for 10 minutes. After the corresponding time, the substrate was taken from the solvent and dived 3 times x1 second in distilled water and dried with nitrogen. **Δ RMS roughness:** -0.80 nm**, Δ atom % (O-C=O):** -0.68.

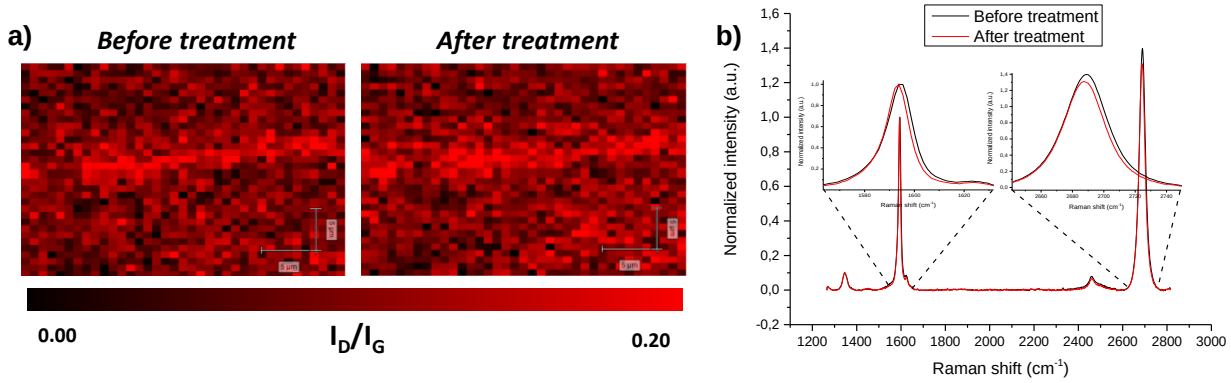

Figure 122. a) Raman mapping of the D band intensity in 30x25 μm² area and b) averaged Raman spectra (≈1000 single-point spectra, λ_{exc} = 532nm) before and after cleaning process of SiO_2/MGFET with THF 10 min.

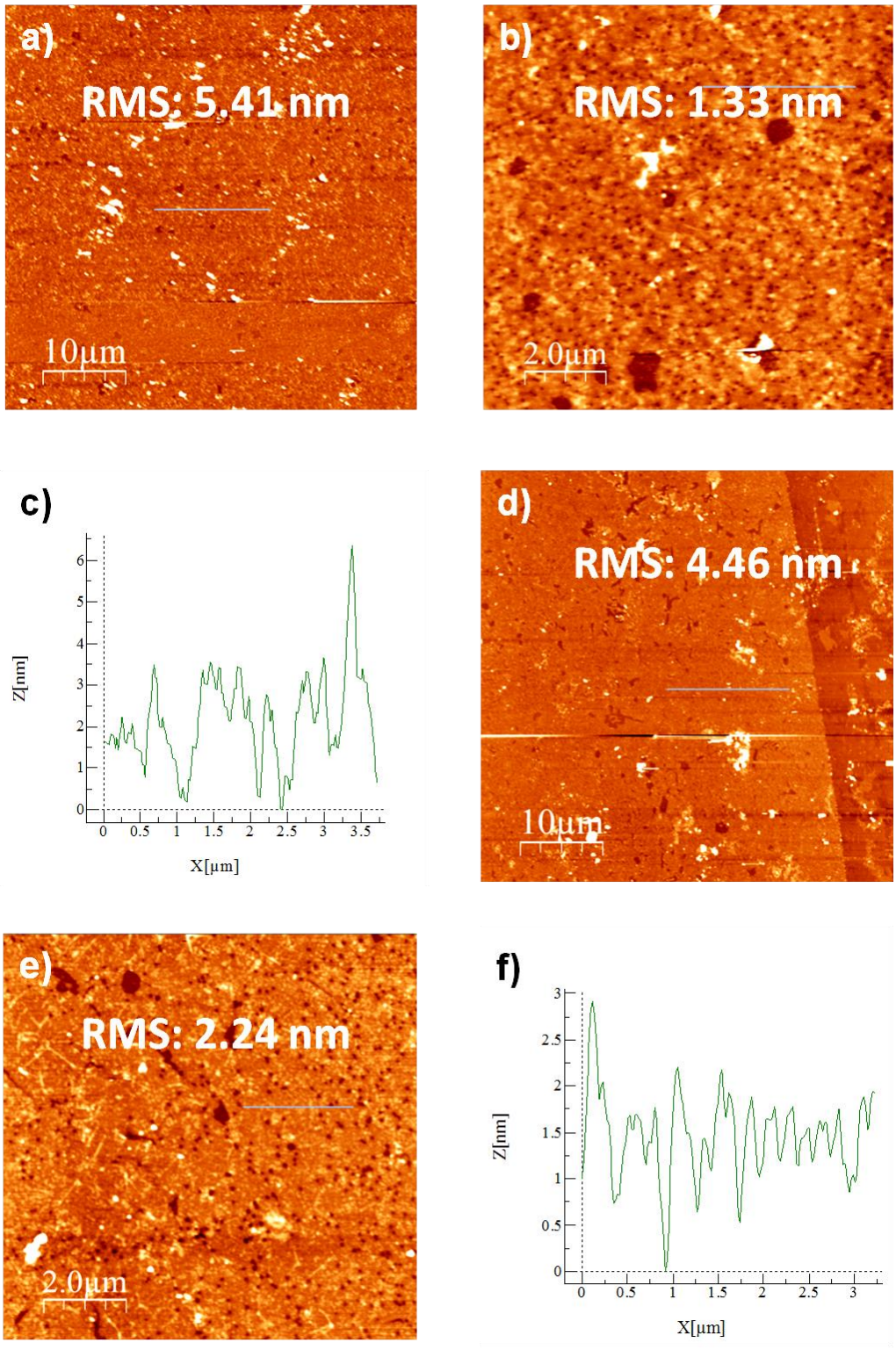

Figure 123. AFM images of SiO_2/MGFET a, b) before and d, e) after cleaning process with THF 10 min at different magnifications. AFM height profiles c) before and f) after cleaning process with THF 10 min (blue lines in b and e images, respectively).

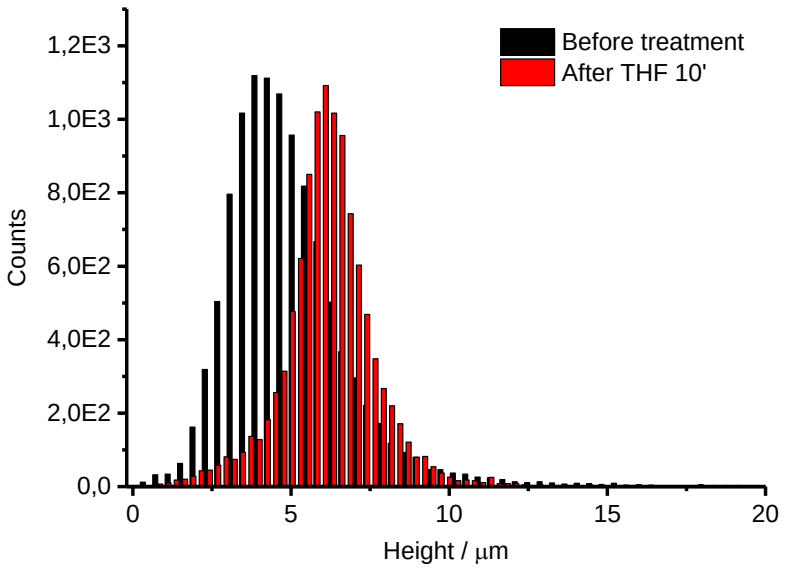

Figure 124. Histogram obtained from the AFM images for SiO_2/MGFET before and after treatment with THF 10 min.

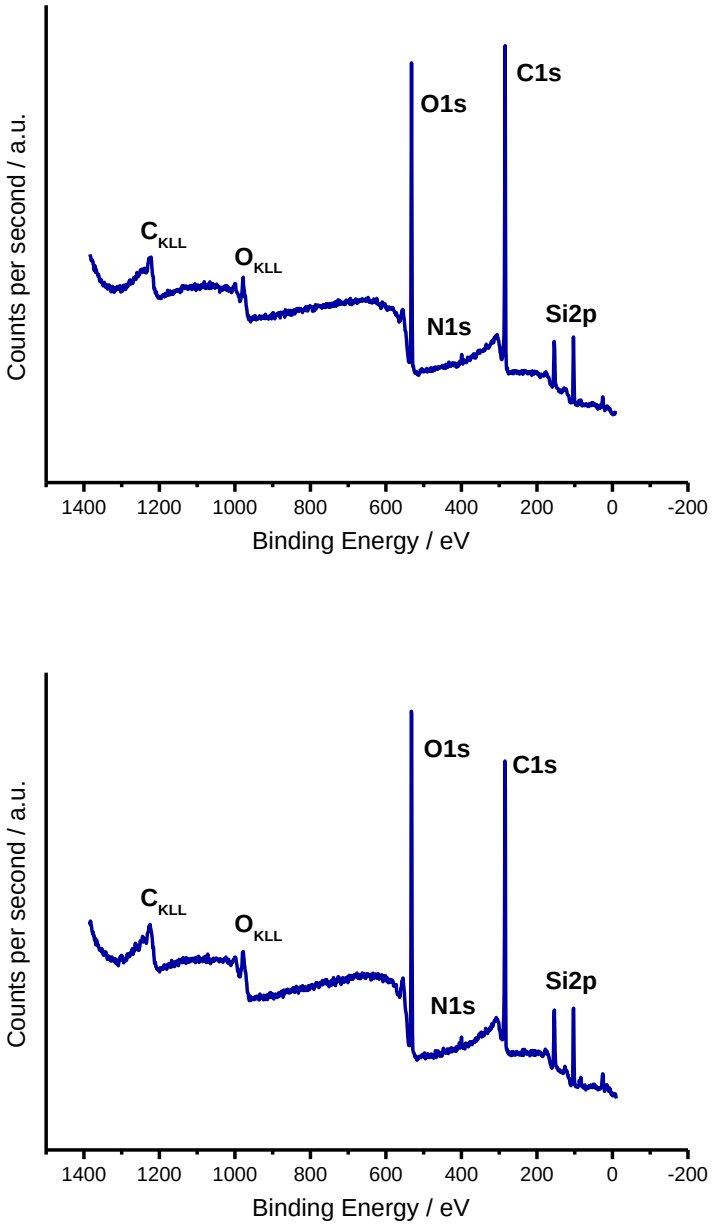

Figure 125. Survey XPS spectra of SiO_2/MGFET before (top) and after (bottom) cleaning process with THF 10 min.

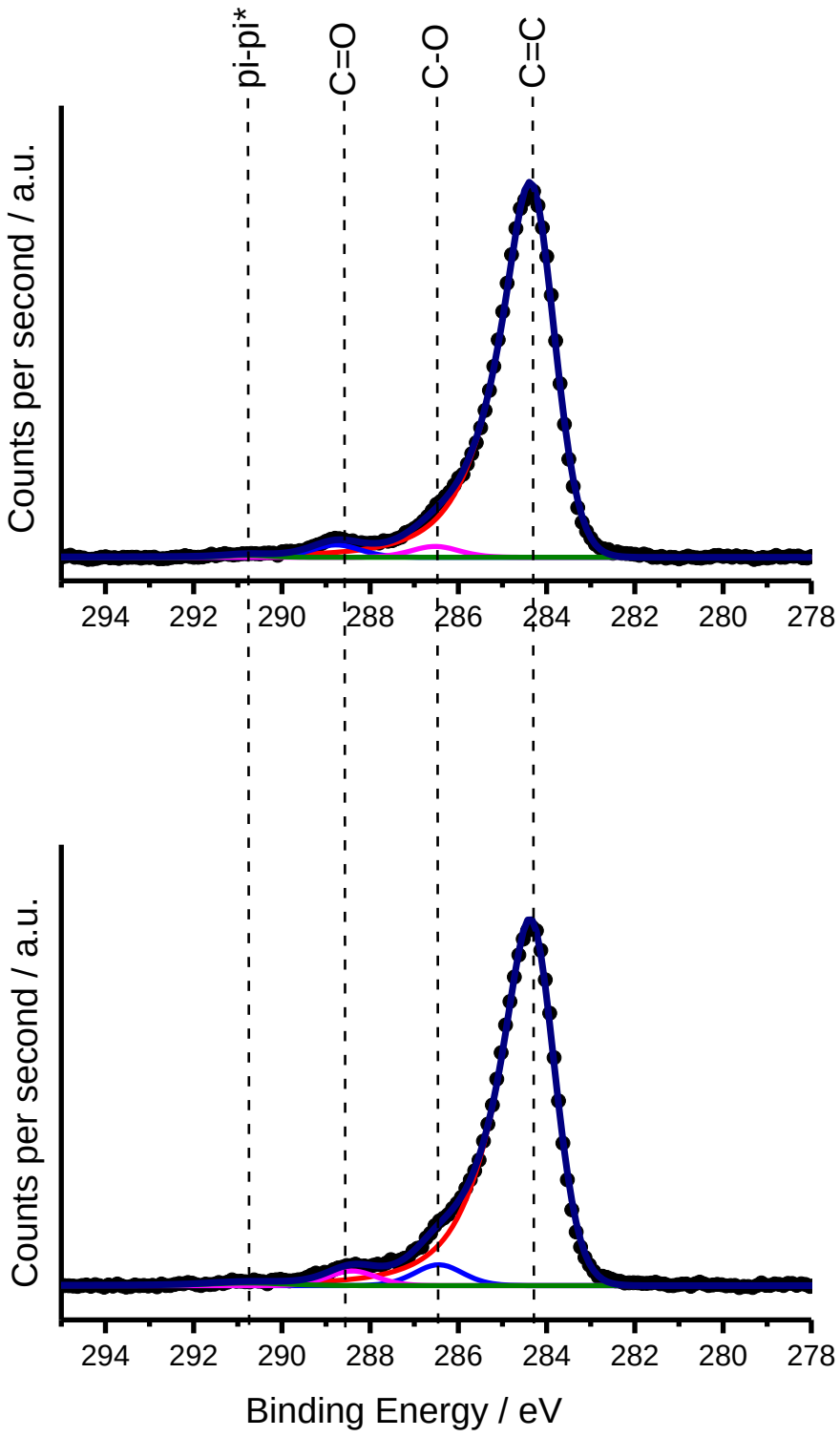

Figure 126. Deconvoluted C1s core level spectra of SiO_2/MGFET (top) before and (bottom) after cleaning process with THF 10 min.

Table 15. C/O/Si atomic percentages before and after the solvent treatment with THF 10 min.

Treatment (Solvent/time)	Before			After			Δ (before-after)		
	C/at%	**O/at%**	**Si/at%**	**C/at%**	**O/at%**	**Si/at%**	**C/at%**	**O/at%**	**Si/at%**
THF/10 min	64.34	19.84	15.83	60.85	22.23	16.92	3.49	-2.39	-1.09

Table 16. Atomic percentages of the C1s component and AFM roughness before and after cleaning process of SiO_2/MGFET with THF 10 min.

Treatment (Solvent/time)	BEFORE				AFTER				Δ (before-after)		
	XPS analysis			AFM roughness (nm)	XPS analysis			AFM Roughness (nm)	C1s component	Δ atom percentage	Δ Roughness (nm)
	C1s component	Position / eV	Atomic / %		C1s component	Position / eV	Atomic /%				
THF/10 min	*C=C*	284.37	86.21	2.44	*C=C*	284.37	94.55	1.64	*C=C*	-8.34	0.8
	C-O	286.60	5.27		*C-O*	286.90	0.75		*C-O*	4.52	
	C=O	287.92	3.14		*C=O*	-	-		*C=O*	3.14	
	O-C=O	288.87	5.38		*O-C=O*	288.68	4.70		*O-C=O*	0.68	
	*Pi-pi**	-	-		*Pi-pi**	-	-		*Pi-pi**	-	

3.3.4. *Cleaning protocol of SiO_2/MGFET with THF for 120 min:*

The SiO_2/MGFET was cleaned by immersion in a glass beaker with 50 mL of THF for 120 minutes. After the corresponding time, the substrate was taken from the solvent and dived 3 times x1 second in distilled water and dried with nitrogen. **Δ RMS roughness:** -0.77 nm**, Δ atom % (O-C=O):** -1.02.

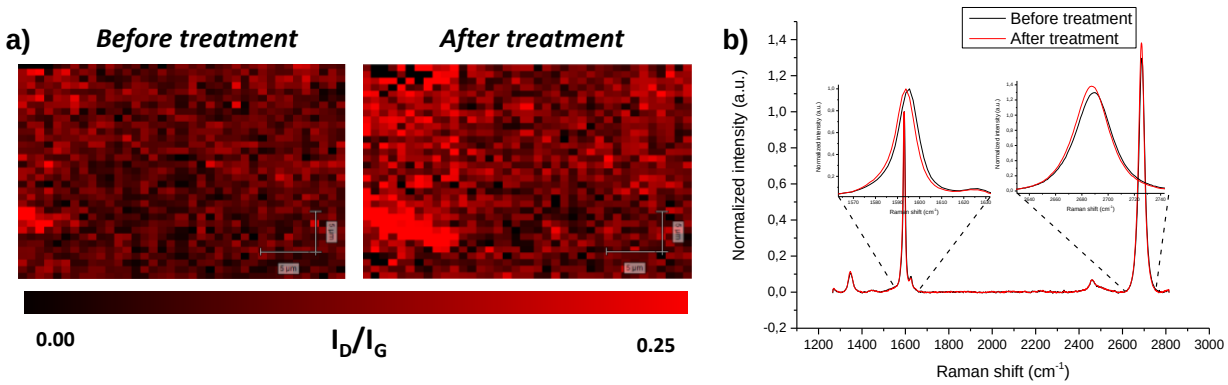

Figure 127. a) Raman mapping of the D band intensity in 30x25 μm² area and b) averaged Raman spectra (≈1000 single-point spectra, λ_{exc} = 532nm) before and after cleaning process of SiO_2/MGFET with THF 120 min.

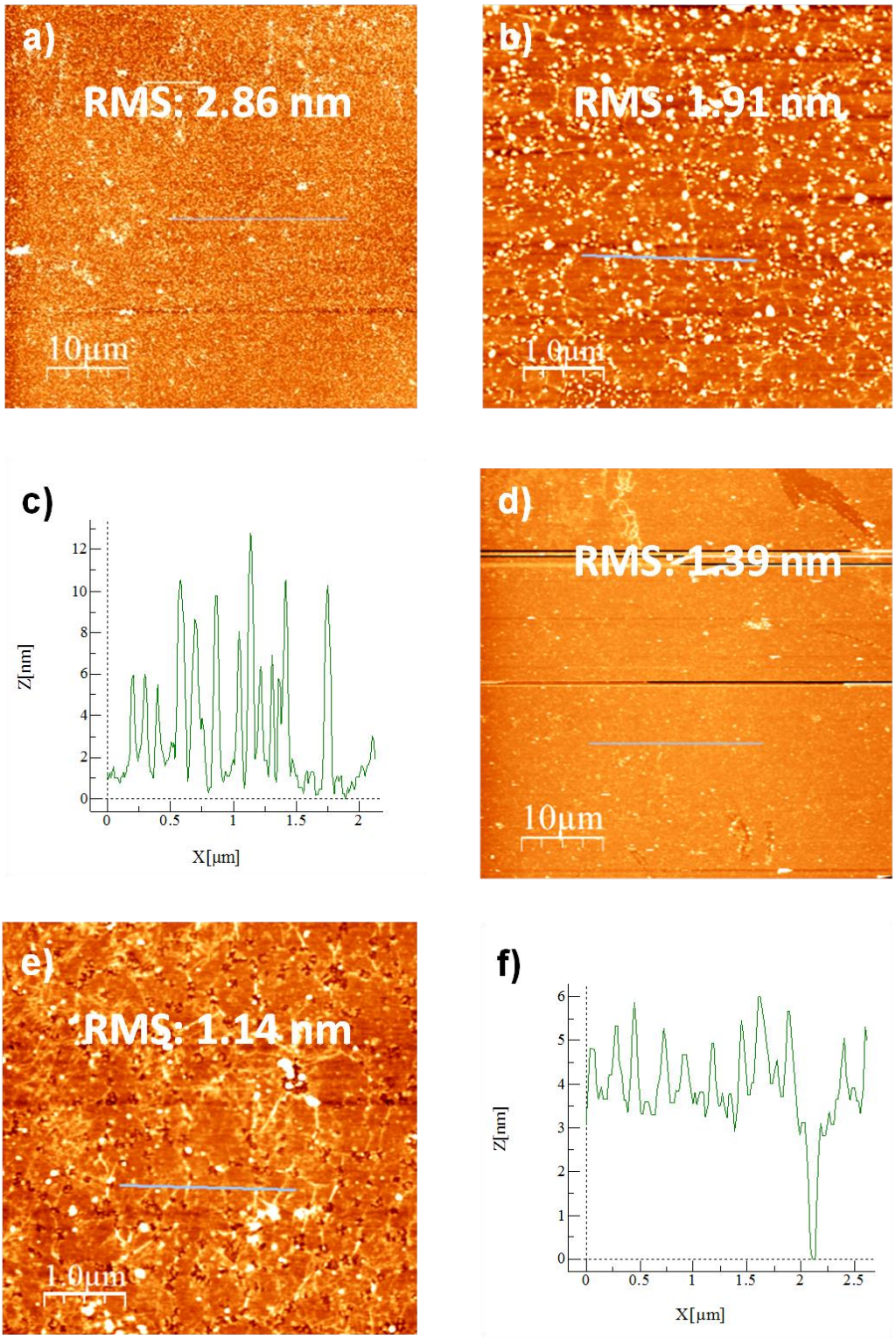

Figure 128. AFM images of SiO_2/MGFET a, b) before and d, e) after cleaning process with THF 120 min at different magnifications. AFM height profiles c) before and f) after cleaning process with THF 120 (blue lines in b and e images respectively).

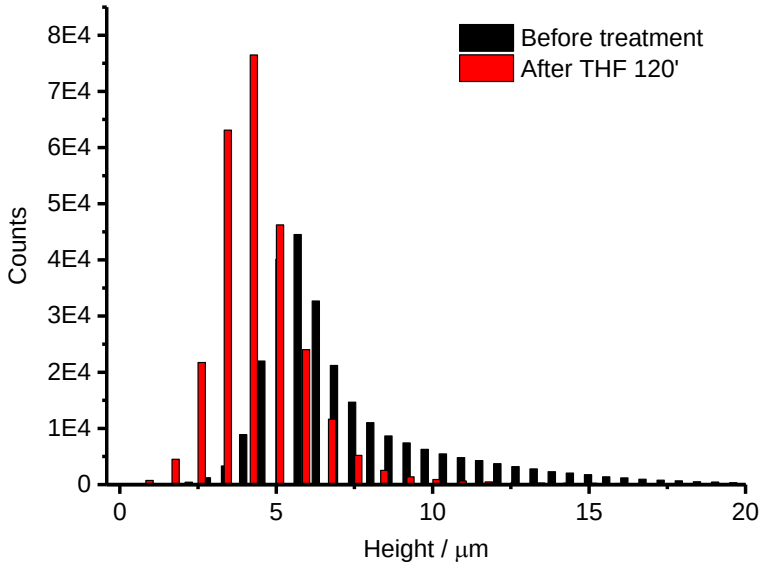

Figure 129. Histogram obtained from the AFM images for SiO_2/MGFET before and after treatment with THF 120 min.

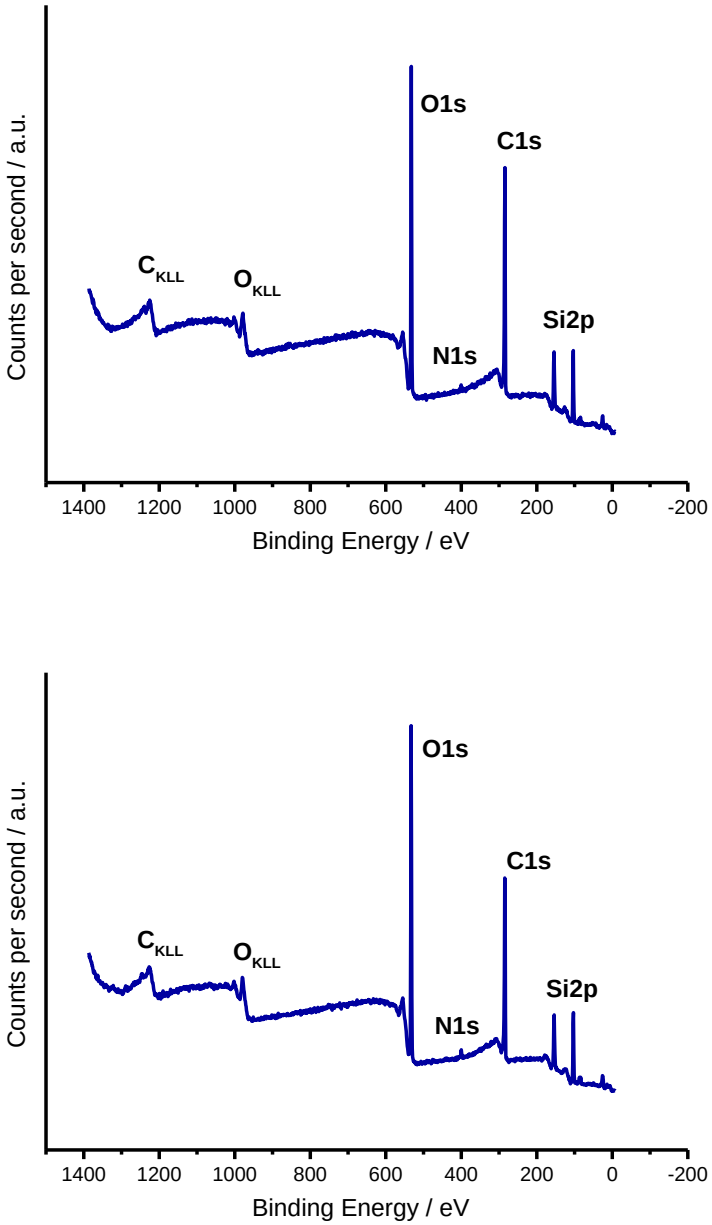

Figure 130. Survey spectra of SiO_2/MGFET before (top) and after (bottom) cleaning process with THF 120 min.

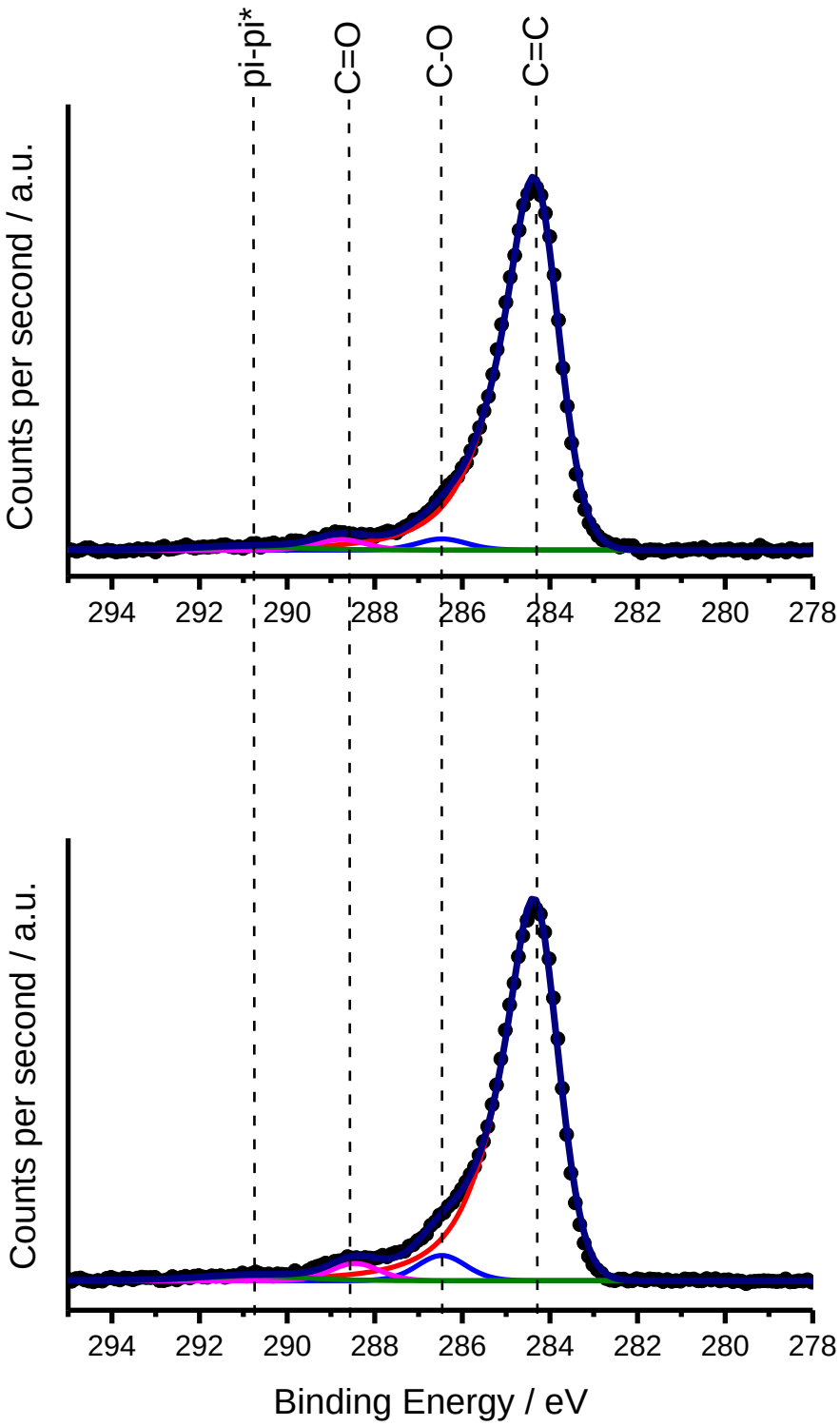

Figure 131. Deconvoluted C1s core level spectra of SiO_2/MGFET (top) before and (bottom) after cleaning process with THF 120 min.

Table 17. C/O/Si atomic percentages before and after the solvent treatment with THF 120 min.

Treatment (Solvent/time)	Before			After			Δ (before-after)		
	C/at%	**O/at%**	**Si/at%**	**C/at%**	**O/at%**	**Si/at%**	**C/at%**	**O/at%**	**Si/at%**
THF 120 min	55.89	24.80	19.31	53.00	26.34	20.66	2.89	-1.54	-1.35

Tabla 18. Atomic percentages of the C1s component and AFM roughness before and after cleaning process of SiO_2/MGFET with THF 120 min.

Treatment (Solvent/time)	BEFORE				AFTER				Δ (before-after)		
	XPS analysis			AFM roughness (nm)	XPS analysis			AFM Roughness (nm)	C1s component	Δ atom percentage	Δ Roughness (nm)
	C1s component	Position / eV	Atomic / %		C1s component	Position / eV	Atomic /%				
	C=C	284.37	88.27		*C=C*	284.37	89.22		*C=C*	-0.95	
	C-O	286.74	5.40		*C-O*	286.66	5.48		*C-O*	-0.08	
THF/120 min	*C=O/O-C=O*	288.70	6.33	1.91	*C=O/O-C=O*		5.31	1.14	*C=O/O-C=O*	1.02	0.77
	O-C=O	-	-		*O-C=O*	-	-		*O-C=O*	-	
	*Pi-pi**	-	-		*Pi-pi**	-	-		*Pi-pi**	-	

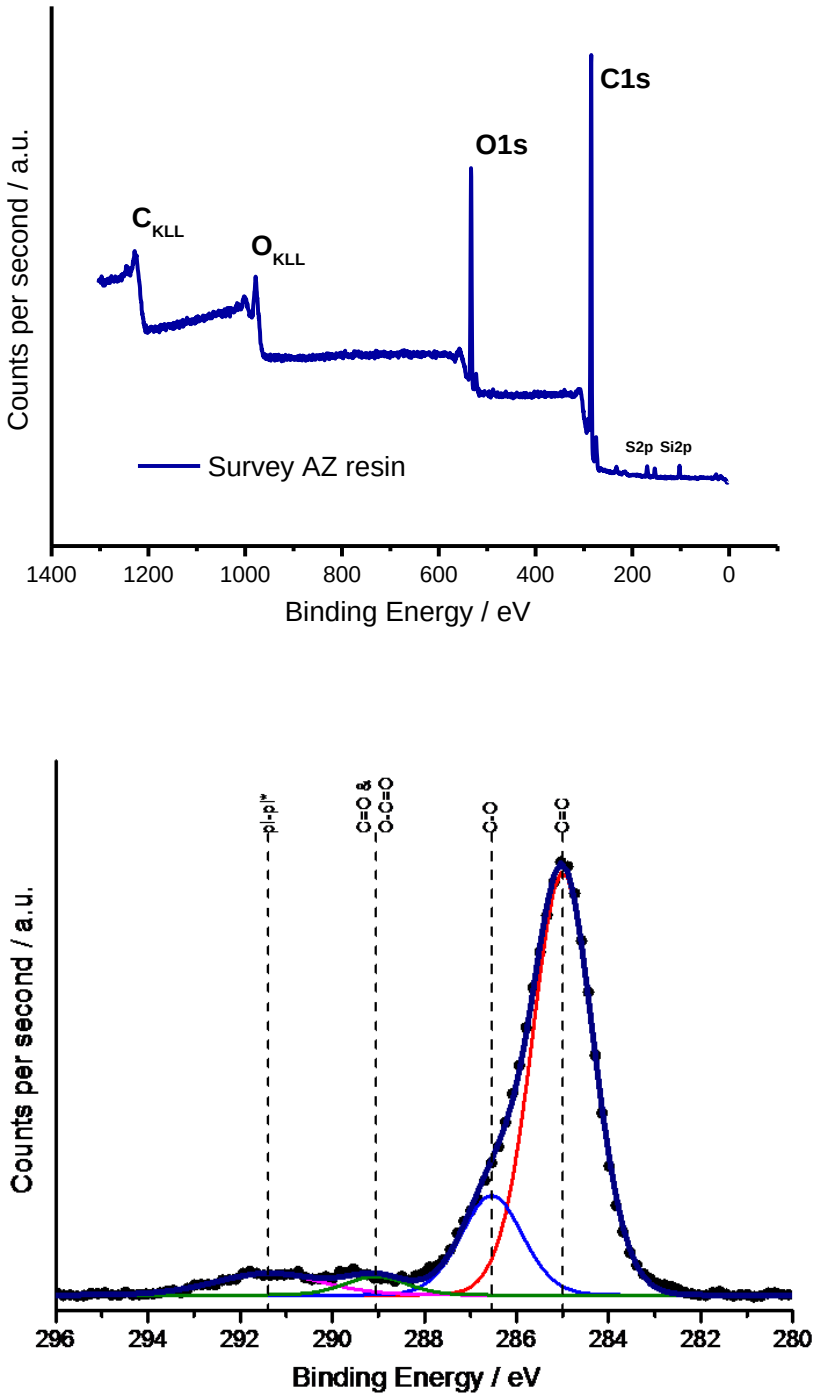

Figure 132. Survey XPS spectrum (top) and Deconvoluted C1s core level spectrum (bottom) of Epoxi resin AZ.

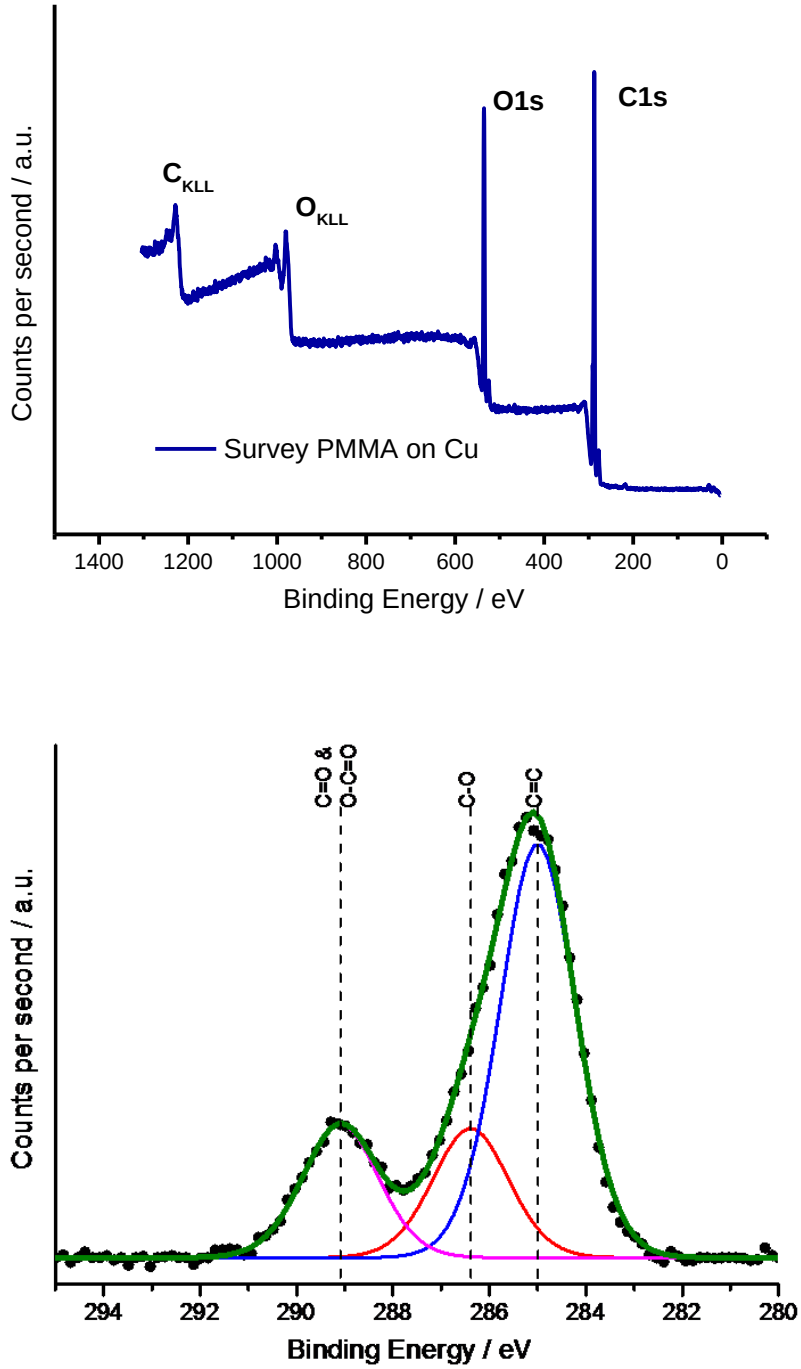

Figure 133. Survey XPS spectrum (top) and Deconvoluted C1s core level spectrum (bottom) of PMMA.

3.3.5. Electronic measurement of the cleaning protocol:

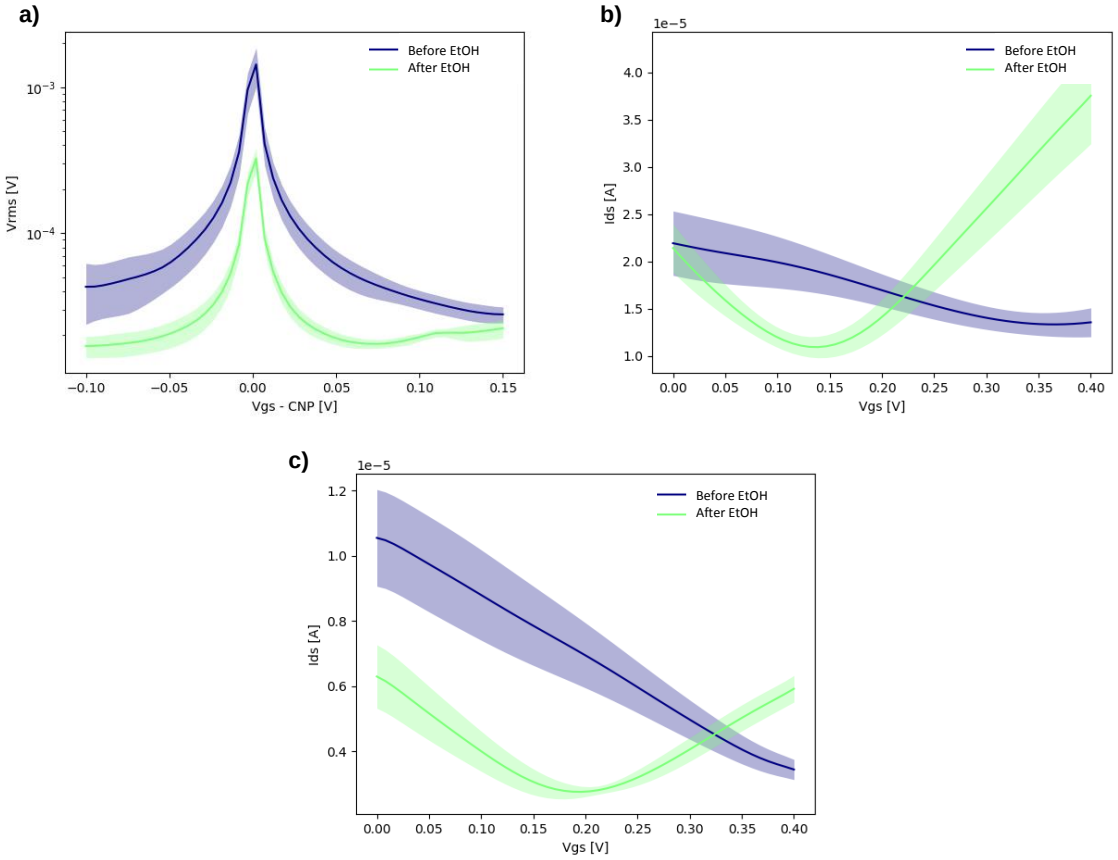

Figure 134. a) *Vrms* and b) *I-V* curve of SiO_2/mGFET before (blue) and after (green) the cleaning process with EtOH for 60 min, and c) *I-V* curve before (blue) and after (green) the cleaning process with EtOH for 10 min.

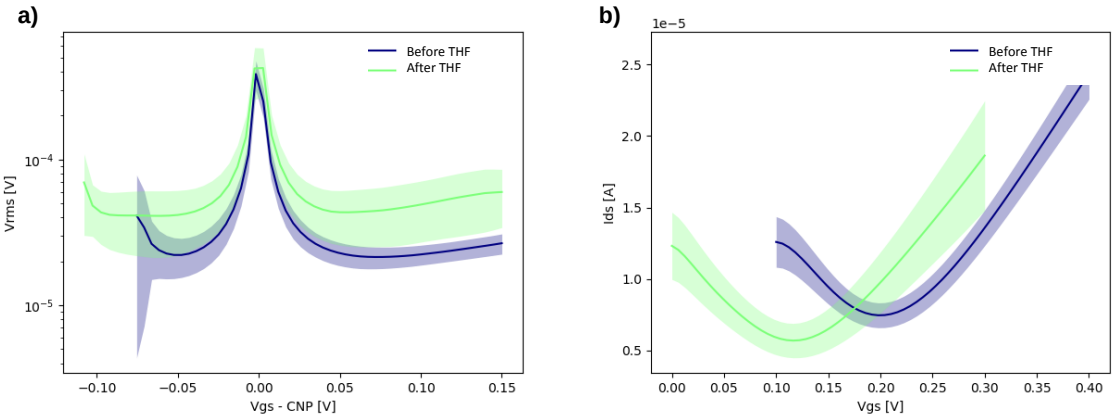

Figure 135. a) *Vrms* and b) *I-V* curve of SiO_2/mGFET before (blue) and after (green) the cleaning process with THF for 120 min.

3.4. Functionalization of CVD Graphene on substrate

3.4.1. CVDG substrate functionalization general method: SiO_2/G-(*p*-(F) Ph)

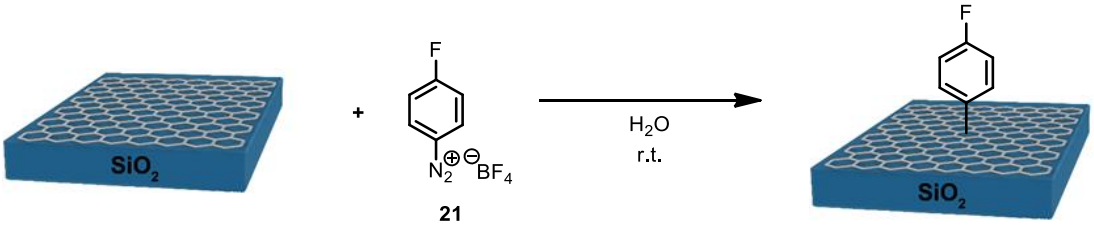

The substrate was fully immersed in a solution of **21** (3.4 mg, 0.016 mmol) in distilled water (10 mL) at r.t. for 2 h. Substrate was taken from the solution reaction and washed by diving 3 times x 1 second in distilled water and dried with nitrogen. **$\Delta(I_D/I_G)$:** 014.

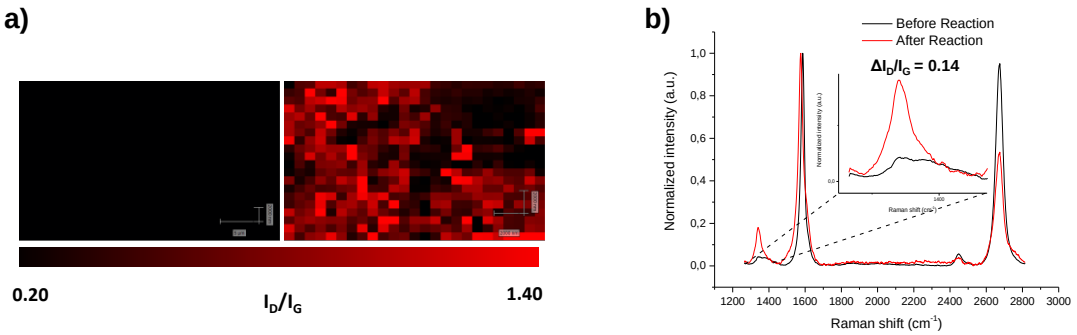

Figure 136. a) Raman mapping of the D band intensity in 30x25 μm² area and b) averaged Raman spectra (≈1000 single-point spectra, λ_{exc} = 532nm) before and after covalent modification of CVDG substrate.

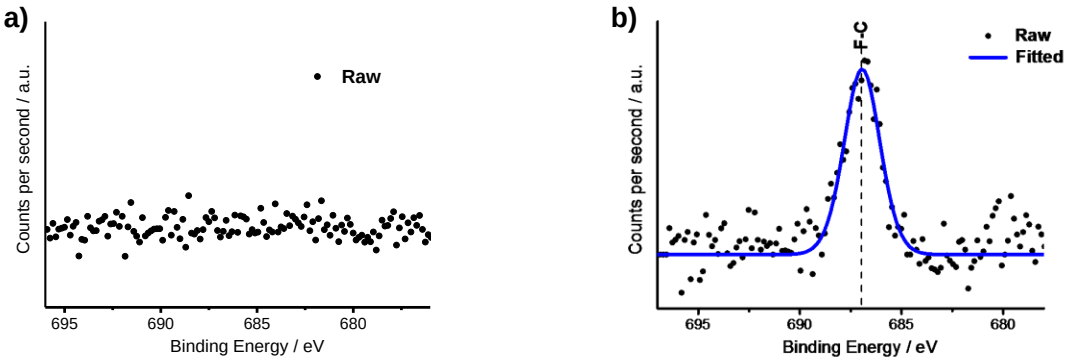

Figure 137. F1s core level in XPS analysis of the reaction regarding the presence of F a) before and b) after reaction.

3.4.2. ***SiO_2/MGFET functionalization general method for thrombin sensing platform*:** SiO_2/MGFET-(*p*-(CH_2CO_2H)Ph).

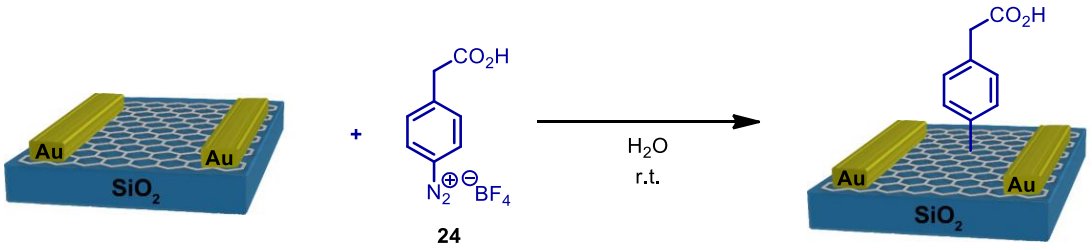

SiO_2/MGFET was placed in a glass beaker with distilled water (10 mL). Then, a solution of 4-(carboxymethyl)benzenediazonium tetrafluoroborate (**24**, 10 mg, 0.04 mmol) in distilled water (2 mL) was added. After 1 h reaction at r.t. the SiO_2/MGFET was taken from the solution reaction and washed by diving 3 times x 1 second in distilled water and dried with nitrogen. **$\Delta(I_D/I_G)$:** 0.31.

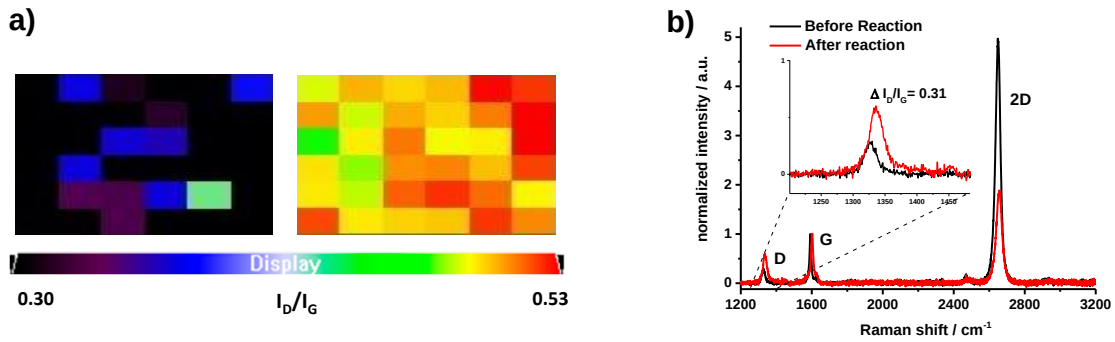

Figure 138. a) Raman mapping of the D band intensity in 20x20 μm^2 area and b) averaged Raman spectra (λ_{exc} = 532nm) before and after covalent modification of SiO_2/MGFET.

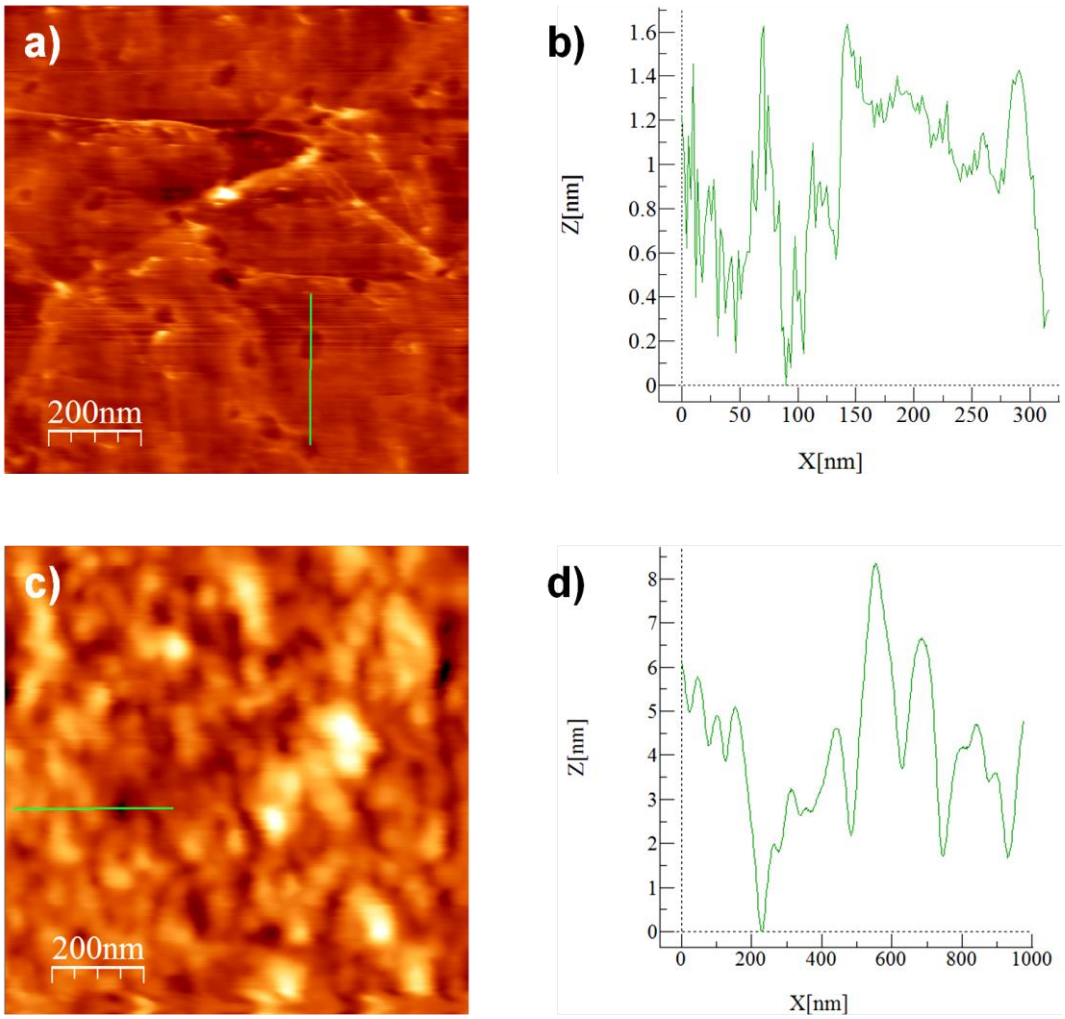

Figure 139. a)AFM images of SiO_2/MGFET before and c) after chemical functionalization. AFM height profiles b) before and d) after chemical modification (green lines in a and c images respectively).

3.4.3. *SiO_2/MGFET functionalization general method for thrombin sensing platform*: SiO_2/MGFET-(3,4-($C_{18}H_{37}O)_2$Ph)

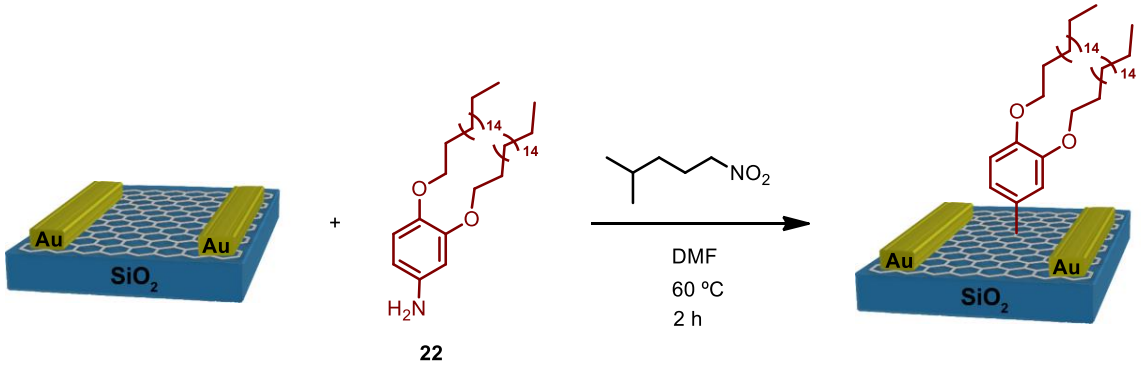

3,4-bis(octadecyloxy)aniline (**22**, 50.4 mg, 0.08 mmol) was placed in a round bottom flask previously purged with argon and dissolved in dry DMF (10mL) under sonication. Then, the SiO_2/MGFET was introduced in the flask and 3-methylbuthylnitrite (16.2 µL, 0.12 mmol) was slowly added dropwise. The reaction mixture was heated to 60 ºC and left without stirring for 2h. The SiO_2/MGFET was taken from the reaction mixture and cleaned by immersion in toluene for 12h and in EtOH for 30'. The modified graphene substrate was dried over a stream of N_2. **$\Delta(I_D/I_G)$:** 0.12.

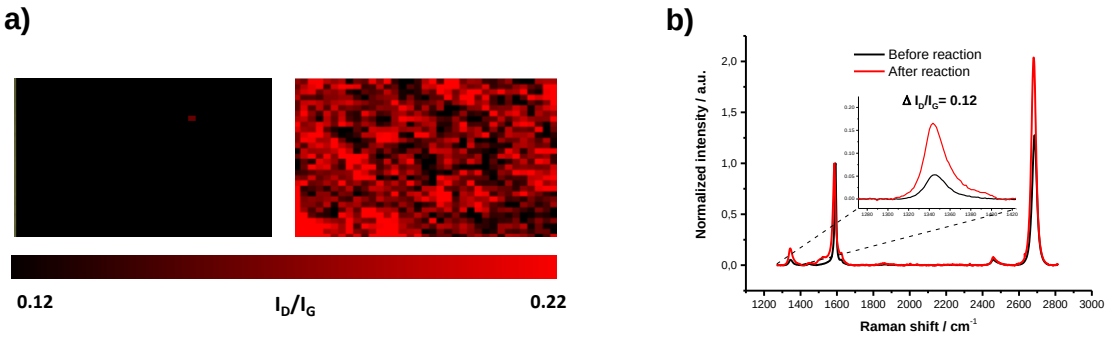

Figure 140. a) Raman mapping of the D band intensity in 30x25 µm² area and b) averaged Raman spectra (≈1000 single-point spectra, λ_{exc} = 532nm) before and after covalent modification of SiO_2/MGFET.

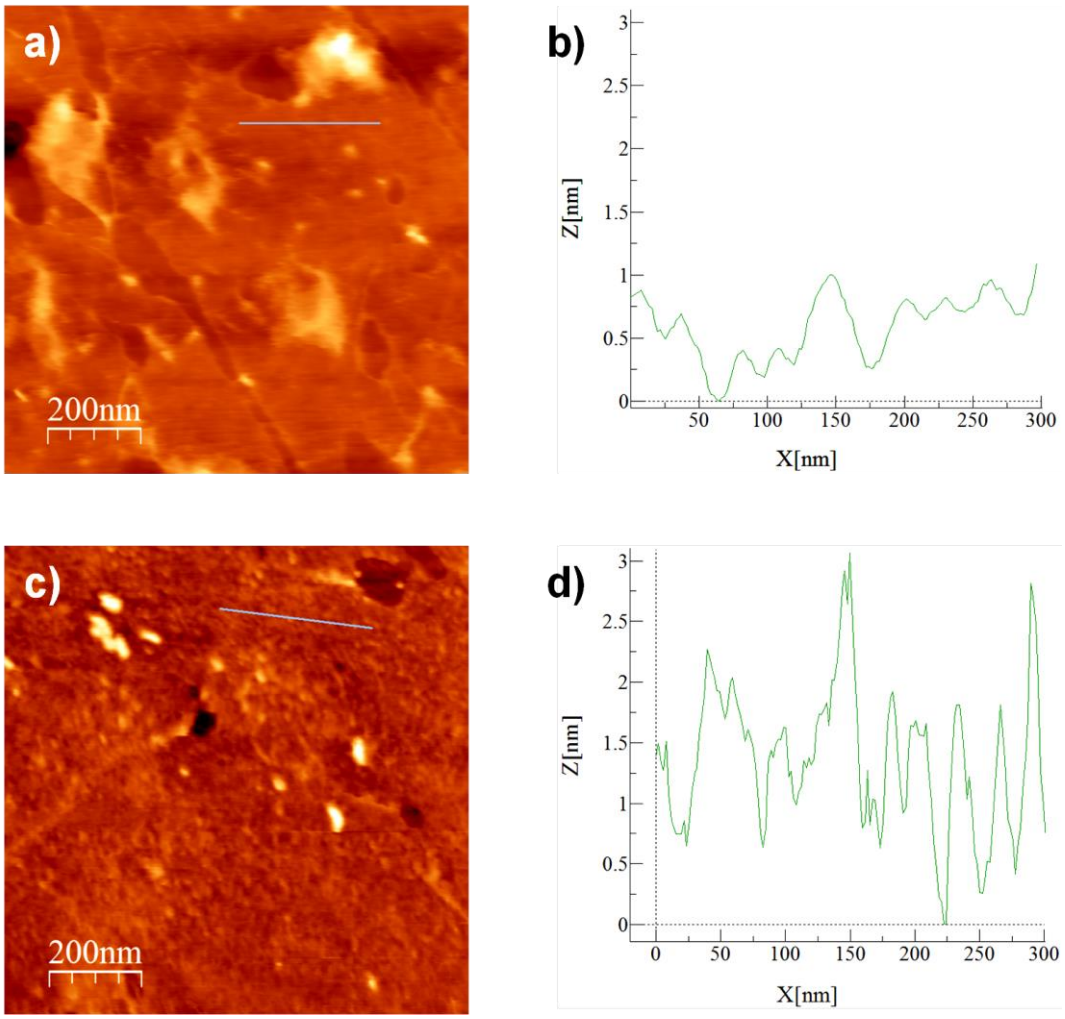

Figure 141. AFM images of SiO_2/MGFET (a) before and (c) after chemical. AFM height profiles (b) before and (d) after chemical modification (blue lines in a and c images respectively).

3.4.4. ***SiO_2/mGFET functionalization general method for thrombin sensing platform*:** SiO_2/mGFET-(*p*-(CH_2CO_2H)Ph).

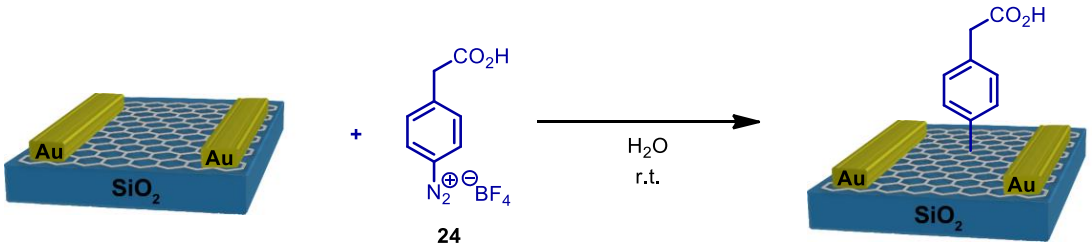

SiO_2/mGFET was placed in a glass beaker with distilled water (10 mL). Then, a solution of 4-(carboxymethyl)benzenediazonium tetrafluoroborate (**24**, 10 mg, 0.04 mmol) in distilled water (2 mL) was added. After 1 h reaction at r.t. the SiO_2/mGFET was taken from the solution reaction and washed by diving 3 times x 1 second in distilled water and dried with nitrogen. **$\Delta(I_D/I_G)$:** 0.07.

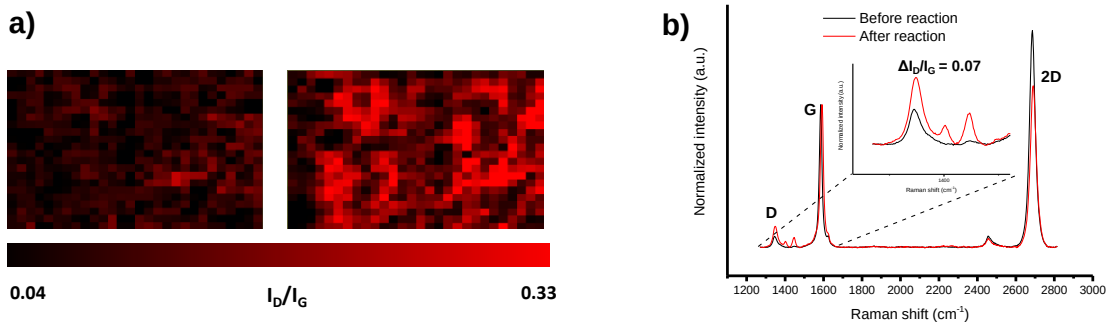

Figure 142. a) Raman mapping of the D band intensity in 30x25 μm² area and b) averaged Raman spectra (≈1000 single-point spectra, λ_{exc} = 532nm) before and after covalent modification of SiO_2/mGFET.

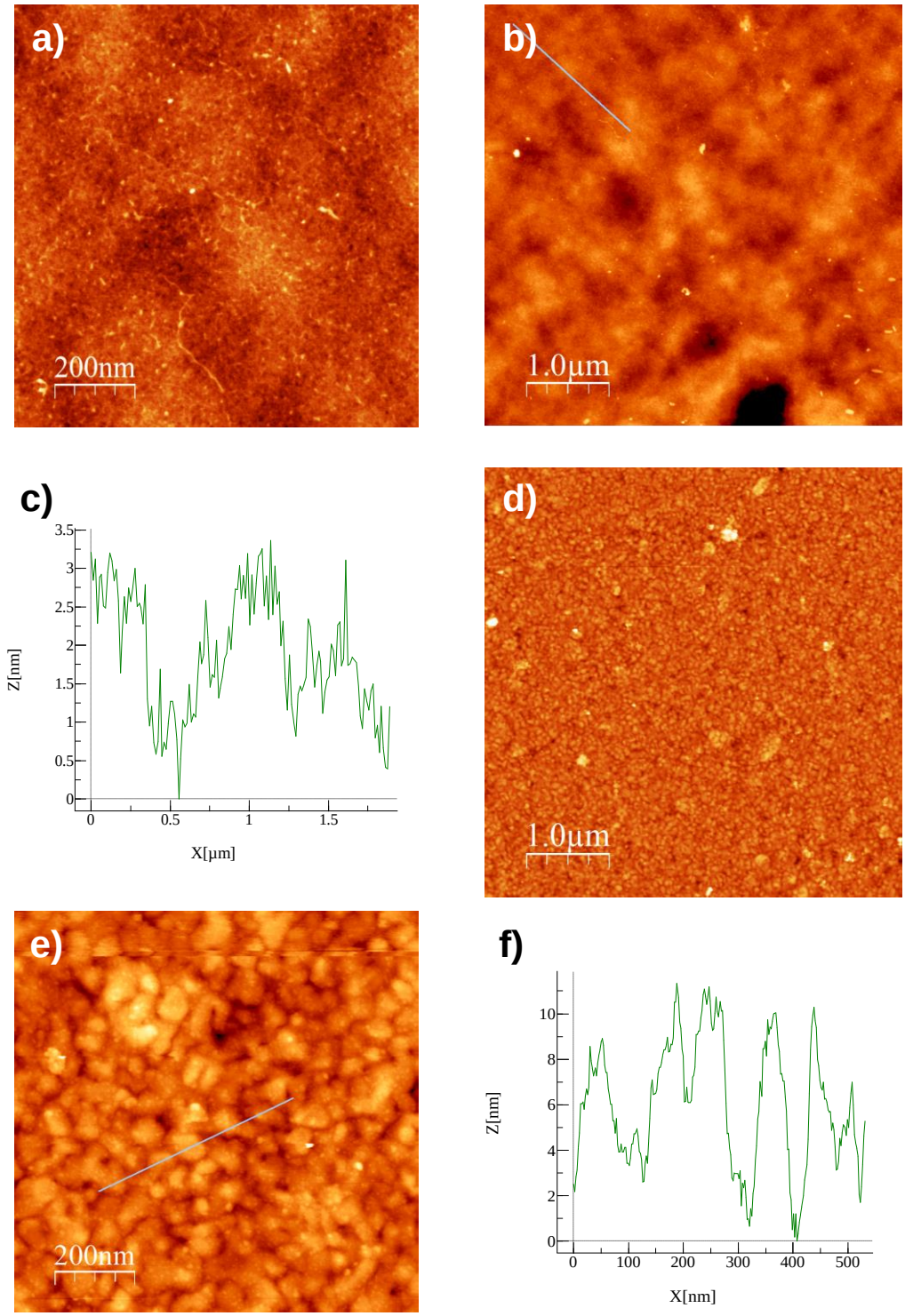

Figure 143. AFM images of SiO_2/mGFET a, b) before and d, e) after chemical modification at different magnifications. AFM height profiles c) before and f) after chemical modification (green lines in b and e images respectively).

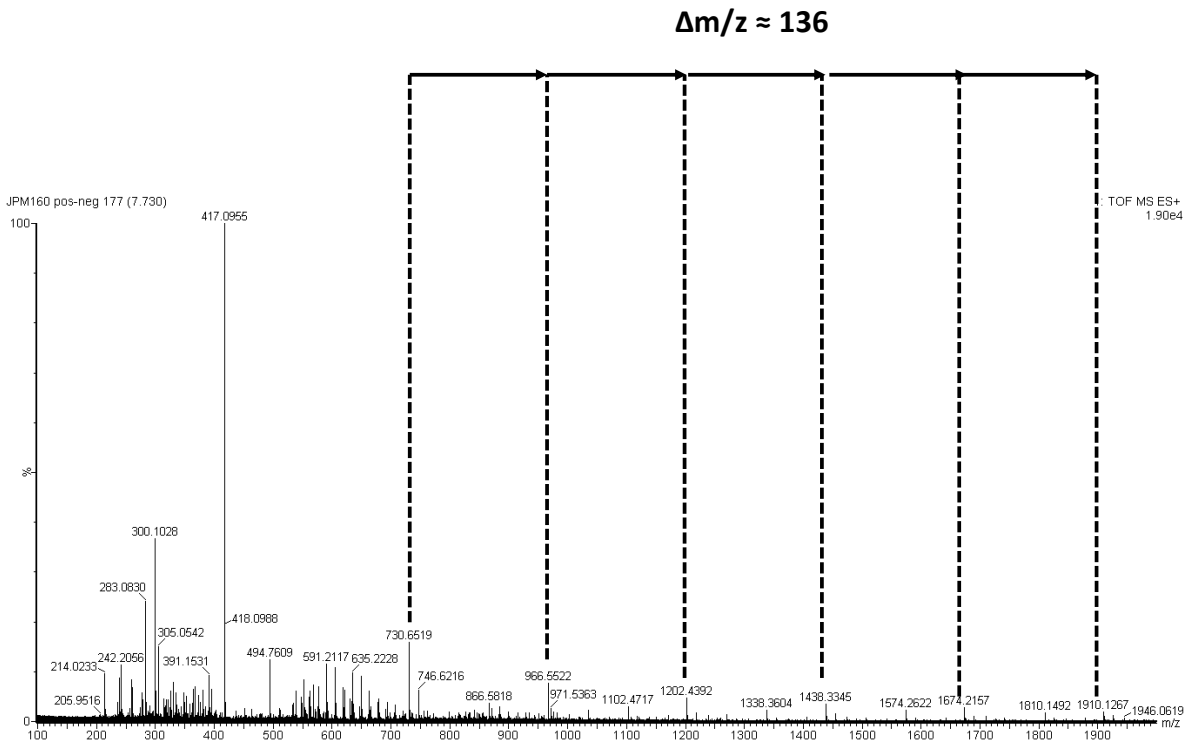

Figure 144.Mass spectroscopy (ES+) mode (m/z 100-2000) Background of the obtained residue.

3.4.5. *SiO_2/mGFET functionalization general method for thrombin sensing platform SLOW ADDITION*: SiO_2/mGFET-(*p*-(CH_2CO_2H)Ph)

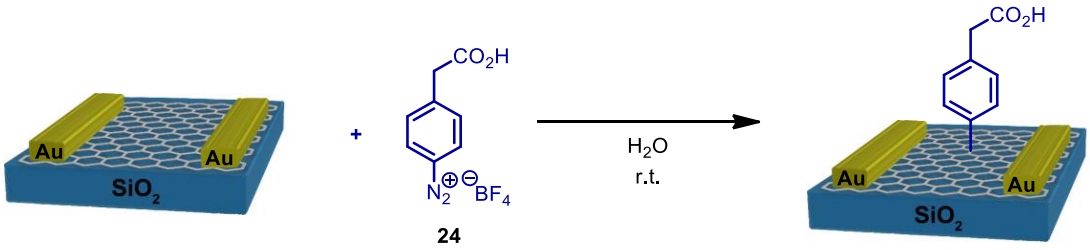

SiO_2/MGFET/SiO_2/mGFET was placed in a glass beaker with distilled water (10 mL). Then, a solution of 4-(carboxymethyl)benzenediazonium tetrafluoroborate (**24**, 10 mg, 0.04 mmol) in distilled water (2 mL) was slowly dropped with a syringe pump (2.5 mL/h ratio). After 1 h reaction at r.t. the SiO_2/mGFET was taken from the solution reaction and washed by diving 3 times x 1 second in distilled water and dried with nitrogen. **$\Delta(I_D/I_G)$:** 0.09.

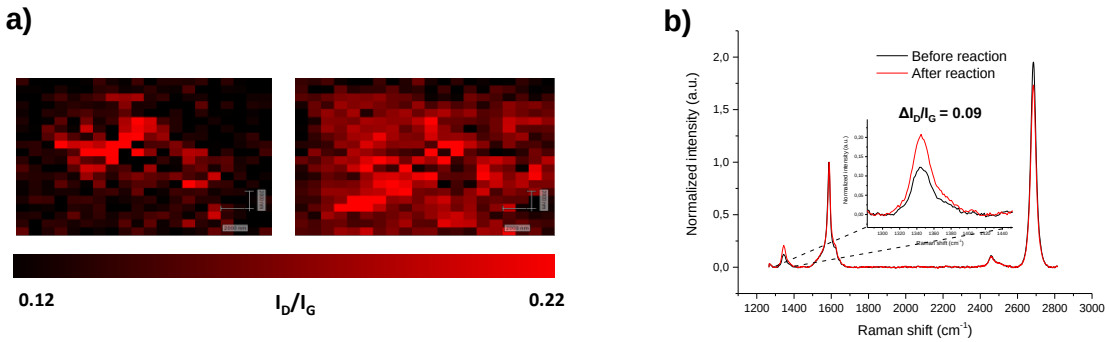

Figure 145. a) Raman mapping of the D band intensity in 20x20 μm² area and b) averaged Raman spectra (λ_{exc} = 532nm) before and after covalent modification of SiO_2/mGFET.

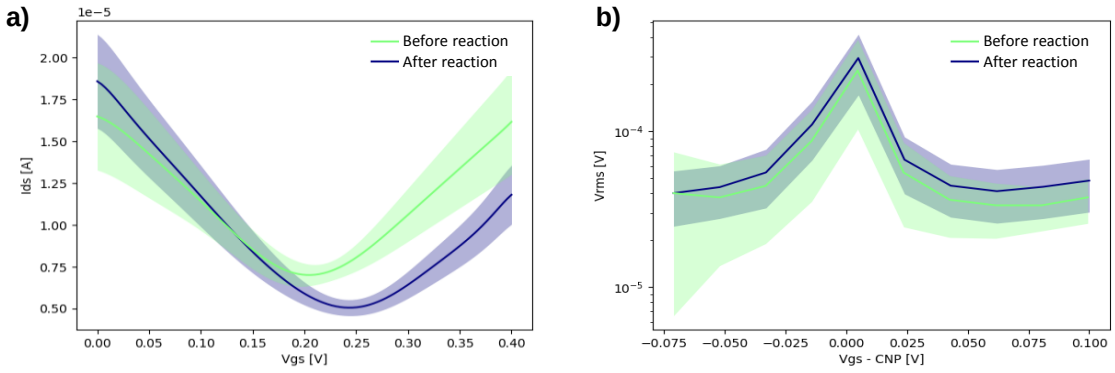

Figure 146. a) I-V curve and b) Vrms performance for the functionalization with 24 before (green) and after (blue) the reaction.

3.4.6. *SiO_2/mGFET functionalization general method for thrombin sensing platform*: SiO_2/mGFET-(3,4-($C_{18}H_{37}O)_2$Ph)

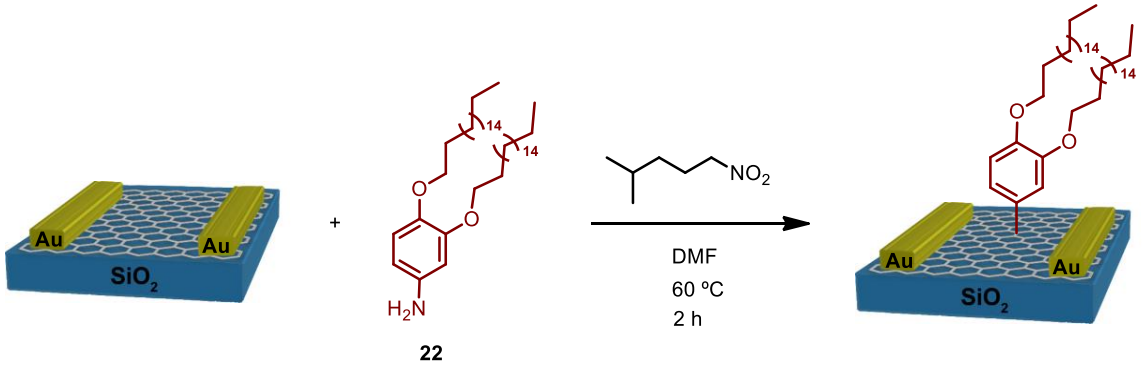

3,4-bis(octadecyloxy)aniline (**22**, 50.4 mg, 0.08 mmol) was placed in a round bottom flask previously purged with argon and dissolved in dry DMF (10mL) under sonication. Then, the SiO_2/mGFET was introduced in the flask and 3-methylbuthylnitrite (16.2 µL, 0.12 mmol) was slowly added dropwise. The reaction mixture was heated to 60 ºC and left without stirring for 2h. The substrate was taken from the reaction mixture and cleaned by immersion in toluene for 12h and in EtOH for 30'. The modified graphene substrate was dried over a stream of N_2. **$\Delta(I_D/I_G)$:** 0.07.

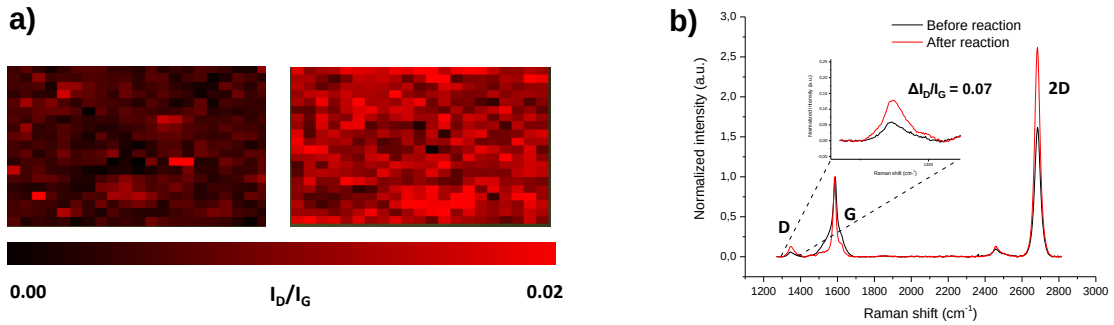

Figure 147. a) Raman mapping of the D band intensity in 30x25 µm² area and b) averaged Raman spectra (≈1000 single-point spectra, λ_{exc} = 532nm) before and after covalent modification of SiO_2/mGFET.

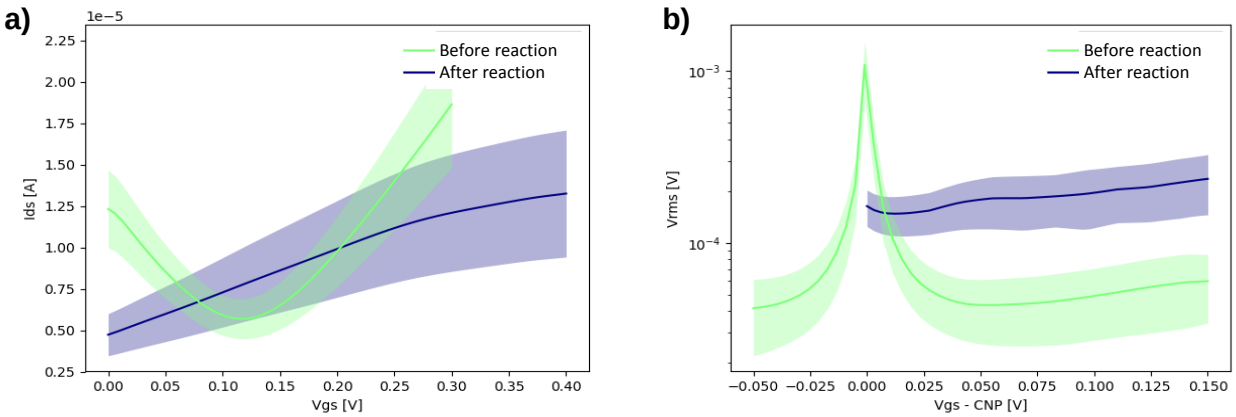

Figure 148. a) *I-V* curve and b) *Vrms* performance for the functionalization with 22 before (green) and after (blue) the reaction.

3.4.7. ***CVD graphene functionalization general method for lectins sensing platform*:** SiO_2/G-(3,4-($C_{18}H_{37}O$)$_2$Ph).

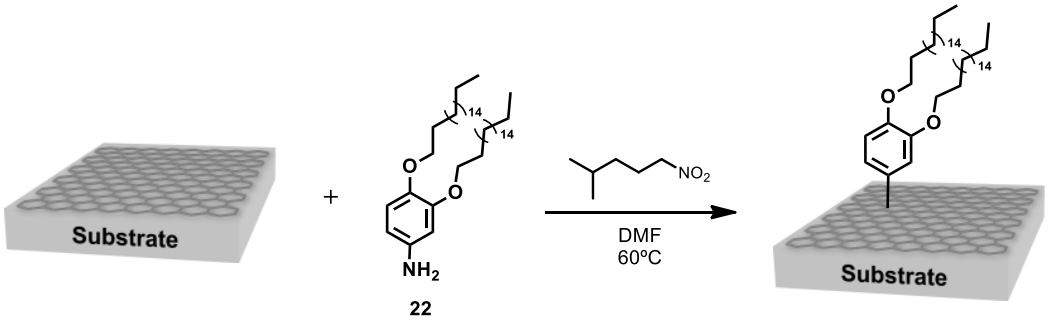

3,4-bis(octadecyloxy)aniline (**22**, 100.8 mg, 0.16 mmol, 2mM) was placed in a round bottom flask previously purged with argon and dissolved in dry DMF (80mL) under sonication. Then, the graphene substrate was introduced in the flask and 3-methylbuthylnitrite (32.3 μL, 0.96 mmol) was slowly added dropwise. The reaction mixture was heated to 60 ºC and left without stirring for 2h. The substrate was taken from the reaction mixture and cleaned by immersion in toluene for 12h and in EtOH for 30′. The modified graphene substrate was dried over a stream of N_2. **Δ(I_D/I_G):** 0.05.

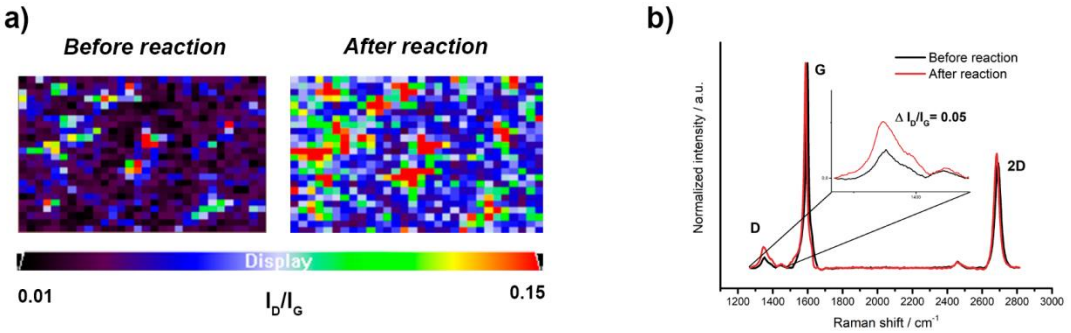

Figure 149. a) Raman mapping of the D band intensity in 30x25 μm² area and b) averaged Raman spectra (≈1000 single-point spectra, λ_{exc} = 532nm) before and after covalent modification of SiO_2/G-(3,4-($C_{18}H_{37}O$)$_2$Ph.

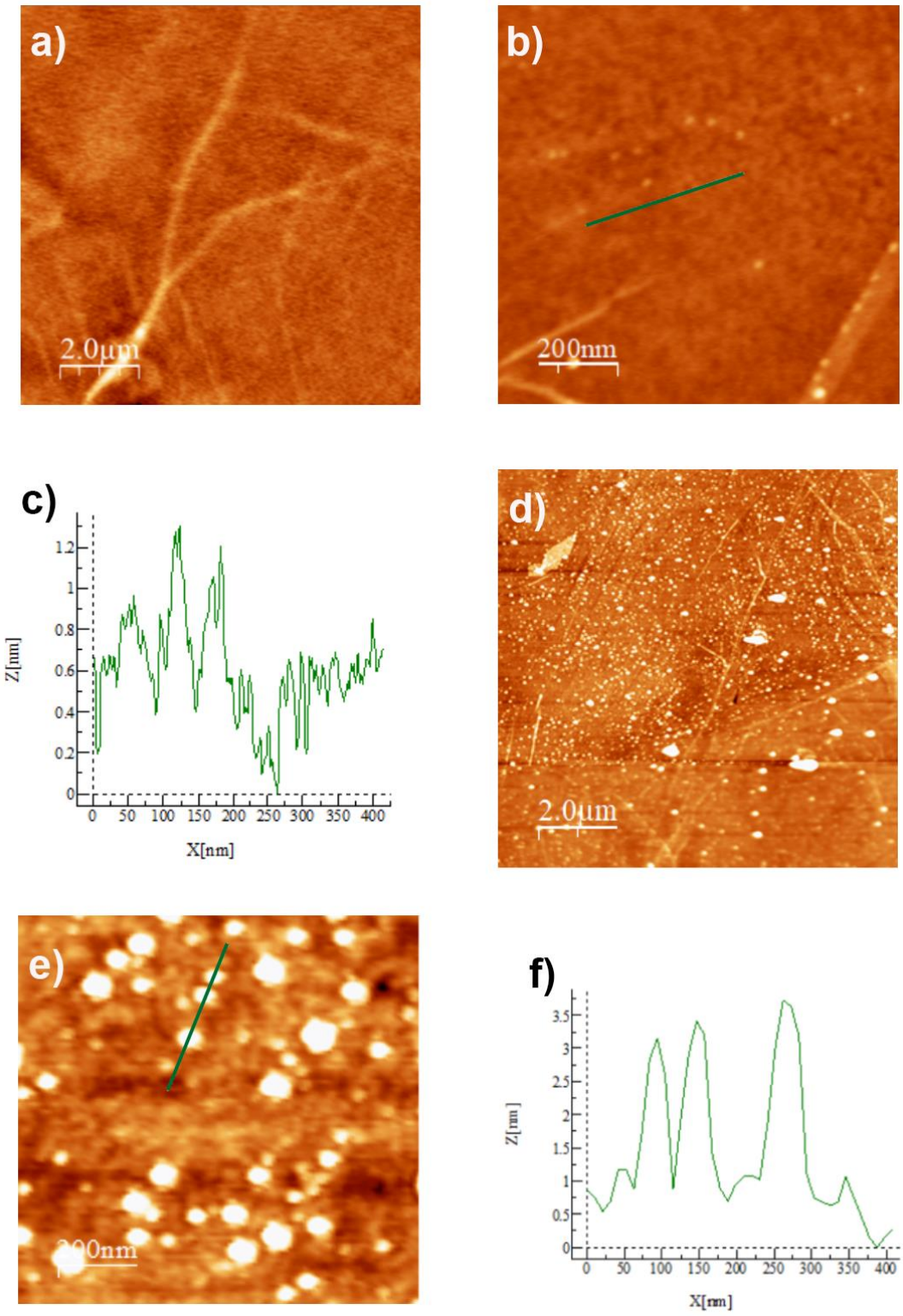

Figure 150. AFM images for SiO_2/G-(3,4-($C_{18}H_{37}O$)$_2$Ph (a, b) before and (d, e) after chemical modification at different magnifications. AFM height profiles (c) before and (f) after chemical modification (green lines in b and e images, respectively).

3.4.8. ***CVD graphene functionalization general method for lectins sensing platform*:** ITO/G-(3,4-($C_{18}H_{37}O)_2$Ph).

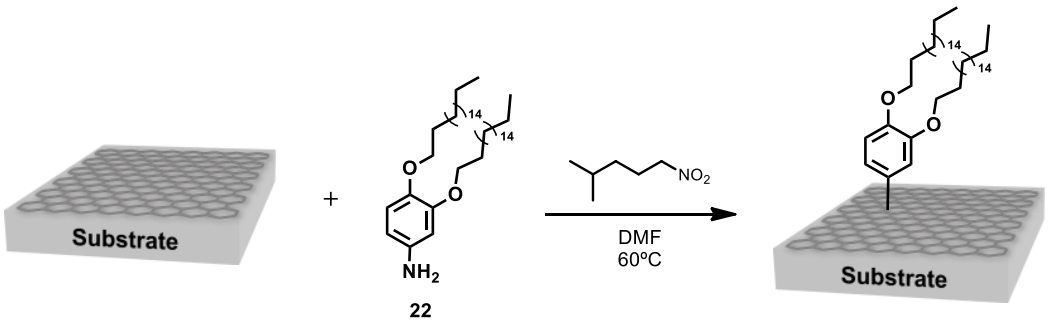

3,4-bis(octadecyloxy)aniline (**22**, 100.8 mg, 0.16 mmol, 2mM) was placed in a round bottom flask previously purged with argon and dissolved in dry DMF (80mL) under sonication. Then, the graphene substrate was introduced in the flask and 3-methylbuthylnitrite (32.3 μL, 0.96 mmol) was slowly added dropwise. The reaction mixture was heated to 60 ºC and left without stirring for 2h. The substrate was taken from the reaction mixture and cleaned by immersion in toluene for 12h and in EtOH for 30′. The modified graphene substrate was dried over a stream of N_2. **$\Delta(I_D/I_G)$:** 0.00.

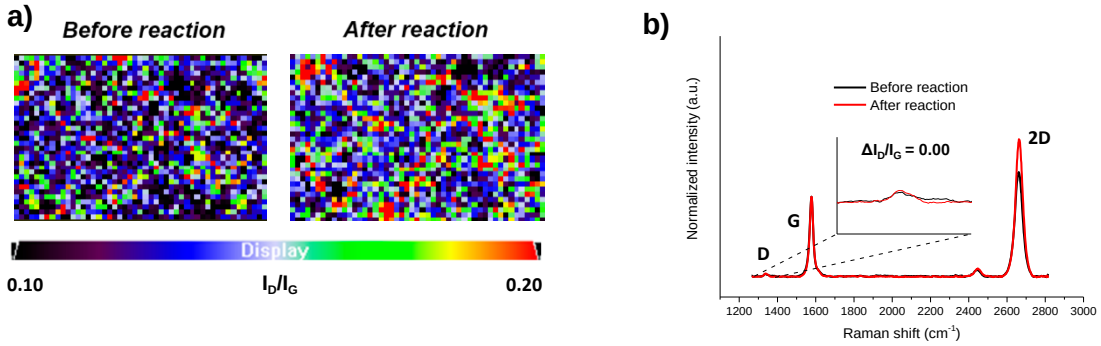

Figure 151. a) Raman mapping of the D band intensity in 30x25 μm² area and b) averaged Raman spectra (≈1000 single-point spectra, λ_{exc} = 532nm) before and after covalent modification of ITO/G-(3,4-($C_{18}H_{37}O)_2$Ph).

3.4.9. ***CVD graphene functionalization general method for lectins sensing platform*:** ITO/G-(3,4-($C_{18}H_{37}O)_2$Ph).

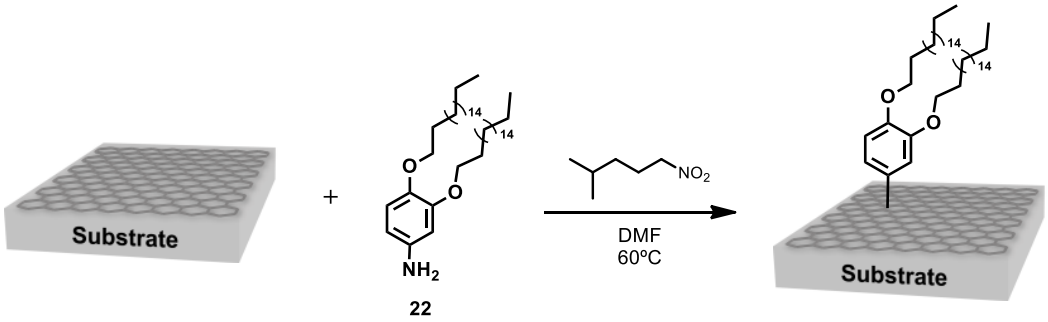

3,4-bis(octadecyloxy)aniline (**22**, 403 mg, 0.64 mmol, 8mM) was placed in a round bottom flask previously purged with argon and dissolved in dry DMF (80mL) under sonication. Then, the graphene substrate was introduced in the flask and 3-methylbuthylnitrite (129 µL, 0.96 mmol) was slowly added dropwise. The reaction mixture was heated to 60 ºC and left without stirring for 2h. The substrate was taken from the reaction mixture and cleaned by immersion in toluene for 12h and in EtOH for 30'. The modified graphene substrate was dried over a stream of N_2. **$\Delta(I_D/I_G)$:** 0.06, $\Delta\theta_c$: 8.2°, **Δ atom % (C1s):** 11.54 and **Δ atom % (O1s): -12**.

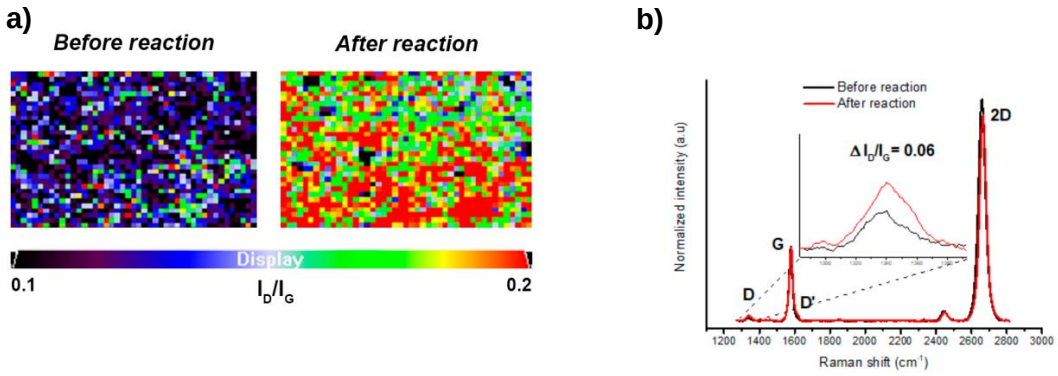

Figure 152. a) Raman mapping of the D band intensity in 30x25 µm² area and b) averaged Raman spectra (≈1000 single-point spectra, λ_{exc} = 532nm) before and after covalent modification of ITO/G-(3,4-($C_{18}H_{37}O)_2$Ph.

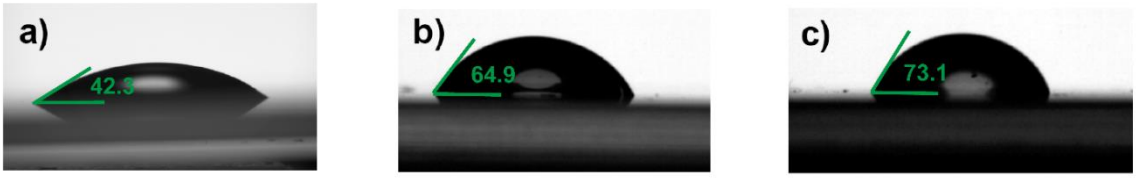

Figure 153. Contact angles of a) ITO-coated glass treated with piranha solution, b) ITO/G c) ITO/G-(3,4-($C_{18}H_{37}O)_2$Ph).

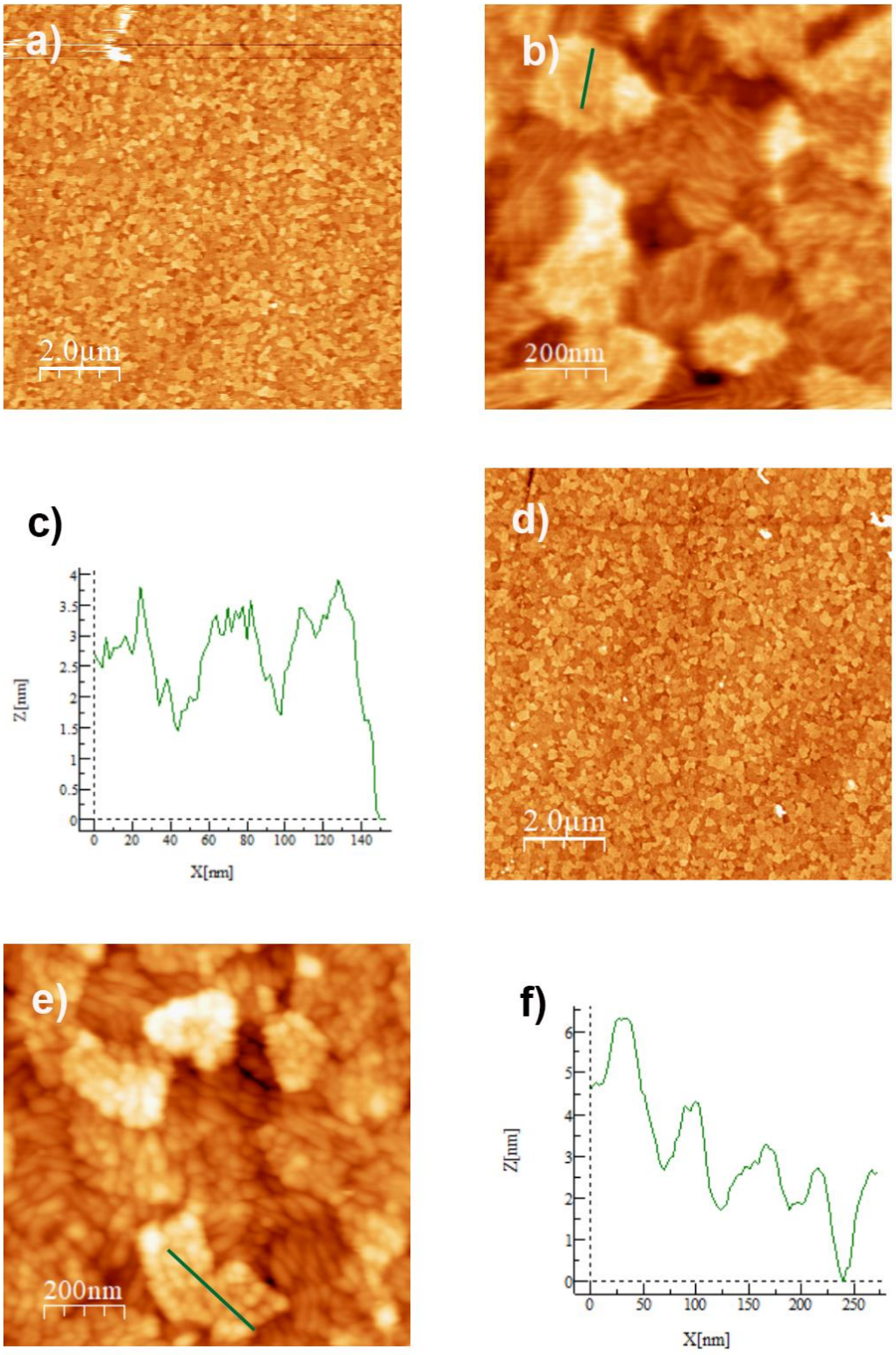

Figure 154. AFM images for ITO/G-(3,4-($C_{18}H_{37}O$)$_2$Ph) (a, b) before and (d,e) after chemical modification at different magnifications. AFM height profiles (c) before and (f) after chemical modification (green lines in b and e images respectively).

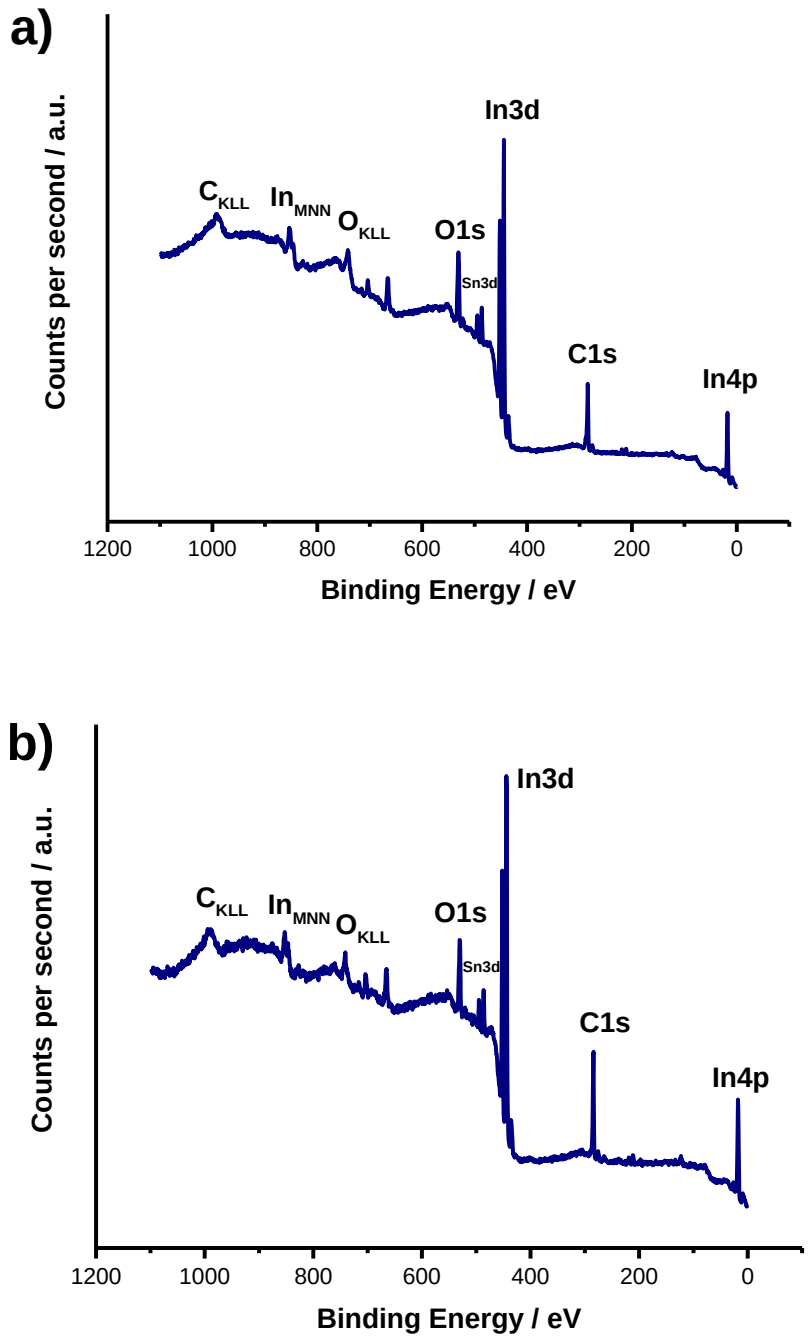

Figure 155. Survey spectra for ITO/G-(3,4-($C_{18}H_{37}O$)$_2$Ph) (a) before and (b) after chemical functionalization.

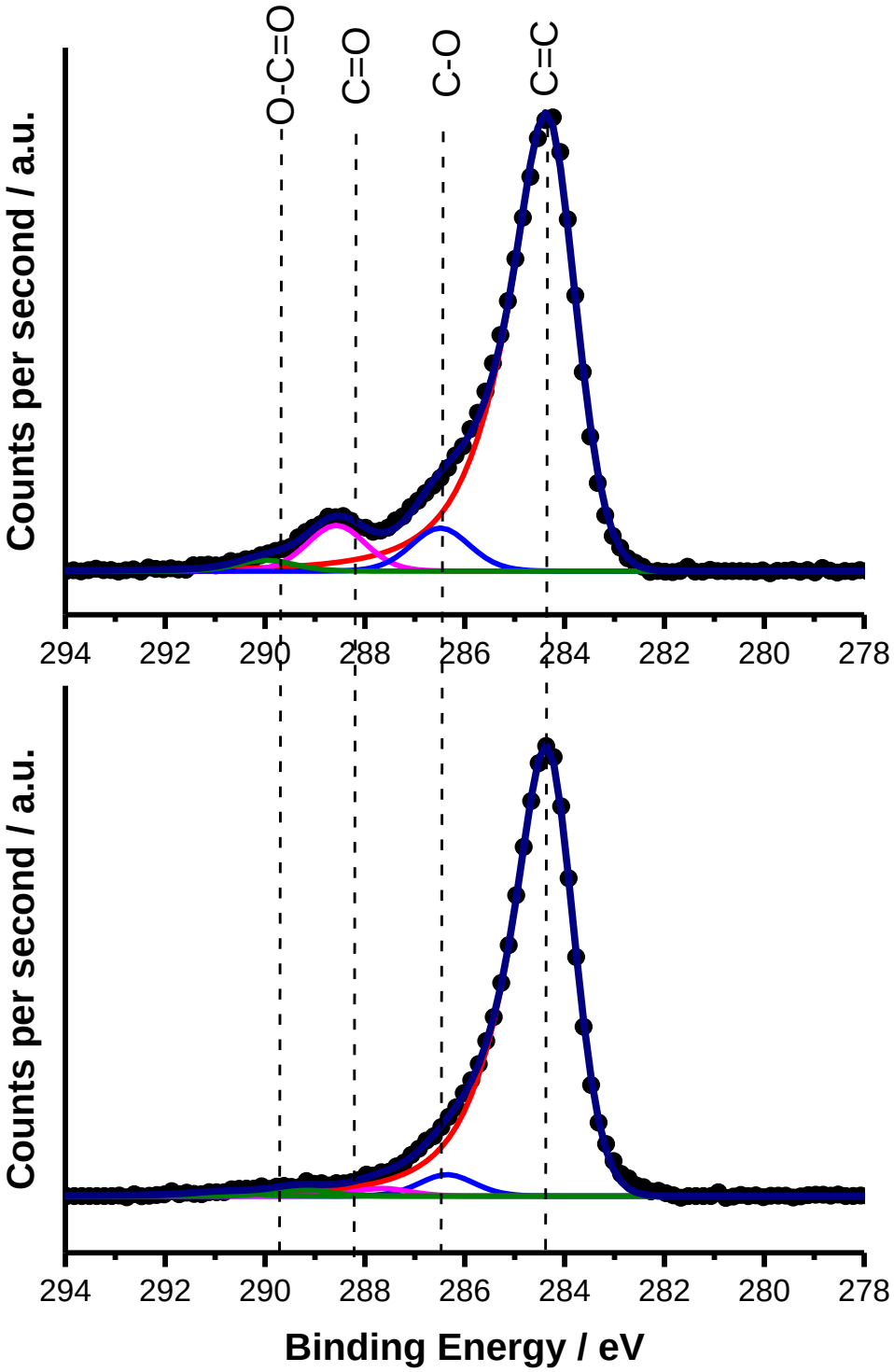

Figure 156. Deconvoluted C1s core level spectra for ITO/G-(3,4-($C_{18}H_{37}O$)$_2$Ph) (top) before and (bottom) after chemical modification.

3.4.10. ***CVD graphene functionalization general method for lectins sensing platform*:** Glass/G-(3,4-($C_{18}H_{37}O$)$_2$Ph).

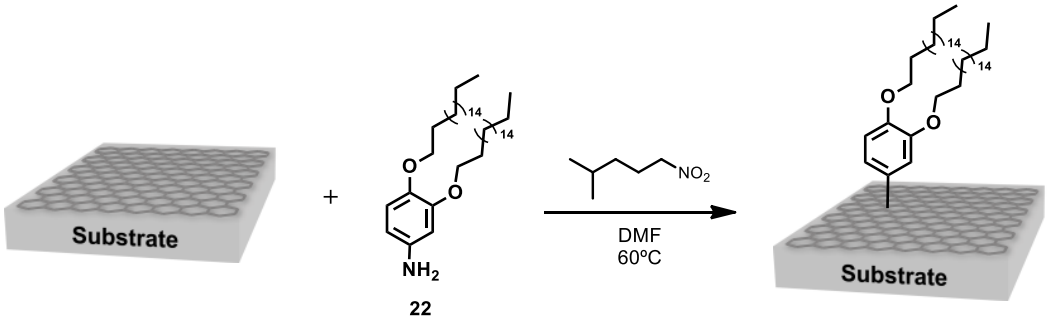

3,4-bis(octadecyloxy)aniline (**22**, 403 mg, 0.64 mmol, 8mM) was placed in a round bottom flask previously purged with argon and dissolved in dry DMF (80mL) under sonication. Then, the graphene substrate was introduced in the flask and 3-methylbuthylnitrite (129 µL, 0.96 mmol) was slowly added dropwise. The reaction mixture was heated to 60 ºC and left without stirring for 2h. The substrate was taken from the reaction mixture and cleaned by immersion in toluene for 12h and in EtOH for 30'. The modified graphene substrate was dried over a stream of N_2. **Δ(I_D/I_G):** 0.01, Δθc: -2.3°, **Δ atom % (C1s):** 8.99 and **Δ atom % (O1s):** -8.99.

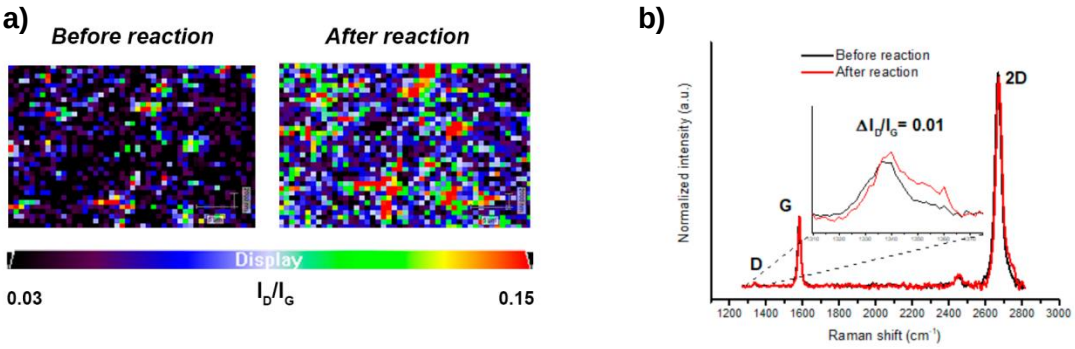

Figure 157. a) Raman mapping of the D band intensity in 30x25 µm² area and b) averaged Raman spectra (≈1000 single-point spectra, λ_{exc} = 532nm) before and after covalent modification of Glass/G-(3,4-($C_{18}H_{37}O$)$_2$Ph).

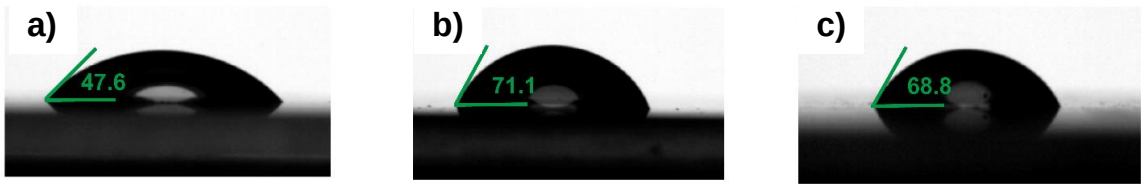

Figure 158. Contact angles of a) bare glass treated with piranha solution, b) Glass/G, c) Glass/G-(3,4-($C_{18}H_{37}O$)$_2$Ph).

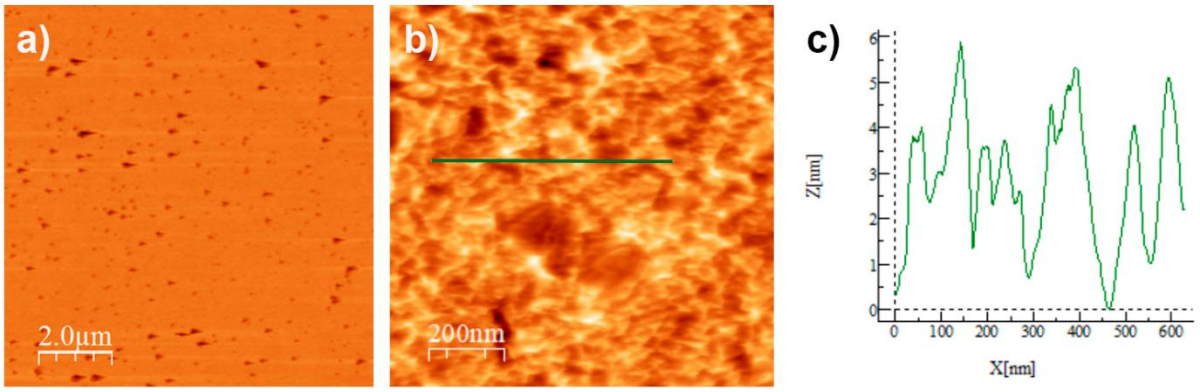

Figure 159. (a, b) AFM images for Glass/G (without chemical modification) at different magnifications and (c) the height profile from the green line.

3.4.11. ***CVD graphene functionalization general method for lectins sensing platform*:** Quartz/G-(3,4-($C_{18}H_{37}O)_2$Ph).

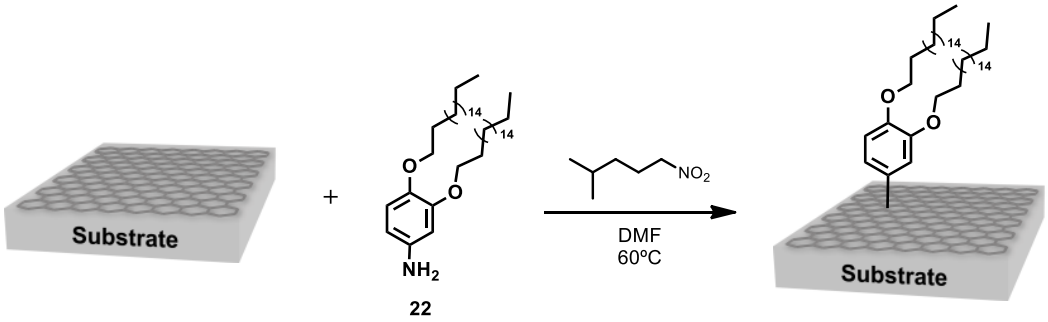

3,4-bis(octadecyloxy)aniline (**22**, 403 mg, 0.64 mmol, 8mM) was placed in a round bottom flask previously purged with argon and dissolved in dry DMF (80mL) under sonication. Then, the graphene substrate was introduced in the flask and 3-methylbuthylnitrite (129 µL, 0.96 mmol) was slowly added dropwise. The reaction mixture was heated to 60 ºC and left without stirring for 2h. The substrate was taken from the reaction mixture and cleaned by immersion in toluene for 12h and in EtOH for 30'. The modified graphene substrate was dried over a stream of N_2. **$\Delta(I_D/I_G)$:** 0.07, **$\Delta\theta_c$**: 10.1°.

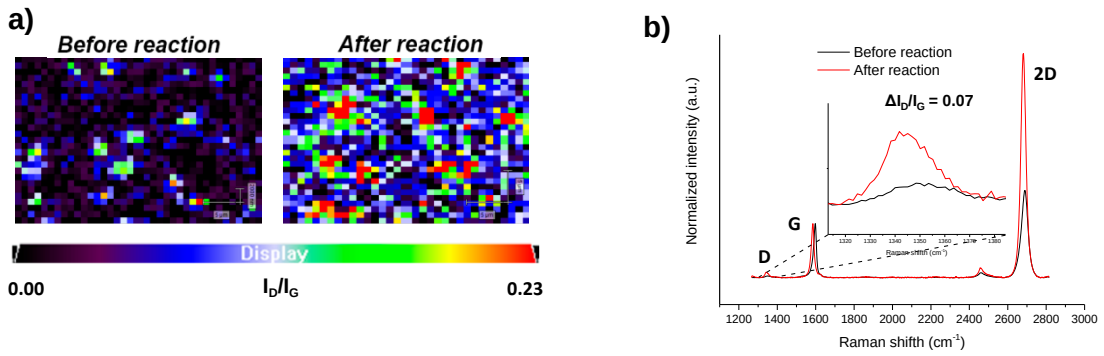

Figure 160. a) Raman mapping of the D band intensity in 30x25 µm² area and b) averaged Raman spectra (≈1000 single-point spectra, λ_{exc} = 532nm) before and after covalent modification of Quartz/G-(3,4-($C_{18}H_{37}O)_2$Ph).

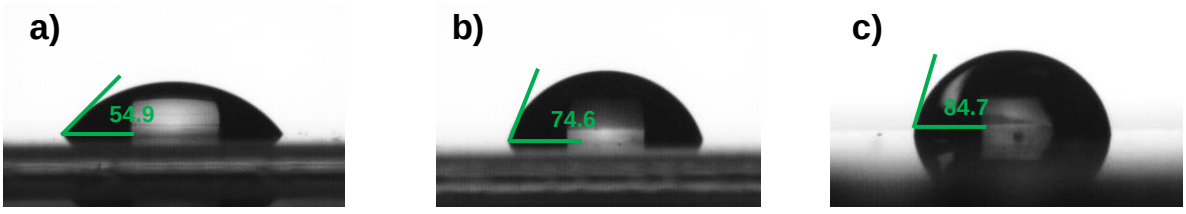

Figure 161. Contact angles of a) Quartz treated with piranha solution, b) Quartz/G and c) Quartz/G-(3,4-($C_{18}H_{37}O)_2$Ph).

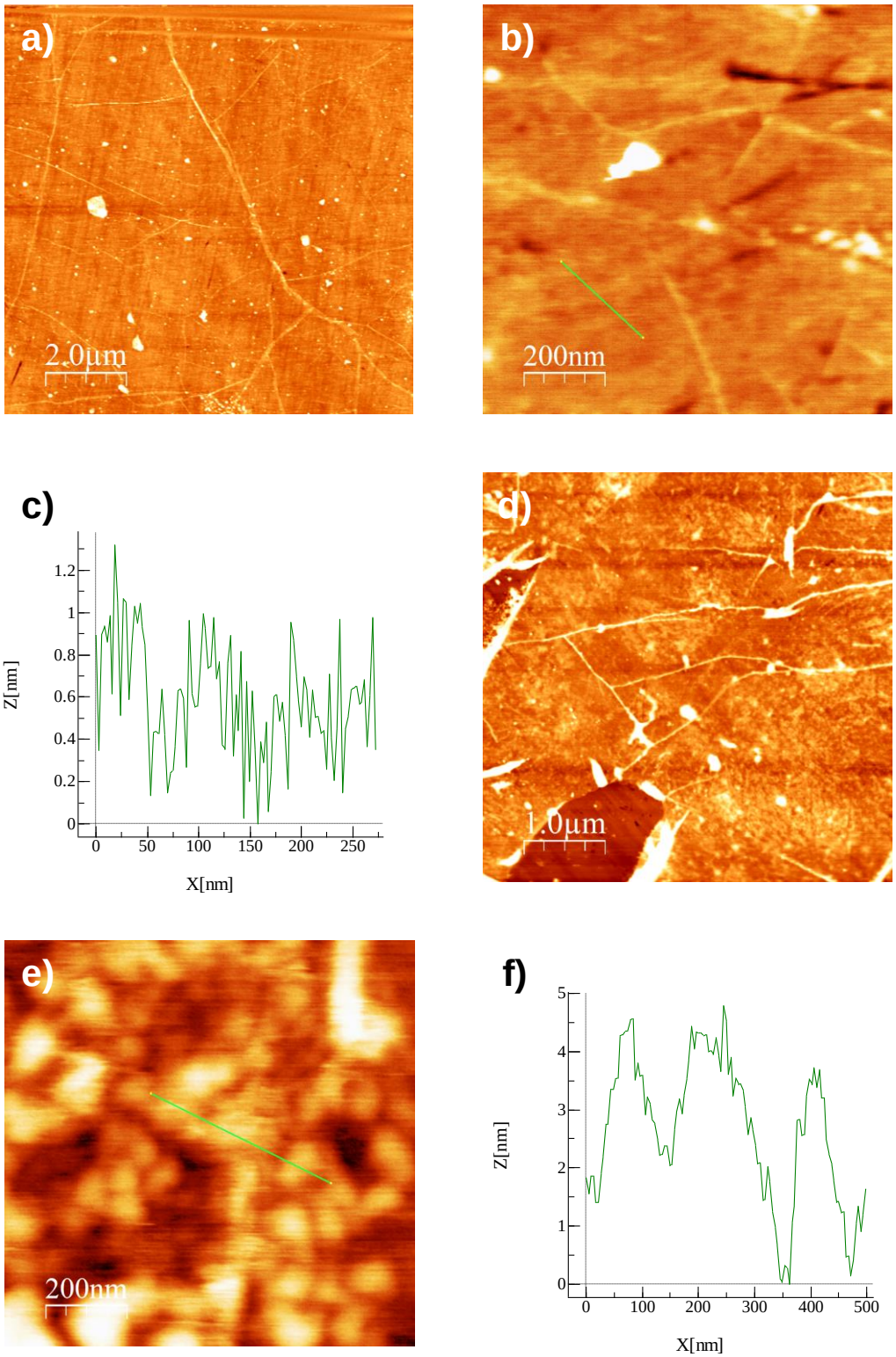

Figure 162. AFM images for Quartz/G-(3,4-($C_{18}H_{37}O)_2$Ph) (a, b) before and (d,e) after chemical modification at different magnifications. AFM height profiles (c) before and (f) after chemical modification (green lines in b and e images respectively).

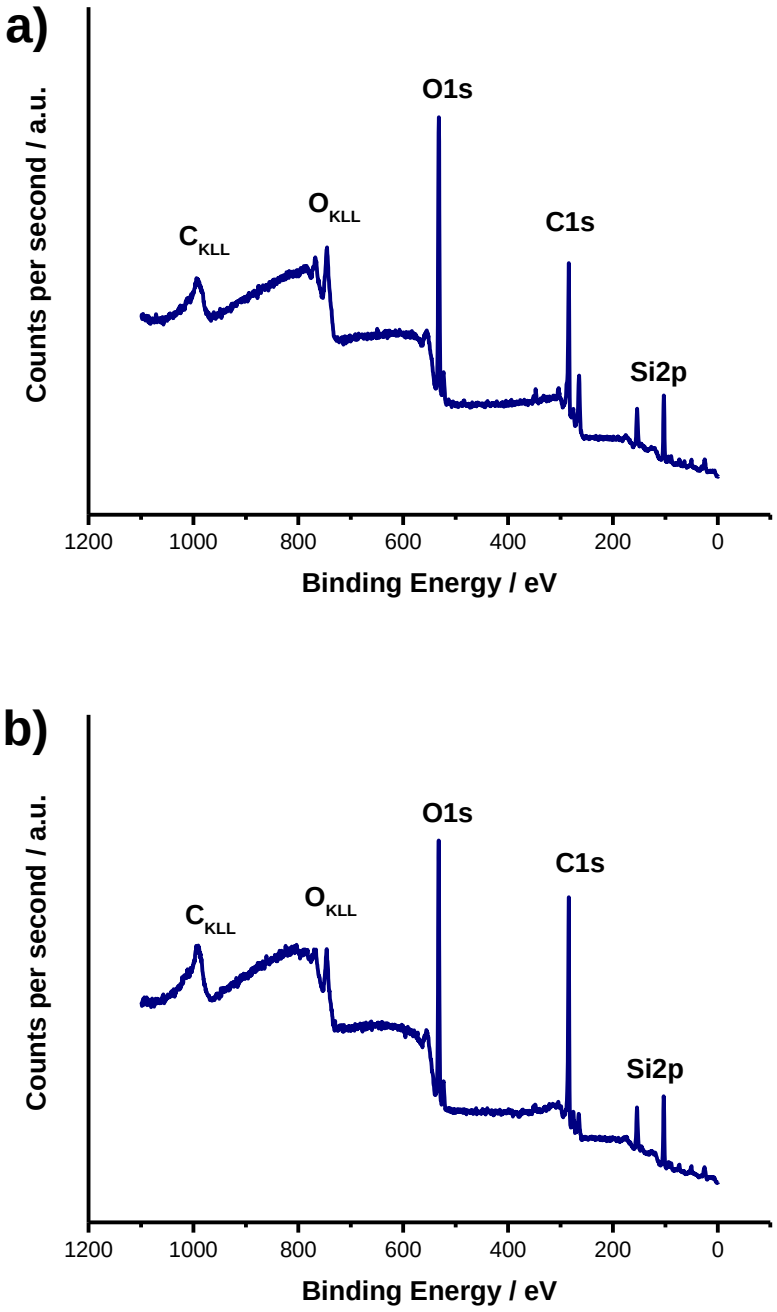

Figure 163. Survey spectra for Glass/G-(3,4-($C_{18}H_{37}O$)$_2$Ph) (a) before and (b) after chemical functionalization.

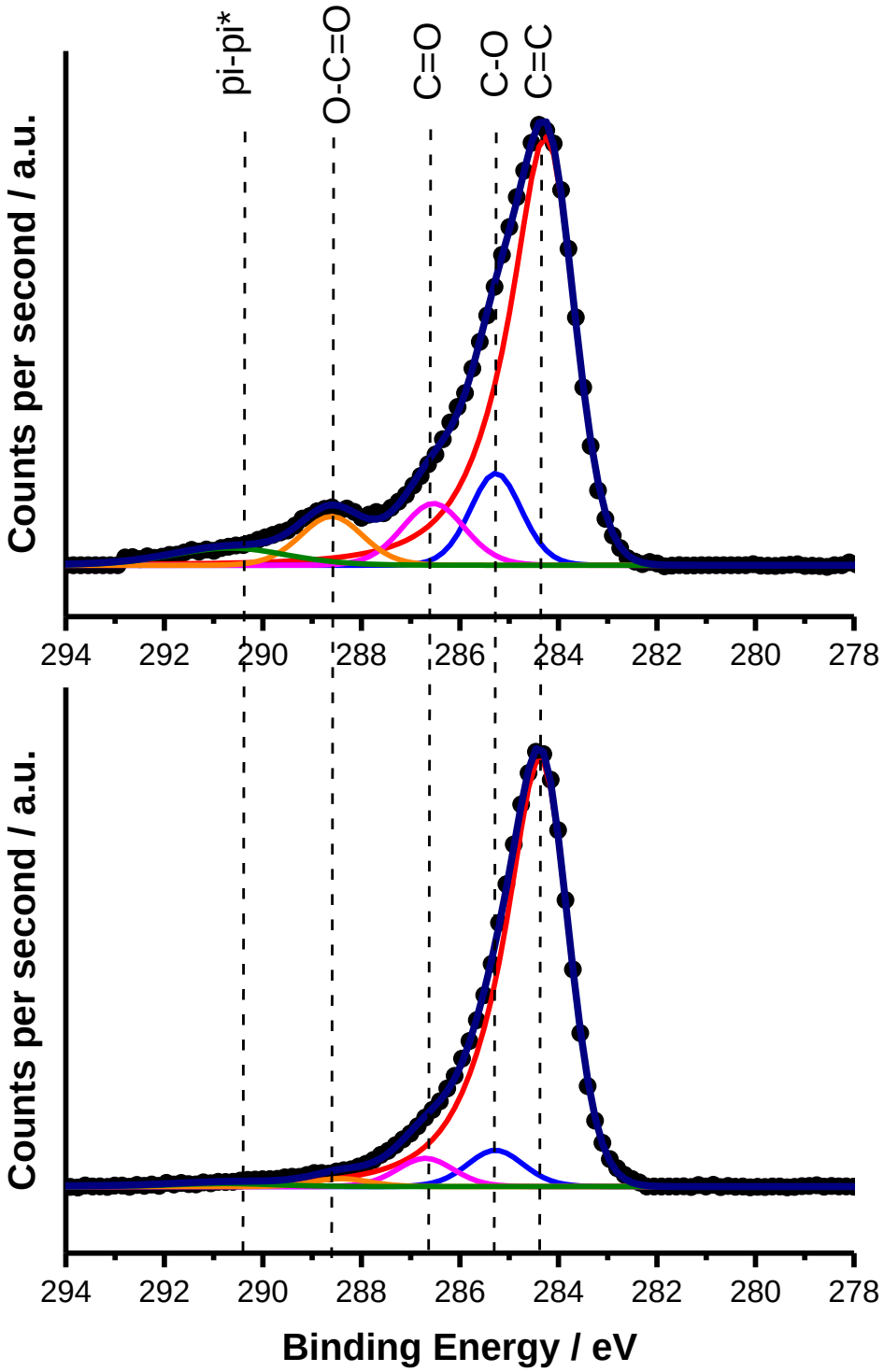

Figure 164. Deconvoluted C1s core level spectra for Glass/G-(3,4-($C_{18}H_{37}O$)$_2$Ph) (top) before and (bottom) after chemical modification.

Table 19. Atomic percentage of S/G-(3,4-($C_{18}H_{37}O)_2$Ph) substrates before and after chemical modification.

Sample		Atomic %	
		C1s	***O1s***
ITO/G-(3,4-($C_{18}H_{37}O)_2$Ph)	***Before reaction***	62.63	37.37
	After reaction	74.17	25.83
Glass/G-(3,4-($C_{18}H_{37}O)_2$Ph)	***Before reaction***	56.55	43.45
	After reaction	65.54	34.46

Table 20. C1s components for ITO/G-(3,4-($C_{18}H_{37}O)_2$Ph) and Glass/G-(3,4-($C_{18}H_{37}O)_2$Ph) before and after chemical modification.

Sample	C1s Component	Before Reaction		After Reaction	
		Binding energy (eV)	*Area (%)*	*Binding energy (eV)*	*Area (%)*
ITO/G-(3,4-($C_{18}H_{37}O)_2$Ph)	C=C/C-C	284.37	82.0	284.37	91.8
	C-O	286.49	7.8	285.28	4.4
	C=O	288.57	8.3	286.70	1.6
	O-C=O	289.99	2.0	288.42	1.5
	pi-pi*	-	-	290.78	0.8
Glass/G-(3,4-($C_{18}H_{37}O)_2$Ph)	C=C/C-C	284.37	64.0	284.37	84.5
	C-O	285.27	12.5	285.28	7.2
	C=O	286.54	10.3	286.70	5.6
	O-C=O	288.61	8.1	288.42	1.6
	pi-pi*	290.67	5.2	290.78	1.1

3.5. Generation of interfaces on CVD graphene for biosensing

3.5.1. Carboxilic group activation:

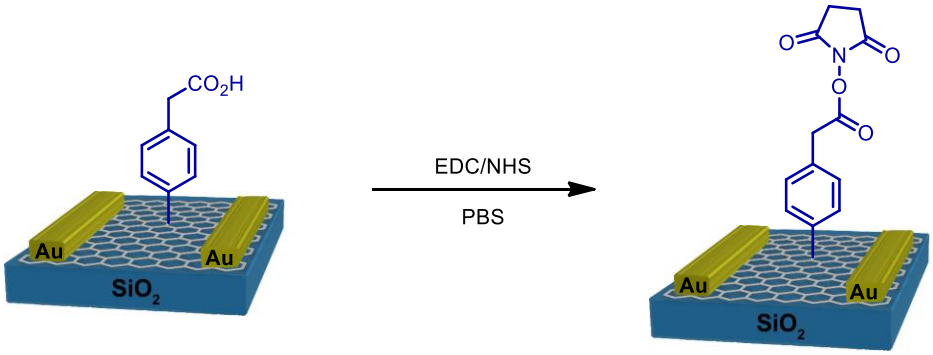

1-ethyl-3-(3-dimethhylaminopropyl carbodiimide (EDC, 9 mg, 0.06 mmol) in PBS (10 nM, 500 μL), was mix with a solution of *N*-hydroxysucciniimide (NHS, 1.15 mg, 0.01 mmol) in PBS (10 nM, 500 μL). The SiO_2/mGFET-(*p*-(CH_2CO_2H)Ph) was incubated with 600 μL of the resulting solution for 1 h. After the incubation, the substrate was washed 3 times with distilled water (500 mL) in order to remove the PBS salts.

3.5.2. Aptamer cross-linking:

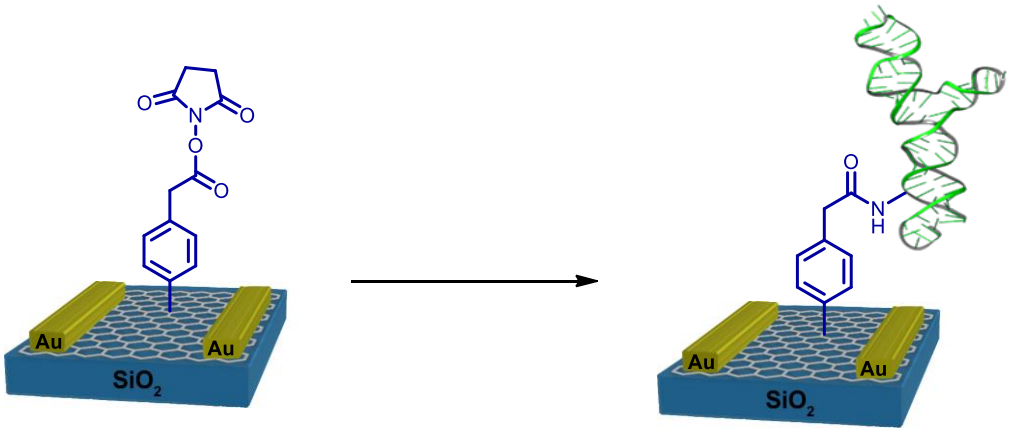

The previously activated functionalized SiO_2/mGFET-(*p*-(CH_2CO_2H)Ph) was incubated with the specific thrombin aptamer-NH_2 solution (1 nM) in PBS (10 mM, 300 μL) overnight. The solution was removed and the substrate was washed 3 times with distilled water. In order to block the free activated carboxylic groups, the substrate was incubated with 300 μL of Ethanolamine (6 μL) in PBS (10 mM, 494 μL) for 20 minutes and washed 3 times with distilled water (500 μL) to remove the PBS salts.

3.5.3. General method for bilayer preparation:

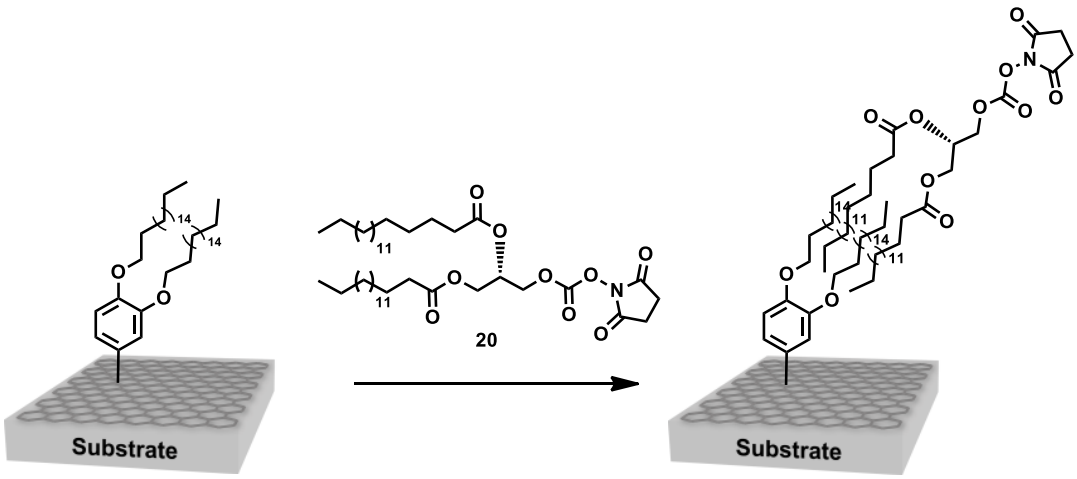

Modified graphene slide (ITO/G-, Glass/G- or Quartz/G-(3,4-($C_{18}H_{37}O)_2$Ph). was incubated overnight at r.t. with (S)-3-((2,5-dioxocyclopentyloxy)carbonyloxy)propane-1,2-diyl dipalmitate (**20**, 1 mM solution in $CHCl_3$). The slide was left to dry under ambient conditions and stored at -20^{0}C or under vacuum.

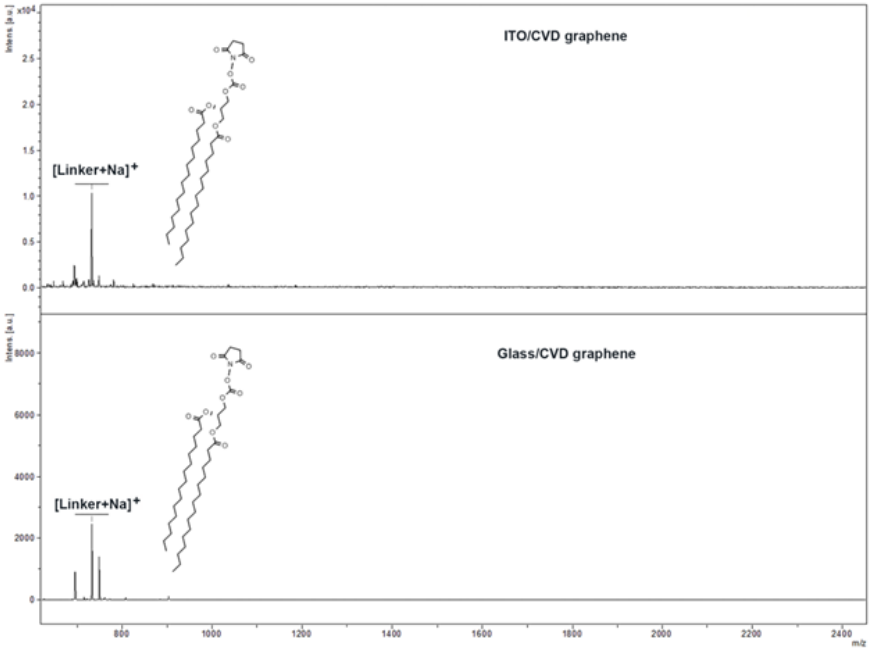

Figure 165. MALDI-tof spectra of bidentate linker on (top) ITO/G-(3,4-($C_{18}H_{37}O)_2$Ph)and on (bottom) Glass/G-(3,4-($C_{18}H_{37}O)_2$Ph); m/z 732.50 [Linker+Na]$^+$.

3.5.4. General method for the carbohydrate printing:

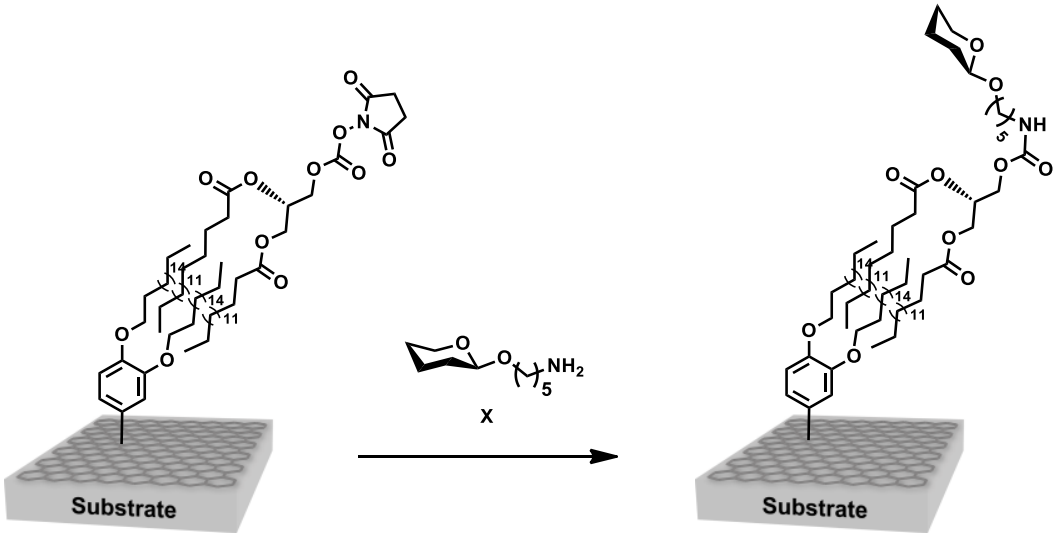

Solutions (100 μM in phosphate buffer 300 mM, pH 8.7) of C5-amino linked carbohydrates (**GlcNAc**, **LacNAc**, **Lac** and **Le^x**) were robotically printed (50 droplets, ≈ 15 nL, ≈ 1.7 pmol) onto slides functionalized with activated bidentate linker at a pitch of 750 μm in both x and y-directions, and left to react overnight at r.t. and controlled humidity of 90%. The slides were quenched by immersion in ethanolamine solution (50 mM in sodium borate buffer pH = 9.0).

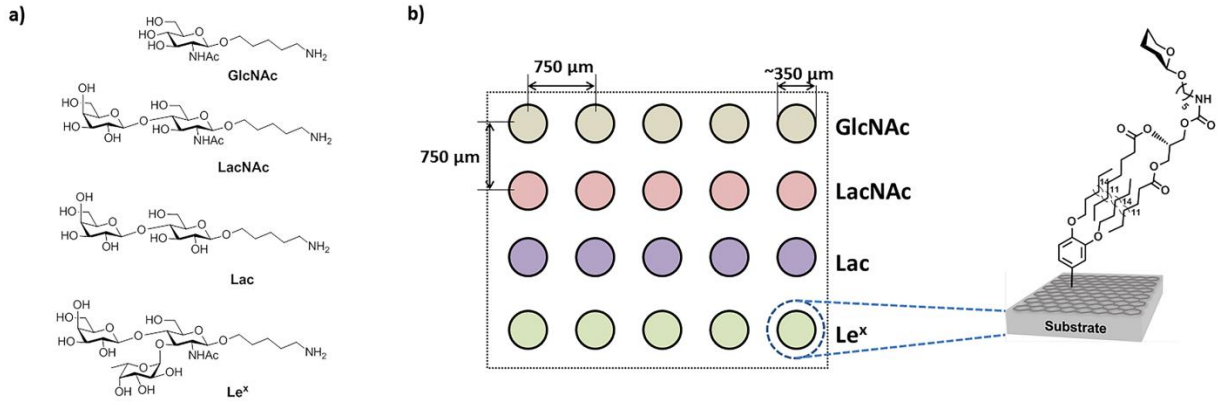

Figure 166. (a) Chemical structure of carbohydrates used in microarray preparation. (b) Schematic representation of the CVD graphene-based glycan array.

3.5.5. *Comparison between hydrophobic ITO and ITO/G-(3,4-($C_{18}H_{37}O$)$_2$Ph).*

Hydrophobic modification of ITO slides was performed as previously described.[265] Briefly, after basic piranha treatment ITO slides were incubated with 2% 3-aminopropyl trietoxysilane (APTES) and cured for 2 hours at 80 °C. After silanization, slide surfaces were reacted overnight with a solution of stearyl succinimide ester in DMF (10mM).

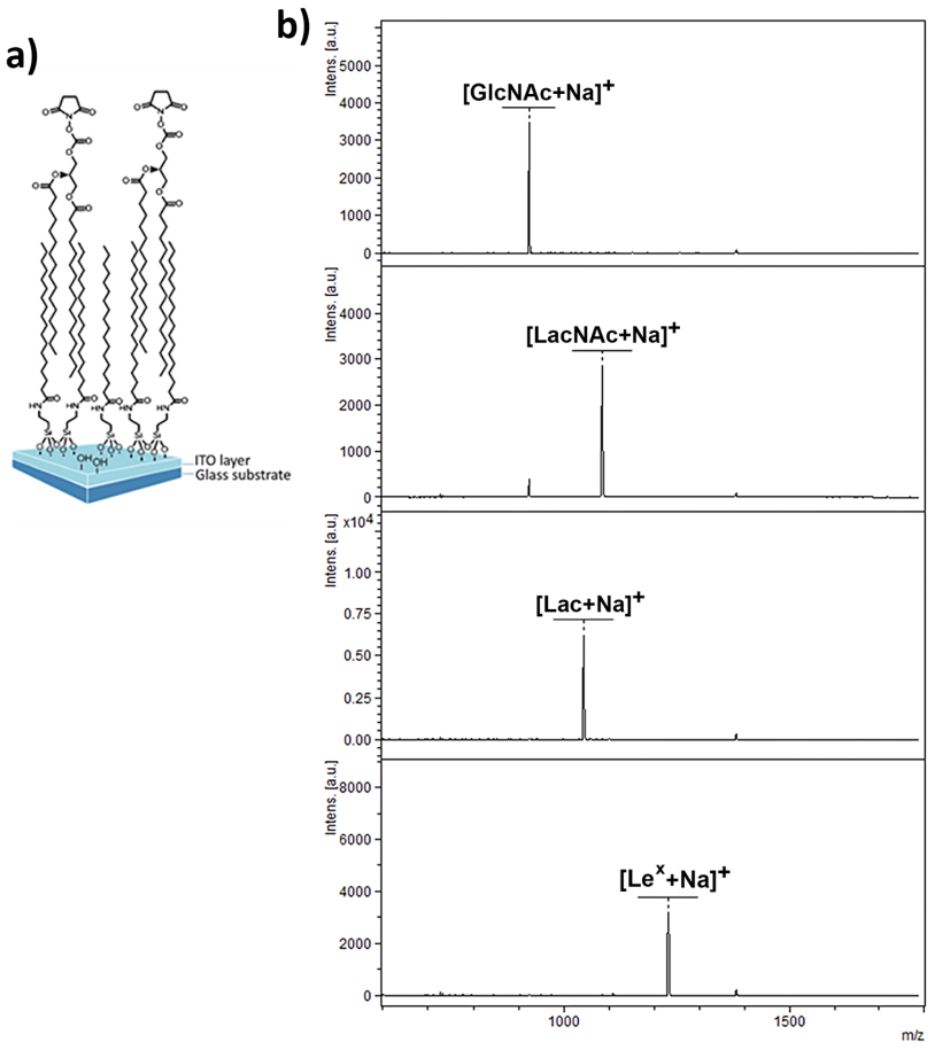

Figure 167. a) Schematic representation of hydrophobic coated ITO slides (lacking CVDG coating) and b) MALDI tof spectra carbohydrates immobilized on hydrophobic ITO slides (lacking CVDG coating).

Table 21. MS detection of different immobilized carbohydrates using APTES modified ITO (lacking CVDG coating), Glass/G-(3,4-($C_{18}H_{37}O)_2$Ph) and ITO/G-(3,4-($C_{18}H_{37}O)_2$Ph).

Carbohydrate	m/z $[M+Na]^+$	ITO/APTES		Glass/G-(3,4-($C_{18}H_{37}O)_2$Ph)		ITO/G-(3,4-($C_{18}H_{37}O)_2$Ph)	
		Peak intensity	S/N	Peak intensity	S/N	Peak intensity	S/N
GlcNAc	923.65	3483	598.9	5292	736.4	6372	642.7
LacNAc	1085.71	2846	386.0	2016	385.3	7452	783.0
Lactose	1044.68	6275	964.4	1577	276.2	23014	1911.9
Le^x	1231.76	3189	526.7	2789	417.1	2783	271.2

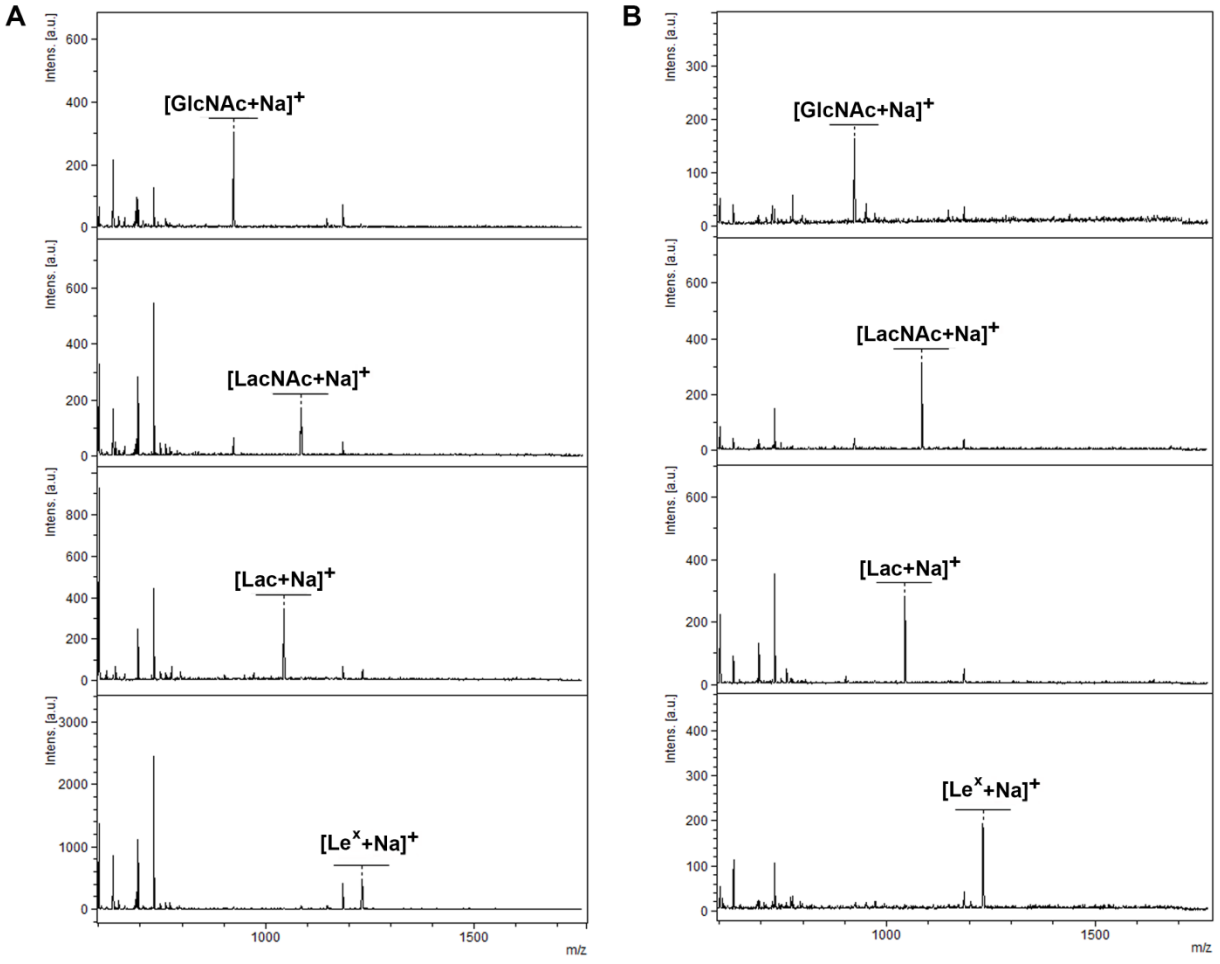

Figure 168. Carbohydrates microarrays prepared on non-functionalized CVDG through direct immobilization of bidentate linker 20. (a) MALDI tof spectra of carbohydrates immobilized on ITO/G and (b) MALDI tof spectra of carbohydrates immobilized on Glass/G.

Table 22. MS detection of different immobilized carbohydrates using non-chemically modified CVDG-based substrate by MALDI-TOF.

Carbohydrate	m/z $[M+Na]^+$	ITO/CVDG w/o C18 chains		Glass/CVDG w/o C18 chains	
		Peak intensity	S/N	Peak intensity	S/N
GlcNAc	923.65	306	88.4	162	30.4
LacNAc	1085.71	174	44.3	314	70.5
Lactose	1044.68	345	71.2	282	68.2
Le^x	1231.76	483	117.8	195	41.1

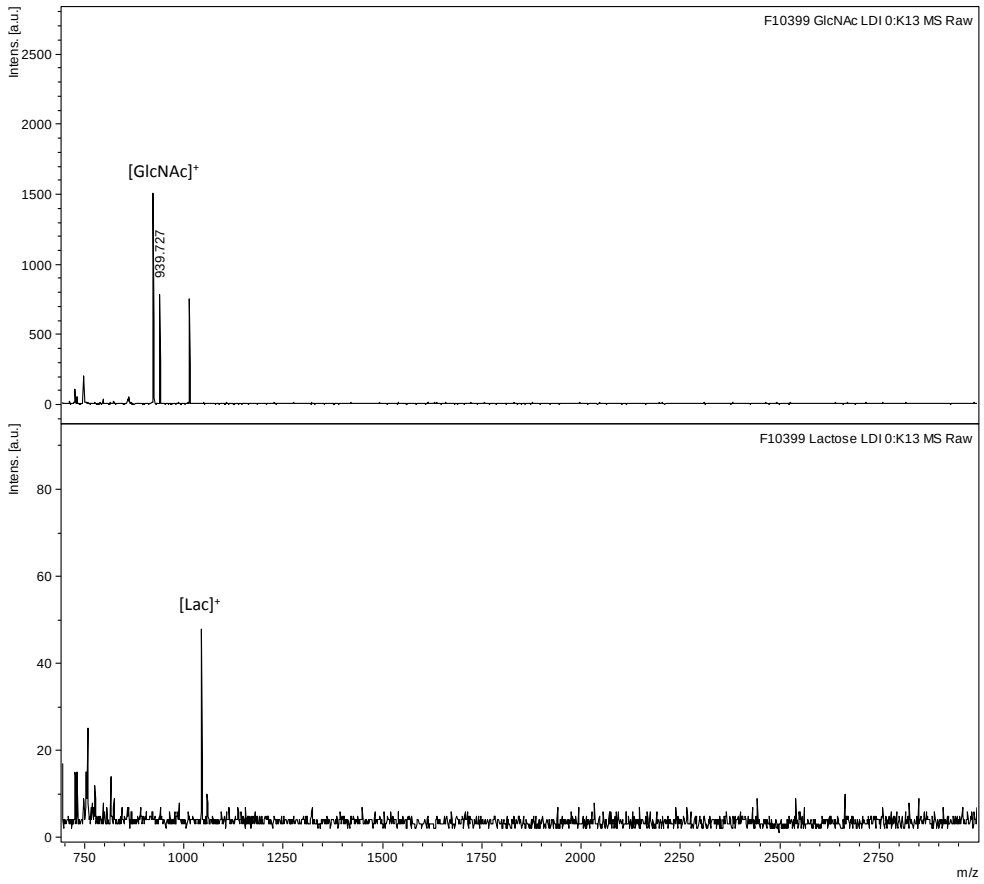

Figure 169. Mass spectra of carbohydrates immobilized on ITO/G-(3,4-$(C_{18}H_{37}O)_2$Ph) microarrays by matrix free LDI.

3.6. Diagnostic approaches

3.6.1. pH sensing

The SiO_2/mGFET or SiO_2/mGFET-(*p*-(CH_2CO_2H)Ph) was located in the g-SGFET-cell and they were incubated in PBS solution (10 mM, 600 μL) with the corresponding pH. After 30'', the measurement was performed. Subsequently, the PBS solution was removed and the cavity was washed 3 times with the next PBS solution with different pH. After measuring, the device was washed by rising in water and dried under N_2 flow.

Tabla 23. Variation of the CNP in function of the pH before and after functionalization for SiO_2/mGFET with 29.4 % I_D/I_G increment.

SiO_2/mGFET		**SiO_2/mGFET-(*p*-(CH_2CO_2H)Ph)**	
pH	CNP	pH	CNP
2.62	0.103724	2.31	0.103319
3.44	0.107748	3.29	0.117198
5.38	0.148747	4.17	0.140891
6.10	0.165847	5.42	0.177761
7.06	0.185346	6.25	0.199734
8.81	0.210641	7.32	0.222358
-	-	8.08	0.226639
-	-	9.35	0.247642

Tabla 24. Variation of the CNP in function of the pH before and after functionalization for SiO_2/mGFET with 10 % I_D/I_G increment.

SiO_2/mGFET		**SiO_2/mGFET-(*p*-(CH_2CO_2H)Ph)**	
pH	CNP	pH	CNP
5.38	0.132082	4.27	0.159257
6.10	0.148514	5.63	0.186802
7.06	0.164845	6.33	0.1982071
8.81	0.189979	7.41	0.214566
-	-	8.61	0.215647

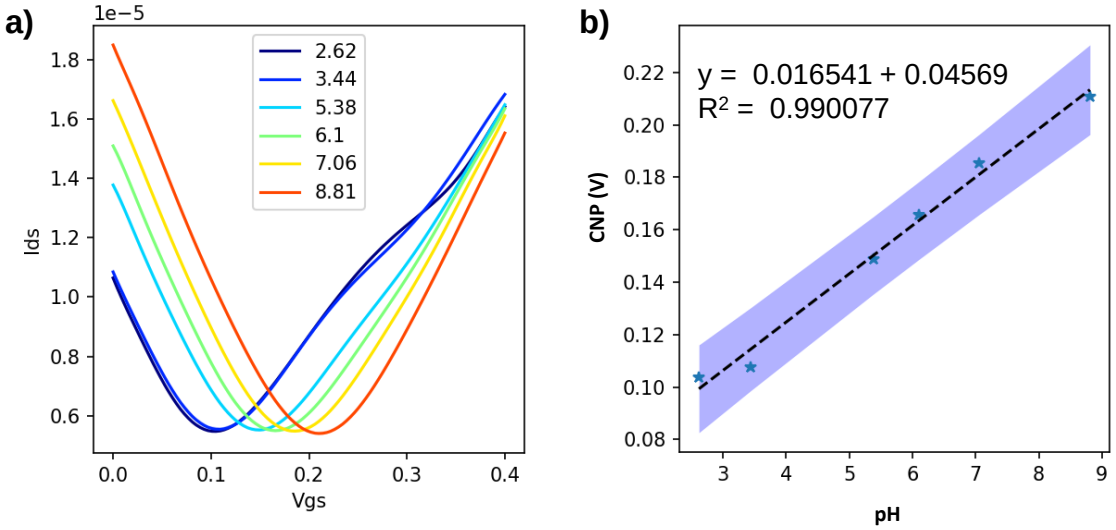

Figure 170. a) I-V curve for the different pH solutions and b) variation of the CNP in function of the pH for SiO_2/mGFET with 29.4 % I_D/I_G increment before functionalization.

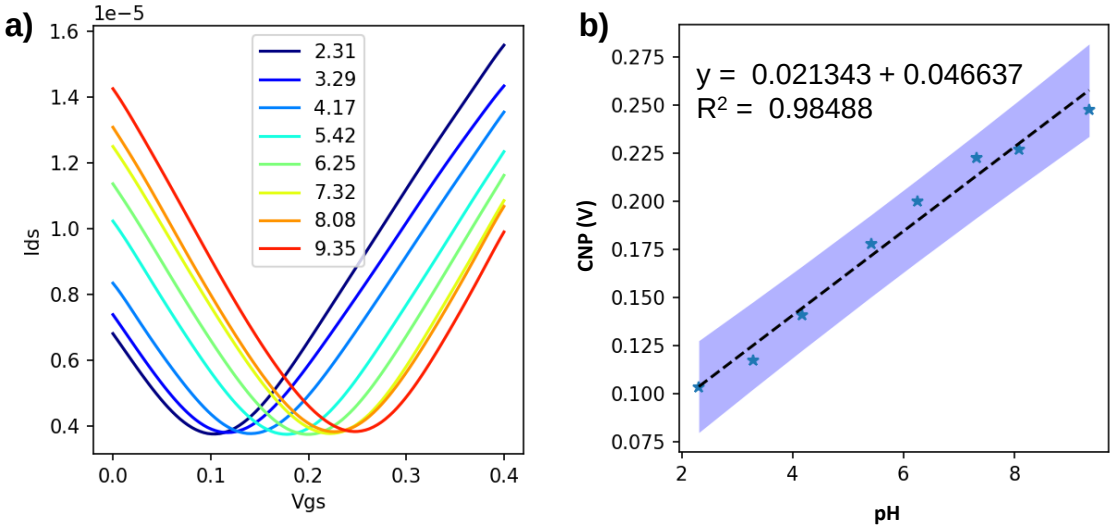

Figure 171. a) I-V curve for the different pH solutions and b) variation of the CNP in function of the pH for SiO_2/mGFET with 29.4 % I_D/I_G increment after functionalizacion.

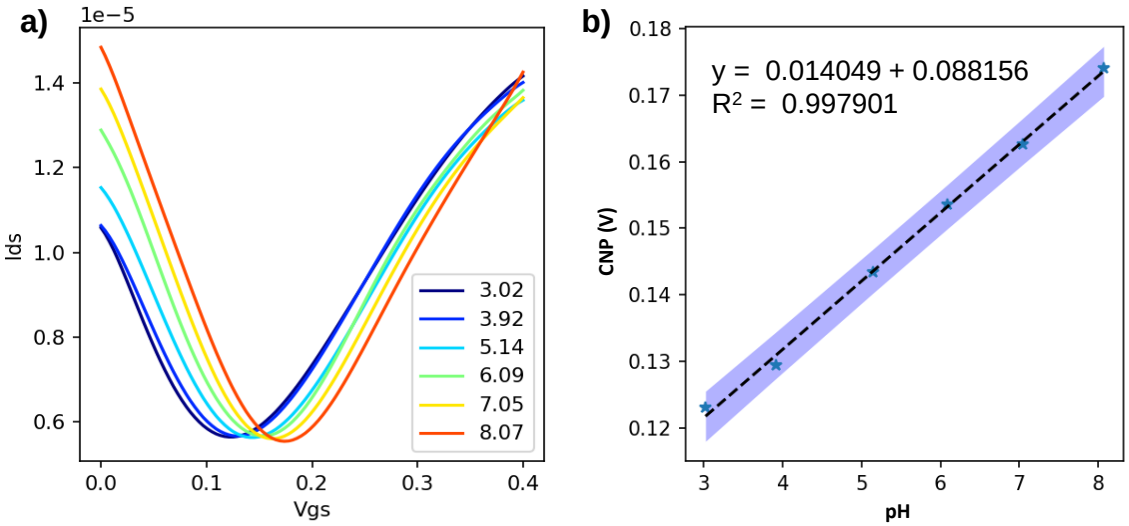

Figure 172. a) I-V curve for the different pH solutions and b) variation of the CNP in function of the pH for SiO_2/mGFET with 10 % I_D/I_G increment before functionalization.

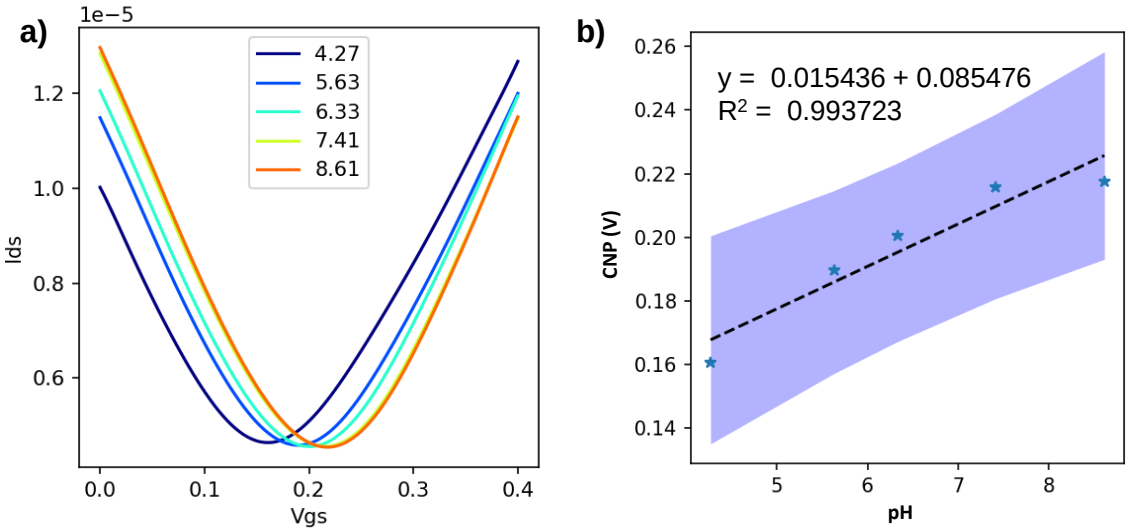

Figure 173. a) I-V curve for the different pH solutions and b) variation of the CNP in function of the pH for SiO_2/mGFET with 10 % I_D/I_G increment after functionalization.

3.6.2. *Lectin incubation*:

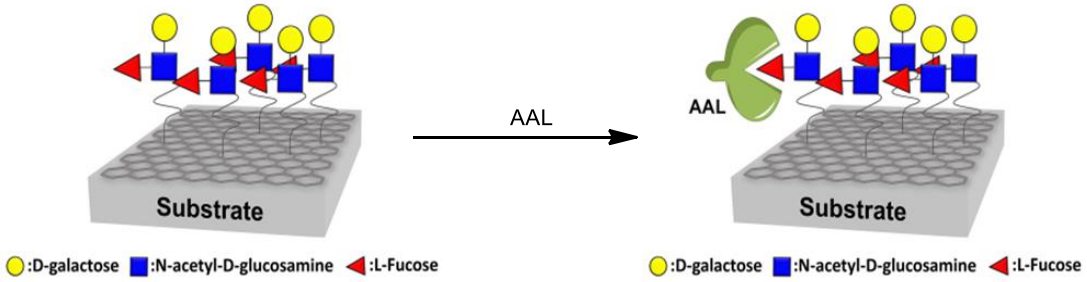

Subarrays were compartmentalized using 8-well ProPlate® incubation chambers from GraceBiolabs and treated with *Aleuria aurantia* lectin (AAL). A solution containing AAL-555 or unconjugated AAL (50 µg/mL in 50 mM Hepes buffer pH=8.0) was incubated at room temperature for one hour. Before removing the incubation chamber the subarrays were washed sequentially with Hepes buffer and water. The complete slides were washed by immersion in water and dried under a stream of argon.

3.6.3. Thrombin Incubation and electric measure:

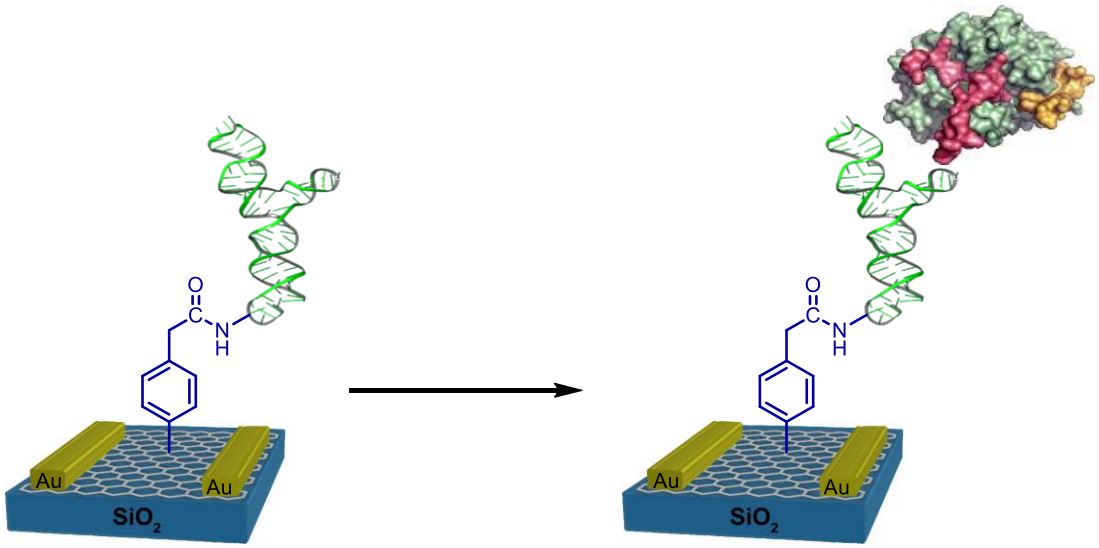

The previous aptamer cross-linked SiO_2/mGFET-(*p*-(CH_2CO_2H)Ph) was deposited in the g-SGFET-cell and a solution of 300 µL of the corresponding thrombin concentration in PBS (10 mM) was incubated for 30 minutes. After the incubation, the solution was removed, and the non-linked thrombin was washed three times with PBS (1 mM, 600 µL). In order to perform the corresponding electronic measurement, PBS (1mM, 600 µL) was added in the cavity cell (Figure 62). After measuring, PBS was removed and the cavity was washed three times with fresh PBS (10 mM, 600 µL). Subsequently, the next thrombin solutions were incubated. For our experiment, an increasing order of the following concentration solutions of thrombin were used: 0.208, 2.080, 20.80 and 208.00 nM.

4. REFERENCES

[1] Partington, J. R.; *A Short History of Chemistry*, Dover Publications, 1989.
[2] Baptista F. R.; Belhout, S. A.; Giordani, S.; Quinn, S. J. Recent developments in carbon nanomaterialsensor. *Chem. Soc. Rev.* **2015**, *44*, 4433-4453.
[3] Georgakilas, V.; Perman, J. A.; Tucek, J.; Zboril, R. Broad Family of Carbon Nanoallotropes: Classification, Chemistry, and Applications of Fullerenes, Carbon Dots, Nanotubes, Graphene, Nanodiamonds, and Combined Superstructures. *Chem. Rev.* **2015**, *115* (11), 4744–4822.
[4] Geim, A. K.; Philip, K. Carbon wonderland. Sci. Am. **2018**, *298* (4) 90-97.
[5] Kroto, H. W.; Heath, J. R.; O'Brien, S. C.; Curl, R. F.; Smalley, R. E. C 60: Buckminsterfullerene. *Nature.* **1985**, *318*, 162–163.
[6] Ugarte, D. Curling and closure of graphitic networks under electron-beam irradiation. *Nature* **1992**, *359*, 707-709.
[7] Xu, X. Y.; Ray, R.; Gu, Y. L.; Ploehn, H. J.; Gearheart, L.; Raker, K.; Scrivens, W. A. Electrophoretic Analysis and Purification of Fluorescent Single-Walled Carbon Nanotube Fragments. *J. Am. Chem. Soc.* **2004**, *126*, 12736-12737.
[8] Radushkevich, L. V.; Lukyanovich, V. M. O structure ugleroda, obrazujucegosja pri termiceskom razlozenii okisi ugleroda na zeleznom kntakte. *Zurn. Fisic. Chim*. **1952**, *26*, 88-95.
[9] Oberlin, A.; Endo, M.; Koyama, T. Filamentous growth of carbon through benzene decomposition. *J. Cryst. Growth* **1976**, *32*, 335-349.
[10] Iijima, S. Helical microtubules of graphitic carbon. *Nature.* **1991**, *354*, 56-58.
[11] Novoselov, K. S.; Geim, A. K.; Morozov, S. V.; Jiang, D.; Zhang, Y.; Dubonos, S. V.; Grigorieva, I. V.; Firsov, A. A. Electric field effect in atomically thin carbon films. *Science*. **2004**, *306*, 666-669.
[12] Bianco, A.; Cheng, H.-M., Enoki, T., Gogotsi, Y., Hurt, R. H., Koratkar, N., Zhang, J. All in the graphene family – A recommended nomenclature for two-dimensional carbon materials. *Carbon*. **2013**, *65*, 1–6.
[13] Wick, P.; Louw-Gaume, A. E.; Kucki, M.; Krug, H. F.; Kostarelos, K.; Fadeel, B.; Bianco, A. Classification Framework for Graphene-Based Materials. *Angew. Chemie Int. Ed.* **2014**, *53*(30), 7714–7718.
[14] Jung, I.; Dikin, D. A.; Piner, R. D.; Ruoff, R. S. Tunable Electrical Conductivity of Individual Graphene Oxide Sheets Reduced at "Low" Temperatures. *Nano Lett.* **2008**, *8*(12), 4283–4287.
[15] Bianco, A. Graphene: Safe or Toxic? The Two Faces of the Medal. *Angew. Chemie Int. Ed.* **2013**, *52*(19), 4986–4997.
[16] Bonaccorso, F.; Lombardo, A.; Hasan, T.; Sun, Z.; Colombo, L.; Ferrari, A. C. Production and Processing of Graphene and 2D Crystals. *Mater. Today.* **2012**, *15* (12), 564–589.
[17] Alonso, J. M.; Díaz-Álvarez, A. E.; Criado, A.; Pérez, D.; Peña, D.; Guitián, E. Cloverphene: A Clover-Shaped Cata-Condensed Nanographene with Sixteen Fused Benzene Rings. *Angew. Chemie Int. Ed.* **2012**, *51* (1), 173–177.
[18] Casiraghi, C.; Hartschuh, A.; Lidorikis, E.; Qian, H.; Harutyunyan, H.; Gokus, T.; Novoselov, K. S.; Ferrari, A. C. Rayleigh Imaging of Graphene and Graphene Layers. *Nano Lett.* **2007**, *7* (9), 2711–2717.
[19] Novoselov, K. S.; Falko, V. I.; Colombo, L.; Gellert, P. R.; Schwab, M. G.; Kim, K. A Roadmap for Graphene. *Nature.* **2012**, *490* (7419), 192–200.
[20] Nicolosi, V.; Chhowalla, M.; Kanatzidis, M. G.; Strano, M. S.; Coleman, J. N. Liquid Exfoliation of Layered Materials. *Science.* **2013**, *340*(6139), 1226419–1226419.
[21] Hernandez, Y.; Nicolosi, V.; Lotya, M.; Blighe, F. M.; Sun, Z.; De, S.; McGovern, I. T.; Holland, B.; Byrne, M.; Gun'Ko, Y. K. High-Yield Production of Graphene by Liquid-Phase Exfoliation of Graphite. *Nat. Nanotechnol.* **2008**, *3* (9), 563–568.
[22] Ciesielski, A.; Samorì, P. Graphene via Sonication Assisted Liquid-Phase Exfoliation. *Chem. Soc. Rev.* **2014**, *43*(1), 381–398.
[23] Johnson, D. W.; Dobson, B. P.; Coleman, K. S. A manufacturing perspective on graphene dispersions. *Curr. Opin. Colloid Interface Sci.* **2015** *20*, 367–382
[24] Brodie B.C. On the atomic weight of graphite. *Philos. Trans. R. Soc. London*. **1859**, *149*, 249-259.
[25] Staudernmaier, L. Verfahren zur darstellung der graphitsäure. *Ber. Dtsch. Chem. Ges*., **1898**, *31*, 1481-1487.
[26] Hummers, W. S.; Offeman, R. E. Preparation of Graphitic Oxide. *J. Am. Chem. Soc.* **1958**, *80*(6), 1339.
[27] Marcano, D. C.; Kosynkin, D. V.; Berlin, J. M.; Sinitskii, A.; Sun, Z.; Slesarev, A.; Tour, J. M. Improved Synthesis of Graphene Oxide. *ACS Nano*. **2010**, 4(8), 4806–4814.
[28] Talyzin, A.V.; Mercier, G.; Klechikov, A.; Hedenstrom, M.; Johnels, D.; Wei, D.; Cotton, D.; Opitz, A.; Moons, E. Brodie vs. hummers graphite oxides for preparation of multi-layered materials. Carbon. **2017**, 115, 430–440.
[29] Higginbotham, A. L.; Kosynkin, D. V.; Sinitskii, A.; Sun, Z.; Tour, J. M. Lower-Defect Graphene Oxide Nanoribbons from Multiwalled Carbon Nanotubes. *ACS Nano*. **2010**, *4*(4), 2059–2069.

[30] Chang, W. T.; Chao, Y. H.; Li, C. W.; Lin, K. L.; Wang, J. J.; Kumar, S. R.; Lue, S. J. Graphene oxide synthesis using microwave-assisted vs. modified Hummer's methods: Efficient fillers for improved ionic conductivity and suppressed methanol permeability in alkaline methanol fuel cell electrolytes. *J. Power Sources.* **2019***, 414, 86–95.*
[31] Tkachev, S. V.; Buslaeva, E. Y.; Naumkin, A. V.; Kotova, S. L.; Laure, I. V.; Gubin, S. P. Reduced Graphene Oxide. *Inorg. Mater.* **2012**, *48(*8), 796–802.
[32] Lavin-Lopez, M. P.; Paton-Carrero, A.; Sanchez-Silva, L.; Valverde, J. L.; Romero, A. Influence of the reduction strategy in the synthesis of reduced graphene oxide. *Adv. Powder Technol.* **2017***, 28*(12), 3195–3203.
[33] McAllister, M. J.; Li, J. L.; Adamson, D. H.; Schniepp, H. C.; Abdala, A. A.; Liu, J.; Herrera-Alonso, M.; Milius, D. L.; Car, R.; Prud'homme, R. K.; Aksay, I. A. Single sheet functionalized graphene by oxidation and thermal expansion of graphite. *Chem. Mater.* **2007**, *19*, 4396-4404.
[34] Park, S.; An, J.; Potts, J. R.; Velamakann, A.; Murali, S.; Ruoss, R. S.; Hydrazine-reduction of graphite and graphene oxide. *Carbon.* **2011**, *49*, 3019-3023.
[35] Zhang, J.; Yang, H.; Shen, G.; Cheng, P.; Guo, S. Reduction of graphene oxide via ascorbic acid. *Chem. Commun*. **2010**, *46*, 1112-1114.
[36] Ramesha, G. K.; Sampath, N. S. Electrochemical reduction of oriented graphene oxide films: an in situ Raman spectroelectrochemical study. *J. Phys. Chem. C*. **2009**, *113*, 7985-7989.
[37] Xie, X.; Zhou, Y.; Huang, K. Advances in Microwave-Assisted Production of Reduced Graphene Oxide. *Front. Chem.* **2019***,* 7*. 355.*
[38] Lee, B. S.; Lee, Y.; Hwang, J. Y.; Choi, Y. C. Structural Properties of Reduced Graphene Oxides Prepared Using Various Reducing Agents. *Carbon Lett.* **2015**, *16*(4), 255–259.
[39] Mishra, N.; Boeckl, J.; Motta, N.; Iacopi, F. Graphene Growth on Silicon Carbide: A Review. *Phys. Status Solidi.* **2016**, *213*(9), 2277–2289.
[40] Kern, W.; Schnable, G. L. Low-Pressure Chemical Vapor Deposition for Very Large-Scale Integration Processing - A Review. *IEEE T. Electron. Dev.* **1979**, *26*, 647-657.
[41] Li, X.; Cai, W.; An, J.; Kim, S.; Nah, J.; Yang, D.; Ruoff, R. S. Large-Area Synthesis of High-Quality and Uniform Graphene Films on Copper Foils. *Science.* **2011***, 324*(5932)*,* 1312–1314.
[42] Mattevi, C.; Kim, H.; Chhowalla, M. A Review of Chemical Vapour Deposition of Graphene on Copper. *J. Mater. Chem.* **2011**, *21* (10), 3324–3334.
[43] Li, X.; Cai, W.; An, J.; Kim, S.; Nah, J.; Yang, D.; Piner, R.; Velamakanni, A.; Jung, I.; Tutuc, E.; Banerjee, S.; Colombo, L.; Ruoff., R. S. Large-Area Synthesis of High-Quality and Uniform Graphene Films on Copper Foils. *Science.* **2009**, 324, 1312–1314.
[44] Li, X.; Cai, W.; Colombo, L.; Ruoff, R. S. Evolution of Graphene Growth on Ni and Cu by Carbon Isotope Labeling. *Nano Lett.* **2009**, 9, 4268-4272.
[45] Yan, K.; Peng, H.; Zhou, Y.; Li, H.; Liu, Z. Formation of Bilayer Bernal Graphene: Layer-by-Layer Epitaxy via Chemical Vapor Deposition. *Nano Letters.* **2011,** *11*(3), 1106–1110.
[46] a) Kim, K.; DaSilva, A.; Huang, S.; Fallahazad, B.; Larentis, S.; Taniguchi, T; Tutuc, E. Tunable moiré bands and strong correlations in small-twist-angle bilayer graphene. *Proc. Nat.l Acad. Sci.* **2017***, 114*(13), 3364–3369. b) Kim, K.; Yankowitz, M.; Fallahazad, B.; Kang, S.; Movva, H. C. P.; Huang, S.; Tutuc, E. Van der Waals Heterostructures with High Accuracy Rotational Alignment. *Nano Letters. **2016,** 16*(3), 1989–1995*.*
[47] Zhang, Y.; Zhang, L.; & Zhou, C. Review of Chemical Vapor Deposition of Graphene and Related Applications. *Acc. Chem. Res.* **2013** *46*(10), 2329–2339*.*
[48] Liang, X.; Sperling, B. A.; Calizo, I.; Cheng, G.; Li, Q.; Zhu, X.; Yuan, H.; Hight Walker, A. R.; Liu, Z.; Peng, L.; Richter, C. A. Toward Clean and Crackless Transfer of Graphene. *ACS Nano*. **2011**, *5*(11), 9144–9153.
[49] Bae, S.; Kim, H.; Lee, Y.; Xu, X.; Park, J.-S.; Zheng, Y.; Balakrishnan, J.; Lei, T.; Kim, H. R.; Song, Y. Roll-to-Roll Production of 30-Inch Graphene Films for Transparent Electrodes. *Nat. Nanotechnol.* **2010**, *5*, 574–578.
[50] Lindwall, N.; Kalabukhov, A.; Yurgens, A. Cleaning graphene using atomic force microscope, *J. Appl. Phys.* **2012**, *111*, 064904.
[51] Prudkovskiya, V.S.; Katin, K.P.; Maslov, M.M.; Puech, P.; Yakimova, R.; Deligeorgis, G. Efficient cleaning of graphene from residual lithographic polymers by ozone treatment. *Carbon*. **2016**, *109*, 154-162
[52] Mao, D. C.; Peng, S. A.; Wang, S. Q.; Zhang, D. Y.; Shi, J. Y.; Wang, X.; Jin, Z. Towards a cleaner graphene surface in graphene field effect transistor via N,N-Dimethylacetamide. *Mater. Res. Express.* **2016**, *3*(9), 095011.
[53] Mao, D. C.; Peng, S. A.; Wang, S. Q.; Zhang, D.Y.; Shi, J. Y.; Wang X.; Jin, Z. Towards a cleaner graphene surface in graphene field effect transistor via N,N-Dimethylacetamide, *Mater. Res. Express.* **2016**, *3,* 095011

[54] Choi, W.; Shehzad, M. A.; Park, S.; Seo, Y. Influence of removing PMMA residues on surface of CVD graphene using a contact-mode atomic force Microscope, *RSC Adv*., **2017**, *7*, 6943-6949.
[55] Lee, C.; Wei, X.; Kysar, J. W.; Hone, J. Measurement of the Elastic Properties and Intrinsic Strength of Monolayer Graphene. *Science.* **2008**, *321*(5887), 385–388.
[56] Nair, R. R.; Blake, P.; Grigorenko, A. N.; Novoselov, K. S.; Booth, T. J.; Stauber, T.; Peres, N. M. R.; Geim, A. K. Fine Structure Constant Defines Visual Transparency of Graphene. *Science.* **2008**, *320*(5881), 1308–1308.
[57] Gokus T.; Nair, R. R.; Bonetti, A. Making graphene luminescent by oxygen plasma treatment. *ACS Nano*, **2009**, *3*: 3963–3968.
[58] Balandin, A. A.; Ghosh, S.; Bao, W.; Calizo, I.; Teweldebrhan, D.; Miao, F.; Lau, C. N. Superior Thermal Conductivity of Single-Layer Graphene. *Nano Lett.* **2008**, *8*(3), 902–907.
[59] Wang, J.; Ma, F.; Liang, W.; Sun, M. Electrical properties and applications of graphene, hexagonal boron nitride (h-BN), and graphene/h-BN heterostructures. Mater. Today Phys. **2017**, *2,* 6-34.
[60] Cooper, D. R.; D'Anjou, B.; Ghattamaneni, N.; Harack, B.; Hilke, M.; Horth, A.; Majlis, N.; Massicotte, M.; Vandsburger, L.; Whiteway, E.; Yu, V. Experimental Review of Graphene. ISRN Condensed Matter Physics (International Scholarly Research Network) **2012**: 1–56.
[61] Castro Neto, A.H.; Guinea, F.; Peres, N. M. R.; Novoselov, K. S.; Geim, A. K. *The electronic properties of graphene. Rev. Mod. Phys.* **2009**, *81*(1), 109-162.
[62] Forsyth, R.; Devadoss, A.; Guy, O. J. Graphene Field Effect Transistors for Biomedical Applications: Current Status and Future Prospects. *Diagnostics.* **2017**, *7*(3), 45
[63] Oostinga, J. B.; Heersche, H. B.; Liu, X.; Morpurgo, A. F.; Vandersypen, L. M. K. Gate-induced insulating state in bilayer graphene devices. *Nat. Mater*, **2007**, *7*(2), 151–157.
[64] Cao, Y.; Fatemi, V.; Demir, A.; Fang, S.; Tomarken, S. L.; Luo, J. Y.; Jarillo-Herrero, P. Correlated insulator behaviour at half-filling in magic-angle graphene superlattices*. Nature,* **2018***, 556(7699), 80–84.*
[65] Gibney, E. How "magic angle" graphene is stirring up physics. *Nature*, **2019** *565*(7737), 15–18.
[66] Cao, Y.; Fatemi, V.; Fang, S.; Watanabe, K.; Taniguchi, T.; Kaxiras, E.; Jarillo-Herrero, P. Unconventional superconductivity in magic-angle graphene superlattices. *Nature*. **2018**, *556*(7699), 43–50.
[67] a) Niyogi, S.; Bekyarova, E.; Hong, J.; Khizroev, S.; Berger, C.; de Heer, W.; Haddon, R. C. Covalent Chemistry for Graphene Electronics. *J. Phys. Chem. Lett.* **2011***, 2*(19), 2487–2498. b) Kuila, T.; Bose, S.; Mishra, A. K.; Khanra, P.; Kim, N. H.; Lee, J. H. Chemical functionalization of graphene and its applications. *Prog. Mater. Sci.* **2012***, 57*(7), 1061–1105.
[68] a) Georgakilas, V.; Tiwari, J. N.; Kemp, K. C.; Perman, J. A.; Bourlinos, A. B.; Kim, K. S.; Zboril, R. Noncovalent Functionalization of Graphene and Graphene Oxide for Energy Materials, Biosensing, Catalytic, and Biomedical Applications. *Chem. Rev.* **2016***, 116*(9), 5464–5519. b) Georgakilas, V.; Otyepka, M.; Bourlinos, A. B.; Chandra, V.; Kim, N.; Kemp, K. C.; Hobza, P.; Zboril, R.; Kim, K. S. Functionalization of Graphene: Covalent and Non-Covalent Approaches, Derivatives and Applications. *Chem. Rev.* **2012**, *112* (11), 6156–6214.
[69] Zhang, H.; Bekyarova, E.; Huang, J.-W.; Zhao, Z.; Bao, W.; Wang, F.; Lau, C. N. Aryl Functionalization as a Route to Band Gap Engineering in Single Layer Graphene Devices. *Nano Letters*, **2011**, 11(10), 4047–4051.
[70] Sreeprasad, T. S.; Berry, *V.;* How Do the Electrical Properties of Graphene Change with its Functionalization? *Small.* **2013**, *9 (*3), 341–350.
[71] Xu, X.; Liu, C.; Sun, Z.; Cao, T.; Zhang, Z.; Wang, E.; Liu, K. Interfacial engineering in graphene band gap. *Chem. Soc. Rev.* **2018**, *47*(9), 3059-3099.
[72] a) Criado, A.; Melchionna, M.; Marchesa, S.; Prato, M. The Covalent Functionalization of Graphene on Substrates. *Angew. Chem. Int. Ed.* **2015**, *54*(37), 10734-10750. b) Deokar, G.; Avila, J.; Razado-Colambo, I.; Codron, J.-L.; Boyaval, C.; Galopin, E.; Vignaud, D. Towards high quality CVD graphene growth and transfer. *Carbon.* **2015***, 89*, 82–92*.*
[73] Surwade, S. P.; Li, Z.; Liu, H. Thermal Oxidation and Unwrinkling of Chemical Vapor Deposition-Grown Graphene. *J. Phys. Chem. C.* **2012***, 116*(38), 20600–20606.
[74] Liu, L.; Ryu, S.; Tomasik, M. R.; Stolyarova, E.; Jung, N.; Hybertsen, M. S.; Flynn, G. W. Graphene Oxidation: Thickness-Dependent Etching and Strong Chemical Doping. *Nano Lett.* **2008***, 8*(7), 1965–1970.
[75] Valenta, L.; Kovaříček, P.; Valeš, V.; Bastl, Z.; Drogowska, K. A.; Verhagen, T. A.; Kalbáč, M. Spatially resolved covalent functionalization patterns on graphene*. Angew. Chem. Int. Ed,* **2018***, 5*(58), 1324-1328.
[76] Itkis, M. E.; Wang, F.; Ramesh, P.; Bekyarova, E.; Niyogi, S.; Chi, X.; Haddon, R. C. Enhanced photosensitivity of electro-oxidized epitaxial graphene. *Appl. Phys. Lett.* **2011***, 98*(9), 093115.
[77] Hossain, M. Z.; Johns, J. E.; Bevan, K. H.; Karmel, H. J.; Liang, Y. T.; Yoshimoto, S.; Hersam, M. C. Chemically homogeneous and thermally reversible oxidation of epitaxial graphene*. Nat. Chem.* **2012***, 4*(4), 305–309.

[78] Elias, D. C.; Nair, R. R.; Mohiuddin, T. M. G.; Morozov, S. V.; Blake, P., Halsall, M. P.; Novoselov, K. S. Control of Graphene's Properties by Reversible Hydrogenation: Evidence for Graphane. *Science.* **2009***, 323*(5914), 610–613.
[79] Pakornchote, T.; Geballe, Z. M.; Pinsook, U.; Taychatanapat, T.; Busayaporn, W.; Bovornratanaraks, T.; Goncharov, A. F. Raman spectroscopy on hydrogenated graphene under high pressure. *Carbon.* **2020***, 156,* 549-557.
[80] a) Robinson, J. T.; Burgess, J. S.; Junkermeier, C. E.; Badescu, S. C.; Reinecke, T. L.; Perkins, F. K.; Zalalutdniov, M. K.; Baldwin, J. W.; Culbertson, J. C.; Sheehan, P. E.; Snow, E. S.; Properties of Fluorinated Graphene Films. *Nano Lett*. **2010**, *10*, 3001-3005. b) Wheeler, V.; Garces, N.; Nyakiti, L.; Myers-Ward, R.; Jernigan, G.; Culbertson, J.; Eddy, C.; Gaskill, K. D.; Fluorine functionalization of epitaxial graphene for uniform deposition of thin high-κ dielectrics *Carbon.* **2012**, *50*, 2307-3014.
[81] Zhang, X.; Hsu, A.; Wang, H.; Song, Y.; Kong, J.; Dresselhaus, M. S.; Palacios, T. Impact of Chlorine Functionalization on High-Mobility Chemical Vapor Deposition Grown Graphene. *ACS Nano*. **2013,** *7*(8), 7262–7270.
[82] Yoshimoto, S.; Mukai, K.; Koitaya, T.; Yoshinobu, J.; Hosaka, S. Monolayer Selective Methylation of Epitaxial Graphene on SiC(0001) through Two-Step Chlorination-Alkylation Reactions. *J. Phys.Chem. C* **2014**, 118, 22096–22101.
[83] Sarkar, S.; Bekyarova, E.; Haddon, R. C. Chemistry at the Dirac Point: Diels Alder Reactivity of Graphene. *Acc. Chem. Res*. **2012**, *45*,673–682.
[84] Sarkar, S.; Bekyarova, E.; Niyogi, S.; Haddon, R. C. Diels-Alder Chemistry of Graphite and Graphene: Graphene as Diene and Dienophile. *J. Am. Chem. Soc*. **2011**, *133*, 3324 –3327.
[85] Li, J.; Li, M.; Zhou, L.-L.; Lang, S.-Y.; Lu, H.-Y.; Wang, D.; Wan, L.-J. Click and Patterned Functionalization of Graphene by Diels–Alder Reaction. *J. Am. Chem. Soc.* **2016**, *138*(24), 7448–7451.
[86] a) Denis, P. A. Organic Chemistry of Graphene: The Diels-Alder Reaction. *Chem. Eur.* **2013***, 19*(46), 15719–15725. b) Cao, Y.; Osuna, S.; Liang, Y.; Haddon, R. C.; Houk, K. N. Diels–Alder Reactions of Graphene: Computational Predictions of Products and Sites of Reaction*. J. Am. Chem. Soc.* **2013***, 135*(46), 17643–17649*.*
[87] Daukiya, L.; Mattioli, C.; Aubel, D.; Hajjar-Garreau, S.; Vonau, F.; Denys, E.; Simon, L. Covalent Functionalization by Cycloaddition Reactions of Pristine Defect-Free Graphene. *ACS Nano.* **2017***, 11*(1), 627–634.
[88] Park, J.; Jin, T.; Liu, C.; Li, G.; Yan, M. Three-Dimensional Graphene–TiO_2 Nanocomposite Photocatalyst Synthesized by Covalent Attachment. *ACS Omega.* **2016***, 1*(3), 351–356*.*
[89] Qin, H.; Hwang, T.; Ahn, C.; Kim, J. A.; Jin, Y.; Cho, Y.; Kim, T. Chemical Amination via Cycloaddition of Graphene for Use in a Glucose Sensor. *J. Nanosci. Nanotechno.* **2016***, 16*(5), 5034–5037.
[90] Dyke, C. A.; Stewart, M. P.; Maya, F.; Tour, J. M. Diazonium-Based Functionalization of Carbon Nanotubes: XPS and GC-MS Analysis and Mechanistic Implications. *Synlett.* **2004**, 1, 155–160.
[91] Yang, M.; Wang, C.; Wei, Q.; Du, B.; Li, H.; Qian, Z. Functionalized Graphene for Biosensing Applications. *Biosens. Nanomater.* **2011**, 1, 221– 235.
[92] Tour, J. M.; Dyke, C. A.; Stewart, M. P.; Maya, F. Diazonium-Based Functionalization of Carbon Nanotubes: XPS and GC-MS Analysis and Mechanistic Implications. Synlett. **2004**, *1*, *155–160.*
[93] Paulus, G. L.; Wang, Q. H.; Strano, M. S. Covalent electron transfer chemistry of graphene with diazonium salts. *Acc. Chem. Res*. **2013**, *46*, 160−170.
[94] Park, M. J.; Choi, H.-H.; Park, B.; Lee, J. Y.; Lee, C.-H.; Choi, Y. S.; Kim, Y.; Yoo, J. M.; Lee, H.; Hong, B. H. Enhanced Chemical Reactivity of Graphene by Fermi Level Modulation. *Chem. Mater.* **2018**, *30*(16), 5602-5609
[95] Hossain, M. Z.; Walsh, M. A.; Hersam, M. C. Scanning Tunneling Microscopy, Spectroscopy, and Nanolithography of Epitaxial Graphene Chemically Modified with Aryl Moieties. *J. Am. Chem. Soc.* **2010**, *132*, 15399–15403.
[96] Greenwood, J.; Phan, T. H.; Fujita, Y.; Li, Z.; Ivasenko, O. Vanderlinden, W.; Van Gorp, H.; Frederickx, W.; Lu, G.; Tahara, K. Covalent Modification of Graphene and Graphite Using Diazonium Chemistry: Tunable Grafting and Nanomanipulation. *ACS Nano.* **2015**, *9*, 5520−5535.
[97] Sampathkumar, K.; Diez-Cabanes, V.; Kovaříček, P.; del Corro, E.; Bouša, M.; Hosek, J.; Kalbac, M.; Frank, O. On the Suitability of Raman Spectroscopy to Monitor the Degree of Graphene Functionalization by Diazonium Salts. *J. Phys. Chem. C.* **2019**, *123*, 22397-22402.
[98] Kovaříček, P.; Vrkoslav, V.; Plšek, J.; Bastl, Z.; Fridrichová, M.; Drogowska, K.; Kalbáč, M. Extended characterization methods for covalent functionalization of graphene on copper. *Carbon.* **2017***, 118,* 200–207.
[99] Min, Q.; Zhang, X.; Chen, X.; Li, S.; Zhu, J.-J. N-doped graphene: an alternative carbon-based matrix for highly efficient detection of small molecules by negative ion MALDI-TOF MS. *Anal. Chem*. **2014**, *86* 9122-9130,
[100] Wang, Q. H.; Jin, Z.; Kim, K. K.; Hilmer, A. J.; Paulus, G. L. C.; Shih, C. J.; Ham, M. H.; Sanchez-Yamagishi, J. D.; Watanabe, K.; Taniguchi, T. Understanding and Controlling the Substrate Effect on

Graphene Electron-Transfer Chemistry via Reactivity Imprint Lithography. *Nat. Chem.* **2012**, *4* (9), 724–732.
[101] Du, X.; Skachko, I.; Barker, A.; Andrei, E. Y. Approaching ballistic transport in suspended graphene. Nat. Nanotechnol. **2008**, 3, 491–495.
[102] Navarro, J. J.; Leret, S.; Calleja, F.; Stradi, D.; Black, A.; Bernardo-Gavito, R.; Miranda, R. Organic Covalent Patterning of Nanostructured Graphene with Selectivity at the Atomic Level. *Nano Lett.* **2015**, *16*(1), 355–361.
[103] Navarro, J. J.; Calleja, F.; Miranda, R.; Pérez, E. M.; Vázquez de Parga, A. L. High yielding and extremely site-selective covalent functionalization of graphene. *Chem. Comm.* **2017***, 53*(75), 10418–10421.
[104] Bisset, M. A.; Konabe, S.; Okada, S.; Tsuji, M.; Ago, H. Enhanced Chemical Reactivity of Graphene Induced by Mechanical Strain. *ACS Nano*, **2013**, *7*, 11, 10335-10343.
[105] De Andres, P. L.; Vergés, J. A. First-principles calculation of the effect of stress on the chemical activity of graphene. *Appl. Phys. Lett.* **2008***, 93*(17), 171915.
[106] Wu, Q.; Wu, Y.; Hao, Y.; Geng, J.; Charlton, M.; Chen, S.; Ren,Y.; Ji, H.; Li, H.; Boukhvalov, D. W.; Piner, R. D.; Bielawski, C. W.; Ruoff, R. S. Selective surface functionalization at regions of high local curvature in graphene, *Chem. Commun*. **2013**, *49*, 677-679.
[107] Deng, S.; Rhee, D.; Lee, W.-K.; Che, S.; Keisham, B.; Berry, V.; Odom, T. W. Graphene Wrinkles Enable Spatially Defined Chemistry, *Nano Lett*. **2019**, *19*, 8, 5640-5646.
[108] a) Koehler, F. M.; Jacobsen, A.; Ensslin, K.; Stampfer, C.; Stark, W. J. *Small* **2010**, *6*,(10), 1125–1130. b) Sharma, R.; Baik, J. H.; Perera, C. J.; Strano, M. S. Anomalously Large Reactivity of Single Graphene Layers and Edges toward Electron Transfer Chemistries*. Nano Lett.* **2010***, 10*(2), 398–405.
[109] Ding, Y.; Peng, Q.; Gan, L.; Wu, R.; Ou, X.; Zhang, Q.; Luo, Z. Stacking-Mode-Induced Reactivity Enhancement for Twisted Bilayer Graphene. *Chem. Mater*. **2016**, *28*, 1034-1039.
[110] Phan, T. H.; Van Gorp, H.; Li Z.; Huynh, T. M. T.; Fujita, Y.; Verstraete, L.; Eyley, S.; Thielemans, W.; Uji-i, H.; Hirsch, B. E.; Mertens, S. F. L.; Greenwood, J.; Ivasenko, O.; De Feyter, S. Graphite and Graphene Fairy Circles: A Bottom-Up Approach for the Formation of Nanocorrals. *ACS Nano.* **2019**, *13*, 5559−5571
[111] a) Bottari, G.; Herranz, M. Á.; Wibmer, L.; Volland, M.; Rodríguez-Pérez, L.; Guldi, D. M.; Torres, T. Chemical functionalization and characterization of graphene-based materials*.* Chem. Soc. Rev. **2017**, *46*(15), 4464–4500. b) Lucherelli, M. A.; Raya, J.; Edelthalhammer, K. F.; Hauke, F.; Hirsch, A.; Abellán, G.; Bianco, A. A straightforward approach to multifunctional graphene. *Chem. Eur.* **2019***, 25*(57), 13218-13223.
[112] Knirsch, K. C.; Schäfer, R. A.; Hauke, F.; Hirsch, A. Mono- and Ditopic Bisfunctionalization of Graphene. *Angew. Chem. Int. Ed.* **2016***, 55*(19), 5861–5864.
[113] a) Singla, R.; Kottantharayil, A. Stable hydroxyl functionalization and p-type doping of graphene by a non-destructive photo-chemical method. *Carbon.* **2019***, 152*, 267-273. b) Liu, H.; Ryu, S.; Chen,Z.; Steigerwald, M. L.; Nuckolls, C.; Brus, L. E. Photochemical Reactivity of Graphene. *J. Am. Chem. Soc.* **2009**, 131(47), 17099-17101. c) Chan, C. K.; Beechem, T. E.; Ohta, T.; Brumbach, M. T.; Wheeler, D. R.; Stevenson, K. J. Electrochemically Driven Covalent Functionalization of Graphene from Fluorinated Aryl Iodonium Salts. *J. Phys. Chem. C.* **2013**, *117*(23), 12038–12044. d) Hess, L. H.; Lyuleeva, A.; Blaschke, B. M.; Sachsenhauser, M.; Seifert, M.; Garrido, J. A.; Deubel, F. Graphene Transistors with Multifunctional Polymer Brushes for Biosensing Applications. *ACS Appl. Mater. Inter.* **2014** *6*(12), 9705–9710. e) Sarkar, S.; Bekyarova, E.; Haddon, R. C. Reversible Grafting of α-Naphthylmethyl Radicals to Epitaxial Graphene. *Angew. Chem. Int. Ed.* **2012***, 51*(20), 4901–4904.
[114] Li, W.; Li, Y.; Xu, K. Azidated graphene: direct azidation from monolayers, click chemistry, and bulk production from graphite. *Nano Letters.* **2020**, *20*(1), 534-539.
[115] Georgakilas, V.; Tiwari, J. N.; Kemp, K. C.; Perman, J. A.; Bourlinos, A. B.; Kim, K. S.; Zboril, R. Noncovalent Functionalization of Graphene and Graphene Oxide for Energy Materials, Biosensing, Catalytic, and Biomedical Applications. *Chem. Rev*. **2016**, *116*, 5464−5519.
[116] Georgakilas, V.; Otyepka, M.; Bourlinos, A. B.; Chandra, V.; Kim, N.; Kemp, K. C.; Kim, K. S. Functionalization of Graphene: Covalent and Non-Covalent Approaches, Derivatives and Applications. *Chem. Rev.* **2012** *112*(11), 6156–6214.
[117] Cunha, E.; Proença, M. F.; Pereira, M. G.; Fernandes, M. J.; Young, R. J.; Strutynski, K.; Melle-Franco, M.; Gonzalez-Debs, M.; Lopes, P.E.; da Conceição Paiva, M. Water Dispersible Few-Layer Graphene Sabilized by a Novel Pyrene Derivative at Micromolar Concentration. *Nanomaterials*, **2018**, *8*, 675-692.
[118] Lee, D. W.; Kim, T.; Lee, M. An Amphiphilic Pyrene Sheet for Selective Functionalization of Graphene. *Chem. Commun*. **2011**, *47*, 8259−8261.
[119] Mann, J. A.; Rodríguez-López, J.; Abruña, H. D.; Dichtel, W. R. Multivalent Binding Motifs for the Noncovalent Functionalization of Graphene. *J. Am. Chem. Soc.* **2011***, 133*(44), 17614–17617

[120] Chandra, V.; Park, J.; Chun, Y.; Lee, J. W.; Hwang, I.-C.; Kim, K. S. Water-Dispersible Magnetite-Reduced Graphene Oxide Composites for Arsenic Removal. *ACS Nano,* **2010**, 4, 3979-3986.
[121] Alegret, N.; Criado, A.; Prato, M. Recent Advances of Graphene-based Hybrids with Magnetic Nanoparticles for Biomedical Applications. *Curr. Med. Chem.* **2017**, *24*(5), 529–536.
[122] Con, H. P.; He, J. J.; Lu, Y.; Yu, S. H. Water soluble magnetic functionalized reduce graphene oxde sheets: In situ synthesis and magnetic resonance imaging applications. *Small*, **2010**, *6*(2) 169-173.
[123] a) Balcioglu, M.; Rana, M.; Yigit, M.V. Doxorubicin loading on graphene oxide, iron oxide and gold nanoparticle hybrid. *J. Mater. Chem. B*. **2013**, *1*(45), 6187-6193. b) Pourjavadi, A.; Tehrani, Z.; Shakerpoor, A. Dendrimer-like supramolecular nanovalves based on polypseudorotaxane and mesoporous silica-coated magnetic graphene oxide: a potential pHsensitive anticancer drug carrier. *Supramol. Chem*., **2016**, *28*(7-8), 624-633.
[124] a) Yang, K.; Hu, L.; Ma, X.; Ye, S.; Cheng, L.; Shi, X.; Li, C.; Li, Y.; Liu, Z. Multimodal imaging guided photothermal therapy using functionalized graphene nanosheets anchored with magnetic nanoparticles. *Adv. Mater*. **2012**, *24*(14), 1868-1872. b) Fu, G.; Zhu, L.; Yang, K.; Zhuang, R.; Xie, J.; Zhang, F. Diffusion-weighted magnetic resonance imaging for therapy response monitoring and early treatment prediction of photothermal therapy. *ACS Appl. Mater. Inter.* **2016**, *8*(8), 5137-5147.
[125] Kanchanapally, R.; Fan, Z.; Singh, A. K.; Sinha, S. S.; Ray, P. C.; Multifunctional hybrid graphene oxide for label-free detection of malignant melanoma from infected blood. *J. Mater. Chem. B,* **2014***, 2*(14), 1934–1937.
[126] Huang, J.; Zhang, L.; Chen, B.; Ji, N.; Chen, F.; Zhang, Y.; Zhang, Z. Nanocomposites of size-controlled gold nanoparticles and graphene oxide: Formation and applications in SERS and catalysis*. Nanoscale.* **2010***, 2*(12), 2733*.*
[127] Mali, K. S.; Greenwood, J.; Adisoejoso, J.; Phillipson, R.; De Feyter, S. Nanostructuring graphene for controlled and reproducible functionalization. *Nanoscale,* **2015***, 7(5), 1566–1585.*
[128] Otero, R.; Gallego, J. M.; Vázquez de Parga, A. L.; Martín, N.; Miranda, R. Molecular self-assemby at solid surfaces. *Adv. Mater.* **2011**, *23*, 5148-5176.
[129] Schwierz, F. Graphene transistors. *Nat. Nanotechnol.* **2010***, 5*(7), 487–496.
[130] Wang, Q. H.; Hersam, M. C. Room-Temperature Molecular-Resolution Characterization of Self-Assembled Organic Monolayers on Epitaxial Graphene. *Nat. Chem*, **2009**, *1*, 206−211.
[131] Xia, Z.; Leonardi, F.; Gobbi, M.; Liu, Y.; Bellani, V.; Liscio, A.; Kovtun, A.; Li, R.; Feng, X.; Orgiu, E.; Samorì, P.; Treossi, E.; and Palermo, V. Electrochemical Functionalization of Graphene at the Nanoscale with Self-Assembling Diazonium Salts. *ACS Nano,* **2016**, *10*(7), 7125-7134.
[132] Li, D.; Zhang, W.; Yu, X.; Wang, Z.; Su, Z.; Wei, G. When biomolecules meet graphene: from molecular level interactions to material design and applications. *Nanoscale.* **2016***, 8*(47), 19491–19509.
[133] Green, N. S.; Norton, M. L. Interactions of DNA with graphene and sensing applications of graphene field-effect transistor devices: A review. *Anal. Chim. Acta*, **2015**, *853*, 127–142.
[134] Zhang, Y.; Wu, C.; Guo, S.; Zhang, J. Interactions of graphene and graphene oxide with proteins and peptides. *Nanotechnol. Rev.* **2013***, 2*(1) 27-45*.*
[135] Hughes, Z. E.; Walsh, T. R. What makes a good graphene-binding peptide? Adsorption of amino acids and peptides at aqueous graphene interfaces*. J. Mater. Chem. B.* **2015***, 3*(16), 3211–3221.
[136] Ferrari, A. C.; Bonaccorso, F.; Falko, V.; Novoselov, K. S.; Roche, S.; Bøggild, P.; Borini, S.; Koppens, F.; Palermo, V.; Pugno, N. Science and Technology Roadmap for Graphene, Related Two-Dimensional Crystals, and Hybrid Systems. *Nanoscale*. **2015**, 7, 4598–4810.
[137] Li, Y.; Feng, Z.; Huang, L.; Essa, K.; Bilotti, E.; Zhang, H.; Peijs, T.; Hao, L. Additive manufacturing high performance graphene-based composited: A review. Compos. Part. A-Appl. S. **2019**, *124*, 105483.
[138] Shuai, C.; Gao, C.; Feng, P.; Peng, S. Graphene-reinforced mechanical properties of calcium silicate scaffolds by laser sintering. *RSC Adv.* **2014**, *4*(25), 12782-12788.
[139] Lin, D.; Richard Liu, C.; Cheng, G. J. Single-layer graphene oxide reinforced metal matrix composites by laser sintering: Microstructure and mechanical property enhancement. Acta Mater. **2014**, *80*, 183-193.
[140] Jariwala, D.; Sangwan, V. K.; Lauhon, L. J.; Marks, T. J.; Hersam, M. C. Carbon nanomaterials for electronics, optoelectronics, photovoltaics, and sensing. *Chem. Soc. Rev.* **2013**, 42, 2824-2860.
[141] Sun, B.; Wang, B.; Su, D.; Xiao, L.; Ahn, H.; Wang, G. Graphene nanosheets as cathode catalysts for lithium-air batteries with an enhanced electrochemical performance. *Carbon*. **2012**, *50*, 727–733.
[142] Raccichini, R.; Varzi, A.; Passerini, S.; Scrosati, B. *Nat.* The role of graphene for electrochemical energy storage. *Mater.* **2015**, *14*, 271-279.
[143] Bae, S.; Kim, H.; Lee, Y.; Xu, X. F.; Park, J. S.; Zheng, Y.; Balakrishnan, J.; Lei, T.; Kim, H. R.; Song, Y. I. Kim, Y. J.; Kim, K. S. Ozyilmaz, B.; Ahn, J. H.; Hong, B. H.; Iijima, S. Roll-to-roll production of 30-inch graphene films for transparent electrodes. *Nat. Nanotechnol.* **2010** ,*5* ,574-578.
[144] Yin, Z.; Wu, S.; Zhou, X.; Huang, X.; Zhang, Q.; Boey, F.; Zhang, H. Electrochemical depositionof ZnO nanorods on transparent reduced graphene oxide electrodes for hybrid solar cells. *Small.* **2010** , *6*, 307-312.

[145] Miao, X.; Tongay, S.; Petterson, M. K.; Berke, K.; Rinzler, A. G.; Appleton, B. R.; Hebard, A. F. High efficiency graphene solar cells by chemical doping. *Nano Lett.* **2012**, *12*, 2745-2750.
[146] Liu, J.; Xue, Y.; Gao, Y.; Yu, D.; Durstock, M.; Dai, L. Hole and electron extraction layers based on graphene oxide derivatives for high-performance bulk heterojunction solar cells. *Adv. Mater.* **2012**, *24*, 2228-2233.
[147] Reina, G.; González-Domínguez, J. M.; Criado, A.; Vázquez, E.; Bianco, A.; Prato, M. Promises, facts and challenges for graphene in biomedical applications. *Chem. Soc. Rev.* **2017**, *46*(15), 4400–4416.
[148] Bianco, A. Graphene: safe of toxic? The two faces of the medals. *Angew. Chem. Int. Ed.* **2013**, 52, 4986-4997.
[149] Zhou, L.; Jiang, H.; Wei, S.; Ge, X.; Zhou, J.; Shen, J. High-efficiency loading of hypocrellin B on graphene oxide for photodynamic therapy. *Carbon*. **2012** *50*(15), 5594–5604.
[150] Sun, X.; Liu, Z.; Welsher, K.; Robinson, J. T.; Goodwin, A.; Zaric, S.; Dai, H. Nano-graphene oxide for cellular imaging and drug delivery. *Nano Res.* **2008**, *1*(3), 203–212.
[151] Zhou, K.; Zhu, Y.; Yang, X.; Li, C. One-pot preparation of graphene/Fe3O4 composites by a solvothermal reaction. *New J. Chem.* **2010***, 34*(12), 2950-2955.
[152] Liu, H.-W.; Hu, S.-H.; Chen, Y.-W.; Chen, S.-Y. Characterization and drug release behavior of highly responsive chip-like electrically modulated reduced graphene oxide–poly(vinyl alcohol) membranes*. J. Mater. Chem.* **2012***, 22*(33), 17311-17320*.*
[153] Wu, J.; Wang, Y.; Yang, X.; Liu, Y.; Yang, J.; Yang, R.; Zhang, N. Graphene oxide used as a carrier for adriamycin can reverse drug resistance in breast cancer cells. *Nanotechnol.* **2012***, 23*(35), 355101.
[154] Li, N.; Zhang, Q.; Gao, S.; Song, Q.; Huang, R.; Wang, L. Three-dimensional Graphene foam as a biocompatible and conductive scaffold for neural stem cells. *Sci. Rep*. **2013**, *3*, 1604.
[155] Fabbro, A.; Scaini, D.; León, V.; Vázquez, E.; Cellot, G.; Privitera, G.; Lombard, L.; Torrisi, F.; Tomarchio, F.; Bonaccorso, F.; Bosi, S.; Ferrari, A. C.; Ballerini, L.; Prato, M. Graphene-Based Interfaces Do Not Alter Target Nerve Cells. *ACS Nano.* **2016**, *10*, 615−623.
[156] Nayak, T. R.; Andersen, H.; Makam, V. S.; Khaw, C.; Bae, S.; Xu, X.; Özyilmaz, B. Graphene for Controlled and Accelerated Osteogenic Differentiation of Human Mesenchymal Stem Cells. *ACS Nano.* **2011**, *5*(6), 4670–4678.
[157] Prasadh, S.; Suresh, S.; Wong, R. Osteogenic Potential of Graphene in Bone Tissue Engineering Scaffolds. *Materials. **2018**, 11*(8), 1430*.*
[158] Pumera, M. Graphene in Biosensing. *Mater. Today*. **2011**, *14*(7-8) 308-315.
[159] Thévenot, D. R.; Toth, K.; Durst, R. A.; Wilson, G. S.Electrochemical biosensors: recommended definitions and classification. *Biosens. Bioelectron.* **2001**, *16*, 121-131.
[160] Pena-Bahamonde, J.; Nguyen, H. N.; Fanourakis, S. K.; Rodrigues, D. F. Recent advances in graphene-based biosensor technology with applications in life science. *J. Nanobiotechnol.* **2018**, 16, 75.
[161] Tiwari, J. N.; Vij, V.; Kemp, K. C.; Kim, K. S. Engineered Carbon-Nanomaterial-Based Electrochemical Sensors for Biomolecules. *ACS Nano*. **2015**, 10*(1), 46–80.*
[162] Shan, C.; Yang, H.; Song, J.; Han, D.; Ivaska, A.; Niu, L. Direct Electrochemistry of Glucose Oxidase and Biosensing for Glucose Based on Graphene. *Analytical Chemistry*. **2009**, *81*(6), 2378–2382*.*
[163]Wang, Y.; Shao, Y.; Matson, D. W.; Li, J.; Lin, Y. Nitrogen-Doped Graphene and Its Application in Electrochemical Biosensing*. ACS Nano.* **2010***, 4*(4), 1790–1798.
[164] Song, Y.; Qu, K.; Zhao, C.; Ren, J.; Qu, X. Graphene Oxide: Intrinsic Peroxidase Catalytic Activity and Its Application to Glucose Detection. *Advanced Materials.* **2010***, 22*(19), 2206–2210.
[165] Fiorani, A.; Merino, J. P.; Zanut, A.; Criado, A.; Valenti, G.; Prato, M.; Paolucci, F. Advanced carbon nanomaterials for electrochemiluminescent biosensor applications. *Curr. Opin. Electrochem.* **2019**, *16,* 66-74.
[166] Yang, L.; Li, Y.; Zhang, Y.; Fan, D.; Pang, X.; Wei, Q.; Du, B. 3D Nanostructured Palladium-Functionalized Graphene-Aerogel Supported Fe_3O_4 for Enhanced $Ru(bpy)_3^{2+}$-Based Electrochemiluminescent Immunosensing of Prostate Specific Antigen. *ACS Appl. Mater. Inter.* **2017**, *9*, 35260-35267.
[167] Zhou, B.; Zhu, M.; Qiu, Y.; Yang, P. Novel Electrochemiluminescence-Sensing Platform for the Precise Analysis of Multiple Latent Tuberculosis Infection Markers. *ACS Appl. Mater. Interfaces.* **2017***, 9*(22), 18493-18500.
[168] Lu, C.-H.; Yang, H.-H.; Zhu, C.-L.; Chen, X.; Chen, G.-N. A Graphene Platform for Sensing Biomolecules. *Angew. Chem. Int. Ed.* **2009***, 48*(26), 4785–4787.
[169] Chang, H.; Tang, L.; Wang, Y.; Jiang, J.; Li, J. Graphene Fluorescence Resonance Energy Transfer Aptasensor for the Thrombin Detection. *Anal. Chem.* **2010***, 82*(6), 2341–2346*.*
[170] Yoon, H. J.; Kim, T. H.; Zhang, Z.; Azizi, E.; Pham, T. M.; Paoletti, C.; Nagrath, S. Sensitive capture of circulating tumour cells by functionalized graphene oxide nanosheets. *Nat. Nanotechnol.* **2013***, 8*(11), 881–881*.*
[171] Mannoor, M. S.; Tao, H.; Clayton, J. D.; Sengupta, A.; Kaplan, D. L.; Naik, R. R.; McAlpine, M. C. Graphene-based wireless bacteria detection on tooth enamel. *Nat. Commun.* **2012**, *3*(1).

[172] Polat, E. O.; Mercier, G.; Nikitskiy, I.; Puma, E.; Galan, T.; Gupta, S.; Koppens, F. Flexible graphene photodetectors for wearable fitness monitoring. *Science Advances,* **2019***, 5*(9)*.*
[173] Huang, H.; Su, S.; Wu, N.; Wan, H.; Wan, S.; Bi, H.; Sun, L. Graphene-Based Sensors for Human Health Monitoring. *Frontiers in Chemistry*, **2019**, *7*, 399.
[174] Shockley, W. A Unipolar "Field-Effect" Transistor*. Proceedings of the IRE.* **1952***, 40(11), 1365–1376.*
[175] a) Nishizawa, J.-I. (1982) Junction Field-Effect Devices. *Semiconductor Devices for Power Conditioning. Springer, Boston, MA.* b) Torsi, L.; Magliulo, M.; Manoli, K.; Palazzo, G. Organic field-effect transistor sensors: a tutorial review. *Chem. Soc. Rev.* **2013***, 42*(22), 8612-8628.
[176] Dodabalapur, A.; Katz, H. E.; Torsi, L.; Haddon, R. C.Organic Heterostructure Field-Effect Transistors. *Science*. **1995**, *269*(5230), 1560-1562.
[177] Zaumseil, J.; Sirringhaus, H. Electron and ambipolar transport in organic field-effect transistors. *Chem. Rev.* **2007**, *107*, 1296–1323.
[178] Geim, A. K.; Novoselov, K. S. The rise of graphene. *Nat. Mater.* **2007**, *6*, 183-191.
[179] Green, N. S.; Norton, M. L. Interaction of DNA with graphene and sensing applications of graphene field-effect transistor devices: a review. *Anal. Chim. Acta*. **2014**, *853*, 127-142.
[180] Mackin, C.; *A Current–Voltage Model for Graphene Electrolyte-Gated Field-Effect Transistors. IEEE T.* Electron Dev. **2014**, *61*(12), 3971-3977.
[181] Pilon, L.; Wang, H.; d'Entremont, A. Recent advances in continuum modeling of interfacial and transport phenomena in electric double layer capacitors. *J. Electrochem. Soc*. **2015**, *162*(5) A5158-A5178.
[182] Grahame, D.C. The electrical double layer and the theory of electrocapillarity. Chem. Rev. **1947**, *41*(3): 441-501.
[183] Oldham, K. B. A Gouy–Chapman–Stern model of the double layer at a (metal)/(ionic liquid) interface. *J. Electroanal. Chem.* **2008**, *613*(2), 131–138.
[184] Brown, M. A.; Goel, A.; Abbas, Z. Effect of Electrolyte Concentration on the Stern Layer Thickness at a Charged Interface. *Angew. Chem. Int. Ed.* **2016***, 55*(11), 3790–3794.
[185] Chen, K.I.; Li, B.R.; Chen, Y.T. Silicon nanowire field-effect transistor-based biosensors for biomedical diagnosis and cellular recording investigation. *Nano Today.* **2011**, *6*, 131–154.
[186] Mao, S. Graphene Field-Effect Transistor Sensors. In Graphene Bioelectronics; Elsevier: Amsterdam, Netherlands, **2018**.
[187] Dong, X.; Shi, Y.; Huang, W.; Chen, P.;Li, L.-J. Electrical Detection of DNA Hybridization with Single-Base Specificity Using Transistors Based on CVD-Grown Graphene Sheets. *Adv. Mater*. **2010**, *22*(14), 1649-1653.
[188] Hwang, M. T.; Heiranian, M.; Kim, Y.; You, S.; Leem, J.; Taqieddin, A.; Bashir, R. Ultrasensitive detection of nucleic acids using deformed graphene channel field effect biosensors. *Nat. Comm.* **2020***, 11*(1) 1543.
[189] Mukherjee, S.; Meshik, X.; Choi, M.; Farid, S.; Datta, D.; Lan, Y.; Stroscio, M. A. A Graphene and Aptamer Based Liquid Gated FET-Like Electrochemical Biosensor to Detect Adenosine Triphosphate. *IEEE T. NanoBiosci.* **2015***, 14*(8), 967–972.
[190] Ohno, Y.; Maehashi, K.; Matsumoto, K. Label-Free Biosensors Based on Aptamer-Modified Graphene Field-Effect Transistors. *J. Am. Chem. Soc.* **2010***, 132*(51), 18012–18013.
[191] Wu, G.; Dai, Z.; Tang, X.; Lin, Z.; Lo, P. K.; Meyyappan, M.; Lai, K. W. C. Graphene Field-Effect Transistors for the Sensitive and Selective Detection of Escherichia coli Using Pyrene-Tagged DNA Aptamer. *Adv. Healthc. Mater.* **2017***, 6*(19), 1700736.
[192] Kwon, J.; Lee, Y.; Lee, T.; Ahn, J.-H. Aptamer-based field-effect transistor for detection of avian influenza virus in chicken serum. *Anal. Chem.* **2020**, *92*(7), 5524-5531.
[193] Kaisti, M. Detection principles of biological and chemical FET sensors. *Biosen. Bioelectron.* **2017***, 98, 437–448.*
[194] Kwak, Y. H.; Choi, D. S.; Kim, Y. N.; Kim, H.; Yoon, D. H.;, Ahn, S.-S.; Seo, S. Flexible glucose sensor using CVD-grown graphene-based field effect transistor. *Biosens.Bioelectron.* **2012***, 37*(1), 82–87.
[195] Niyonambaza, S. D.; Kumar, P.; Xing, P.; Mathault, J.; De Koninck, P.; Boisselier, E.; Miled, A. A Review of Neurotransmitters Sensing Methods for Neuro-Engineering Research. *Appl. Sci.* **2019***, 9*(21), 4719*.*
[196] Hess, L. H.; Lyuleeva, A.; Blaschke, B. M.; Sachsenhauser, M.; Seifert, M.; Garrido, J. A.; Deubel, F. Graphene Transistors with Multifunctional Polymer Brushes for Biosensing Applications. *ACS Appl. Mater. Inter.* **2014***, 6*(12), 9705–9710*.*
[197] a) Seo, G.; Lee, G.; Kim, M. J.; Baek, S.-H.; Choi, M.; Ku, K. B.; Kim, S. I. Rapid Detection of COVID-19 Causative Virus (SARS-CoV-2) in Human Nasopharyngeal Swab Specimens Using Field-Effect Transistor-Based Biosensor. *ACS Nano,* **2020***.* b) Andoy, N. M.; Filipiak, M. S.; Vetter, D.; Gutiérrez-Sanz, Ó.; Tarasov, A. Graphene-Based Electronic Immunosensor with Femtomolar Detection Limit in Whole Serum. *Adv. Mater. Technol.* **2018**, 1800186*.*

[198] Seo, G.; Lee, G., Kim, M. J.; Baek, S.-H.; Choi, M.; Ku, K. B.; Kim, S. I. Rapid Detection of COVID-19 Causative Virus (SARS-CoV-2) in Human Nasopharyngeal Swab Specimens Using Field-Effect Transistor-Based Biosensor. *ACS Nano,* **2020***.*
[199] Kanai, Y.; Ohmuro-Matsuyama, Y.; Tanioku, M.; Ushiba, S.; Ono, T.; Inoue, K.; Matsumoto, K. Graphene field effect transistor-based immunosensor for ultrasensitive noncompetitive detection of small antigens. *ACS Sensors,* **2020**.
[200] Hébert, C.; Masvidal-Codina, E.; Suarez-Perez, A.; Calia, A. B.; Piret, G.; Garcia-Cortadella, R.; Illa, X.; Del Corro Garcia, E.; De la Cruz Sanchez, J. M.; Casals, D. V.; Prats-Alfonso, E.; Bousquet, J.; Godignon, P.; Yvert, B.; Villa, R.; Sanchez-Vives, M. V.; Guimerà-Brunet, A.; Garrido, J. A. Flexible Graphene Solution-Gated Field-Effect Transistors: Efficient Transducers for Micro-Electrocorticography, *Adv. Funct. Mater.* **2017**, 28(12), 1703976
[201] Masvidal-Codina, E.; Illa, X.; Dasilva, M.; Calia, A. B.; Dragojević, T.; Vidal-Rosas, E. E.; Prats-Alfonso, E.; Martínez-Aguilar, J.; De la Cruz, J. M.; Garcia-Cortadella, R.; Godignon, P.; Rius, G.; Camassa, A.; Del Corro, E.; Bousquet, J.; Hébert, C.; Durduran, T.; Villa, R.; Sanchez-Vives, M. V.; Garrido, J. A.; Guimerà-Brunet, A. High-resolution mapping of infraslow cortical brain activity enabled by graphene microtransistors, *Nat. Mater.* **2019**, *18*, 280–288.
[202] a) Leopold, J.; Popkova, Y.; Engel, K.; Schiller, J. Recent Developments of Useful MALDI Matrices for the Mass Spectrometric Characterization of Lipids. *Biomolecules.* **2018***, 8*(4), 173*.* b) Wang, J.; Liu, Q.; Liang, Y.; Jiang, G. Recent progress in application of carbon nanomaterials in laser desorption/ionization mass spectrometry. *Anal. Bioanal. Chem.* **2016***, 408*(11), 2861–2873.
[203] Peterson, D. S. Matrix-free methods for laser desorption/ionization mass spectrometry. *Mass Spectrometry Reviews*, **2007**, *26*, 19–34
[204] Lu, M.; Yang, X.; Yang, Y.; Qin, P.; Wu, X.; Cai, Z. Nanomaterials as Assisted Matrix of Laser Desorption/Ionization Time-of-Flight Mass Spectrometry for the Analysis of Small Molecules*. Nanomaterials.* **2017***, 7*(4), 87*.*
[205] Dong, X.; Cheng, J.; Li, J.; Wang, Y. Graphene as a Novel Matrix for the analysis of Small Molecules by MALDI-TOF. *Anal. Chem*. **2010**, *82*, 6208–6214.
[206] Zhou, D.; Guo, S.; Zhang, M.; Liu, Y.; Chen, T.; Li, Z. Mass spectrometry imaging of small molecules in biological tissues using graphene oxide as matrix. *Anal. Chim. Acta*. **2017** *962*, 52-59.
[207] Zhang, W.; Han, H.; Bai, H.; Tong, W.; Zhang, Y.; Ying, W.; Qin, W.; Qian, X. A highly efficient and visualized method for glycan enrichment by self-assembling pyrene derivative functionalized free graphene oxide. *Anal. Chem. **2013**, 85* 2703–2709
[208] López de Laorden, C.; Beloqui, A.; Yate, L.; Calvo, J.; Puigivila, M.; Llop, J.; Reichardt, N. C. Nanostructured Indium Tin Oxide Slides for Small-Molecule Profiling and Imaging Mass Spectrometry of Metabolites by Surface-Assisted Laser Desorption Ionization MS. *Anal. Chem*. **2015**, *87*, 431−440.
[209] Wei, J.; Buriak, J.M.; Siuzdak, G. Desorption-ionization mass spectrometry on porous silicon. *Nature*, **1999**, *399*, 243–246.
[210] Chen, C. T.; Chen, Y. C. Desorption/ionization mass spectrometry on nanocrystalline titania sol-gel-deposited films. *Rapid Commun. Mass Spectrom*. **2004**, *18,* 1956–1964.
[211] Peterson, D. S.; Luo, Q. Z.; Hilder, E. F.; Svec, F.; Frechet, J. M. J. Porous polymer monolith for surface-enhanced laser desorption/ionization time-of- flight mass spectrometry of small molecules. *Rapid Commun Mass Spectrom*. **2004**, *18*, 1504–1512.
[212] Go, E. P.; Apon, J. V.; Luo, G.; Saghatelian, A.; Daniels, R. H.; Sahi, V.; Dubrow, R.; Cravatt, B. F.; Vertes, A.; Siuzdak, G. Desorption/ionization on silicon nanowires. *Anal. Chem.* **2005**, *77*, 1641–1646.
[213] Qian, K.; Zhou, L.; Liu, J.; Yang, J.; Xu, H.; Yu, M.; Yu, C. Laser Engineered Graphene Paper for Mass Spectrometry Imaging. *Scientific Reports*. **2013**, *3*(1), 1415.
[214] Kang, H.; Yun, H.; Lee, S. W.; Yeo, W.-S. Analysis of small biomolecules and xenobiotic metabolism using converted graphene-like monolayer plates and laser desorption/ionization time-of-flight mass spectrometry*. Talanta.* **2017***, 168,* 240–245*.*
[215] Wang, D.; Huang, X.; Li, J.; He, B.; Liu, Q.; Hu, L.; Jiang, G. 3D printing of graphene-doped target for “matrix-free” laser desorption/ionization mass spectrometry *Chem. Commun.* **2018***, 54,* 2723–2726.
[216] Wu, J.-B.; Lin, M.-L.; Cong, X.; Liua, H.-N.; Tan, P.-H. Raman spectroscopy of graphene-based materials and its applications in related devices. *Chem. Soc. Rev*. **2018**, *47*, 1822-1873.
[217] Ferrari, A.C. Raman spectroscopy of graphene and graphite: Disorder, electron–phonon coupling, doping and nonadiabatic effects. *Solid State Commun.* **2007**, *143*, 47-57.
[218] Ferrari, A. C. Raman spectroscopy as a versatile tool for studing the properties of graphene. *Nature Nanotechnol.* **2013**, *8*, 235-246.
[219] Milani, A.; Tommasini, M.; Russo, V.; Bassi, A. L.; Lucotti, A.; Cataldo, F.; Casari, C. S. Raman spectroscopy as tool to investigate the structure and electronic properties of carbon-atom wires. Beilstein *J. Nanotechnol*. **2015**, *6*, 480–491.

[220] Sulleiro, M. V.; Quiroga, S.; Pena, D.; Perez, D.; Guitian, E. Microwave-induced covalent functionalization of few-layer graphene with arynes under solvent-free conditions. *Chem. Commun.* **2018**, *54*, 2086-2089.
[221] Scanning electron microscopy (SEM) analysis of tribofilms enhanced by fullerene-like nanoparticles. István Zoltán Jenei Thesis, Stockholms universitet **2012**
[222] Hernandez, Y.; Nicolosi, V.; Lotya, M.; Blighe, F. M.; Sun, Z. Y.; De, S.; McGovern, I. T.; Holland, B.; Byrne, M.; Gun'ko, Y. K.; Boland, J. J.; Niraj, P.; Duesberg, G.; Krishnamurthy, S.; Goodhue, R.; Hutchison, J.; Scardaci, V.; Ferrari, A. C.; Coleman, J. N. High-yield production of graphene by liquid-phase exfoliation of graphite. *Nat. Nanotechnol.* **2008**, *3*, 563-568.
[223] Binnig, G.; Quate, C. F.; Gerber, C. Atomic force microscope. *Phys. Rev. Lett.***1986**, *56*, 930–933.
[224] Guo D.; Xie, G.; Luo, J.; Mechanical Properties of nanoparticles: basics and applications. *J. Phys. D: Appl. Phys.* **2014**, *47*, 013001.
[225] Bruker. Peakforce tapping. How AFM Shold Be, 2012, *14*.
[226] Jalili, N.; Laxminarayana, K. A review of atomic force microscopy imaging systems: Application to molecular metrology and biological sciences. *Mechatronics.* **2004**, *14,* 907–945.
[227] https://www.bruker.com/cn/products/mass-spectrometry-and-separations/maldi-toftof.html
[228] Karas, M.; Krüger, R. Ion Formation in MALDI: The Cluster Ionization Mechanism". *Chem. Rev*. **2003**, *103*(2), 427–440.
[229] de Gennes, P. G. Wetting: Statics and dynamics, *Rev. Mod. Phys.* **1985**, *57*, 827-863.
[230] Neurological disorders: public health challenges, World Health Organization 2006, ISBN 978 92 4 156336 9
[231] Jiang, X.; Sui, X.; Lu, Y.; Yan, Y.; Zhou, C.; Li, L.; Chai, X. In vitro and *in vivo* evaluation of a photosensitive polyimide thin-film microelectrode array suitable for epiretinal stimulation. *J. Neuroeng. Rehabil.* **2013**, *10*(1), 1.
[232] Obien, M. E. J.; Deligkaris, K.; Bullmann, T.; Bakkum, D. J. Revealing neuronal function through microelectrode array recordings. *Front. Neurosci.* **2015**, *8*, 423.
[233] Nemani, K. V.; Moodie, K. L.; Brennick, J. B.; Su, A.; Gimi, B. In vitro and *in vivo* evaluation of SU-8 biocompatibility. *Mater. Sci. Eng. C*. **2013**. *33*(7), 4453-4459.
[234] Lathrop, J. W. The Diamond Ordnance Fuze Laboratory's Photolithographic Approach to Microcircuits, *IEEE Ann. Hist. Comput.* **2013**. *35*, 48–55.
[235] Masvidal, E. Modelling and fabrication of graphene solution-gated field-effect transistors for electrophysiological applications (Master thesis). Universitat Autònoma de Barcelona, Barcelona. **2016**.
[236] Narasimhan, B.; Mallapragrada, S. K. Dissolution of amorphous and semicrystalline polymers: mechanisms and novel applications. *Recent DEV. Macromol. Res.* **1998**, *3* (2), 311-324.
[237] Miller-Chou, B. A.; Koenig, J. L., A review of polymer dissolution. *Progress in Polymer Science* 2003, *28* (8), 1223-1270.
[238] Crank, J.; Park, G. S. Diffusion in polymers. *New York: Academic Press*. **1968**, 219-257.
[239] Barton, A. F. M. CRC handbook of polymer-liquid interaction parameters and solubility parameters. *CRC Press*. **1990**.
[240] Polymer Handbook, 4th ed. Edited by Brandup, J.; Immergut, E. H.; Grulke, E. A. Associate Editors: Abe, A.; Bloch, D. R. John Wley and Sons, New York, 1999, volume 2, chapter VII.
[241] Susi, T.; Scardamaglia, M.; Mustonen, K.; Tripathi, M.; Mittelberger, A.; Al-Hada, M.; Amati, M.; Sezen, H.; Bittencourt, C.; Kotakoski, J. Intrinsic core level photoemission of suspended monolayer graphene. *Phys. Rev. Materials*. **2018**, *2*, 074005.
[242] Gadelmawla, E. S.; Koura, M. M.; Maksoud, T. M. A.; Elewa, I, M.; Soliman, H. H. *J. Mater. Process.* **2002**, *123*, 133-145.
[243] a) Lin, L.; Zhang, J.; Su, H.; Li, J.; Sun, L.; Wang, Z.; Liu, Z. Towards super-clean graphene. *Nat. Commun.* **2019***, 10*(1). b) Choi, W.; Shehzad, M. A.; Park, S.; Seo, Y. Influence of removing PMMA residues on surface of CVD graphene using a contact-mode atomic force microscope*. RSC Advances.* **2017***, 7*(12), 6943–6949.
[244] Miller-Chou, B. A.; Koenig, J. L. A review of polymer dissolution. *Progress in Polymer Science.* **2003***, 28*(8), 1223–1270.
[245] Ouano, A. C.; Carothers, J. A. Dissolution dynamics of some polymers: Solvent-polymer boundaries. *Polym. Eng. Sci.* **1980***, 20*(2), 160–166.
[246] a) Schaefer, N.; Garcia-Cortadella, R.; Calia, A. B.; Mavredakis, N.; Illa, X.; Masvidal-Codina, E.; Garrido, J. A. Improved metal-graphene contacts for low-noise, high-density microtransistor arrays for neural sensing*. Carbon,* **2020**, *161*, 647-655. b) Hébert, C.; Masvidal-Codina, E.; Suarez-Perez, A.; Calia, A. B.; Piret, G.; Garcia-Cortadella, R.; Garrido, J. A. Flexible Graphene Solution-Gated Field-Effect Transistors: Efficient Transducers for Micro-Electrocorticography. *Adv. Funct. Mater.* **2017***, 28*(12), 1703976.
[247] Larrimore, L.; Nad, S.; Zhou, X.; Abruña, H.; McEuen, P. L. Probing Electrostatic Potentials in Solution with Carbon Nanotube Transistors. *Nano Lett.* **2006***, 6*(7), 1329–1333*.*

[248] Lipka, K.; Bülow, H. H. Lactic acidosis following convulsions, *Acta Anaesthesiol. Scand*. **2003**, 47, 616-618.
[249] Bouša, D.; Pumera, M.; Sedmidubský, D.; Šturala, J.; Luxa, J.; Mazánek, V.; Sofer, Z. Fine tuning of graphene properties by modification with aryl halogens. *Nanoscale.* **2016***, 8*(3), 1493–1502.
[250] Bahr, J. L.; Tour, J. M. Highly Functionalized Carbon Nanotubes Using in Situ Generated Diazonium Compounds*. Chem. Mater.* **2001***, 13*(11), 3823–3824*.*
[251] Marzaro, G.; Guiotto, A.; Pastorini, G.; Chilin, A. A novel approach to quinazolin-4(3H)-one via quinazoline oxidation: an improved synthesis of 4-anilinoquinazolines. *Tetrahedron.* **2010***, 66*(4), 962–968.
[252] Gelder, E. A.; Jackson, S. D.; Lok, C. M. A study of Nitrobenzene hydrogenation over palladium/carbon catalysts. *Catal. Lett*. **2002**, *84*(3/4), 205–208.
[253] Deng, S.; Berry, V. Wrinkled, rippled and crumpled graphene: an overview of formation mechanism, electronic properties, and applications. *Mater. Today.* **2016** *19*(4), 197–212.
[254] Badawi, H. M.; Förner, W. Analysis of the infrared and Raman spectra of phenylacetic acid and mandelic (2-hydroxy-2-phenylacetic) acid. Spectrochim. Acta A. **2011***, 78*(3), 1162–1167.
[255] Fu, W.; Nef, C.; Knopfmacher, O.; Tarasov, A.; Weiss, M.; Calame, M.; Schönenberger, C. Graphene Transistors Are Insensitive to pH Changes in Solution. *Nano Letters.* **2011***, 11*(9), 3597–3600.
[256] Haslam, C.; Damiati, S.; Whitley, T.; Davey, P.; Ifeachor, E.; Awan, S. Label-Free Sensors Based on Graphene Field-Effect Transistors for the Detection of Human Chorionic Gonadotropin Cancer Risk Biomarker. *Diagnostics*, **2018**, *8*(1), 5.
[257] Handbook of immunoblotting of protein, Edited by Ole J. Bjerrum and Niels H. H. Heegaard. CRC Press INC, Florida, 2000, Volume II.
[258] Balamurugan, S.; Obubuafo, A.; Soper, S. A.; Spivak, D. A. Surface immobilization methods for aptamer diagnostic applications. *Anal. Bioanal. Chem.* **2007***, 390*(4), 1009–1021.
[259] Wu, Z.-S.; Guo, M.-M.; Zhang, S.-B.; Chen, Jiang, J.-H.; Shen, G.-L.; Yu, R.-Q. Reusable Electrochemical Sensing Platform for Highly Sensitive Detection of Small Molecules Based on Structure-Switching Signaling Aptamers*. Anal. Chem.* **2007***, 79*(7), 2933–2939*.*
[260] a) Baldrich, E.; Restrepo, A.; O'Sullivan, C. K. Aptasensor development: elucidation of critical parameters for optimal aptamer performance. *Anal. Chem.* **2004**, *76*, 7053–7063. b) Schlensog, M. D.; Gronewold, T. M. A.; Tewes, M.; Famulok, M.; Quandt, E. A love-wave biosensor using nucleic acids as ligands. Sens. *Acutators B* **2004**, *101*, 308–315. c) Minunni, M.; Tombelli, S.; Gullotto, A.; Luzi, E.; Mascini, M. Development of biosensors with aptamers as bio-recognition element: the case of HIV-1 Tat protein. *Biosens. Bioelectron*, **2004**, *20*, 1149–1156.
[261] Cheng, C.; Li, S.; Thomas, A.; Kotov, N. A. Haag, R. Functional Graphene Nanomaterials Based Architechtures: Biointeractions, Fabrications, and Emerging Biologcal Applications. *Chem. Rev.* **2017**, *117*, 1826-1914.
[262] Cummings, R. D.; Etzler, M. E. Antibodies and Lectins in Glycan Analysis *Essentials of Glycobiology* ed A Varki, R Cummings and J Esko (Cold Spring Harbor Laboratory Press, Cold Spring Harbor (NY)) 2009, 1–25.
[263] Serna, S.; Ercinbengoa M.; Marimón, J. M.; Reichardt, N. C. Measuring Bacterial Glycosyl Hydrolase Activity with a Soluble Capture Probe by Mass Spectrometry. *Anal. Chem*. **2018**, *90*, 12536-43.
[264] Noh, S.; Suman, C. K.; Lee, D.; Kim, S.; Lee, C. Study of Buffer Layer Thickness on Bulk Heterojunction Solar Cell. *J. Nanosci. Nanotechnol.* **2010***, 10*(10), 6815–6818.
[265] a) Kumarathasan, P.; Das, D.; Salam, M. A.; Mohottalage, S.; DeSilva, N.; Simard, B.; Vincent, R. Mass spectrosmetr-based proteomic assessment of the invitro toxicity of carbon nanotubes. *Curr. Top. Biochem.* **2012***, 14*(1), 15-26. b) Wang, P.; Giese, R. W. Recommendations for quantitative analysis of small molecules by matrix-assisted laser desorption ionization mass spectrometry. *Journal of Chromatography A.* **2017***, 1486, 35–41.*
[266] Beloqui, A.; Calvo, J.; Serna, S.; Yan, S.; Wilson, I. B. H.; Martin-Lomas, M.; Reichardt, N. C. Analysis of microarrays by MALDI-TOF MS. *Angew. Chemie- Int. Ed.* **2013***,* 52, 7477–7481.
[267] Meléndrez, D.; Jowitt, T.; Iliut, M.; Verre, A. F.; Goodwin, S.; Vijayaraghavan, A. Adsorption and binding dynamics of graphene-supported phospholipid membranes using the QCM-D technique. *Nanoscale.* **2018***, 10*(5), 2555–2567*.*
[268] Ghazarian, H.; Idoni, B.; Oppenheimer, S. B. A glycobiology review: Carbohydrates, lectins and implications in cancer therapeutics. *Acta Histochemica.* **2011***, 113*(3), 236–247*.*
[269] Gray, C. J.; Sánchez-Ruíz, A.; Šardzíková, I.; Ahmed, Y. A.; Miller, R. L.; Reyes-Martinez, J. E.; Pallister, E.; Huang, K.; Both, P.; Hartmann, M.; Roberts, H. N.; Šardzík, R.; Mandal, S.; Turnbull, J. E.; Eyers, C. E.; Flitsch, S. L. Label-Free Discovery Array Platform for the Characterization of Glycan Binding Proteins and Glycoproteins. *Anal. Chem.* **2017***, 89*, 4444–4451.
[270] Norton, P.; Comunale, M. A.; Herrera, H.; Wang, M.; Houser, J.; Wimmerova, M.; Romano, P. R.; Mehta, A. Development and application of a novel recombinant Aleuria aurantia lectin with enhanced core

fucose binding for identification of glycoprotein biomarkers of hepatocellular carcinoma. *Proteomics.* **2016***, 16*, 3126–3136.
[271] a) Ji, D. K.; Zhang, Y.; He, X. P.; Chen, G. R. An insight into graphene oxide associated fluorogenic sensing of glycodye-lectin interactions. *J. Mater. Chem. B.* **2015**, *3,* 6656–6661. b) Chen, Q.; Wei, W.; Lin, J. M. Homogeneous detection of concanavalin A using pyrene-conjugated maltose assembled graphene based on fluorescence resonance energy transfer. *Biosens. Bioelectron.* **2011***,* 26, 4497–502.
[272] Masvidal, E. Modelling and fabrication of graphene solution-gated field-effect transistors for electrophysiological applications (Master thesis). Universitat Autònoma de Barcelona, Barcelona. **2016**.